

From Nuclei to Compact Stars

Contents

1	Topics	1317
2	Participants	1319
2.1	ICRANet	1319
2.2	External on going collaborations	1319
2.3	Postdocs	1320
2.4	Graduate Students	1320
3	Relevant Results (before 2014)	1323
3.1	Nuclear and Atomic Astrophysics	1323
3.2	White Dwarfs Physics and Structure	1327
3.3	White Dwarf Astrophysics	1328
3.4	Neutron Star Physics and Structure	1330
3.5	Neutron Star Astrophysics	1333
3.6	Radiation Mechanisms of White Dwarfs and Neutron Stars . .	1335
3.7	Exact Solutions of the Einstein and Einstein-Maxwell Equations in Astrophysics	1336
3.8	Critical Fields and Non-Linear Electrodynamics Effects in Astrophysics	1338
4	Publications (before 2014)	1339
4.1	Refereed Journals	1339
4.2	Conference Proceedings	1341
5	Highlights 2014	1347
5.1	Nuclear and Atomic Astrophysics	1347
5.2	White Dwarfs Physics and Structure	1348
5.3	White Dwarfs Astrophysics	1349
5.4	Neutron Star Physics and Structure	1350
5.5	Neutron Star Astrophysics	1352
5.6	Radiation Mechanisms of White Dwarfs and Neutron Stars . .	1355
5.6.1	Gravitational Waves Radiation	1355
5.7	Exact Solutions of the Einstein and Einstein-Maxwell Equations in Astrophysics	1356
5.8	Critical Fields and Non-linear Electrodynamics Effects in Astrophysics	1357

6 Publications 2014	1359
6.1 Refereed Journals	1359
6.1.1 Printed	1359
6.1.2 Accepted for publication or in press	1366
6.1.3 Submitted	1368
6.1.4 In preparation	1370
Bibliography	1373

1 Topics

The study of compact objects such as white dwarfs, neutron stars and black holes requires the interplay between nuclear and atomic physics together with relativistic field theories, e.g., general relativity, quantum electrodynamics, quantum chromodynamics, as well as particle physics. In addition to the theoretical physics aspects, the study of astrophysical scenarios characterized by the presence of a compact object has also started to be focus of extensive research within our group. The research which has been done and is currently being developed within our group can be divided into the following topics:

- **Nuclear and Atomic Astrophysics.** Within this subject of research we study the properties and processes occurring in compact stars in which nuclear and atomic physics have to be necessarily applied. We focus on the properties of nuclear matter under extreme conditions of density and pressure found in these objects. The equation of state of the matter in compact star interiors is studied in detail taking into account all the interactions between the constituents within a full relativistic framework.
- **White Dwarfs Physics and Structure.** The aim of this part of our research is to construct the structure of white dwarfs within a self-consistent description of the equation of state of the interior together with the solution of the hydrostatic equilibrium equations in general relativity. Both unmagnetized and magnetized white dwarfs are studied.
- **White Dwarfs Astrophysics.** We are within this topic interested in the astrophysics of white dwarfs both isolated and in binaries systems. Magnetized white dwarfs, soft gamma repeaters, anomalous X-ray pulsars, white dwarf pulsars, cataclysmic variables, binary white dwarf mergers, and type Ia supernovae are studied. The role of a realistic white dwarf interior structure is particularly emphasized.
- **Neutron Stars Physics and Structure.** We calculate the properties of the interior structure of neutron stars using realistic models of the nuclear matter equation of state within the general relativistic equations of equilibrium. Strong, weak, electromagnetic and gravitational interactions have to be jointly taken into due account within a self-consistent

fully relativistic framework. Both unmagnetized and magnetized neutron stars are studied.

- **Neutron Stars Astrophysics.** We study astrophysical systems harboring neutron stars such as isolated and binary pulsars, low and intermediate X-ray binaries, inspiraling and merging double neutron stars. Most extreme cataclysmic events involving neutron stars and their role in the explanation of extraordinarily energetic astrophysical events such as gamma-ray bursts are analyzed in detail.
- **Radiation Mechanisms of White Dwarfs and Neutron Stars.** We here study the possible emission mechanisms of white dwarfs and neutron stars. We are thus interested in both electromagnetic and gravitational radiation at work in astrophysical systems such as compact star magnetospheres, inspiraling and merging relativistic double neutron stars, neutron star-white dwarfs, and neutron star-black hole binaries represent some examples.
- **Exact Solutions of the Einstein and Einstein-Maxwell Equations in Astrophysics.** We analyze the ability of analytic exact solutions of the Einstein and Einstein-Maxwell equations to describe the exterior spacetime of compact stars such as white dwarfs and neutron stars. The problem of matching between interior and exterior spacetimes is addressed in detail. The effect of the quadrupole moment on the properties of the spacetime is also investigated. Particular attention is given to the application of exact solutions in astrophysics, e.g. the dynamics of particles around compact stars and its relevance in astrophysical systems such as X-ray binaries.
- **Critical Fields and Non-linear Electrodynamics Effects in Astrophysics.** We study the conditions under which ultrastrong electromagnetic fields can develop in astrophysical systems such as neutron stars and in the process of gravitational collapse to a black hole. The effects of non-linear electrodynamics minimally coupled to gravity are investigated. New analytic and numeric solutions to the Einstein-Maxwell equations representing black holes or the exterior field of a compact star are obtained and analyzed. The consequences on extreme astrophysical systems, for instance gamma-ray bursts, is studied.

2 Participants

2.1 ICRANet

- D. Arnett (Steward Observatory, University of Arizona, USA)
- D. Bini (Istituto Nazionale per l'Applicazione del Calcolo, Italy)
- L. Izzo (ICRANet, University of Rome, Italy)
- H. Kleinert (Free University of Berlin , Germany)
- V. Popov (ITEP, Moscow, Russia)
- J. A. Rueda (ICRANet, University of Rome, Italy)
- R. Ruffini (ICRANet, University of Rome, Italy)
- G. Vereschagin (ICRANet, University of Rome, Italy)
- S.-S. Xue (ICRANet, University of Rome, Italy)

2.2 External on going collaborations

- K. Boshkayev (Al-Farabi Kazakh National University, Kazakhstan)
- C. Cherubini (Università Campus Biomedico, Rome, Italy)
- S. Chiapparini (Universidade do Estado do Rio de Janeiro, Brazil)
- S. B. Duarte (Centro Brasileiro de Pesquisas Físicas, Brazil)
- S. Filippi (Università Campus Biomedico, Rome, Italy)
- C. L. Fryer (University of Arizona, Los Alamos National Laboratory, USA)
- E. Gacía-Berro (Universitat Politècnica de Catalunya, Spain)
- P. LorénAguilar (University of Exeter, United Kingdom)
- S. O. Kepler (Universidade Federal do Rio Grande do Sul, Brazil)

- B. Külebi (Institut de Ciències de l'Espai, Spain)
- M. Malheiro (Instituto Tecnológico de Aeronáutica, Brazil)
- R. M. Jr. Marinho (Instituto Tecnológico de Aeronáutica, Brazil)
- G. Mathews (University of Notre Dame, USA)
- D. P. Menezes (Universidade Federal de Santa Catarina, Brazil)
- H. Mosquera-Cuesta (Instituto Federal de Educacao, Ciência e Tecnologia do Ceará, Brazil)
- R. Negreiros (Universidade Federal de Fluminense, Brazil)
- L. Pachón (Universidad de Antioquia, Colombia)
- H. Quevedo (Universidad Nacional Autónoma de México, Mexico)
- C. Valenzuela (Universidad del Valle, Colombia)
- C. A. Z. Vasconcellos (Universidade Federal do Rio Grande do Sul, Brazil)

2.3 Postdocs

- R. Belvedere (ICRANet-Rio, Universidade Federal Fluminense)
- R. Camargo (ICRANet, University of Rome, Italy)
- J. G. Coelho (ICRANet, University of Rome, Italy)
- S. M. de Carvalho (ICRANet-Rio, Universidade Federal Fluminense)

2.4 Graduate Students

- L. Becerra (ICRANet, University of Rome, Italy)
- D. L. Cáceres (ICRANet, University of Rome, Italy)
- F. Cipolletta (ICRANet, University of Rome, Italy)
- M. Muccino (ICRANet, University of Rome, Italy)
- F. G. Oliveira (ICRANet, University of Rome, Italy and Université de Nice Sophia-Antipolis, France)

- J. P. Pereira (ICRANet, University of Rome, Italy and Université de Nice Sophia-Antipolis, France)
- M. L. Warren (University of Notre Dame, USA)
- Y. Wu (ICRANet, University of Rome, Italy and Université de Nice Sophia-Antipolis, France)

3 Relevant Results (before 2014)

3.1 Nuclear and Atomic Astrophysics

One of the main objectives have been to construct a unified approach for nuclei, superheavy nuclei up to atomic numbers of the order of 10^5 – 10^6 , and what we have denominated “nuclear matter cores of stellar dimensions”:

- characterized by atomic number of the order of 10^{57} ;
- composed by a degenerate fluid of neutrons, protons and electrons in β -equilibrium;
- globally neutral configurations;
- expected to be kept at nuclear density by self gravity.

The study of all these objects going from the microscopic to the macroscopic is at the base of the theory of white dwarfs, neutron stars, hyperon stars, strange quark stars, and other related compact objects. It is known that the Thomas-Fermi model has been extensively applied in atomic physics, also has been applied extensively in atomic physics in its relativistic form as well as in the study of atoms with heavy nuclei (see Gombás, 1949, for instance). Similarly there have been considerations of relativistic Thomas-Fermi model for quark stars pointing out the existence of critical electric fields on their surfaces (Alcock et al., 1986). Similar results have also been obtained in the transition at very high densities, from the normal nuclear matter phase in the core to the color-flavor-locked phase of quark matter in the inner core of hybrid stars (Alford et al., 2001). However, no example exists to the application of the electromagnetic Thomas-Fermi model to white dwarfs and neutron stars.

The analysis of superheavy nuclei has historically represented a major field of research, developed by Prof. V. Popov and Prof. W. Greiner and their schools. This same problem was studied in the context of the relativistic Thomas-Fermi equation also by R. Ruffini and L. Stella, already in the '80s. The recent approach was started with the Ph.D. Thesis of M. Rotondo and has shown the possibility to extrapolate this treatment of superheavy nuclei to the case of nuclear matter cores of stellar dimensions (Ruffini et al., 2007). The very unexpected result has been that also around these massive cores there is the distinct possibility of having an electromagnetic field close to the

critical value

$$E_c = \frac{m_e^2 c^3}{e \hbar} \approx 1.3 \times 10^{16} \text{ Volt cm}^{-1},$$

localized in a very narrow shell of the order of the electron Compton wavelength (see Fig. 3.1).

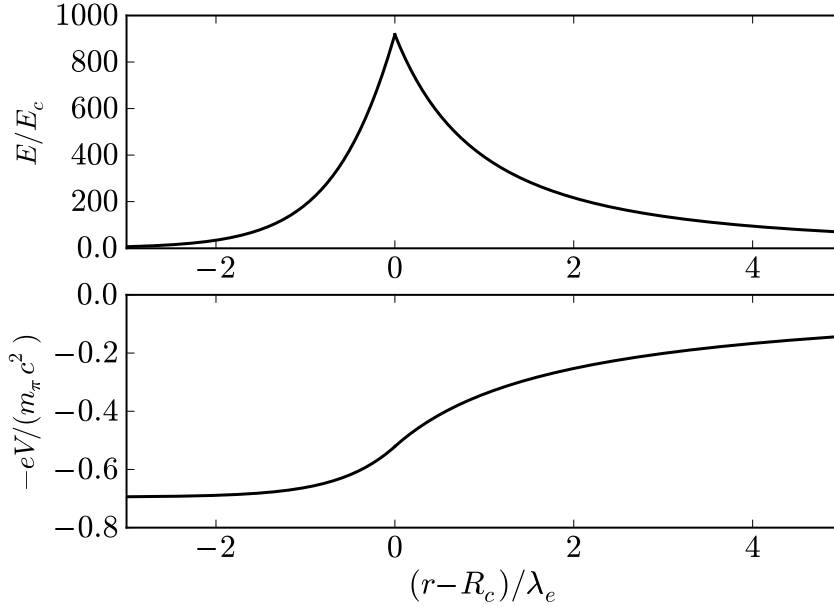


Figure 3.1: Upper panel: electric field around the surface of a nuclear matter core of stellar dimensions in units of the critical field E_c . Lower panel: electron Coulomb potential $-eV$. Here R_c denotes the core radius and $\lambda_e = \hbar / (m_e c)$ is the electron Compton wavelength.

The welcome result was that all the analytic work developed by Prof. V. Popov and the Russian school can be applied using scaling laws satisfied by the relativistic Thomas-Fermi equation to the case of nuclear matter cores of stellar dimensions, if the β -equilibrium condition is properly taken into account. This has been the result obtained and published by Ruffini, Rotondo and Xue already in 2007. Since then, a large variety of problems has emerged, which have seen the direct participation of ICRANet Professors, graduate students, postdocs, as well as collaborators worldwide including Prof. V. W. Greiner, Prof. Popov, Prof. D. Arnett, and insightful discussions in Pescara with the Nobel Prize Awarded, Prof. G. 't Hooft.

One of the crucial issues to be debated is the stability of such cores under the competing effects of self-gravity and Coulomb repulsion. It has been demonstrated their stability against nuclear fission, as opposed to the case of heavy nuclei (Rotondo et al., 2011d, see). In particular, on the basis of Newtonian gravitational energy considerations it has been found the existence of

a possible new island of stability for mass numbers

$$A > A_R = 0.039 \left(\frac{N_p}{A} \right)^{1/2} \left(\frac{m_{\text{Planck}}}{m_n} \right)^3 ,$$

where N_p is the number of protons, A is the total number of baryons, m_n is the neutron mass and $m_{\text{Planck}} = \sqrt{\hbar c / G}$ is the Planck mass.

The equilibrium against Coulomb repulsion originates now from the combined effect of the screening of the relativistic electrons, of the surface tension due to strong interactions, and of the gravitational interaction of these massive cores. By enforcing the condition of β -equilibrium, it has been also obtained a generalization to the relation between the mass number A and atomic number N_p which encompasses phenomenological expressions (see Rotondo et al., 2011d, for further details).

All these considerations have been made for an isolated core with constant proton density whose boundary has been sharply defined by a step function. No external forces are exerted. Consequently, the Fermi energy of the electrons has been assumed to be equal to zero.

Different aspects concerning these macroscopic systems have been also considered. For instance, the analysis of the electron distribution around such cores in both the case of global charge neutrality and the case of not global charge neutrality has been presented by R. Ruffini, M. Rotondo and S.-S. Xue in *Neutral nuclear core versus super charged one*, Proc. 11th Marcel Grossmann Meeting, 2008.

The assumption of a sharp proton density profile has been relaxed and, consequently, a smooth surface modeled by a Woods-Saxon-like proton distribution has been introduced in *The Extended Nuclear Matter Model with Smooth Transition Surface* by Jorge A. Rueda H., B. Patricelli, M. Rotondo, R. Ruffini, S.-S. Xue, , Proc. 3rd Stueckelberg Workshop on Relativistic Field Theories, 2008. The presence of overcritical electric fields close to their surface has been confirmed also in this more general case.

The existence of the scaling laws of the ultrarelativistic Thomas-Fermi equation (Rotondo et al., 2011d,a) has led to the very exciting possibility of having macroscopic configurations of nuclear matter in β -equilibrium exhibiting strong electric fields on their surfaces. In order to go one step further towards a more realistic description of macroscopic configurations as white dwarfs and neutron stars, further improvements and extensions must be applied to the starting model.

It is therefore interesting, in order to approach both the complex problem of a neutron star core and its interface with the neutron star crust and the problem of the equilibrium of gas in a white dwarf taking into account all possible global electromagnetic interactions between the nucleus and the relativistic electrons, to extend the model to the compressed case in which the Fermi energy of electrons turns to be positive.

The analysis of globally neutral and compressed configurations composed by a nucleus made of relativistic degenerate neutrons and protons surrounded by relativistic degenerate electrons in β -equilibrium has been recently accomplished. This work generalized the Feynman-Metropolis-Teller treatment of compressed atoms to relativistic regimes, and the concept of compressed nuclear matter cores of stellar dimensions was introduced (see Rotondo et al., 2011a, for details).

In the relativistic generalization of the Feynman-Metropolis-Teller approach, the equation to be integrated is the relativistic Thomas-Fermi equation. The integration of this equation does not admit any regular solution for a point-like nucleus and both the nuclear radius and the nuclear composition have necessarily to be taken into account. This introduces a fundamental difference from the non-relativistic Thomas-Fermi model where a point-like nucleus was adopted.

Due to the introduction of the concept of Wigner-Seitz cells, the study of degenerate compressed matter in white dwarfs can be addressed. This problem presents, still today, open issues of great interest such as the equilibrium of the electron gas and the associated nuclear component, taking into account the electromagnetic, the gravitational and the weak interactions formulated in a correct special and general relativistic framework. A complete analysis of the properties of such configurations as a function of the compression can be duly done through the relativistic generalization of the Feynman-Metropolis-Teller approach (see Rotondo et al., 2011b, for details).

It has been then possible to derive a consistent equation of state for compressed matter which generalizes both the uniform free-electron fluid approximation, adopted for instance by Chandrasekhar (1931) in his famous treatment of white dwarfs, and the well-known work of Salpeter (1961) which describes the electrodynamic and relativistic effects by a sequence of approximations. Apart from taking into account all possible electromagnetic and special relativistic corrections to the equation of state of white dwarf matter, the new equation of state that incorporates the β -equilibrium condition, leads to a self-consistent calculation of the onset for inverse β -decay as function of the Fermi energy of electrons or the density of the system. This is very important for the analysis of the stability of white dwarfs against gravitational collapse (see Rotondo et al., 2011a, for details). The extension of the above works to the case of finite temperatures has been part of the PhD thesis work of S. M. de Carvalho. Details can be found in the chapter Highlights of 2014 in chapter 5.

A related topic of current interest concerns the case of rotating nuclear matter cores of stellar dimensions. The induced magnetic field by electric field rotation has been recently obtained (Boshkayev et al., 2012, see). Such analysis has been done in the framework of classical electrodynamics under the assumption of uniform rigid rotation of the macroscopic nuclear cores in the non-compressed case. For rotation periods of the order of ~ 10 ms, overcriti-

cal magnetic fields has been obtained near the surface of the configuration.

In neutron star cores, nuclear matter is under very extreme conditions of density and pressure. The importance of the strong interactions between nucleons at such extreme pressures it has been known for years (see e.g. Cameron, 1970; Shapiro and Teukolsky, 1983). However, due to the absence of a complete theory of the strong interactions, and due to the impossibility of performing terrestrial experiments with similar extreme pressure-density conditions, the equation of state of nuclear matter at densities larger than the nuclear saturation density $\sim 2.7 \times 10^{14}$ g/cm³, is yet unknown. The construction of nuclear equations of state combined with a fully consistent formulation of the equations of equilibrium in general relativity both for white dwarfs and neutron stars is an active topic of research within our group (see below). In the recent past, some graduate theses of our group were devoted to this topic, for instance the works of M. Rotonondo and Jorge A. Rueda, which were soon followed by the ones of D. Pugliese, R. Belvedere, K. Boshkayev, and S. M. de Carvalho. Y. Wu has devoted part of his PhD work to compute the interfacial properties between the core and the crust of neutron stars. The recent developments in all these topics can be found in the Highlights of 2014 in chapter 5.

3.2 White Dwarfs Physics and Structure

The generalization of the Feynman-Metropolis-Teller treatment to relativistic regimes, which led to a new equation of state of white dwarf matter, has been recently used to construct equilibrium configurations of white dwarfs in general relativity (Rotonondo et al., 2011a). The description of the inverse β -decay within the relativistic Feynman-Metropolis-Teller equation of state in conjunction with general relativity, leads to a self-consistent calculation of the critical mass of white dwarfs (see Fig. 3.2). The numerical value of the mass, of the radius, and of the critical mass of white dwarfs turn to be smaller with respect to the ones obtained with approximate equations of state (see e.g. Hamada and Salpeter, 1961). Therefore, the analysis of compressed atoms following the relativistic Feynman-Metropolis-Teller treatment has important consequences in the determination of the mass-radius relation of white dwarfs, leading to the possibility of a direct confrontation of these results with observations.

The generalization of the above general relativistic theory of white dwarfs to the case of rotation was accomplished as part of the thesis work of K. Boshkayev (see Boshkayev et al., 2013b). The entire family of uniformly rotating stable white dwarfs has been already obtained by studying the mass-shedding, the inverse β -decay, pycnonuclear reactions, as well as the axisymmetric instabilities. Both the maximum mass and the minimum(maximum) rotation period(frequency) have been obtained for selected nuclear compositions.

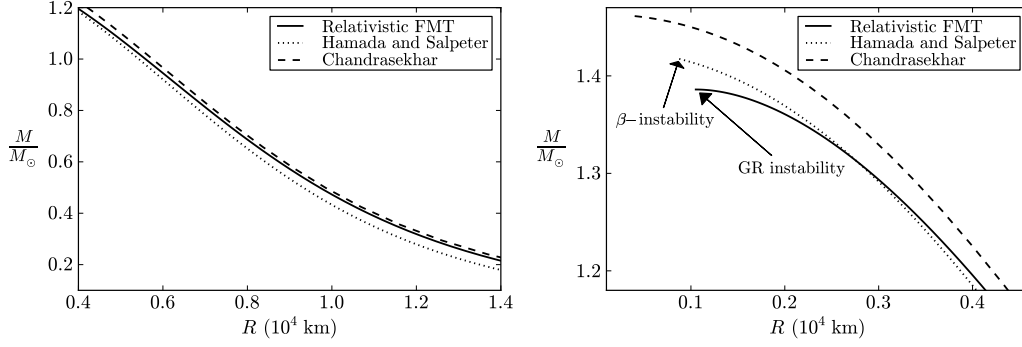


Figure 3.2: Reproduced from Rotondo et al. (2011a). Mass-Radius relation of general relativistic carbon white dwarfs.

The solution of the hydrostatic equilibrium equations in general relativity for white dwarfs at finite temperatures was recently accomplished within the PhD work of S. M. de Carvalho. The analysis of the equilibrium of magnetized white dwarfs is part of the PhD thesis of D. L. Cáceres. We refer to chapter 5 for further details on these two works.

3.3 White Dwarf Astrophysics

The knowledge of the white dwarf structure is relevant for the several astrophysical scenarios such as the evolution of massive white dwarfs and type Ia supernovae. Besides, it has been successfully applied to the description of soft-gamma-ray repeaters (SGRs) and anomalous X-ray pulsars (AXPs) within a model based on rotation powered white dwarfs, as shown by Malheiro et al. (2012). SGRs and AXPs are a class of compact objects that show interesting observational properties: rotational periods in the range $P \sim (2-12)$ s, a narrow range with respect to the wide range of ordinary pulsars $P \sim (0.001-10)$ s; spin-down rates $\dot{P} \sim (10^{-13}-10^{-10})$, larger than ordinary pulsars $\dot{P} \sim 10^{-15}$; strong outburst of energies $\sim (10^{41}-10^{43})$ erg, and for the case of SGRs, giant flares of even large energies $\sim (10^{44}-10^{47})$ erg, not observed in ordinary pulsars.

The recent observation of SGR 0418+5729 with a rotational period of $P = 9.08$ s, an upper limit of the first time derivative of the rotational period $\dot{P} < 6.0 \times 10^{-15}$, and an X-ray luminosity of $L_X = 6.2 \times 10^{31}$ erg/s, promises to be an authentic Rosetta Stone, a powerful discriminant for alternative models of SGRs and AXPs. The loss of rotational energy of a neutron star with this spin-down rate \dot{P} cannot explain the X-ray luminosity of SGR 0418+5729, excluding the possibility of identifying this source as an ordinary spin-down powered pulsar. The inferred upper limit of the surface magnetic field of SGR 0418+5729 $B < 7.5 \times 10^{12}$ G, describing it as a neutron star within the mag-

netic braking scenario, is well below the critical field challenging the power mechanism based on magnetic field decay purported in the magnetar scenario.

We have shown that the observed upper limit on the spin-down rate of SGR 0418+5729 is, instead, perfectly in line with a model based on a massive fast rotating highly magnetized white dwarf of mass $M = 1.4M_{\odot}$, radius $R = 10^3$ km, and moment of inertia $I \approx 10^{49}$ g cm². We analyze the energetics of all SGRs and AXPs including their outburst activities and show that they can be well explained through the change of rotational energy of the white dwarf associated to the observed sudden changes of the rotational period, the glitches. All SGRs and AXPs can be interpreted as rotating white dwarfs that generate their energetics from the rotational energy and therefore there is no need to invoke the magnetic field decay of the magnetar model (see Fig. 3.3). The above calculation of the range of minimum rotation periods of massive white dwarfs, $0.3 \lesssim P_{min} \lesssim 2.2$ seconds, depending on the nuclear composition (Boshkayev et al., 2013b), implies the rotational stability of SGRs and AXPs. The relatively long minimum period of ⁵⁶Fe rotating white dwarfs ~ 2.2 seconds, implies that the objects describing SGRs and AXPs have are made of chemical compositions lighter than ⁵⁶Fe, e.g. ¹²C or ¹⁶O.

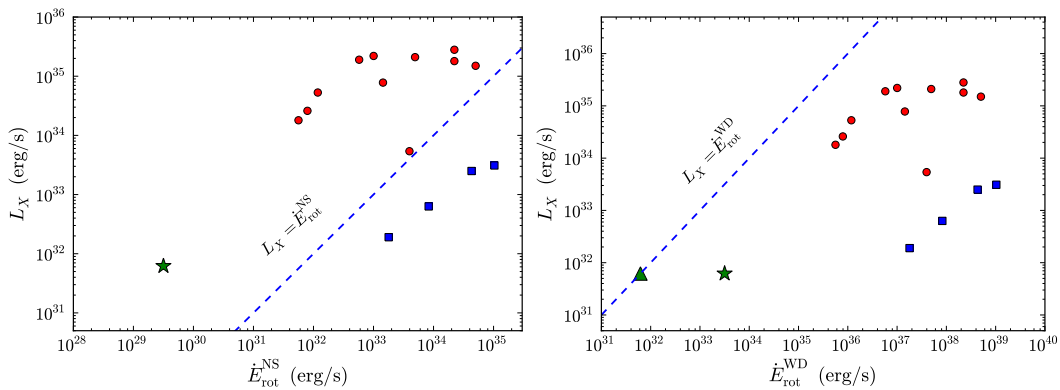


Figure 3.3: Reproduced from Malheiro et al. (2012). Luminosity to rotational energy loss ratio of SGRs and AXPs for both neutron stars (left panel) as a white dwarfs (right panel).

We have analyzed within the white dwarf model of SGRs and AXPs, SGR 0418+5729 and Swift J1822.3-1606 the so-called *low magnetic field magnetars* (see Boshkayev et al., 2013a, for details). The request of the rotational stability of the white dwarf gives bounds for the mass, radius, moment of inertia and magnetic field, through the analysis of constant rotation period sequences of uniformly rotating white dwarfs. We have also analyzed the emission properties of these two objects in the optical band, and inferred the cyclotron frequencies associated to their magnetic fields which might cause absorption features in the optical wavelengths. Concerning the emission of SGRs and

AXPs in the high-energy bands, such as X and gamma-rays, they are currently being analyzed as part of the PhD work of D. L. Cáceres.

We have also considered the possible progenitors of these massive, fast rotating, highly magnetized white dwarfs. Recent smoothed particle hydrodynamics (SPH) simulations of white dwarfs mergers (García-Berro et al., 2012) indicate that the outcomes of these binaries are white dwarfs with the above desirable properties, and thus they can be progenitors of SGRs and AXPs. Specifically, the products of these mergers consist of a hot central white dwarf surrounded by a heavy rapidly rotating disk. We applied these considerations to the specific case of 4U 0142+61 and show that the merger of a double degenerate system can explain the characteristics of this peculiar AXP (see Rueda et al., 2013, for details).

The request of the rotational stability of the white dwarf outcome of the merger gives bounds for the mass, radius, moment of inertia and magnetic field. Assuming a carbon composition, we find that the mass and radius of 4U 0142+61 must be in the range $1.16\text{--}1.39 M_{\odot}$ and $0.0014\text{--}0.0086 R_{\odot}$. We followed the post-merger cooling and rotation evolution of the newly formed white dwarf. We show that this scenario accounts for the observed infrared excess and the emission observed in the other optical bands. We demonstrate that the observed properties of 4U 0142+6 are consistent with a $\sim 1.2 M_{\odot}$ white dwarf, remnant of the coalescence of an original system made of two white dwarfs of masses $0.6 M_{\odot}$ and $1.0 M_{\odot}$. Finally, we infer a post-merging age $\tau_{\text{WD}} \approx 64$ kyr, and a magnetic field $B \approx 2 \times 10^8$ G. Evidence for such a magnetic field may come from the possible detection of the electron cyclotron absorption feature observed between the *B* and *V* bands at a frequency $\nu \approx 10^{15}$ Hz in the spectrum of 4U 0142+61. Details can be found in (Rueda et al., 2013).

3.4 Neutron Star Physics and Structure

In the earliest description of neutron stars in the works of Tolman (1939) and Oppenheimer and Volkoff (1939) only a gas of neutrons was considered and the equations of equilibrium (hereafter TOV equations) were written in the Schwarzschild metric. They considered the model of a degenerate gas of neutrons to hold from the center to the border, with the density monotonically decreasing away from the center.

In the intervening years, more realistic neutron star models have been presented challenging the original considerations of Tolman (1939) and Oppenheimer and Volkoff (1939). The TOV equations considered the existence of neutrons all the way to the surface of the star. The presence of neutrons, protons and electrons in β -equilibrium were instead introduced by Harrison et al. (1965). Still more important, the neutron stars have been shown to be composed of two sharply different components: the core at nuclear

and supra-nuclear densities consisting of degenerate neutrons, protons and electrons in β -equilibrium and a crust of white dwarf like material, namely a nuclei lattice in a background of degenerate electrons (see Harrison et al., 1965; Baym et al., 1971, for details). Further works describing the nuclear interactions were later introduced. Clearly all these considerations departed profoundly from the Oppenheimer and Volkoff (1939) assumption.

The matching between the core and the crust is still today an open issue in neutron star physics. In order to handle with this interesting problem, a step-by-step procedure is needed. In such a case, the neutron, proton, and electron fluid is confined within the core radius due to the compression exerted by the crust component of the neutron star.

Most of the effort have been given to the construction of self-consistent solutions of the equations of equilibrium for neutron stars in general relativity taking into account the traditionally neglected electromagnetic interaction. In nearly all the scientific literature on neutron stars, a “local approach”, where the equation of state of neutron star matter is constructed ignoring global gravitational and Coulomb effects by assuming not only flat space but also local charge neutrality, has been traditionally used. The gravitational effects are then taken into account by embedding such an equation of state into the TOV equations of hydrostatic equilibrium.

We have introduced a new approach which thanks to the existence of scaling laws can apply to compressed atoms as well as to massive nuclear matter cores of stellar dimensions. This approach on the compressed atom has already given a new contribution in the study of white dwarfs. It represents the first self-consistent calculation taking into due account the electromagnetic contribution in a relativistic treatment of the Thomas-Fermi equation, within global formulation of the equilibrium of white dwarfs in general relativity.

The application of the above results to the case of neutron stars is much more complex and it has been approached stepwise. As a first step we have considered the application of this novel approach to the case of a system of neutrons, protons, and electrons in β -equilibrium at zero temperatures within general relativity (Rotondo et al., 2011c). The crucial role of the generalized Fermi energy of particles, for short Klein potentials, and their constancy on the entire equilibrium configuration has been outlined. This first solution, although does not represent a complete realistic model for a neutron star, contains all the essential physics of the phenomenon of gravito-polarization in neutron star interiors: the existence of an electric potential and consequently an electric field over the entire configuration has been there evidenced. We have there proved, for the case of this simplified example where strong interactions are neglected, that the traditional approach of describing the system imposing the condition of local charge neutrality and solving the corresponding TOV equations is conceptually inconsistent. We have then substitute the condition of local charge neutrality with the condition of global

charge neutrality and derived the correct equations which we have called the Einstein-Maxwell-Thomas-Fermi system. The boundary conditions are also different from a traditional Cauchy data with the values of the functions and first derivatives at the center into a boundary condition at the center and delicate eigenvalue problem at the boundary determining the condition of charge neutrality at the border. The conceptual differences and the alternative mathematical equations of the two approaches, the ones imposing local versus global charge neutrality, lead to the presence of additional electrodynamic global structures. However, in this specific simple example, they do not give significant quantitative differences in the mass-radius relation for the equilibrium configurations. A very different situation occurs when strong interactions are also taken into account.

The next step was to introduce self-consistently the strong interactions in the construction of the equilibrium configurations. We have thus generalized the Einstein-Maxwell-Thomas-Fermi equations to the case of strong interactions, see (Rueda et al., 2011) for details. There, the major aim has been to prove the constancy of the Klein potentials in the case in which the nuclear interactions are described by a Lagrangian including in addition to the gravitational, electromagnetic, and weak interactions, also the presence of σ , ω , and ρ virtual mesons that mediate the nuclear interactions.

We have also extended to finite temperatures the theoretical treatment of gravito-polarization for a system of neutrons, protons and electrons in β -equilibrium, taking into account strong interactions modeled through the exchange of σ , ω and ρ virtual mesons (see Rueda et al., 2011, for details). The crucial role of the Klein potentials of particles is outlined as well as the condition of isothermality of Tolman. We have shown that, the gravito-polarization effect although energetically much weaker than the corresponding gravitational and thermal effects, do survive in the case of finite temperatures. Their role, when strong interactions are considered, is of fundamental astrophysical importance.

The construction of realistic neutron stars with core and crust satisfying global (but not local) charge neutrality has been already accomplished in (Belvedere et al., 2012). The solutions lead to a new structure of the star: a positively charged core at supranuclear densities surrounded by an electronic distribution of thickness $\sim \hbar/(m_e c) \sim 10^2 \hbar/(m_\pi c)$ of opposite charge, as well as a neutral crust at lower densities. Inside the core there is a Coulomb potential well of depth $\sim m_\pi c^2/e$. The constancy of the Klein potentials in the transition from the core to the crust, impose the presence of an overcritical electric field $\sim (m_\pi/m_e)^2 E_c$. For each central density, an entire family of core-crust interface boundaries can be constructed, each of them reaching the neutrality point at a different electron density at the edge of the crust. This leads consequently to crusts with masses and thickness smaller than the ones obtained from the traditional TOV treatment, resulting in a novel neutron star mass-radius relation (see Fig. 3.4).

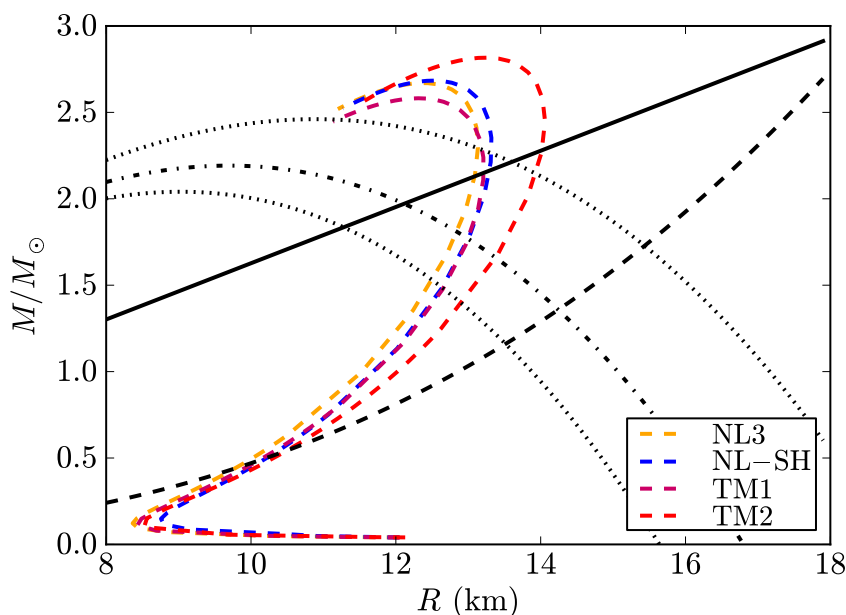


Figure 3.4: Reproduced from Belvedere et al. (2012). Mass-Radius relation for selected nuclear equations of state and comparison with observational constraints.

This important work has been recently generalized to the case of uniform rotation as part of the PhD thesis of R. Belvedere. The analysis of the properties of the core-crust interface, such as its surface and Coulomb energies, have been studied by Y. Wu during his PhD research. The thermal properties of neutron stars accounting for the above interior structure has been studied by S. M. de Carvalho in her PhD thesis, also in collaboration with R. Nereiros from Universidade Federal Fluminense from Brazil. The establishment of conditions of macroscopic equilibrium of compact stars with phase-transitions in their interiors, such as the one occurring from the crust to the core, has been one of the main topics of the PhD research of Jonas P. Pereira. Further details about these works can be found in Highlights of 2014 in chapter 5.

3.5 Neutron Star Astrophysics

We start by studying the possible progenitors and emission mechanisms leading to the most energetic radiation observed in astrophysics, the gamma-ray bursts (GRBs). Focus is given to the termed GRB-Supernova connection and to Short GRBs. The binary progenitors of these systems are studied in detail with particular emphasis on the role played by neutron stars.

It is understood that the Supernovae (SNe) associated to GRBs are of type

Ib/c. However, the temporal coincidence of the GRB and the SN represents still a major enigma of Relativistic Astrophysics. A novel concept has been recently proposed for explaining the temporal coincidence of some GRBs with an associated SN in terms of the gravitational collapse of a neutron star to a Black Hole (BH), induced by a type Ib/c SN explosion (see Rueda and Ruffini, 2012, and the report of activities of the GRB group). There, based on the pioneer idea of Ruffini et al. (2008), the specific case of a close (orbital period < 1 h) binary system composed of an evolved star with a neutron star companion has been considered (see Fig. 3.5). We have computed in (Rueda and Ruffini, 2012) the accretion rate onto the neutron star of the material expelled from the explosion of the core progenitor as a type Ib/c SN, and give the explicit expression of the accreted mass as a function of the nature of the components and binary parameters. We showed that the NS can reach, in a few seconds, the critical mass and consequently gravitationally collapses to a Black Hole. This gravitational collapse process leads to the emission of the GRB.

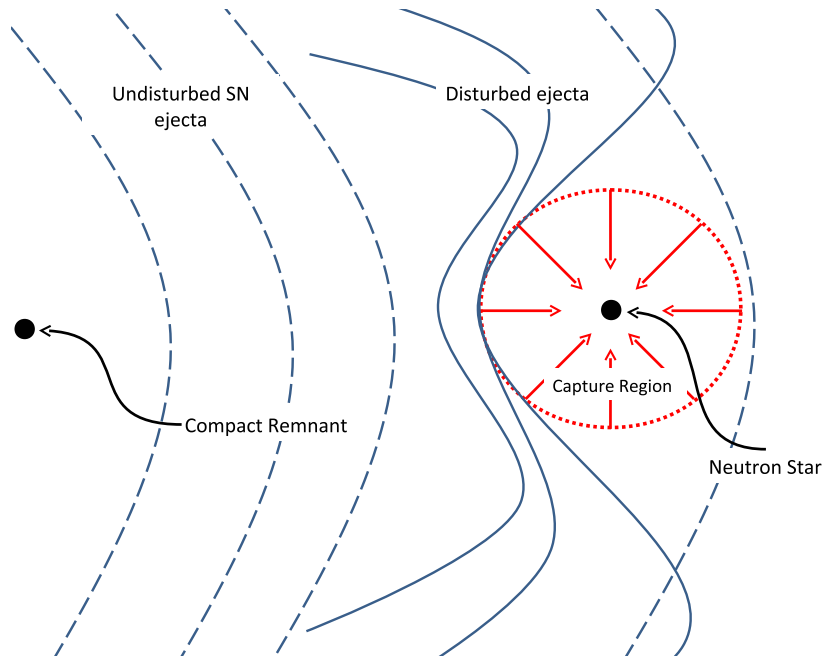


Figure 3.5: Reproduced from Rueda and Ruffini (2012). Mass-Radius relation for selected nuclear equations of state and comparison with observational constraints.

We have recently applied in (Izzo et al., 2012) the above considerations to the case of GRB 090618 (see also report of activities of the GRB group), for which there is evidence of a SN ~ 10 days after the GRB occurrence. We compute the progenitor binary parameters: the mass of the neutron star companion, M_{NS} , and the mass of the SN core progenitor, M_{core} , are in the following mass ranges: $1.8 \lesssim M_{NS}/M_{\odot} \lesssim 2.1$ and $3 \leq M_{core}/M_{\odot} \leq 8$. We have also discussed in (Rueda and Ruffini, 2012; Izzo et al., 2012) the

complementarity of these considerations to alternative processes explaining long and short GRBs. A great further step toward the understanding of these systems has been recently achieved with the first full numerical simulations of the above process of induced gravitational collapse. This work has been done in collaboration with C. L. Fryer from Los Alamos National Laboratory in New Mexico. We refer to the chapter 5, Highlights 2014, for additional details on this interesting subject.

It is clear that after the occurrence of the SN and the GRB emission, the outcome is represented, respectively, by a NS and a BH. A possible strong evidence of the NS formation is represented by the observation of a characteristic late ($t = 10^8$ – 10^9 s) X-ray emission that has been interpreted as originated by the young ($t \sim 1$ minute–(10–100) years), hot ($T \sim 10^7$ – 10^8 K) NS, which we have called neo-NS (see Negreiros et al., 2012, for details). The traditional study of neutron star cooling has been generally applied to quite old objects as the Crab Pulsar (957 years) or the Central Compact Object in Cassiopeia A (330 years) with an observed surface temperature $\sim 10^6$ K. However, as we just mentioned in GRB-SN systems there is possible evidence of the cooling of neutron stars with surface temperatures $\sim 10^7$ – 10^8 K. The traditional thermal processes taking place in the neutron star crust might be enhanced by the extreme high temperature conditions of neo-neutron star and therefore the study of the thermal behavior especially of the crust of neo-neutron stars deserves the appropriate attention. In the chapter 5, Highlights 2014, we summarize the new results on this latter issue which was part of the PhD work of S. M. de Carvalho.

3.6 Radiation Mechanisms of White Dwarfs and Neutron Stars

We here study the possible emission mechanisms of white dwarfs and neutron stars. We are interested in both electromagnetic and gravitational radiation at work in astrophysical systems such as compact star magnetospheres, as well as inspiraling and merging of relativistic binary systems such as double neutron stars, neutron star-white dwarfs, and neutron star-black hole binaries. This is a relatively new research topic within our group and therefore no results prior to 2014 can be listed here. We have instead our first results in the present year 2014, which can be found in the chapter 5, Highlights 2014.

3.7 Exact Solutions of the Einstein and Einstein-Maxwell Equations in Astrophysics

We analyze the ability of analytic exact solutions of the Einstein-Maxwell equations to describe the exterior spacetime of compact stars like white dwarfs and neutron stars. The problem of matching between interior and exterior spacetimes is addressed in detail. The effect of the quadrupole moment on the properties of the spacetime is also investigated. Particular attention is given to the application of exact solutions in astrophysics, e.g. the dynamics of particles around compact stars and its relevance in astrophysical systems such as X-ray binaries.

Thus, whether analytic exact vacuum(electrovacuum) solutions of the Einstein(Einstein-Maxwell) field equations can accurately describe or not the exterior spacetime of compact stars remains still an interesting open question. As an attempt to establish their level of accuracy, the radii of the Innermost Stable Circular Orbits (ISCOs) of test particles given by analytic exterior spacetime geometries have been compared with the ones given by numerical solutions for neutron stars obeying a realistic equation of state. It has been so shown that the six-parametric solution of Pachón et al. (2006) (hereafter PRS) is more accurate to describe the neutron star ISCO radii than other analytic models.

In this line, Pachón et al. (2012) have recently proposed an additional test of accuracy for analytic exterior geometries based on the comparison of orbital frequencies of neutral test particles. The Keplerian, frame-dragging, as well as the precession and oscillation frequencies of the radial and vertical motions of neutral test particles for the Kerr and PRS geometries have been computed in (Pachón et al., 2012). Then, they were compared with the numerical values obtained by Morsink and Stella (1999) for realistic neutron stars. Contrary to what previously stated in the literature, it has been identified the role of high-order multipole moments such as the mass quadrupole and current octupole in the determination of the orbital frequencies, especially in the rapid rotation regime. These results are relevant to cast a separatrix between black holes and neutron star signatures as well as probe the nuclear matter equation of state and neutron star parameters from the Quasi-Periodic Oscillations (QPOs) observed in low mass X-Ray binaries. We refer to (Pachón et al., 2012) for further details (see Fig. 3.6).

We have performed a detailed analysis of the possibility of extracting the first multipole moments of a compact object, namely the mass, angular momentum and quadrupole moment, by extending the relativistic precession model of QPOs to the Hartle-Thorne solution and applying it to the low mass X-ray binary GX 5–1. Details can be found in the chapter 5 Highlights 2014.

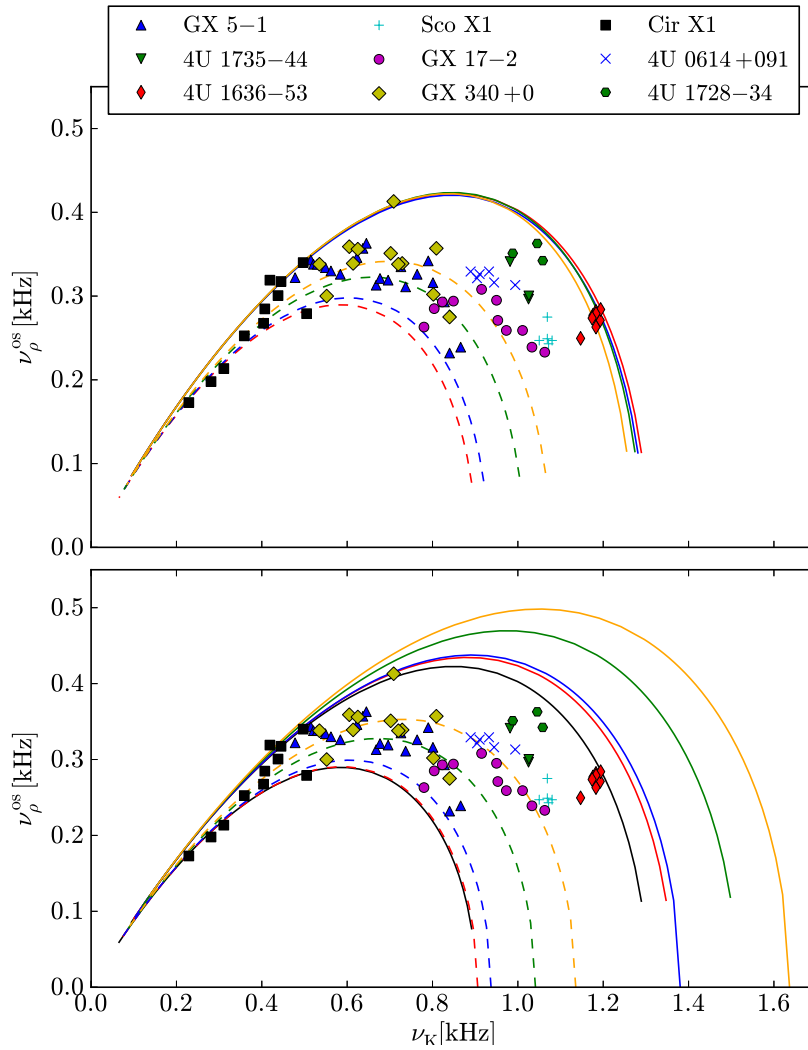


Figure 3.6: Reproduced from Pachón et al. (2012). Periastron oscillation frequency, ν_ρ^{OS} , as a function of the Keplerian frequency ν_K for selected NS realistic models. We indicate the QPO frequencies observed in the sources GX 5-1, 4U 1735-44, 4U 1636-53, Sco X1, GX 17-2, GX 340+0, Cir X1, 4U 0614+091, and 4U 1728-34. The solid curves depict the results for the models M1 (solid) and M2 (dashed) with red lines, for the models M3 (solid) and M4 (dashed) with blue lines, for the models M5 (solid) and M6 (dashed) with green lines while orange lines stands for the results from models M7 (solid) and M8 (dashed). In the upper panel we present the results derived from the $\text{PRS}_{s=0}$ solution while in the lower panel we present the results for the Kerr solution. In the lower panel we have added, to guide the eye, the inner red dashed and outer red solid curves of the upper panel using black lines.

3.8 Critical Fields and Non-Linear Electrodynamics Effects in Astrophysics

We turn now to a more theoretical topic: the effects of non-linear electrodynamics minimally coupled to gravity. We construct new analytic and numerical solutions to the Einstein-Maxwell equations representing black holes or the exterior field of a compact star. Some astrophysical applications are studied in detail such as the extractable energy of black holes, the mass-formula of the black hole. This topic has been just recently open within our group and thus new results has been obtained in the present year 2014; they are part of the PhD thesis of Jonas P. Pereira. Details can be found in the chapter 5 Highlights 2014.

4 Publications (before 2014)

4.1 Refereed Journals

1. Jorge A. Rueda, G. Aznar-Siguán, K. Boshkayev, E. García-Berro, L. Izzo, P. Lorén-Aguilar, R. Ruffini, *A white dwarf merger as progenitor of the AXP 4U 0142+61?*, *ApJ Letters* **772**, L24 (2013).
2. K. Boshkayev, L. Izzo, Jorge A. Rueda, R. Ruffini, *SGR 0418+5729, Swift J1822.3-1606, and 1E 2259+586 as massive fast rotating highly magnetized white dwarfs*, *A&A*. **555**, A151 (2013).
3. D. Pugliese, H. Quevedo, J. A. Rueda, R. Ruffini, *Charged Boson Stars*, *Phys. Rev. D* **88**, 024053 (2013).
4. G. B. Pisani, L. Izzo, R. Ruffini, C. L. Bianco, M. Muccino, A. V. Penacchioni, J. A. Rueda, Y. Wang, *Novel distance indicator for gamma-ray bursts associated with supernovae*, *A&A Lett.* **552**, L5 (2013).
5. A. V. Penacchioni, R. Ruffini, C. L. Bianco, L. Izzo, M. Muccino, G. B. Pisani, J. A. Rueda, *GRB 110709B in the induced gravitational collapse paradigm*, *A&A* **551**, A133 (2013).
6. K. Boshkayev, Jorge A. Rueda, R. Ruffini, I. Siutsou, *On general relativistic uniformly rotating white dwarfs*, *ApJ* **762**, 117 (2013).
7. R. Ruffini, C. R. Argüelles, B. M. O. Fraga, A. Geralico, H. Quevedo, J. A. Rueda, I. Siutsou, *Black Holes in Gamma Ray Bursts and Galactic Nuclei*, *Int. J. Mod. Phys. D* **22**, 1360008 (2013).
8. Jorge A. Rueda, R. Ruffini, *On the general relativistic Thomas-Fermi theory of white dwarfs and neutron stars*, *Il Nuovo Cimento C* **36**, 145 (2013).
9. Jorge A. Rueda, R. Ruffini, *On the Einstein-Maxwell-Thomas-Fermi equations for white dwarfs and neutron stars*, *Int. J. Mod. Phys. D.* **22**, 1360007 (2013).
10. L. Izzo, Jorge A. Rueda, R. Ruffini, *GRB 090618: a candidate of a neutron star gravitational collapse to a black hole induced by a type Ib/c supernova*, *A&A*, **548**, L5 (2012).

11. Jorge A. Rueda, R. Ruffini, *On the induced gravitational collapse of a neutron star to a black hole by a type Ib/c supernova*, *ApJ* **758**, L7 (2012).
12. L. A. Pachón, Jorge A. Rueda, C. Valenzuela, *On the relativistic precession and oscillation frequencies of test particles around rapidly rotating compact stars*, *ApJ* **756**, 82 (2012).
13. L. Izzo, R. Ruffini, A. V. Penacchioni, C. L. Bianco, L. Caito, S. K. Chakrabarti, J. A. Rueda, A. Nandi, B. Patricelli, *A double component in GRB 090618: a proto-black hole and a genuinely long gamma-ray burst*, *A&A* **543**, A10 (2012).
14. M. Malheiro, Jorge A. Rueda, R. Ruffini, *SGRs and AXPs as rotation-powered massive white dwarfs*, *Publ. Astron. Soc. Japan* **64**, 56 (2012).
15. R. Belvedere, D. Pugliese, Jorge A. Rueda, R. Ruffini, S.-S. Xue, *Neutron star equilibrium configurations within a fully relativistic theory with strong, weak, electromagnetic, and gravitational interactions*, *Nucl. Phys. A* **883**, 1 (2012).
16. R. Negreiros, C. L. Bianco, Jorge A. Rueda, R. Ruffini, *Cooling of young neutron stars in GRB associated to supernovae*, *A&A* **540**, A12 (2012).
17. Jorge A. Rueda, R. Ruffini, and S.-S. Xue, *The Klein first integrals in an equilibrium system with electromagnetic, weak, strong and gravitational interactions*, *Nucl. Phys. A* **872**, 286 (2011).
18. M. Rotondo, Jorge A. Rueda, R. Ruffini, S.-S. Xue, *Relativistic Feynman-Metropolis-Teller theory for white dwarfs in general relativity*, *Phys. Rev. D* **84**, 084007 (2011).
19. M. Rotondo, Jorge A. Rueda, R. Ruffini, S.-S. Xue, *The self-consistent general relativistic solution for a system of degenerate neutrons, protons and electrons in β -equilibrium*, *Phys. Lett. B* **701**, 667 (2011).
20. M. Rotondo, Jorge A. Rueda, R. Ruffini, S.-S. Xue, *Relativistic Thomas-Fermi treatment of compressed atoms and compressed nuclear matter cores of stellar dimensions*, *Phys. Rev. C* **83**, 045805 (2011).
21. M. Rotondo, R. Ruffini, S.-S. Xue, and V. S. Popov, *On gravitationally and electrostatically bound nuclear matter cores of stellar dimensions*, *Int. J. Mod. Phys. D* **20**, 1995 (2011).
22. Jorge A. Rueda, R. Ruffini, *Towards a Relativistic Thomas-Fermi Theory of White Dwarfs and Neutron Stars*, *Int. J. Mod. Phys. E* **20**, 141 (2011).

23. K. Boshkayev, Jorge A. Rueda, R. Ruffini, *On the Maximum Mass of General Relativistic Uniformly Rotating White Dwarfs*, Int. J. Mod. Phys. E **20**, 136 (2011).
24. Jorge A. Rueda, M. Rotondo, R. Ruffini, S.-S. Xue, *On compressed nuclear matter: from nuclei to neutron stars*, Int. J. Mod. Phys. D **20**, 1789 (2011).
25. Jorge A. Rueda, Michael Rotondo, Remo Ruffini, She-Sheng Xue, *A self-consistent approach to neutron stars*, J. Korean Phys. Soc. **57**, 560 (2010).
26. e^-e^+ pair creation by vacuum polarization around electromagnetic black holes, C. Cherubini, A. Gericco, Jorge A. Rueda H., R. Ruffini, Phys. Rev. D **79**, 124002 (2009).
27. R. Ruffini, M. Rotondo and S.-S. Xue, *Electrodynamics for nuclear Matter in bulk*, Int. J. Mod. Phys. D **16**, 1 (2007).
28. R. Ruffini and L. Stella, *Some comments on the relativistic Thomas-Fermi model and the Vallarta-Rosen equation*, Phys. Lett. B **102**, 442 (1981).
29. J. Ferreira, R. Ruffini and L. Stella, *On the relativistic Thomas-Fermi model*, Phys. Lett. B **91**, 314 (1980).

4.2 Conference Proceedings

1. S. Martins de Carvalho, Jorge A. Rueda, M. Rotondo, C. R. Argëlles, R. Ruffini, *The relativistic Feynman-Metropolis-Teller theory at zero and finite temperatures*, Int. J. Mod. Phys. S. **23**, 244 (2013).
2. K. Boshkayev, Jorge A. Rueda, R. Ruffini, *On the Maximum Mass and Minimum Rotation Period of Relativistic Uniformly Rotating White Dwarfs*, Int. J. Mod. Phys. S. **23**, 193 (2013).
3. R. Belvedere, Jorge A. Rueda, R. Ruffini, *Neutron Star Cores in the General Relativistic Thomas-Fermi Treatment*, Int. J. Mod. Phys. S. **23**, 185 (2013).
4. D. Pugliese, Jorge A. Rueda, R. Ruffini, S.-S. Xue, *A general relativistic Thomas-Fermi treatment of neutron stars cores II. Generalized Fermi energies and beta equilibrium*, Int. J. Mod. Phys. Conf. S. **12**, 198 (2012).
5. K. Boshkayev, M. Rotondo, R. Ruffini, *On Magnetic Fields in Rotating Nuclear Matter Cores of Stellar Dimensions*, Int. J. Mod. Phys.: Conf. S. **12**, 58 (2012).
6. M. Rotondo, Jorge A. Rueda, R. Ruffini, S.-S. Xue, *On Degenerate Compressed Atoms and Compressed Nuclear Matter Cores of Stellar Dimensions*, Int. J. Mod. Phys. Conf. S. **12**, 203 (2012).

7. R. Belvedere, Jorge A. Rueda, R. Ruffini, S.-S. Xue *Neutron star equilibrium configurations within a fully relativistic theory with strong, weak, electromagnetic, and gravitational interactions*, Current Issues on Relativistic Astrophysics, South Korea (2012).
8. K. Boshkayev, Jorge A. Rueda, R. Ruffini, *SGRs and AXPs AXPs as Massive Fast Rotating Highly Magnetized White Dwarfs*, Current Issues on Relativistic Astrophysics, South Korea (2012).
9. S. Martins de Carvalho, Jorge A. Rueda, R. Ruffini, *On the relativistic Feynman-Metropolis-Teller equation of state at finite temperatures and low-mass white dwarfs*, Current Issues on Relativistic Astrophysics, South Korea (2012).
10. Jorge A. Rueda, R. Ruffini, *Fundamental interactions in neutron stars*, 13th Marcel Grossmann Meeting, Sweden (2012).
11. S. Martins de Carvalho, Jorge A. Rueda, R. Ruffini, *On the relativistic Feynman-Metropolis-Teller equation of state at finite temperatures and low-mass white dwarfs*, 13th Marcel Grossmann Meeting, Sweden (2012).
12. K. Boshkayev, Jorge A. Rueda, R. Ruffini, *SGRs and AXPs as Massive Fast Rotating Highly Magnetized White Dwarfs: Bounds on the Mass, Moment of Inertia and Magnetic Fields*, 13th Marcel Grossmann Meeting, Sweden (2012).
13. K. Boshkayev, Jorge A. Rueda, R. Ruffini, *On General Relativistic Uniformly Rotating White Dwarfs*, 13th Marcel Grossmann Meeting, Sweden (2012).
14. R. Belvedere, Jorge A. Rueda, R. Ruffini, S.-S. Xue *Neutron star equilibrium configurations within a fully relativistic theory with strong, weak, electromagnetic, and gravitational interactions*, 13th Marcel Grossmann Meeting, Sweden (2012).
15. Jorge A. Rueda, *SGRs and AXPs as massive fast rotating highly magnetized white dwarfs*, 39th COSPAR Scientific Assembly, India (2012).
16. K. Boshkayev, *Fast Rotating White Dwarfs as Precursors of Type Ia supernovae and Millisecond Pulsars*, 39th COSPAR Scientific Assembly, India (2012).
17. R. Belvedere, Jorge A. Rueda, R. Ruffini, *Moment of inertia, radii, surface emission from a new theoretical understanding of Neutron Stars*, 39th COSPAR Scientific Assembly, India (2012).

18. K. Boshkayev, Jorge A. Rueda, R. Ruffini, *Rotating white dwarfs and their stability*, CompStar: the physics and astrophysics of compact stars, Tahiti (2012).
19. R. Belvedere, Jorge A. Rueda, R. Ruffini, *Neutron star equilibrium configurations within a fully relativistic theory with strong, weak, electromagnetic, and gravitational interactions*, CompStar: the physics and astrophysics of compact stars, Tahiti (2012).
20. K. Boshkayev, Jorge A. Rueda, R. Ruffini, *Stability of Rotating Nuclear Matter Cores of Stellar Dimensions*, CompStar: Equation of State for Compact Star Interiors and Supernovae, Croatia (2012).
21. R. Belvedere, Jorge A. Rueda, R. Ruffini, *Neutron star equilibrium configurations*, CompStar: Equation of State for Compact Star Interiors and Supernovae, Croatia (2012).
22. Jorge A. Rueda, R. Ruffini, S.-S. Xue, *Electrostatic Configurations Crossover Neutron Star Core*, Proc. 12th Marcel Grossmann Meeting, 1042 (2012).
23. Jorge A. Rueda, M. Rotondo, R. Ruffini, S.-S. Xue, *A New Family of Neutron Star Models: Global Neutrality versus Local Neutrality*, Proc. 12th Marcel Grossmann Meeting, 1039 (2012).
24. M. Rotondo, Jorge A. Rueda, R. Ruffini, S.-S. Xue, *From Compressed Atoms to Compressed Massive Nuclear Density Cores*, Proc. 12th Marcel Grossmann Meeting, 1036 (2012).
25. M. Malheiro, Jorge A. Rueda, R. Ruffini, *SGRs and AXPs: White Dwarf Pulsars versus Magnetars*, Proc. "The X-ray Universe 2011", Germany (2011).
26. R. Belvedere, Jorge A. Rueda, R. Ruffini, *Mass, Radius and Moment Of Inertia of Neutron Stars*, Proc. 2nd Ferrara Workshop on "X-ray Astrophysics up to 511 keV", Italy (2011).
27. S. Martins de Carvalho, C. Argüelles, Jorge A. Rueda, R. Ruffini, *SGRs and AXPs: White Dwarf Pulsars versus Magnetars*, Proc. "The X-ray Universe 2011", Germany (2011).
28. Jorge A. Rueda, M. Rotondo, R. Ruffini, and S.-S. Xue, *On the relativistic Feynman-Metropolis-Teller equation of state and general relativistic white-dwarfs*, Proceedings of Science, PoS(Texas2010), 269 (2011).
29. D. Pugliese, Jorge A. Rueda, R. Ruffini, and S.-S. Xue, *A general relativistic Thomas-Fermi treatment of neutron star cores*, Proceedings of Science, PoS(Texas 2010), 271 (2011).

30. R. Belvedere, *On the structure of the crust of neutron stars*, Proceedings of Science, PoS(Texas 2010), 270 (2011).
31. K. Boshkayev, *On the Stability of Rotating Nuclear Matter Cores of Stellar Dimensions*, Proceedings of Science, PoS(Texas 2010), 275 (2011).
32. K. Boshkayev, Jorge A. Rueda, and R. Ruffini, *On the minimum rotational period of fast rotating white dwarfs*, Proc. Erasmus Mundus IRAP PhD Workshop "From Nuclei to White Dwarfs to Neutron Stars", Eds. A. Mezzacappa, World Scientific (2011).
33. Jorge A. Rueda, D. Pugliese, M. Rotondo, R. Ruffini, S.-S. Xue, *A general relativistic Thomas-Fermi treatment of neutron stars cores I. The case of non-interacting particles*, Proc. 2nd Galileo-Xu Guangqi Meeting, Italy (2010).
34. K. Boshkayev, M. Rotondo, and R. Ruffini, *On Magnetic Fields in Rotating Nuclear Matter Cores of Stellar Dimensions*, Proc. 2nd Galileo-Xu Guangqi Meeting, Italy (2010).
35. R. Mohammadi, Jorge A. Rueda, R. Ruffini, and S.-S. Xue, *The solution of the Thomas-Fermi equation in the presence of strong magnetic fields*, Proc. 2nd Galileo-Xu Guangqi Meeting, Italy (2010).
36. Jorge A. Rueda, R. Ruffini, S.-S. Xue, *On the electrostatic structure of neutron stars*, AIP Conf. Proc. 1205, 143 (2010).
37. Jorge A. Rueda H., B. Patricelli, M. Rotondo, R. Ruffini, S.-S. Xue, *The Extended Nuclear Matter Model with Smooth Transition Surface*, Proc. 3rd Stueckelberg Workshop on Relativistic Field Theories, Italy (2008).
38. B. Patricelli, J. A. Rueda H., R. Ruffini *On the Crust of Neutron Stars*, Proc. 3rd Stueckelberg Workshop on Relativistic Field Theories, Pescara, Italy (2008).
39. R. Ruffini, M. Rotondo and S.-S. Xue, *Neutral nuclear core vs super charged one*, Proc. 11th Marcel Grossmann Meeting, Eds. R. Jantzen, H. Kleinert, R. Ruffini, World Scientific, Singapore (2008).
40. B. Patricelli, M. Rotondo and R. Ruffini, *On the Charge to Mass Ratio of Neutron Cores and Heavy Nuclei*, AIP Conf. Proc. **966**, 143 (2008).
41. M. Rotondo, R. Ruffini and S.-S. Xue, *On the Electrodynamical properties of Nuclear matter in bulk*, AIP Conf. Proc. **966**, 147 (2008).
42. B. Patricelli, M. Rotondo, J. A. Rueda H. and R. Ruffini, *The Electrodynamics of the Core and the Crust components in Neutron Stars*, AIP Conf. Proc. **1059**, 68 (2008).

43. R. Ruffini, *The Role of Thomas-Fermi approach in Neutron Star Matter*, Proceedings of the 9th International Conference "Path Integrals-New trends and perspectives", Eds. W. Janke and A. Pelster, World Scientific, Singapore (2008).
44. R. Ruffini, M. Rotondo, S.-S. Xue, *The Thomas-Fermi Approach and Gamma-Ray Bursts*, AIP Conf. Proc. **1053**, 243 (2008).
45. Jorge A. Rueda, B. Patricelli, M. Rotondo, R. Ruffini, and S. S. Xue, *The Extended Nuclear Matter Model with Smooth Transition Surface*, Proc. 3rd Stueckelberg Workshop on Relativistic Field Theories, Italy (2008).

5 Highlights 2014

5.1 Nuclear and Atomic Astrophysics

The extension of the relativistic Feynman-Metropolis-Teller treatment to the case of finite temperatures has been part of the PhD work of S. M. de Carvalho, and the results has been recently published, see de Carvalho et al. (2014). The inclusion of finite temperature effects is relevant in view of the recent discoveries of ultra-low mass white dwarfs with masses $\lesssim 0.2M_{\odot}$, which are companion of neutron stars in relativistic binaries (Antoniadis et al., 2012, 2013, see, e.g.,). These low-mass white dwarfs represent the perfect arena for testing the equation of state of compressed matter since the central densities of these objects are $\lesssim 10^6 \text{ g cm}^{-3}$, where the degenerate approximation breaks down and so thermal effects cannot be neglected (see Fig. 5.1).

Turning to neutron stars, we have recently investigated in Razeira et al. (2014b,a) extensions of the traditional $\sigma - \omega - \rho$ relativistic nuclear mean field model applied to the nuclear matter in neutron stars, by introducing many-body correlations within a quantum hadrodynamics (QHD) model with parameterized couplings. We considered the whole fundamental baryon octet ($n, p, \Sigma^-, \Sigma^0, \Sigma^+, \Lambda, \Xi^-, \Xi^0$) and the many-body forces are simulated by non-linear self-couplings and meson-meson interaction terms involving scalar-isoscalar (σ, σ^*), vector-isoscalar (ω, ϕ), vector-isovector (ρ), and scalar-isovector (δ).

Concerning neutron stars satisfying global but not local charge neutrality, we have already shown that a transition layer will develop between their core and crust of, at densities of the order of the nuclear saturation value. In (Rueda et al., 2014), we have used relativistic mean field theory together with the Thomas-Fermi approximation to study the detailed structure of this transition layer and calculate its surface and Coulomb energy. We find that the surface tension is proportional to a power-law function of the baryon number density in the core bulk region. We also analyzed the influence of the electron component and the gravitational field on the structure of the transition layer and the value of the surface tension, to compare and contrast with known phenomenological results in nuclear physics. Based on the above results we study the instability against Bohr-Wheeler surface deformations in the case of neutron stars obeying global charge neutrality. Assuming the core-crust transition at nuclear density $\rho_{core} \approx 2.7 \times 10^{14} \text{ g cm}^{-3}$, we find that the instability sets the upper limit to the crust density, $\rho_{crust}^{crit} \approx 1.2 \times 10^{14} \text{ g cm}^{-3}$

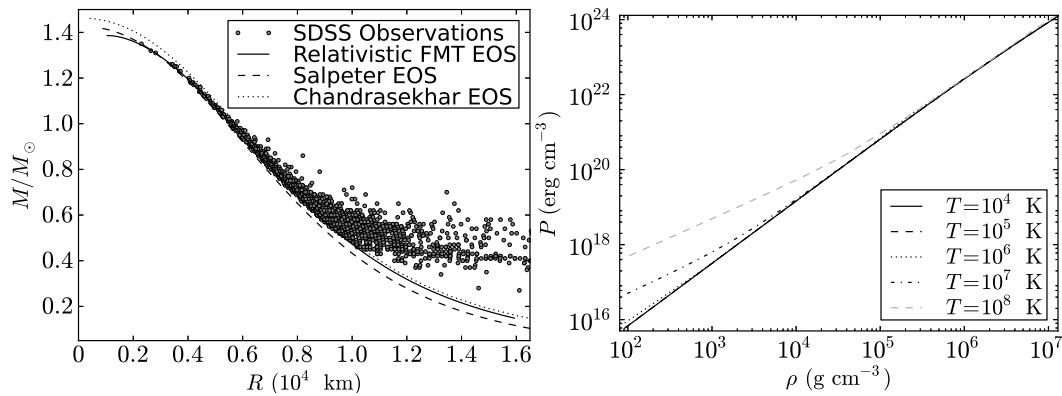


Figure 5.1: Reproduced from de Carvalho et al. (2014). Left panel: mass-radius relation of helium white dwarfs at zero temperatures contrasted with observations, deviations at low masses is evident. Right panel: Equation of state for selected temperatures.

This result implies a nonzero lower limit to the maximum electric field of the core-crust transition surface and makes inaccessible a limit of almost local charge neutrality at $\rho_{crust} \approx \rho_{core}$. The general framework can be also applied to study the stability of sharp phase transitions in hybrid stars as well as in strange stars, both bare and with outer crust. The results of this work open the way to a more general analysis of the stability of these transition surfaces, accounting for other effects such as gravitational binding, centrifugal repulsion, magnetic field induced by rotating electric field, and therefore magnetic dipole-dipole interactions.

Following the above treatment, we have just submitted a new article to Phys. Rev. C [J. A. Rueda, Y. Wu, S.-S. Xue, *Surface tension of heavy atoms*]. We compute the surface properties of atoms in which some of the electrons have penetrated into nuclear cores. Taking into account the strong, weak, and electromagnetic interactions, we numerically study the structure of heavy atoms and calculate the surface tension and Coulomb energy. We analyze the influence of the electron component on the structure of heavy atoms and the surface tension to compare and contrast with known phenomenological results in nuclear physics and the results of the core-crust interface of neutron stars with global charge neutrality. Based on these results we study the instability against Bohr-Wheeler surface deformations in the case of heavy atoms. The results in this article provide the evidence of strong effects of the electromagnetic interaction and electrons on structure of heavy atoms.

5.2 White Dwarfs Physics and Structure

It has been recently purported by Das and Mukhopadhyay (2013) that the presence of a extremely large uniform magnetic field of order 10^{18} G in the

interior of a white dwarf, increases its maximum mass from the traditional Chandrasekhar value, $\approx 1.44 M_{\odot}$, to a new upper bound $\approx 2.58 M_{\odot}$. Such a much larger limit would make these astrophysical objects viable candidates for the explanation of the superluminous population of type Ia supernovae. We have shown in (Coelho et al., 2014) that the new mass limit was obtained neglecting several macro and micro physical aspects such as gravitational, dynamical stability, breaking of spherical symmetry, general relativity, inverse β decay, and pycnonuclear fusion reactions. These effects are relevant for the self-consistent description of the structure and assessment of stability of these objects. When accounted for, they lead to the conclusion that the existence of such ultramagnetized white dwarfs in nature is very unlikely due to violation of minimal requests of stability, and therefore the canonical Chandrasekhar mass limit of white dwarfs has to be still applied.

5.3 White Dwarfs Astrophysics

Recent observations of relativistic white dwarf-neutron star binaries has led to the discovery that the white dwarfs in these systems are extremely light with masses $\lesssim 0.2M_{\odot}$ (Antoniadis et al., 2012, 2013). These objects should have densities lower than $\sim 10^6 \text{ g cm}^{-3}$, where thermal effects are expected to become relevant. In this line, we have generalized in (de Carvalho et al., 2014) the relativistic Feynman-Metropolis-Teller treatment to the case of finite temperatures. We have used this new equation of state to construct the mass-radius relation of white dwarfs at finite temperatures in a wide range of central densities. We analyze the particular case of the white dwarf companion of the pulsar PSR J1738+0333, which is expected to have a mass $\sim 0.18 M_{\odot}$ (Antoniadis et al., 2012). Using the observed surface effective temperature and surface gravity of the white dwarf we infer that the central white dwarf core temperature should be about $\sim 2 \times 10^7 \text{ K}$ (see Fig. 5.2). In addition to the analysis of white dwarfs, we have in (de Carvalho et al., 2014) extrapolated the formulation of the finite temperature relativistic FMT treatment to compressed nuclear matter cores of stellar dimensions. These systems have total mass numbers $A \approx (m_{\text{Planck}}/m_n)^3$ or mass $M_{\text{core}} \approx M_{\odot}$, where m_{Planck} and m_n are the Planck and the nucleon mass. For $T \ll m_e c^2/k_B \approx 5.9 \times 10^9 \text{ K}$, a family of equilibrium configurations can be obtained with analytic solutions of the ultrarelativistic Thomas-Fermi equation at finite temperatures. Such configurations fulfill global but not local charge neutrality and have strong electric fields on the core surface. We find that the maximum electric field at the core surface is enhanced at finite temperatures with respect to the degenerate case.

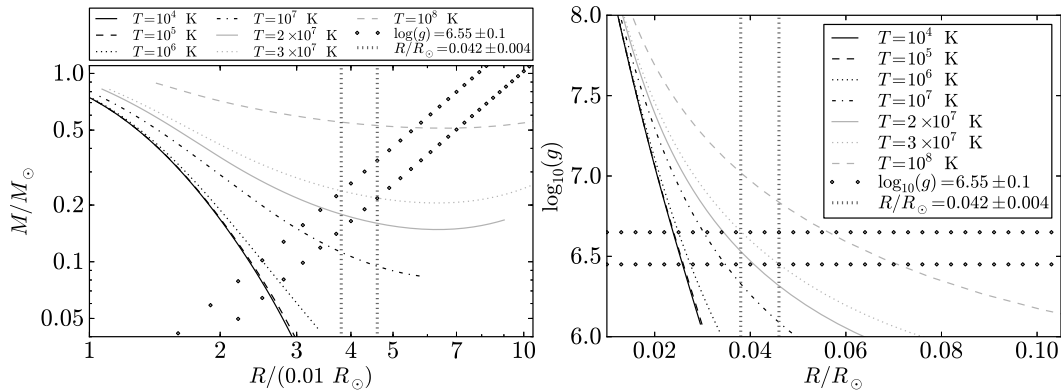


Figure 5.2: Reproduced from de Carvalho et al. (2014). Left panel: theoretical mass-radius relation of helium white dwarfs for selected interior temperatures and surface gravity g and observed photometric radius of the white dwarf companion of PSR J1738+0333. Right panel: Equation of state for selected temperatures. Theoretical surface gravity as a function of the radius for the same white dwarfs of the left panel.

5.4 Neutron Star Physics and Structure

In our previous treatment of neutron stars, we formulated a model fulfilling global but not local charge neutrality. The full system of equilibrium equations formed a coupled system that we have denominated Einstein-Maxwell-Thomas-Fermi (EMTF) equations. From the microphysical point of view, the weak interactions are accounted for via the request of the β stability of nuclear matter, and the strong interactions by introducing a relativistic nuclear $\sigma - \omega - \rho$ model, where σ , ω and ρ are the mediator massive mesons. In (Belvedere et al., 2014) we examine the equilibrium configurations of slowly rotating neutron stars by using the Hartle formalism in the case of the EMTF equations indicated above. We integrate these equations of equilibrium for different central densities ρ_c and circular angular velocities Ω and compute the mass M , polar R_p and equatorial R_{eq} radii, angular momentum J , eccentricity ϵ , moment of inertia I , as well as quadrupole moment Q of the configurations. Both the Keplerian mass-shedding limit and the axisymmetric secular instability are used to construct the new mass-radius relation. We compute the maximum and minimum masses and rotation frequencies of neutron stars. We compare and contrast all the results for the global and local charge neutrality cases (see Fig. 5.3).

There is the need of seeking for potential observations which could reveal this new structure of the neutron star. Since the thermal evolution of a neutron star is strongly sensitive to its microscopic and macroscopic properties, one possibility to unveil the neutron star structure is represented by observing their cooling-down. We have recently computed in (S. M. de Carvalho,

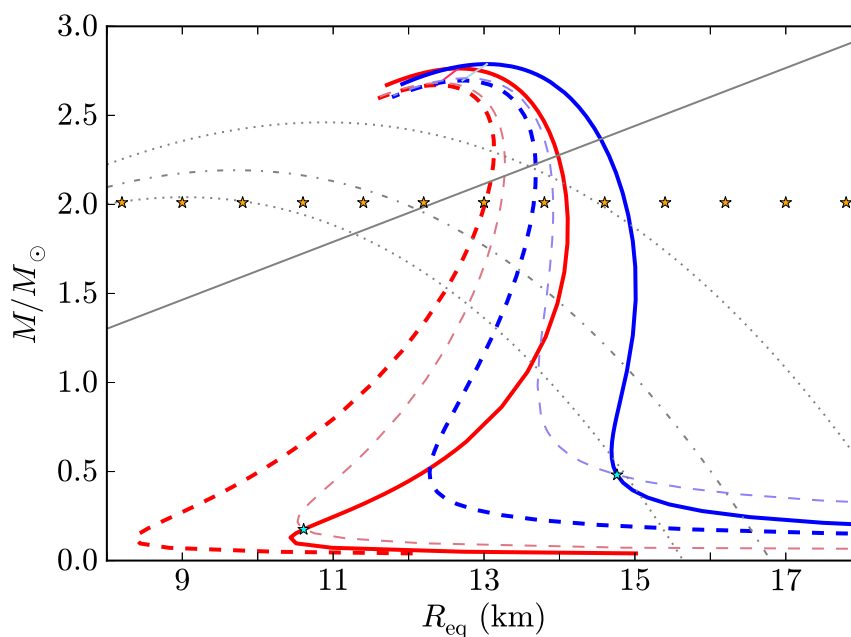


Figure 5.3: Reproduced from Belvedere et al. (2014). Comparison of the mass-radius relation of uniformly rotating neutron stars under the constraints of global and local charge neutrality.

R. Negreiros, J. A. Rueda, R. Ruffini, to appear in Phys. Rev. C) the cooling curves by integrating numerically the energy balance and transport equations in general relativity, for globally neutral neutron stars with crusts of different masses and sizes, according to this theory for different core-crust transition interfaces. In the simulation we consider all the main radiation emissivities, heat capacity, thermal conductivity, and possible superconductivity of the nucleons. We compare and contrast our study with known results for local charge neutrality. We found a new behavior for the relaxation time, depending upon the density at the base of the crust, ρ_{crust} . In particular, we find that the traditional increase of the relaxation time with the crust thickness holds only for configurations whose density of the base of the crust is greater than $\approx 5 \times 10^{13} \text{ g cm}^{-3}$ (see Fig. 5.4). The reason for this is that neutron star crusts with very thin or absent inner crust have some neutrino emission process blocked which keep the crust hotter for longer times. Therefore, accurate observations of the thermal relaxation phase in the first years of evolution of newly-born neutron stars might give crucial information on the core-crust transition which may aid us in probing the inner composition/structure of these objects.

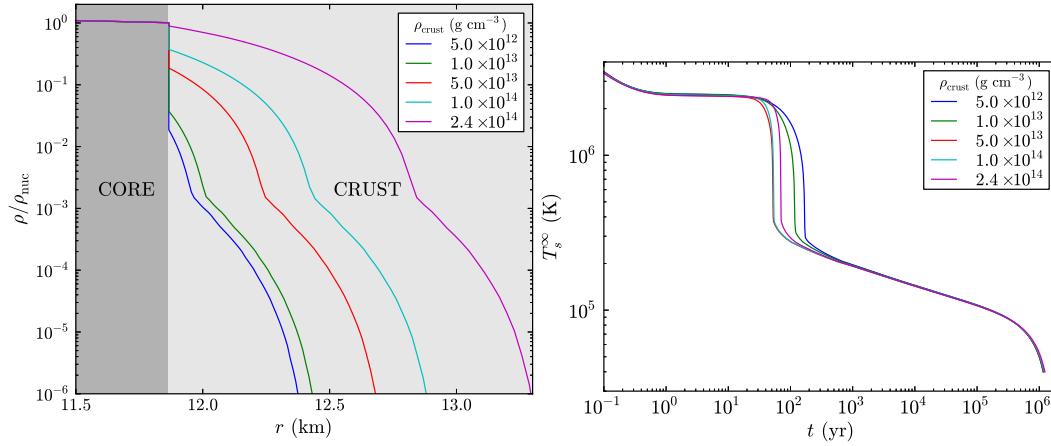


Figure 5.4: Reproduced from S. M. de Carvalho, R. Negreiros, J. A. Rueda, R. Ruffini, to appear in Phys. Rev. C. Left panel: density profile inside globally neutral neutron stars for different densities at the edge of the crust. Right panel: Evolution of the surface temperature of the neutron stars of the left panel.

5.5 Neutron Star Astrophysics

There is an interesting class of pulsars referred to as *high-magnetic field pulsars*, which are thought to be transition objects between pulsars and magnetars. The reason for this is that using fiducial of mass $M = 1.4 M_\odot$, radius $R = 10$ km, and moment of inertia, $I = 10^{45}$ g cm 2 for a neutron star, the magnetic fields inferred using the traditional magneto-dipole rotating model of pulsars appear to be very close and some of them even higher than the critical field of quantum electrodynamics, $B_c \approx 4.4 \times 10^{13}$ G. In addition, their X-ray luminosities appear higher than the rotational energy loss of the object, avoiding their explanation as rotation-powered pulsars. However, we have recently shown in (R. Belvedere, J. A. Rueda, R. Ruffini, to appear in ApJ) that the use of realistic parameters of rotating neutron stars obtained from numerical integration of the self-consistent axisymmetric general relativistic equations of equilibrium with realistic interior equation of state leads to values of the magnetic field and radiation efficiency of pulsars very different from estimates based on fiducial parameters. Furthermore, we compared and contrasted the magnetic field inferred from the traditional Newtonian rotating magnetic dipole model with respect to the one obtained from its general relativistic analog which takes into due account the effect of the finite size of the source. We have indeed shown that all the high-magnetic field pulsars can be described as canonical rotation-powered objects driven by the rotational energy of the neutron star, and with magnetic fields lower than the quantum critical field for any value of the neutron star mass (see Fig. 5.5).

We turn now to the role of neutron stars in the induced gravitational col-

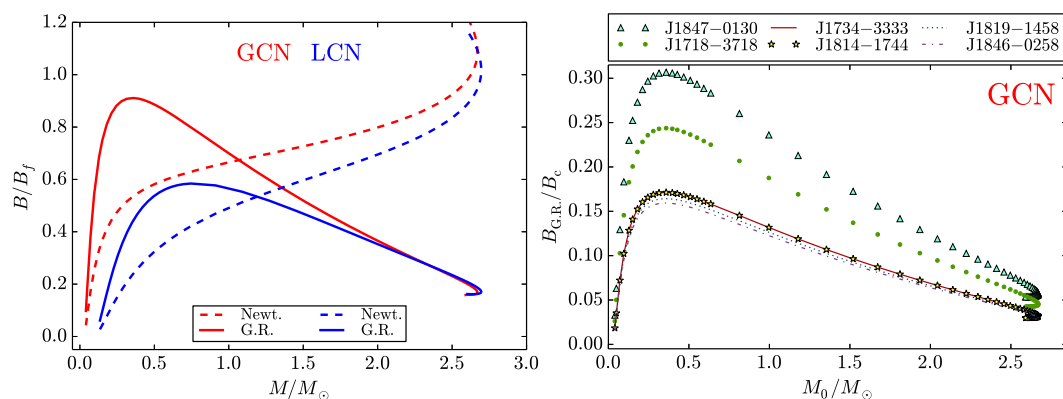


Figure 5.5: Reproduced from R. Belvedere, J. A. Rueda, R. Ruffini, to appear in ApJ. Left panel: ratio of the magnetic field (Newtonian and General Relativistic) to the fiducial value. Right panel: magnetic field $B_{G.R.}$ of the high-magnetic field pulsars as obtained from the general relativistic magnetodipole formula in units of critical magnetic field, as function of the mass (in solar masses), for static neutron stars in the global charge neutrality case.

lapse (IGC) paradigm of gamma-ray bursts (GRBs) associated with supernovae (SNe) Ic. The progenitor of those sources is a tight binary system composed of a carbon-oxygen (CO) core and a neutron star (NS) companion. The explosion of the SN leads to hypercritical accretion onto the NS companion, which reaches the critical mass, hence inducing its gravitational collapse to a black hole (BH) with consequent emission of the GRB. The first estimates of this process by Rueda and Ruffini (2012) were based on a simplified model of the binary parameters and the Bondi-Hoyle-Lyttleton accretion rate. We present new results in (Fryer et al., 2014) with the first full numerical simulations of the IGC phenomenon. We simulate the core-collapse and SN explosion of CO stars to obtain the density and ejection velocity of the SN ejecta. We follow the hydrodynamic evolution of the accreting material falling into the Bondi-Hoyle surface of the NS all the way up to its incorporation in the NS surface. The simulations go up to BH formation when the NS reaches the critical mass. For appropriate binary parameters, the IGC occurs in short timescales $\sim 10^2$ – 10^3 s owing to the combined effective action of the photon trapping and the neutrino cooling near the NS surface (see Fig. 5.6). We also show that the IGC scenario leads to a natural explanation for why GRBs are associated only with SNe Ic with totally absent or very little helium.

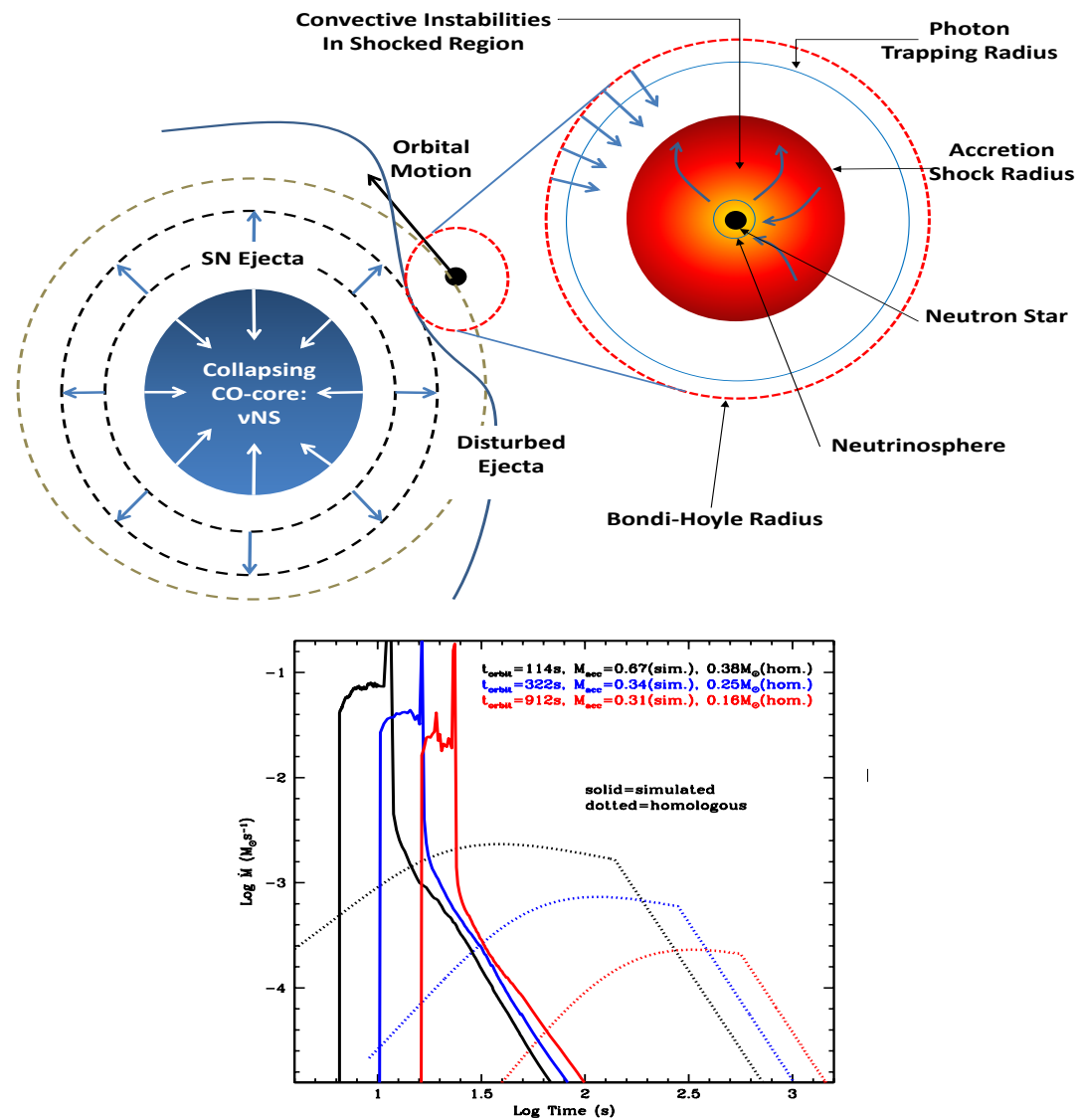


Figure 5.6: Reproduced from Fryer et al. (2014). Upper panel: Sketch of the hypercritical accretion process within the induced gravitational collapse scenario. Lower panel: Simulated accretion rates onto the neutron star companion of the CO core undergoing SN explosion.

5.6 Radiation Mechanisms of White Dwarfs and Neutron Stars

5.6.1 Gravitational Waves Radiation

The progress obtained from the Fermi-GBM and Konus-Wind satellites has been used to identify through the analysis of GRB 090227B (Muccino et al., 2013) the new class of genuinely short GRBs: short bursts with the same inner engine of the long GRBs but endowed with a severely low value of the baryon load, $B \equiv M_B c^2 / E_{tot}^{GRB} \lesssim 5 \times 10^{-5}$, where M_B is the mass of the baryons engulfed by the expanding ultrarelativistic e^+e^- plasma of energy E_{tot}^{GRB} . The emission from these GRBs mainly consists in a first emission, the peak GRB (P-GRB), followed by a softer emission squeezed on the first one. The typical separation between the two components is expected to be shorter than 1–10 ms.

A special case is GRB 090227B. From the 16 ms time-binned light curves it has been found a significant thermal emission in the first 96 ms, which has been identified with the P-GRB. The subsequent emission is identified with the extended afterglow. The P-GRB of 090227B has the highest temperature ever observed, $k_B T = 517$ keV, where k_B is the Boltzmann constant. Other properties of the GRB have been computed, e.g. the total energy emitted E_{tot}^{GRB} , Baryon load B , Lorentz factor at transparency Γ_{tr} , cosmological redshift z , intrinsic duration of the GRB emission Δt , and average density of the CircumBurst Medium (CBM) $\langle n_{CBM} \rangle$; we refer to Muccino et al. (2013) for further details.

These quantitative results lead to the conclusion that the progenitor of GRB 090227B is a neutron star binary: (1) the natal kicks velocities imparted to a neutron star binary at birth can be even larger than 200 km s^{-1} and therefore a binary system can runaway to the halo of its host galaxy, clearly pointing to a very low average number density of the CBM; (2) the very large total energy, which we can indeed infer in view of the absence of beaming, and the very short time scale of emission point again to a neutron star binary; (3) as we shall show below the very small value of the baryon load is strikingly consistent with two neutron stars having small crusts, in line with the recent neutron star theory (Belvedere et al., 2012). This first identification of a genuinely short GRB has allowed us to compute for the first time the total energy release in form of gravitational waves from a neutron star binary merger that leads to the emission of a GRB, which we have show, Oliveira et al. (2014).

In Oliveira et al. (2014), we show that the observations of the genuinely short GRB 090227B lead to crucial information on the binary neutron star progenitor. The data obtained from the electromagnetic spectrum allows to probe crucial aspects of the correct theory of neutron stars and their equation of state. The baryon load parameter B obtained from the analysis of GRB

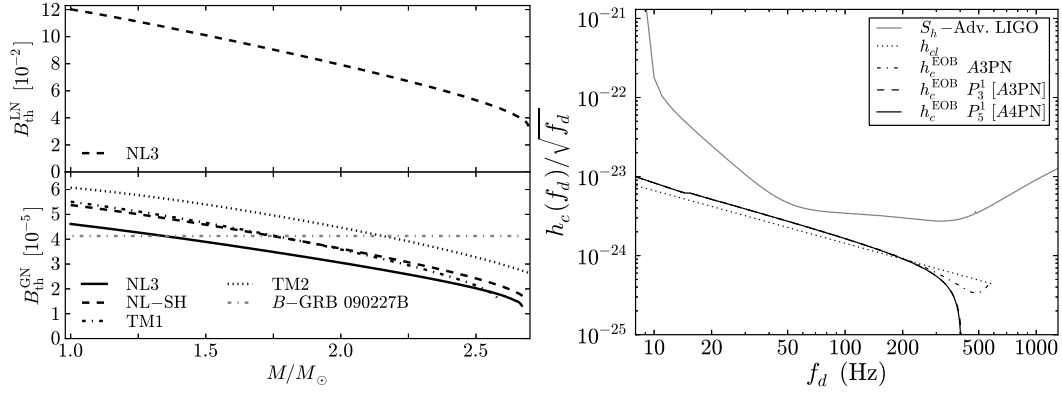


Figure 5.7: Reproduced from Oliveira et al. (2014). Left panel: theoretical baryon load from a neutron star binary merger assuming it comes from the crust mass of the binary components. Right panel: signal-to-noise ratio expected at Advanced LIGO for a neutron star merger leading to a GRB at the cosmological redshift of GRB 090227B estimated by Muccino et al. (2013), $z \approx 1.6$.

090227B, leads to a remarkable agreement of the baryonic matter expected to be ejected in a neutron star binary merger and validate a choice of the parameters of the binary components, $M_1 = M_2 = 1.34M_{\odot}$, and $R_1 = R_2 = 12.24$ km.

We computed the dynamics of the neutron star binary progenitor prior to the merger and emission of the GRB. We compare and contrast the classic description of the dynamics with the more general one given by the framework of the effective one-body formalism, which we use up to 4-PN order. We estimate the detectability of GRB 090227B by the Advanced LIGO interferometer, by computing the signal-to-noise ratio up to the contact point of the binary components, for the theoretically cosmological redshift inferred by Muccino et al. (2013), $z = 1.61$ (see Fig. 5.7). We also estimate the redshift at which Advanced LIGO would detect this GRB with a signal-to-noise ratio equal to five; we obtained $z \approx 0.08$. From the dynamics, we then estimated the total energy release in form of gravitational waves and concluded that the emission of electromagnetic radiation in a GRB by a binary neutron star system is at least one order of magnitude larger than the gravitational wave emission.

5.7 Exact Solutions of the Einstein and Einstein-Maxwell Equations in Astrophysics

In the light of the relativistic precession model, we have presented in (K. Boshkayev, D. Bini, J. A. Rueda, A. Geralico, M. Muccino, I. Siutsou, Grav. Cosm. 20, 233, 2014), a detailed analysis of the the kilohertz quasi-periodic oscillations

of low-mass X-ray binaries of the atoll and Z sources, on the basis of the relativistic precession model. We have extended previous analyses made in the Schwarzschild and Kerr backgrounds by deriving the epicyclic frequencies for the Hartle-Thorne exterior spacetime. In particular, we perform an analysis for the Z source GX 5–1 and show that the QPOs data can provide information on the parameters, namely, the mass, angular momentum and quadrupole moment of compact objects in low-mass X-ray binaries.

5.8 Critical Fields and Non-linear Electrodynamics Effects in Astrophysics

We have presented in (Pereira et al., 2014) a generalization of the Christodoulou-Ruffini mass formula for charged black holes in the weak field limit of non-linear Lagrangians for electrodynamics, i.e. for theories in which the electric fields are much smaller than the scale (threshold) fields introduced by the nonlinearities. We have shown generically that the black hole outer horizon never decreases, and demonstrated that reversible transformations are, indeed, fully equivalent to constant horizon solutions for nonlinear theories encompassing asymptotically flat black hole solutions. This result is used to decompose, in an analytical and alternative way, the total mass-energy of nonlinear charged black holes, circumventing the difficulties faced to obtain it via the standard differential approach. It is also proven that the known first law of black hole thermodynamics is the direct consequence of the mass decomposition for general black hole transformations. From all the above we finally show a most important corollary: for relevant astrophysical scenarios nonlinear electrodynamics decreases the extractable energy from a black hole with respect to the Einstein-Maxwell theory. Physical interpretations for these results are also discussed.

6 Publications 2014

6.1 Refereed Journals

6.1.1 Printed

1. J. G. Coelho, R. M. Jr. Marinho, M. Malheiro, R. Negreiros, Jorge A. Rueda, R. Ruffini, *Dynamical Instability of White Dwarfs and Breaking of Spherical Symmetry Under the Presence of Extreme Magnetic Fields*, ApJ 794, 86 (2014).

Massive, highly magnetized white dwarfs with fields up to 10^9 G have been observed and theoretically used for the description of a variety of astrophysical phenomena. Ultramagnetized white dwarfs with uniform interior fields up to 10^{18} G have been recently purported to obey a new maximum mass limit, $M_{\max} \approx 2.58 M_{\odot}$, which largely overcomes the traditional Chandrasekhar value, $M_{\text{Ch}} \approx 1.44 M_{\odot}$. Such a larger limit would make these astrophysical objects viable candidates for the explanation of the superluminous population of Type Ia supernovae. We show that several macro and micro physical aspects such as gravitational, dynamical stability, breaking of spherical symmetry, general relativity, inverse β decay, and pycnonuclear fusion reactions are of most relevance for the self-consistent description of the structure and assessment of stability of these objects. It is shown in this work that the first family of magnetized white dwarfs indeed satisfy all the criteria of stability, while the ultramagnetized white dwarfs are very unlikely to exist in nature since they violate minimal requests of stability. Therefore, the canonical Chandrasekhar mass limit of white dwarfs still has to be applied.

2. Chris L. Fryer, Jorge A. Rueda, R. Ruffini, *Hypercritical Accretion, Induced Gravitational Collapse, and Binary-Driven Hypernovae*, ApJ Lett. 793, L36 (2014).

The induced gravitational collapse (IGC) paradigm has been successfully applied to the explanation of the concomitance of gamma-ray bursts (GRBs) with supernovae (SNe) Ic. The progenitor is a tight binary system composed of a carbon-oxygen (CO) core and a neutron star (NS) companion. The explosion of the SN leads to hypercritical accretion onto the NS companion, which reaches the critical mass, hence induc-

ing its gravitational collapse to a black hole (BH) with consequent emission of the GRB. The first estimates of this process were based on a simplified model of the binary parameters and the Bondi-Hoyle-Lyttleton accretion rate. We present here the first full numerical simulations of the IGC phenomenon. We simulate the core-collapse and SN explosion of CO stars to obtain the density and ejection velocity of the SN ejecta. We follow the hydrodynamic evolution of the accreting material falling into the Bondi-Hoyle surface of the NS all the way up to its incorporation in the NS surface. The simulations go up to BH formation when the NS reaches the critical mass. For appropriate binary parameters, the IGC occurs in short timescales $\sim 10^2\text{--}10^3$ s owing to the combined effective action of the photon trapping and the neutrino cooling near the NS surface. We also show that the IGC scenario leads to a natural explanation for why GRBs are associated only with SNe Ic with totally absent or very little helium.

3. M. Razeira, A. Mesquita, C. A. Z. Vasconcellos, R. Ruffini, J. A. Rueda, R. O. Gomes, *Strangeness content of neutron stars with strong Σ -hyperon repulsion*, *Astronomische Nachrichten* 335, 739 (2014).

A new constraint on the equation of state and composition of the matter on neutron stars has been provided by the measurement of the mass $2.01 \pm 0.04 M_{\odot}$ for PSR J0348 +0432. In this contribution we investigate the role of many-body correlations in the maximum mass of neutron stars using the effective relativistic QHD-model with parameterized couplings. The complete expression of our QHD interaction Lagrangian exhausts the whole fundamental baryon octet (n , p , Σ^- , Σ^0 , Σ^+ , Λ , Ξ^- , Ξ^0) and includes many-body forces simulated by nonlinear self-couplings and meson-meson interaction terms involving scalar-isoscalar (σ , σ^*), vector-isoscalar (ω , ϕ), vector-isovector (ρ), and scalar-isovector (δ). We study the behavior of the asymmetry parameter, which describes the relative neutron excess in the system as well as the behavior of the strangeness asymmetry parameter, which specifies the strangeness content in the system and is strictly connected with the appearance of a particular hyperon species in the extreme case where the Σ^- experiences such a strong repulsion that it does not appear at all in nuclear matter.

4. M. Razeira, A. Mesquita, C. A. Z. Vasconcellos, R. Ruffini, J. A. Rueda, R. O. Gomes, *Effective field theory for neutron stars with strong Σ -hyperon repulsion*, *Astronomische Nachrichten* 335, 733 (2014).

We investigate the role of many-body correlations in the maximum mass of neutron stars using the effective relativistic QHD-model with parameterized couplings which represents an extended compilation of other effective models found in the literature. Our model exhausts

the whole fundamental baryon octet ($n, p, \Sigma^-, \Sigma^0, \Sigma^+, \Lambda, \Xi^-, \Xi^0$) and simulates corrections to the minimal Yukawa couplings by considering many-body nonlinear self-couplings and meson-meson interaction terms involving scalar-isoscalar (σ, σ^*), vector-isoscalar (ω, ϕ), vector-isovector (ρ) and scalar-isovector (δ). Following recent experimental results, we consider in our calculations the extreme case where the Σ^- experiences such a strong repulsion that it does not appear at all in nuclear matter.

5. R. Ruffini, L. Izzo, M. Muccino, G. B. Pisani, J. A. Rueda, Y. Wang, C. Barbarino, C. L. Bianco, M. Enderli, M. Kovacevic, *Induced gravitational collapse at extreme cosmological distances: the case of GRB 090423*, *A&A* 569, A39 (2014).

The induced gravitational collapse (IGC) scenario has been introduced in order to explain the most energetic gamma ray bursts (GRBs), $E_{iso} = 10^{52} - 10^{54}$ erg, associated with type Ib/c supernovae (SNe). It has led to the concept of binary-driven hypernovae (BdHNe) originating in a tight binary system composed by a FeCO core on the verge of a SN explosion and a companion neutron star (NS). Their evolution is characterized by a rapid sequence of events: 1) the SN explodes, giving birth to a new NS (ν NS). The accretion of SN ejecta onto the companion NS increases its mass up to the critical value; 2) the consequent gravitational collapse is triggered, leading to the formation of a black hole (BH) with GRB emission; 3) a novel feature responsible for the emission in the GeV, X-ray, and optical energy range occurs and is characterized by specific power-law behavior in their luminosity evolution and total spectrum; 4) the optical observations of the SN then occurs. We investigate whether GRB 090423, one of the farthest observed GRB at $z = 8.2$, is a member of the BdHN family. We compare and contrast the spectra, the luminosity evolution, and the detectability in the observations by Swift of GRB 090423 with the corresponding ones of the best known BdHN case, GRB 090618. Identification of constant slope power-law behavior in the late X-ray emission of GRB 090423 and its overlapping with the corresponding one in GRB 090618, measured in a common rest-frame, represents the main result of this article. This result represents a very significant step on the way to using the scaling law properties, proven in Episode 3 of this BdHN family, as a cosmological standard candle. Having identified GRB 090423 as a member of the BdHN family, we can conclude that SN events, leading to NS formation, can already occur, namely at 650 Myr after the Big Bang. It is then possible that these BdHNe stem from 40–60 M_{\odot} binaries. They are probing the Population II stars after the completion and possible disappearance of Population III stars.

6. Jonas P. Pereira, Herman J. Mosquera-Cuesta, J. A. Rueda, R. Ruffini, *On*

the black hole mass decomposition in nonlinear electrodynamics, Phys. Lett. B 734, 396 (2014).

In the weak field limit of nonlinear Lagrangians for electrodynamics, i.e. theories in which the electric fields are much smaller than the scale (threshold) fields introduced by the nonlinearities, a generalization of the Christodoulou-Ruffini mass formula for charged black holes is presented. It proves that the black hole outer horizon never decreases. It is also demonstrated that reversible transformations are, indeed, fully equivalent to constant horizon solutions for nonlinear theories encompassing asymptotically flat black hole solutions. This result is used to decompose, in an analytical and alternative way, the total mass-energy of nonlinear charged black holes, circumventing the difficulties faced to obtain it via the standard differential approach. It is also proven that the known first law of black hole thermodynamics is the direct consequence of the mass decomposition for general black hole transformations. From all the above we finally show a most important corollary: for relevant astrophysical scenarios nonlinear electrodynamics decreases the extractable energy from a black hole with respect to the Einstein-Maxwell theory. Physical interpretations for these results are also discussed.

7. F. G. Oliveira, J. A. Rueda, R. Ruffini, *Gravitational Waves versus X-Ray and Gamma-Ray Emission in a Short Gamma-Ray Burst*, ApJ 787, 150 (2014).

Recent progress in the understanding of the physical nature of neutron star equilibrium configurations and the first observational evidence of a genuinely short gamma-ray burst (GRB), GRB 090227B, allows us to give an estimate of the gravitational waves versus the X-ray and gamma-ray emission in a short GRB.

8. R. Ruffini, L. Izzo, M. Muccino, G. B. Pisani, J. A. Rueda, Y. Wang, C. Barbarino, C. L. Bianco, M. Enderli, M. Kovacevic, *On binary-driven hypernovae and their nested late X-ray emission*, A&A Lett. 565, L10 (2014).

The induced gravitational collapse (IGC) paradigm addresses the very energetic (10^{52} – 10^{54} erg) long gamma-ray bursts (GRBs) associated to supernovae (SNe). Unlike the traditional “collapsar” model, an evolved FeCO core with a companion neutron star (NS) in a tight binary system is considered as the progenitor. This special class of sources, here named “binary-driven hypernovae” (BdHNe), presents a composite sequence composed of four different episodes with precise spectral and luminosity features. We first compare and contrast the steep decay, the plateau, and the power-law decay of the X-ray luminosities of three selected BdHNe (GRB 060729, GRB 061121, and GRB 130427A). Second, to explain the different sizes and Lorentz factors of the emitting regions

of the four episodes, for definiteness, we use the most complete set of data of GRB 090618. Finally, we show the possible role of r-process, which originates in the binary system of the progenitor. We compare and contrast the late X-ray luminosity of the above three BdHNe. We examine correlations between the time at the starting point of the constant late power-law decay t_a^* , the average prompt luminosity $\langle L_{iso} \rangle$, and the luminosity at the end of the plateau L_a . We analyze a thermal emission (~ 0.97 – 0.29 keV), observed during the X-ray steep decay phase of GRB 090618. The late X-ray luminosities of the three BdHNe, in the rest-frame energy band 0.3–10 keV, show a precisely constrained “nested” structure. In a space-time diagram, we illustrate the different sizes and Lorentz factors of the emitting regions of the three episodes. For GRB 090618, we infer an initial dimension of the thermal emitter of $\sim 7 \times 10^{12}$ cm, expanding at $\Gamma \approx 2$. We find tighter correlations than the Dainotti-Willingale ones. We confirm a constant slope power-law behavior for the late X-ray luminosity in the source rest frame, which may lead to a new distance indicator for BdHNe. These results, as well as the emitter size and Lorentz factor, appear to be inconsistent with the traditional afterglow model based on synchrotron emission from an ultra-relativistic ($\Gamma \sim 10^2$ – 10^3) collimated jet outflow. We argue, instead, for the possible role of r-process, originating in the binary system, to power the mildly relativistic X-ray source.

9. J. A. Rueda, R. Ruffini, Y. Wu, S.-S. Xue, *Surface tension of the core-crust interface of neutron stars with global charge neutrality*, Phys. Rev. C 89, 035804 (2014).

It has been shown recently that taking into account strong, weak, electromagnetic, and gravitational interactions, and fulfilling the global charge neutrality of the system, a transition layer will happen between the core and crust of neutron stars, at the nuclear saturation density. We use relativistic mean field theory together with the Thomas-Fermi approximation to study the detailed structure of this transition layer and calculate its surface and Coulomb energy. We find that the surface tension is proportional to a power-law function of the baryon number density in the core bulk region. We also analyze the influence of the electron component and the gravitational field on the structure of the transition layer and the value of the surface tension, to compare and contrast with known phenomenological results in nuclear physics. Based on the above results we study the instability against Bohr-Wheeler surface deformations in the case of neutron stars obeying global charge neutrality. Assuming the core-crust transition at nuclear density $\rho_{core} \approx 2.7 \times 10^{14}$ g cm $^{-3}$, we find that the instability sets the upper limit to the crust density, $\rho_{crust}^{crit} \approx 1.2 \times 10^{14}$ g cm $^{-3}$. This result implies a nonzero lower limit to the maximum electric field of the core-crust transition

surface and makes inaccessible a limit of quasilocal charge neutrality in the limit $\rho_{crust} \approx \rho_{core}$. The general framework presented here can be also applied to study the stability of sharp phase transitions in hybrid stars as well as in strange stars, both bare and with outer crust. The results of this work open the way to a more general analysis of the stability of these transition surfaces, accounting for other effects such as gravitational binding, centrifugal repulsion, magnetic field induced by rotating electric field, and therefore magnetic dipole-dipole interactions.

10. S. M. de Carvalho, M. Rotonondo, J. A. Rueda, R. Ruffini, *Relativistic Feynman-Metropolis-Teller treatment at finite temperatures*, Phys. Rev. C 89, 015801 (2014).

The Feynman-Metropolis-Teller treatment of compressed atoms has been recently generalized to relativistic regimes and applied to the description of static and rotating white dwarfs in general relativity. We present here the extension of this treatment to the case of finite temperatures and construct the corresponding equation of state (EOS) of the system; applicable in a wide regime of densities that includes both white dwarfs and neutron star outer crusts. We construct the mass-radius relation of white dwarfs at finite temperatures obeying this new EOS and apply it to the analysis of ultra-low-mass white dwarfs with $M \lesssim 0.2 M_{\odot}$. In particular, we analyze the case of the white dwarf companion of PSR J1738 + 0333. The formulation is then extrapolated to compressed nuclear matter cores of stellar dimensions, systems with mass numbers $A \approx (m_{\text{Planck}}/m_n)^3$ or mass $M_{\text{core}} \approx M_{\odot}$, where m_{Planck} and m_n are the Planck and the nucleon mass. For $T \ll m_e c^2/k_B \approx 5.9 \times 10^9$ K, a family of equilibrium configurations can be obtained with analytic solutions of the ultrarelativistic Thomas-Fermi equation at finite temperatures. Such configurations fulfill global but not local charge neutrality and have strong electric fields on the core surface. We find that the maximum electric field at the core surface is enhanced at finite temperatures with respect to the degenerate case.

11. R. Belvedere, K. Boshkayev, J. A. Rueda, R. Ruffini, *Uniformly rotating neutron stars in the global and local charge neutrality cases*, Nucl. Phys. A 921, 33 (2014).

In our previous treatment of neutron stars, we have developed the model fulfilling global and not local charge neutrality. In order to implement such a model, we have shown the essential role by the Thomas-Fermi equations, duly generalized to the case of electromagnetic field equations in a general relativistic framework, forming a coupled system of equations that we have denominated Einstein-Maxwell-Thomas-Fermi (EMTF) equations. From the microphysical point of view, the weak

interactions are accounted for by requesting the β stability of the system, and the strong interactions by using the $\sigma - \omega - \rho$ nuclear model, where σ , ω and ρ are the mediator massive mesons. Here we examine the equilibrium configurations of slowly rotating neutron stars by using the Hartle formalism in the case of the EMTF equations indicated above. We integrate these equations of equilibrium for different central densities ρ_c and circular angular velocities Ω and compute the mass M , polar R_p and equatorial R_{eq} radii, angular momentum J , eccentricity ϵ , moment of inertia I , as well as quadrupole moment Q of the configurations. Both the Keplerian mass-shedding limit and the axisymmetric secular instability are used to construct the new mass-radius relation. We compute the maximum and minimum masses and rotation frequencies of neutron stars. We compare and contrast all the results for the global and local charge neutrality cases.

12. R. Belvedere, J. A. Rueda, R. Ruffini, *Static and rotating neutron stars fulfilling all fundamental interactions*, J. Kor. Phys. Soc. 65, 897 (2014).

We summarize the key ingredients of a new neutron star model fulfilling global, but not local, charge neutrality. The model is described by what we have called the Einstein-Maxwell-Thomas-Fermi equations, which account for the strong, weak, electromagnetic, and gravitational interactions, as well as thermodynamical equilibrium, within the framework of general relativity and relativistic nuclear mean field theory. We show the results for both the static and uniformly rotating neutron stars and discuss some astrophysical implications.

13. K. Boshkayev, J. A. Rueda, R. Ruffini, I. Siutsou, *General relativistic white dwarfs and their astrophysical implications*, J. Kor. Phys. Soc. 65, 855 (2014).

We present recent results on general relativistic uniformly rotating white dwarfs. Namely, on the basis of the general relativistic Feynman-Metropolis-Teller theory for white dwarfs we focus on the applications of the general relativistic uniformly rotating white dwarfs to several astrophysical phenomena related to the spin-up and spin-down stages, delayed gravitational collapse of super-Chandrasekhar white dwarfs, where we estimate the “spinning down” lifetime due the magnetic dipole breaking. In addition we describe the physical properties of Soft Gamma Repeaters and Anomalous X-Ray Pulsars (SGRs and AXPs) as massive fast rotating highly magnetized white dwarfs following Malheiro et al. (2012). We describe one of the so-called low magnetic field magnetars SGR 0418+5729 as a massive fast rotating highly magnetized white dwarf. We give bounds for the mass, radius, moment of inertia, and magnetic field for these sources by requesting the stability of realistic general relativistic uniformly rotating configurations.

14. S. M. de Carvalho, J. A. Rueda, R. Ruffini, *On the cooling of globally-neutral neutron stars*, J. Kor. Phys. Soc. 65, 861 (2014).

We compute the thermal evolution of neutron stars taking account the strong, weak, electromagnetic and gravitational interactions within the framework of general relativity, and satisfying the condition of global but not local charge neutrality. We focus on the isothermal phase following the thermal relaxation of the star and compared with observational data from isolated neutron stars.

15. D. L. Cáceres, J. A. Rueda, R. Ruffini, *On the stability of ultra-magnetized white dwarfs*, J. Kor. Phys. Soc. 65, 846 (2014).

It has been recently proposed that ultra-magnetized white dwarfs with interior fields up to 10^{18} G have a critical mass limit, $M_{\max} \approx 2.58 M_{\odot}$, which surpasses the traditional Chandrasekhar limit $M_{\text{ch}} \approx 1.44 M_{\odot}$. We show that several stability criteria and fundamental physical aspects that take place when huge magnetic fields and high densities are present have been neglected in the determination of such a new mass limit for white dwarfs, invalidating that result.

16. K. Boshkayev, D. Bini, J. A. Rueda, A. Geralico, M. Muccino, I. Siutsou, *What Can We Extract from Quasiperiodic Oscillations?*, Gravitation and Cosmology 20, 233 (2014).

In the light of the relativistic precession model, we present a detailed analysis extending the ones performed in the Schwarzschild and Kerr spacetimes. We consider the kilohertz quasi-periodic oscillations in the Hartle-Thorne spacetime which describes a rotating and deformed object. We derive analytic formulas for epicyclic frequencies in the Hartle-Thorne spacetime, and by means of these frequencies we interpret the kilohertz quasi-periodic oscillations of low-mass X-ray binaries of the atoll and Z sources, on the basis of the relativistic precession model. Particularly we perform an analysis for the Z source GX 5-1. We show that the quasi-periodic oscillations data can provide information on the parameters, namely, the mass, angular momentum and quadrupole moment of compact objects in low-mass X-ray binaries.

6.1.2 Accepted for publication or in press

1. R. Belvedere, Jorge A. Rueda, R. Ruffini, *On the magnetic field of pulsars with realistic neutron star configurations*, to appear in ApJ.

We have recently developed a neutron star model fulfilling global and not local charge neutrality, both in the static and in the uniformly rotating cases. The model is described by the coupled Einstein-Maxwell-Thomas-Fermi (EMTF) equations, in which all fundamental interactions

are accounted for in the framework of general relativity and relativistic mean field theory. Uniform rotation is introduced following the Hartle's formalism. We show that the use of realistic parameters of rotating neutron stars obtained from numerical integration of the self-consistent axisymmetric general relativistic equations of equilibrium leads to values of the magnetic field and radiation efficiency of pulsars very different from estimates based on fiducial parameters assuming a neutron star mass, $M = 1.4 M_{\odot}$, radius $R = 10$ km, and moment of inertia, $I = 10^{45}$ g cm². In addition, we compare and contrast the magnetic field inferred from the traditional Newtonian rotating magnetic dipole model with respect to the one obtained from its general relativistic analog which takes into due account the effect of the finite size of the source. We apply these considerations to the specific high-magnetic field pulsars class and show that, indeed, all these sources can be described as canonical pulsars driven by the rotational energy of the neutron star, and with magnetic fields lower than the quantum critical field for any value of the neutron star mass.

2. S. Martins de Carvalho, R. Negreiros, Jorge A. Rueda, R. Ruffini, *Thermal evolution of neutron stars with global and local neutrality*, to appear in Phys. Rev. C.

Globally neutral neutron stars, obtained from the solution of the called Einstein-Maxwell-Thomas-Fermi equations that account for all the fundamental interactions, have been recently introduced. These configurations have a more general character than the ones obtained with the traditional Tolman-Oppenheimer-Volkoff, which impose the condition of local charge neutrality. The resulting configurations have a less massive and thinner crust, leading to a new mass-radius relation. Signatures of this new structure of the neutron star on the thermal evolution might be a potential test for this theory. We compute the cooling curves by integrating numerically the energy balance and transport equations in general relativity, for globally neutral neutron stars with crusts of different masses and sizes, according to this theory for different core-crust transition interfaces. We compare and contrast our study with known results for local charge neutrality. We found a new behavior for the relaxation time, depending upon the density at the base of the crust, ρ_{crust} . In particular, we find that the traditional increase of the relaxation time with the crust thickness holds only for configurations whose density of the base of the crust is greater than $\approx 5 \times 10^{13}$ g cm⁻³. The reason for this is that neutron star crusts with very thin or absent inner crust have some neutrino emission process blocked which keep the crust hotter for longer times. Therefore, accurate observations of the thermal relaxation phase of neutron stars might give crucial information on the core-crust transition which may aid us in probing the inner composition/structure

of these objects.

3. R. Ruffini, Y. Wang, M. Kovacevic, C. L. Bianco, M. Enderli, M. Muccino, A. V. Penacchioni, G. B. Pisani, J. A. Rueda, *GRB 130427A and SN 2013cq: A Multi-wavelength Analysis of An Induced Gravitational Collapse Event*, to appear in ApJ.

We have performed our data analysis of the observations by Swift and Fermi satellites in order to probe the induced gravitational collapse (IGC) paradigm for GRBs associated with supernovae (SNe), in the “terra incognita” of GRB 130427A. We compare and contrast our data analysis with those in the literature. We have verified that the GRB 130427A conforms to the IGC paradigm by examining the power law behavior of the luminosity in the early 10^4 s of the Swift-XRT observations. This has led to the successful prediction of the occurrence of SN 2013cq and to the identification of the four different episodes of the “binary driven hypernovae” (BdHNe). The exceptional quality of the data has allowed the identification of novel features in Episode 3 including: a) the confirmation and the extension of the existence of the recently discovered “nested structure” in the late X-ray luminosity in GRB 130427A, as well as the identification of a spiky structure at 10^2 s in the cosmological rest-frame of the source; b) a power law emission of the GeV luminosity light curve and its onset at the end of Episode 2 c) different Lorentz Γ factors for the emitting regions of the X-ray and GeV emissions in this Episode 3. These results make it possible to test the details of the physical and astrophysical regimes at work in the BdHNe: 1) a newly born neutron star and the supernova ejecta, originating in Episode 1, 2) a newly formed black hole originating in Episode 2, and 3) the possible interaction among these components, observable in the standard features of Episode 3.

6.1.3 Submitted

1. Jonas P. Pereira, Jorge A. Rueda, *Stability of Stratified Stars*, submitted to ApJ.

We analyze the stability of stars with interfacial layers against radial perturbations within a generalized distributional approach. We formulate here the treatment for both neutral and charged stratified stars in Newtonian and Einstein’s gravity. We obtain the boundary condition connecting two any phases and show its relevance for realistic models of compact stars with phase transitions, owing to the modification of the star’s set of eigenmodes with respect to the continuous case.

2. Jonas P. Pereira, J. G. Coelho, Jorge A. Rueda, *Stability of thin-shell interfaces inside compact stars*, submitted to Phys. Rev. D.

We use the thin-shell Darmois-Israel formalism to model and assess the stability of the interfaces separating phases, e.g. the core and the crust, within compact stars. We exemplify this treatment in the simplest case of an incompressible star, in constant pressure phase transitions, and in the case of strange quark stars with crust.

3. Jonas P. Pereira, A. Geralico, Jorge A. Rueda, *Mass-Energy decomposition of Einstein-Born-Infeld black holes*, submitted to Phys. Rev. D.

We analyze the consequences of the recently found generalization of the Christodoulou-Ruffini black hole mass decomposition for nonlinear theories of electromagnetism in the case of Einstein-Born-Infeld black holes, which are characterized by the parameters M , Q , and b , the latter which establishes departures from the linear Maxwell behavior. We show in this context that black holes with $2b|Q| \leq 1$, irrespective of the irreducible black hole mass, M_{irr} , possess only one horizon (not a degenerated one). This would naturally lead to an upper limit to the charge of black holes. Whenever the complementary inequality takes place, the irreducible masses of black holes that generalize Reissner-Nordström black holes are constrained to a range irreducible masses. For the remaining irreducible masses, just solutions with a sole horizon are possible. Assuming that black holes emit thermal uncharged scalar particles, we further show that one satisfying $2b|Q| > 1$ takes an infinite amount of time to reach the zero temperature, settling down exactly at its minimum energy. Finally, we argue that depending on the fundamental parameter b , the radiation (electromagnetic plus gravitational) coming from Einstein-Born-Infeld black holes could differ significantly from Einstein-Maxwell ones. Hence, it could be used to assess such a parameter.

4. J. A. Rueda, R. Ruffini, Y. Wu, S.-S. Xue, *Surface tension of heavy atoms*, submitted to Phys. Rev. C.

Based on the relativistic mean field theory and the Thomas-Fermi approximation, we study the surface properties of heavy atoms in which some of the electrons have penetrated into nuclear cores. Taking into account the strong, weak, and electromagnetic interactions, we numerically study the structure of heavy atoms and calculate the surface tension and Coulomb energy. We analyze the influence of the electron component on the structure of heavy atoms and the surface tension to compare and contrast with known phenomenological results in nuclear physics and the results of the core-crust interface of neutron stars with global charge neutrality. Based on these results we study the instability against Bohr-Wheeler surface deformations in the case of heavy atoms. The results in this article provide the evidence of strong effects of the electromagnetic interaction and electrons on structure of heavy atoms.

5. R. Belvedere, Jorge A. Rueda, R. Ruffini, *On the Keplerian frequency and moment of inertia of neutron stars*, submitted to Phys. Rev. C.

In our previous treatments of static and rotating neutron stars, we have developed a neutron star model fulfilling global, but not local, charge neutrality. The model is described by what we have called the Einstein-Maxwell-Thomas-Fermi (EMTF) equations, which take into account the strong, weak, electromagnetic, and gravitational interactions within general relativity. Uniform rotation is introduced via the Hartle formalism. We compare and contrast here the moment of inertia and the sequence of maximally rotating (Keplerian) neutron stars obtained from the solution of the EMTF equations, with the claimed universal analytic formulas 1) for the Keplerian sequence by Lattimer & Prakash (2004), and 2) for the moment of inertia as a function of the compactness by Ravenhall & Pethick (1994) and by Lattimer & Schutz (2005). We show that those simple universal analytic formulas cannot properly describe the above properties of neutron stars, irrespective of the condition of charge neutrality applied, namely local or global, leading to inaccurate qualitative and quantitative results.

6.1.4 In preparation

1. L. Becerra, Chris L. Fryer, J. A. Rueda, R. Ruffini, *Hypercritical accretion in binary-driven hypernovae*.
2. L. Becerra, Chris L. Fryer, S. O. Kepler, J. A. Rueda, R. Ruffini, *The role of angular momentum in binary-driven hypernovae*.
3. L. Becerra, F. G. Oliveira, J. A. Rueda, R. Ruffini, *Mass loss, orbital binding, and gravitational wave emission in binary-driven hypernovae*.
4. K. Boshkayev, J. A. Rueda, *Induced compression by angular momentum loss in super-Chandrasekhar white dwarfs*.
5. K. Boshkayev, M. Muccino, J. A. Rueda, *Extracting neutron star multipole moments from QPOs in low-mass X-ray binaries*.
6. F. Cipolletta, C. Cherubini, J. A. Rueda, R. Ruffini, S. Filippi, *Rapidly rotating neutron stars with realistic relativistic mean-field nuclear equation of state*.
7. R. Camargo, F. Cipolletta, J. A. Rueda, R. Ruffini, *Accuracy of the slow-rotation approximation in the description of neutron stars*.
8. R. Camargo, D. P. Menezes, J. A. Rueda, R. Ruffini, *Rapidly rotating neutron stars with relativistic mean-field hadronic models satisfying nuclear matter constraints*.

9. R. Camargo, F. Cipolletta, D. P. Menezes, J. A. Rueda, R. Ruffini, *Slowly versus rapidly rotating neutron stars with relativistic mean-field hadronic models.*
10. R. Camargo, J. A. Rueda, R. Ruffini, C. A. Z. Vasconcellos, *Rapidly rotating neutron stars with strong sigma-hyperon repulsion.*
11. R. Camargo, J. A. Rueda, R. Ruffini, C. A. Z. Vasconcellos, *The effects of hyperons on the structure of rapidly rotating neutron stars.*
12. R. Belvedere, S. Chiapparini, S. B. Duarte, J. A. Rueda, R. Ruffini, *Rapidly rotating neutron stars with extended hadronic nuclear models with Δ -resonances.*
13. R. Negreiros, Brett Vern Carlson, S. M de Carvalho, *Using cooling for probing proton-superconductivity in the interior of neutron stars.*
14. S. M. Carvalho, R. Negreiros, J. A. Rueda, *Strange stars versus globally neutral neutron stars: structure and cooling.*
15. D. L. Cáceres, J. G. Coelho, J. A. Rueda, *Thermal X-ray emission of massive, fast rotating, highly magnetized white dwarfs.*
16. D. L. Cáceres, R. Camargo, J. G. Coelho, J. A. Rueda, R. Ruffini; *CXOU J1647: canonical white dwarf and neutron star versus magnetar.*
17. D. L. Cáceres, R. Camargo, J. G. Coelho, J. A. Rueda, R. Ruffini, *SGRs and AXPs as rotation-powered neutron stars and white dwarfs.*
18. J. G. Coelho, J. A. Rueda, R. Ruffini, *The canonicity of pulsars: torques, breaking index, and radiation efficiency.*
19. D. L. Cáceres, Jorge A. Rueda, R. Ruffini, *On the minimum mass of magnetized neutron stars.*

Bibliography

- ALCOCK, C., FARHI, E. AND OLINTO, A.
«Strange stars».
Astrophysical Journal, **310**, pp. 261–272 (1986).
- ALFORD, M., RAJAGOPAL, K., REDDY, S. AND WILCZEK, F.
«Minimal color-flavor-locked-nuclear interface».
Physical Review D, **64(7)**, pp. 074017–+ (2001).
- ANTONIADIS, J., FREIRE, P.C.C., WEX, N., TAURIS, T.M., LYNCH, R.S., VAN KERKWIJK, M.H., KRAMER, M., BASSA, C., DHILLON, V.S., DRIEBE, T. ET AL.
Science, **340**, p. 6131 (2013).
- ANTONIADIS, J., VAN KERKWIJK, M.H., KOESTER, D., FREIRE, P.C.C., WEX, N., TAURIS, T.M., KRAMER, M. AND BASSA, C.G.
«The relativistic pulsar-white dwarf binary PSR J1738+0333 - I. Mass determination and evolutionary history».
Monthly Notices of the Royal Astronomical Society, **423**, pp. 3316–3327 (2012).
- BAYM, G., BETHE, H.A. AND PETHICK, C.J.
«Neutron star matter».
Nuclear Physics A, **175**, pp. 225–271 (1971).
- BELVEDERE, R., BOSHKAYEV, K., RUEDA, J.A. AND RUFFINI, R.
«Uniformly rotating neutron stars in the global and local charge neutrality cases».
Nuclear Physics A, **921**, pp. 33–59 (2014).
- BELVEDERE, R., PUGLIESE, D., RUEDA, J.A., RUFFINI, R. AND XUE, S.S.
«Neutron star equilibrium configurations within a fully relativistic theory with strong, weak, electromagnetic, and gravitational interactions».
Nuclear Physics A, **883**, pp. 1–24 (2012).
- BOSHKAYEV, K., IZZO, L., RUEDA HERNANDEZ, J.A. AND RUFFINI, R.
«SGR 0418+5729, Swift J1822.3-1606, and 1E 2259+586 as massive, fast-rotating, highly magnetized white dwarfs».
Astronomy & Astrophysics, **555**, A151 (2013a).

- BOSHKAYEV, K., ROTONDO, M. AND RUFFINI, R.
«On Magnetic Fields in Rotating Nuclear Matter Cores of Stellar Dimensions».
International Journal of Modern Physics Conference Series, **12**, pp. 58–67 (2012).
- BOSHKAYEV, K., RUEDA, J.A., RUFFINI, R. AND SIUTSOV, I.
«On General Relativistic Uniformly Rotating White Dwarfs».
Astrophysical Journal, **762**, 117 (2013b).
- CAMERON, A.G.W.
«Neutron Stars».
Annual Review of Astronomy and Astrophysics, **8**, pp. 179–+ (1970).
- CHANDRASEKHAR, S.
«The Maximum Mass of Ideal White Dwarfs».
Astrophysical Journal, **74**, pp. 81–+ (1931).
- COELHO, J.G., MARINHO, R.M., MALHEIRO, M., NEGREIROS, R., CÁCERES, D.L., RUEDA, J.A. AND RUFFINI, R.
«Dynamical Instability of White Dwarfs and Breaking of Spherical Symmetry Under the Presence of Extreme Magnetic Fields».
Astrophysical Journal, **794**, 86 (2014).
- DAS, U. AND MUKHOPADHYAY, B.
«New Mass Limit for White Dwarfs: Super-Chandrasekhar Type Ia Supernova as a New Standard Candle».
Physical Review Letters, **110(7)**, 071102 (2013).
- DE CARVALHO, S.M., ROTONDO, M., RUEDA, J.A. AND RUFFINI, R.
«Relativistic Feynman-Metropolis-Teller treatment at finite temperatures».
Physical Review C, **89(1)**, 015801 (2014).
- FRYER, C.L., RUEDA, J.A. AND RUFFINI, R.
«Hypercritical Accretion, Induced Gravitational Collapse, and Binary-Driven Hypernovae».
Astrophysical Journal, **793**, L36 (2014).
- GARCÍA-BERRO, E., LORÉN-AGUILAR, P., AZNAR-SIGUÁN, G., TORRES, S., CAMACHO, J., ALTHAUS, L.G., CÓRSICO, A.H., KÜLEBI, B. AND ISERN, J.
«Double Degenerate Mergers as Progenitors of High-field Magnetic White Dwarfs».
Astrophysical Journal, **749**, 25 (2012).
- GOMBÁS, P.
Die Statistische Theorie des Atoms und Ihre Anwendungen (1949).

- HAMADA, T. AND SALPETER, E.E.
«Models for Zero-Temperature Stars.»
Astrophysical Journal, **134**, pp. 683–+ (1961).
- HARRISON, B.K., THORNE, K.S., WAKANO, M. AND WHEELER, J.A.
Gravitation Theory and Gravitational Collapse (1965).
- IZZO, L., RUEDA, J.A. AND RUFFINI, R.
«GRB 090618: a candidate for a neutron star gravitational collapse onto a black hole induced by a type Ib/c supernova.»
Astronomy & Astrophysics, **548**, L5 (2012).
- MALHEIRO, M., RUEDA, J.A. AND RUFFINI, R.
«SGRs and AXPs as Rotation-Powered Massive White Dwarfs.»
Publications of the Astronomical Society of Japan, **64**, p. 56 (2012).
- MORSINK, S.M. AND STELLA, L.
«Relativistic Precession around Rotating Neutron Stars: Effects Due to Frame Dragging and Stellar Oblateness.»
Astrophysical Journal, **513**, pp. 827–844 (1999).
- MUCCINO, M., RUFFINI, R., BIANCO, C.L., IZZO, L. AND PENACCHIONI, A.V.
«GRB 090227B: The Missing Link between the Genuine Short and Long Gamma-Ray Bursts.»
Astrophysical Journal, **763**, 125 (2013).
- NEGREIROS, R., RUFFINI, R., BIANCO, C.L. AND RUEDA, J.A.
«Cooling of young neutron stars in GRB associated to supernovae.»
Astronomy & Astrophysics, **540**, A12 (2012).
- OLIVEIRA, F.G., RUEDA, J.A. AND RUFFINI, R.
«Gravitational Waves versus X-Ray and Gamma-Ray Emission in a Short Gamma-Ray Burst.»
Astrophysical Journal, **787**, 150 (2014).
- OPPENHEIMER, J.R. AND VOLKOFF, G.M.
«On Massive Neutron Cores.»
Physical Review, **55**, pp. 374–381 (1939).
- PACHÓN, L.A., RUEDA, J.A. AND SANABRIA-GÓMEZ, J.D.
«Realistic exact solution for the exterior field of a rotating neutron star.»
Physical Review D, **73(10)**, pp. 104038–+ (2006).
- PACHÓN, L.A., RUEDA, J.A. AND VALENZUELA-TOLEDO, C.A.
«On the Relativistic Precession and Oscillation Frequencies of Test Particles around Rapidly Rotating Compact Stars.»
Astrophysical Journal, **756**, 82 (2012).

- PEREIRA, J.P., MOSQUERA CUESTA, H.J., RUEDA, J.A. AND RUFFINI, R.
«On the black hole mass decomposition in nonlinear electrodynamics».
Physics Letters B, **734**, pp. 396–402 (2014).
- RAZEIRA, M., MESQUITA, A., VASCONCELLOS, C.A.Z., RUFFINI, R.,
RUEDA, J.A. AND GOMES, R.O.
«Effective field theory for neutron stars with strong Σ^- -hyperon repulsion».
Astronomische Nachrichten, **335**, p. 733 (2014a).
- RAZEIRA, M., MESQUITA, A., VASCONCELLOS, C.A.Z., RUFFINI, R.,
RUEDA, J.A. AND GOMES, R.O.
«Strangeness content of neutron stars with strong Σ^- -hyperon repulsion».
Astronomische Nachrichten, **335**, p. 739 (2014b).
- ROTONDO, M., RUEDA, J.A., RUFFINI, R. AND XUE, S.S.
«Relativistic Feynman-Metropolis-Teller theory for white dwarfs in general relativity».
Physical Review D, **84(8)**, 084007 (2011a).
- ROTONDO, M., RUEDA, J.A., RUFFINI, R. AND XUE, S.S.
«Relativistic Thomas-Fermi treatment of compressed atoms and compressed nuclear matter cores of stellar dimensions».
Physical Review C, **83(4)**, 045805 (2011b).
- ROTONDO, M., RUEDA, J.A., RUFFINI, R. AND XUE, S.S.
«The self-consistent general relativistic solution for a system of degenerate neutrons, protons and electrons in β -equilibrium».
Physics Letters B, **701**, pp. 667–671 (2011c).
- ROTONDO, M., RUFFINI, R., XUE, S.S. AND POPOV, V.
«On Gravitationally and Electrostatically Bound Nuclear Matter Cores of Stellar Dimensions».
International Journal of Modern Physics D, **20**, pp. 1995–2002 (2011d).
- RUEDA, J.A., BOSHKAYEV, K., IZZO, L., RUFFINI, R., LORÉN-AGUILAR, P.,
KÜLEBI, B., AZNAR-SIGUÁN, G. AND GARCÍA-BERRO, E.
«A White Dwarf Merger as Progenitor of the Anomalous X-Ray Pulsar 4U 0142+61?»
Astrophysical Journal, **772**, L24 (2013).
- RUEDA, J.A. AND RUFFINI, R.
«On the Induced Gravitational Collapse of a Neutron Star to a Black Hole by a Type Ib/c Supernova».
Astrophysical Journal, **758**, L7 (2012).

- RUEDA, J.A., RUFFINI, R., WU, Y.B. AND XUE, S.S.
«Surface tension of the core-crust interface of neutron stars with global charge neutrality».
Physical Review C, **89(3)**, 035804 (2014).
- RUEDA, J.A., RUFFINI, R. AND XUE, S.S.
«The Klein first integrals in an equilibrium system with electromagnetic, weak, strong and gravitational interactions».
Nuclear Physics A, **872**, pp. 286–295 (2011).
- RUFFINI, R., BERNARDINI, M.G., BIANCO, C.L., CAITO, L., CHARDONNET, P., CHERUBINI, C., DAINOTTI, M.G., FRASCHETTI, F., GERALICO, A., GUIDA, R. ET AL.
«On Gamma-Ray Bursts».
In H. Kleinert, R.T. Jantzen and R. Ruffini (eds.), *The Eleventh Marcel Grossmann Meeting On Recent Developments in Theoretical and Experimental General Relativity, Gravitation and Relativistic Field Theories*, pp. 368–505 (2008).
- RUFFINI, R., ROTONDO, M. AND XUE, S.
«Electrodynamics for Nuclear Matter in Bulk».
International Journal of Modern Physics D, **16**, pp. 1–9 (2007).
- SALPETER, E.E.
«Energy and Pressure of a Zero-Temperature Plasma.»
Astrophysical Journal, **134**, pp. 669–+ (1961).
- SHAPIRO, S.L. AND TEUKOLSKY, S.A.
Black holes, white dwarfs, and neutron stars: The physics of compact objects (1983).
- TOLMAN, R.C.
«Static Solutions of Einstein’s Field Equations for Spheres of Fluid».
Physical Review, **55**, pp. 364–373 (1939).

DYNAMICAL INSTABILITY OF WHITE DWARFS AND BREAKING OF SPHERICAL SYMMETRY UNDER THE PRESENCE OF EXTREME MAGNETIC FIELDS

J. G. COELHO^{1,2,3}, R. M. MARINHO², M. MALHEIRO², R. NEGREIROS⁴, D. L. CÁCERES^{1,3}, J. A. RUEDA^{1,3}, AND R. RUFFINI^{1,3}

¹ Dipartimento di Fisica and ICRA, Sapienza Università di Roma, P.le Aldo Moro 5, I-00185 Rome, Italy; jaziel.coelho@icranet.org, jorge.rueda@icra.it

² Departamento de Física, Instituto Tecnológico de Aeronáutica, ITA, São José dos Campos, 12228-900 SP, Brazil; m.malheiro@ita.br

³ ICRA Net, Piazza della Repubblica 10, I-65122 Pescara, Italy

⁴ Instituto de Física, Universidade Federal Fluminense, UFF, Niterói, 24210-346 RJ, Brazil

Received 2014 April 8; accepted 2014 August 15; published 2014 September 25

ABSTRACT

Massive, highly magnetized white dwarfs with fields up to 10^9 G have been observed and theoretically used for the description of a variety of astrophysical phenomena. Ultramagnetized white dwarfs with uniform interior fields up to 10^{18} G have been recently purported to obey a new maximum mass limit, $M_{\max} \approx 2.58 M_{\odot}$, which largely overcomes the traditional Chandrasekhar value, $M_{\text{Ch}} \approx 1.44 M_{\odot}$. Such a larger limit would make these astrophysical objects viable candidates for the explanation of the superluminous population of Type Ia supernovae. We show that several macro and micro physical aspects such as gravitational, dynamical stability, breaking of spherical symmetry, general relativity, inverse β decay, and pycnonuclear fusion reactions are of most relevance for the self-consistent description of the structure and assessment of stability of these objects. It is shown in this work that the first family of magnetized white dwarfs indeed satisfy all the criteria of stability, while the ultramagnetized white dwarfs are very unlikely to exist in nature since they violate minimal requests of stability. Therefore, the canonical Chandrasekhar mass limit of white dwarfs still has to be applied.

Key words: stars: magnetic field – white dwarfs

Online-only material: color figure

1. INTRODUCTION

There is an increasing interest of the astrophysics community on highly magnetized white dwarfs (HMWDs) both from the theoretical and observational point of view. HMWDs with surface fields from 10^6 G up to 10^9 G have been confirmed observationally mainly via Zeeman splitting of the spectral lines (Külebi et al. 2009, 2010a; Kepler et al. 2010, 2013). Besides their high magnetic fields, most of them have been shown to be massive and responsible for the high-mass peak at $1 M_{\odot}$ of the white dwarf distribution; for instance, REJ 0317–853 with $M \approx 1.35 M_{\odot}$ and $B \approx (1.7\text{--}6.6) \times 10^8$ G (Barstow et al. 1995; Külebi et al. 2010b); PG 1658+441 with $M \approx 1.31 M_{\odot}$ and $B \approx 2.3 \times 10^6$ G (Liebert et al. 1983; Schmidt et al. 1992); and PG 1031+234 with the highest magnetic field $B \approx 10^9$ G (Schmidt et al. 1986; Külebi et al. 2009).

From the theoretical point of view, massive, rapidly rotating HMWDs have been proposed as an alternative scenario to the magnetar model for the description of soft-gamma repeaters and anomalous X-ray pulsars (Morini et al. 1988; Paczynski 1990; Malheiro et al. 2012; Boshkayev et al. 2013a; Rueda et al. 2013; Coelho & Malheiro 2013a, 2013b, 2014). Such white dwarfs were assumed to have fiducial parameters $M = 1.4 M_{\odot}$, $R = 10^8$ cm, $I = 10^{49}$ g cm², and magnetic fields $B \sim 10^7\text{--}10^{10}$ G, inferred using a typical oblique rotating magnetic dipole model and the observed rotation periods, $P \sim (2\text{--}12)$ s, and spin-down rates, $\dot{P} \sim 10^{-11}$ s s⁻¹.

Super-Chandrasekhar white dwarfs with high magnetic fields have been recently used to explain some properties of supernovae. Their masses overcome the traditional Chandrasekhar limit,

$$M_{\text{Ch}} = 2.015 \frac{\sqrt{3\pi}}{2} \frac{m_{\text{Pl}}^3}{(\mu_e m_{\text{H}})^2} \approx 1.44 M_{\odot}, \quad (1)$$

where $\mu_e \approx 2$ is the mean molecular weight per electron, m_{H} the mass of hydrogen atom, and $m_{\text{Pl}} = \sqrt{\hbar c/G}$ is the Planck mass.

Since such objects should be metastable, the magnetic braking of magnetized, $B \sim 10^6\text{--}10^8$ G, super-Chandrasekhar white dwarfs with $M \sim 1.5 M_{\odot}$ have been adopted to explain the delayed time distribution of Type Ia supernovae (see Ilkov & Soker 2012 for details). The explosion would be delayed for a time typical of the spin-down timescale due to magnetic braking, providing the result of the merging process is a magnetized super-Chandrasekhar white dwarf rather than a sub-Chandrasekhar one.

Super-Chandrasekhar white dwarfs have been also claimed to be able to explain the observed properties of some peculiar superluminous Type Ia supernovae, which need white dwarf progenitors with masses $(2.1\text{--}2.8) M_{\odot}$, depending on the amount of nickel needed to successfully explain both the low kinetic energies and high luminosity of these supernovae (Howell et al. 2006; Hicken et al. 2007; Yamanaka et al. 2009; Scalzo et al. 2010; Silverman et al. 2011; Taubenberger et al. 2011).

Following this idea, Das & Mukhopadhyay (2013) recently purported that the effects of a quantizing strong and uniform magnetic field on the equation of state (EOS) of a white dwarf would increase its critical mass up to a new value, $M_{\max} \approx 2.58 M_{\odot}$, significantly exceeding the Chandrasekhar limit (Equation (1)). This result would imply these objects as viable progenitors of the above superluminous Type Ia supernovae. This new mass limit would be reached, in principle, for extremely large interior magnetic fields of the order of 10^{18} G.

Therefore, since HMWDs are acquiring a most relevant role in astrophysical systems, it is of major importance to assess the validity of the assumption of the existence in nature of these objects on theoretical grounds. The effect of chemical

composition, general relativity, and inverse β decay on the determination of the maximum stable mass of non-rotating white dwarfs was studied both qualitatively and quantitatively in Rotondo et al. (2011). The extension to the uniformly rotating case, including the analysis of rotational instabilities (mass-shedding and secular instability), inverse β decay, and pycnonuclear reactions, was analyzed in Boshkayev et al. (2013b). It was shown in the latter that white dwarfs might have rotation periods as short as 0.3 s. However, the above theoretical analyses considered the white dwarf to be unmagnetized.

We show in this work that several macro and micro physical aspects such as gravitational, dynamical stability, breaking of spherical symmetry, general relativity, inverse β decay, and pycnonuclear fusion reactions are relevant for the self-consistent description of the structure and assessment of stability of ultramagnetized white dwarfs. Our analysis leads to two major conclusions.

1. In the particular case of sub-Chandrasekhar white dwarfs (or slightly exceeding the Chandrasekhar limiting value, e.g., by rotation) with surface magnetic fields in the observed range, i.e., $B \sim 10^6$ – 10^9 G, the unmagnetized approximation for the description of the structure parameters, e.g., mass and radius, is approximately correct and therefore the results of Rotondo et al. (2011) and Boshkayev et al. (2013b) can be safely used for the static and uniformly rotating cases, respectively.
2. The new mass limit, $M_{\max} \approx 2.58 M_{\odot}$, (Das & Mukhopadhyay 2013) for ultramagnetized white dwarfs (see Equation (7) below) neglects all the above macro and micro physical aspects relevant for the self-consistent description of the structure and assessment of stability of these objects. When accounted for, they lead to the conclusion that the existence of such ultramagnetized white dwarfs in nature is very unlikely due to violation of minimal requests of stability. Indeed, all these ignored effects make improbable that a white dwarf could reach such a hypothetical extreme state either in single or binary evolution.

Therefore, the canonical Chandrasekhar mass limit of white dwarfs has to be still applied and consequently, ultramagnetized white dwarfs cannot be used as progenitors of superluminous supernovae.

2. ULTRAMAGNETIZED WHITE DWARFS

In a recent work, Das & Mukhopadhyay (2013) studied the effects of extreme magnetic field in the mass and radius of white dwarfs. They showed that the EOS of a degenerate electron gas in presence of a magnetic field B directed along the z -axis, in the limit $B \rightarrow \infty$ when all electrons are constrained to the lowest Landau level, obeys a polytrope-like,

$$P = K_m \rho^2, \quad K_m = \frac{m_e c^2 \pi^2 \lambda_e^3}{(\mu_e m_H)^2 B_D}, \quad (2)$$

with λ_e as the electron Compton wavelength and $B_D = B/B_c$ as the magnetic field in units of the critical field $B_c = m_e^2 c^3 / (e \hbar) = 4.41 \times 10^{13}$ G. For obtaining the above expression, in Das & Mukhopadhyay (2013), the density of the system was assumed to be given by $\rho = \mu_e m_H n_e$, so determined only by the nuclei component where n_e is the electron number density.

Then, the Lane–Emden solution of Newtonian self-gravitating polytropes of index $n = 1$ was used to obtain the

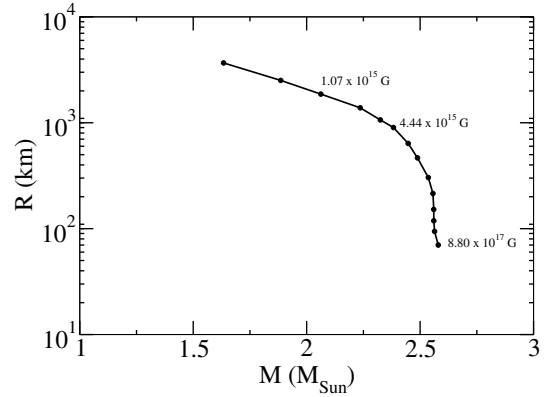


Figure 1. Mass–radius relation of magnetized white dwarfs. The curve represents the evolutionary track of the white dwarf with the increase of the uniform magnetic field inside the star obtained in Das & Mukhopadhyay (2013).

mass of an ultramagnetized white dwarf,

$$M = 4\pi^2 \rho_c \left(\frac{K_m}{2\pi G} \right)^{3/2}, \quad (3)$$

and the corresponding radius

$$R = \sqrt{\frac{\pi K_m}{2G}}, \quad (4)$$

where ρ_c is the central density.

In the present limit of one Landau level with high-electron Fermi energies, E_e^F , $E_e^F = E_{\max}^F \gg m_e c^2$, with

$$E_{\max}^F = m_e c^2 \sqrt{1 + 2B_D} \approx m_e c^2 \sqrt{2B_D}, \quad (5)$$

the maximum possible value of E_e^F , ρ_c becomes

$$\rho_c = \frac{\pi M}{4R^3} = \frac{\mu_e m_H}{\sqrt{2\pi^2 \lambda_e^3}} B_D^{3/2}. \quad (6)$$

Introducing Equation (6) into Equation (3), Das & Mukhopadhyay (2013) obtained the mass limit of ultramagnetized white dwarfs:

$$M_{\max} = \pi^{3/2} \frac{m_{\text{Pl}}^3}{(\mu_e m_H)^2} \approx 2.58 M_{\odot}, \quad (7)$$

when $\rho_c \rightarrow \infty$ and $R \rightarrow 0$. This upper bound is larger than the canonical Chandrasekhar limit given by Equation (1).

In Figure 1, we reproduce the evolutionary track of the white dwarf proposed in Das & Mukhopadhyay (2013). The magnetic field along the curve is increasing as a consequence of accretion of matter onto the star. It can be seen in the plot how the star reaches the maximum mass limit (Equation (7)) while reducing its radius.

At this point, it is already possible to identify some of the assumptions in the model of Das & Mukhopadhyay (2013), which led to the above results and which, as we show below, are unjustified, invalidating their final conclusions. (1) The EOS assumed in the limit of very intense magnetic fields, $B \rightarrow \infty$; (2) a uniform magnetic field is adopted; (3) the huge magnetic fields and the obtained mass–radius relation explicitly violate even the absolute upper limit to the magnetic field imposed by the virial theorem; (4) dynamical instabilities due to quadrupole

deformation are not taken into account; (5) spherical symmetry is assumed for all values of the magnetic field; (6) the role of the magnetic field in the hydrostatic equilibrium equations is neglected; (7) general relativistic effects are ignored, even if the final configuration is almost as compact as a neutron star and the magnetic energy is larger than the matter energy density; (8) microphysical effects such as inverse β decay and pycnonuclear fusion reactions, important in a regime where the electrons are highly relativistic, $E_e^F \gg m_e c^2$, are neglected; and (9) the magnetic field, the density, and the electron Fermi energy are assumed to increase with time inside the star as a consequence of a continuous accretion process onto the white dwarf.

3. EQUATION OF STATE AND VIRIAL THEOREM VIOLATION

Being much lighter, the electrons in the white dwarf interior are more easily disturbed by a magnetic field than the ions. Eventually, the electron gas might become quantized in Landau levels, providing the magnetic field is larger than the critical field B_c . However, for “moderate” values of the field, i.e., $B \sim B_c$, the EOS deviates still very little from the unmagnetized one. Thus, appreciable effects are seen only when the electrons occupy only the lower Landau levels, which is possible for $B_D \sim [E_{\max}^F / (m_e c^2)]^2$. Since the electrons in massive white dwarfs are ultrarelativistic with Fermi energies, $E_e^F \gtrsim 10 m_e c^2$ (Rotondo et al. 2011), it implies the necessity of magnetic fields, $B_D \gtrsim 10^2$ ($B \gtrsim 4 \times 10^{15}$ G), in order to have non-negligible magnetic field effects. It can be checked from the virial theorem that such large magnetic fields cannot develop in the interior of the white dwarf since they violate the absolute upper bound imposed by the virial theorem applied to a white dwarf that is approaching the Chandrasekhar mass limit.

The limiting field can be computed following the argument by Chandrasekhar & Fermi (1953) in their seminal work. There exists a magnetic field limit, B_{\max} , above which an equilibrium configuration is impossible because the electromagnetic energy, W_B , exceeds the gravitational energy, W_G , therefore becoming gravitationally unbound. If one includes the forces derived from the magnetic field, one can write the virial scalar relation for an equilibrium configuration as (Chandrasekhar & Fermi 1953)

$$3\Pi + W_B + W_G = 0, \quad (8)$$

where $\Pi = \int P dV$, with P the pressure of the system, W_B the positive magnetic energy, and W_G the negative gravitational potential energy. The quantity Π satisfies $\Pi = (\gamma - 1)U$ for a polytrope, $P = K\rho^\gamma$, where U is the total kinetic energy of particles. Since the total energy of the configuration can be written as $E = U + W_B + W_G$, then one can eliminate U from Equation (8) to obtain $E = -[(\gamma - 4/3)/(\gamma - 1)](|W_G| - W_B)$, and therefore the necessary condition for the stability of the star, $E < 0$, is given by

$$(3\gamma - 4)|W_G| \left(1 - \frac{W_B}{|W_G|}\right) > 0. \quad (9)$$

From this expression, we can recover, in absence of magnetic field ($W_B = 0$), the known condition for bound unmagnetized polytropes $\gamma < 4/3$, or $n < 3$ in terms of the polytrope index n defined by $\gamma = 1 + 1/n$. The presence of a magnetic field weakens the stability and no matter the value of γ , the star becomes gravitationally unbound when the magnetic energy

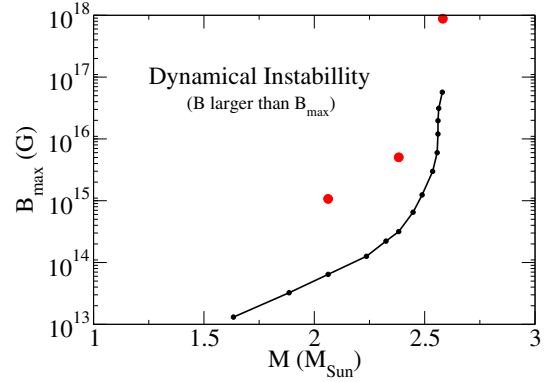


Figure 2. Maximum magnetic field B_{\max} as a function of the star mass. We show (red dots) the three values of the magnetic field of Table 1 that are above the B_{\max} line in the dynamical instability region.

(A color version of this figure is available in the online journal.)

exceeds the gravitational one; i.e., $W_B > |W_G|$. This condition clearly implies an upper bound for the magnetic field, obtained for $W_B = |W_G|$. In order to determine such a limit, we first obtain an expression for the magnetic energy of the star, which considering a constant magnetic field can be written as

$$W_B = \frac{B^2}{8\pi} \frac{4\pi R^3}{3} = \frac{B^2 R^3}{6}. \quad (10)$$

As we discussed above, the EOS used by Das & Mukhopadhyay (2013) adopts a polytrope-like form with $\gamma = 2$ or $n = 1$ under extreme magnetic fields, such that only one Landau level is populated and $E_F \gg m_e c^2$. Thus, the gravitational energy density of the spherical star configuration is (Shapiro & Teukolsky 1983)

$$W_G = -\frac{3}{5-n} \frac{GM^2}{R} = -\frac{3}{4} \frac{GM^2}{R}, \quad (11)$$

where M and R are the mass and star radius, respectively, and G is the Newton gravitational constant. Using the above expressions and expressing M and R in units of solar mass and solar radius, we find that the maximum value of magnetic field B_{\max} is given by

$$B_{\max} = 2.24 \times 10^8 \frac{M}{M_\odot} \left(\frac{R_\odot}{R}\right)^2 \text{ G}. \quad (12)$$

In the case of a Chandrasekhar white dwarf with the maximum mass $M = 1.44M_\odot$ and a radius of 3000 km, consistent with the recent calculation of massive white dwarfs (Boshkayev et al. 2013b), we obtain $B_{\max} \sim 1.7 \times 10^{13}$ G. This value is clearly lower than the critical field $B_c = 4.4 \times 10^{13}$ G.

In order to quantify how strong the violation of the virial theorem produced by the magnetic fields used in Das & Mukhopadhyay (2013) is, we choose three star configurations whose values of M and R lie in the region of high-mass configuration, $M > 2M_\odot$ (see red points in Figure 2). Using the approximation of Equation (6), we obtain the corresponding constant magnetic field B of these stars configurations. We compare these values of B with the maximum value, B_{\max} , allowed by the virial theorem (Equation (12)). In Figure 2, we present the virial limit B_{\max} as a function of the star mass obtained by Equation (12) using the values of mass and radius shown in Figure 1. In this figure, we show that such extreme magnetic fields with $B > B_{\max}$

Table 1
Mass–Radius Configurations of Magnetized White Dwarfs of Das & Mukhopadhyay (2013) with the Correspondent Magnetic Field B , the Maximum Virial Magnetic Field B_{\max} , Magnetic Energy W_B , Gravitational W_G , the Ratio of $W_B/|W_G|$, the Magnetic Field Contribution to the Total Energy Density ρ_B , and the Values of Eccentricity in Units of the Spherical Star Radius ϵ/R

M (M_\odot)	R (km)	B (G)	B_{\max} (G)	W_B ($\times 10^{51}$ erg)	$ W_G $ ($\times 10^{51}$ erg)	$W_B/ W_G $	ρ_B (g cm^{-3})	ϵ/R
2.58	7.02×10^1	8.80×10^{17}	5.70×10^{16}	4.43×10^4	1.88×10^2	235	3.40×10^{13}	−195.14
2.38	9.60×10^2	4.44×10^{15}	2.81×10^{14}	2.90×10^3	1.17×10^1	248	8.71×10^8	−204.16
2.06	1.86×10^3	1.07×10^{15}	6.49×10^{13}	1.23×10^3	4.52	273	5.10×10^7	−223.03

and the magnetized white dwarfs of Table 1 are in the instability region, violating the virial theorem. In Table 1, we show also for these configurations the magnetic energy, W_B , and the magnitude of the gravitational energy, $|W_G|$. These results indicate that the magnetic field obtained in Das & Mukhopadhyay (2013) are at least one order of magnitude larger than the maximum magnetic field allowed, B_{\max} . As a consequence, for the three star configurations, $W_B/|W_G| \sim 250$, well above the stability condition that requires $W_B/|W_G| \sim 1$. Thus, these white dwarf are unstable and unbound.

The repulsive magnetic force due to a possible variable magnetic field, as discussed in Malheiro et al. (2007), was not considered. Furthermore, a uniform magnetic field in the z -direction inside the star yields a dipole external field (Chandrasekhar & Fermi 1953). In this case, even if the magnetic fields are continuous at the star surface, their derivatives are not, producing a repulsive magnetic force at the surface. This force will push against the attractive gravitational force such that for a large magnetic field, the magnetic force will overcome the gravitational one, destabilizing the star. This physical situation is exactly the same expressed in the virial theorem condition for the star stability ($W_B < |W_G|$) discussed above. Ostriker & Hartwick (1968) analyzed the effect of magnetic fields in white dwarfs and concluded that they lead to stars with larger masses but also larger radii. One of the main consequences of the increasing magnetic field is that even a small ratio of magnetic to gravitational energy will produce an appreciable increase in the radii of magnetized white dwarfs. Consequently, it leads to a reduction of the central density, even for small mass changes. These conclusions were also confirmed in Suh & Mathews (2000), where the effect of magnetic fields in the mass–radius relation for magnetic white dwarfs were also investigated. Thus, the very compact magnetized white dwarf configuration obtained in Das & Mukhopadhyay (2013), in which large magnetic field implies large mass and *small* radius, are possible only because the effect of the repulsive magnetic force (Lorentz force) has not been properly considered. Since in Das & Mukhopadhyay (2013) it is considered the influence of a very large constant magnetic fields in the star mass and radius, assuming values for the magnetic field larger than the above limits, we conclude that these extremely magnetized white dwarfs must be unstable and unbound. The limiting magnetic field values B_{\max} shown in Figure 2 and Table 1 are clearly obtained with the radii given in Das & Mukhopadhyay (2013), which are much smaller than the self-consistent solution to the equilibrium equations would give. Since the maximum magnetic field depends on R^{-2} , see Equation (12), the real maximum possible field would actually be smaller than the one computed here.

Indeed, it is worth noting that Equation (12) can be also expressed as a limit to the magnetic flux: $\Phi_{\max} \sim B_{\max} R^2 \approx 1.1 \times 10^{30} (M/M_\odot) \text{G cm}^2$. For the hypothetical new maximum mass

(Equation (7)), $M = 2.58 M_\odot$, this maximum magnetic flux is $\Phi_{\max} \approx 2.8 \times 10^{30} \text{G cm}^2$. It is interesting that Equations (2)–(6) imply magnetic flux-freezing, namely a constant value of the magnetic flux, $\Phi_{\text{frozen}}/B_c \sim B_D R^2 = \pi^3 (\hbar c/G) (\mu_e m_{\text{H}})^{-2} \lambda_e^2 \approx 2 \times 10^{18} \text{cm}^2$, or $\Phi_{\text{frozen}} \sim B R^2 \approx 8.74 \times 10^{31} \text{G cm}^2$. This constant value highly overcomes the above maximum possible magnetic flux, Φ_{\max} , which shows in a different way the violation of the stability limit imposed by the virial theorem by the solution presented by Das & Mukhopadhyay (2013).

4. BREAKING OF SPHERICAL SYMMETRY AND QUADRUPOLE INSTABILITY

It was shown by Chandrasekhar & Fermi (1953) that the figure of equilibrium of an incompressible fluid sphere with an internal uniform magnetic field that matches an external dipole field is not represented by a sphere. The star becomes oblate by contracting along the axis of symmetry, namely along the direction of the magnetic field. Thus, we consider the fluid sphere to be deformed in such a way that the equation of the bounding surface is given by

$$r(\mu) = R + \epsilon P_l(\mu), \quad (13)$$

where $\mu = \cos \theta$, where θ is the polar angle and $P_l(\mu)$ denotes the Legendre polynomial of the order of l . It is easy to see that the deviation from the spherical configuration is given by the term $P_l(\mu)$, thus in Chandrasekhar & Fermi (1953), such a perturbation was called “ P_l - deformation.” They have also concluded that the term with $l = 2$ contributes to the corresponding change in the internal magnetic energy density (for all other values of l , the change in the magnetic energy is of the second order in ϵ). The quantity ϵ satisfies $\epsilon \ll R$ and measures the deviations from a spherical configuration. The polar and equatorial radii are $R_p = R + \epsilon P_l(1)$ and $R_{\text{eq}} = R + \epsilon P_l(0)$, respectively, thus $\epsilon = -(2/3)(R_{\text{eq}} - R_p)$ and therefore $\epsilon/R = -(2/3)(R_{\text{eq}} - R_p)/R$ for the axisymmetric deformed configuration with $l = 2$.

It was shown by Chandrasekhar & Fermi (1953) that such an axisymmetrically deformed object is favorable energetically with respect to the spherical star. Thus the star becomes unstable and proceeds to collapse along the magnetic field axis, turning into an oblate spheroidal shape with $\epsilon < 0$. The contraction continues until the configuration reaches a value of ϵ/R given by

$$\frac{\epsilon}{R} = -\frac{35}{24} \frac{B^2 R^4}{GM^2}. \quad (14)$$

Using the expression for B_{\max} given by Equation (12), one obtains

$$\frac{\epsilon}{R} = -\frac{315}{384} \left(\frac{B}{B_{\max}} \right)^2 \simeq -0.8 \left(\frac{B}{B_{\max}} \right)^2. \quad (15)$$

Therefore, when the internal magnetic field is close to the limit set by the virial theorem, the star deviates to a highly oblate shape.

We show in the last column of Table 1, the “ P_I -deformation,” ϵ/R , calculated for three configurations discussed before. The results show that $|\epsilon/R| \gtrsim 2 \times 10^2$, which implies that the star has a highly oblate shape and thus the spherical symmetry is strongly broken. Therefore, in order to account for the deformation caused by the presence of a magnetic field, a more consistent calculation considering cylindrical symmetry (see, e.g., Chandrasekhar & Fermi 1953; Ostriker & Hartwick 1968) is mandatory. It is worth mentioning that if we consider the quantum nature of the EOS of a Fermi gas subjected at fields $B \gg B_c$, the actual shape of equilibrium is defined by a the total (matter+field) pressures parallel and perpendicular to the magnetic field that are different and vanish at the star surface (Chaichian et al. 2000; Pérez Martínez et al. 2003, 2008; Strickland et al. 2012).

5. MICROSCOPIC INSTABILITIES

It is known that at sufficiently high densities in the interior of white dwarfs, the inverse β decay or electron capture process becomes energetically favorable and therefore a nucleus (Z, A) transforms into a different nucleus ($Z - 1, A$) by capturing energetic electrons. Such a process destabilizes the star since the electrons are the main responsible for the pressure in a white dwarf (Harrison et al. 1958, 1965; Shapiro & Teukolsky 1983). The process sets in when the electron chemical potential reaches the threshold energy, ϵ_Z^β , given by the difference of the nuclear binding energy between the initial and final nucleus. For helium, carbon, oxygen, and iron, ϵ_Z^β is approximately 20.6, 13.4, 10.4, and 3.7 MeV, respectively (see, e.g., Tuli 2011). For unmagnetized general relativistic white dwarfs, this occurs at a critical density $\rho_{\text{crit}}^\beta \approx 1.4 \times 10^{11}$, 4.0×10^{10} , 1.9×10^{10} , and $1.2 \times 10^9 \text{ g cm}^{-3}$, respectively, for the same chemical compositions (see Table II in Rotondo et al. 2011).

This instability was recently analyzed by Chamel et al. (2013) for the ultramagnetized white dwarfs discussed in Das & Mukhopadhyay (2013). Using Equation (5), it can be seen that the electron capture process limits the magnetic field to values lower than (see, e.g., Chamel et al. 2013)

$$B_D^\beta = \frac{1}{2} \left(\frac{\epsilon_Z^\beta}{m_e c^2} \right)^2 \approx 812.6, 342.3, 207.9, 26.2, \quad (16)$$

or $B \approx 3.6 \times 10^{16}$, 1.5×10^{16} , 9.1×10^{15} , and 1.1×10^{15} G, where we have used the previously mentioned values of ϵ_Z^β for helium, carbon, oxygen, and iron, respectively. We can show that the electron capture in the configurations of Das & Mukhopadhyay (2013) occurs even at critical central densities lower than in the unmagnetized case. Indeed, by introducing the limiting values of Equation (16) into Equation (6), we obtain the values of the critical densities $\rho_{\text{crit}}^\beta \approx 9.6 \times 10^{10}$, 2.6×10^{10} , 1.2×10^{10} , and $6.0 \times 10^8 \text{ g cm}^{-3}$, respectively, for helium, carbon, oxygen, and iron. These densities are much smaller than the ones of the massive ultramagnetized white dwarfs considered by Das & Mukhopadhyay (2013): the configurations approaching the maximum mass (Equation (7)) have magnetic fields $B_D \gtrsim 10^4$ ($B \gtrsim 4 \times 10^{17}$ G) and therefore central densities $\rho_c \gtrsim 4 \times 10^{12} \text{ g cm}^{-3}$. At such high densities, higher than the neutron drip value ($\rho_{\text{drip}} \approx 4.3 \times 10^{11} \text{ g cm}^{-3}$), the less

bound neutrons in nuclei start to drip out forming a free Fermi gas (Baym et al. 1971). The neutron drip process then starts when $\rho_c = \rho_{\text{drip}}$, where ρ_c is given by Equation (6). For a carbon composition, it occurs for a magnetic field $B_D \approx 531$, or $B \approx 2.3 \times 10^{16}$ G (see, e.g., Chamel et al. 2013). It is important to clarify that extremely large magnetic fields ($> 10^{17}$ G) are needed to modify the neutron drip value appreciable and we refer the reader to Chamel et al. (2012) for an analysis of the influence of strong magnetic fields on the precise value of the neutron drip density and pressure.

As discussed by Chamel et al. (2013), pycnonuclear fusion reactions might establish a more stringent limit with respect to the inverse β decay in an ultramagnetized white dwarf. Carbon fusion leads to ^{24}Mg , which undergoes electron capture and thus inverse β decay instability, at a density of approximately $\rho_{\text{crit,Mg}}^\beta \approx 3 \times 10^9 \text{ g cm}^{-3}$. Therefore, if C+C fusion occurs at rates high enough at densities lower than $\rho_{\text{crit,Mg}}^\beta$ to produce appreciable amounts of ^{24}Mg in times shorter than a Hubble time, then this process imposes a more tight constraint to the density of the white dwarf. Based on the up-to-date astrophysical S -factors computed in Gasques et al. (2005), we recently computed in Boshkayev et al. (2013b) the pycnonuclear carbon fusion rates in white dwarfs. We found, for instance, that C+C fusion occurs at a timescale of 0.1 Myr at a density $\rho_{\text{pyc}}^{\text{C+C}} \approx 1.6 \times 10^{10} \text{ g cm}^{-3}$. Since $\rho_{\text{pyc}}^{\text{C+C}} < \rho_{\text{crit,C}}^\beta \approx 2.6 \times 10^{10} \text{ g cm}^{-3}$, this implies that C+C pycnonuclear fusion does limit further the magnetic field strength with respect to the inverse β decay instability of carbon. Indeed, using Equation (6), we obtain that such a density is reached for a magnetic field $B_{D,\text{pyc}}^{\text{C+C}} \approx 246.6$, or $B_{\text{pyc}}^{\text{C+C}} \approx 1.1 \times 10^{16}$ G, a value lower than $B_D^{\beta,\text{C}} \approx 342.3$ or $B_C^\beta \approx 1.5 \times 10^{16}$ G. Longer reaction times implies lower densities and thus lower magnetic fields.

It is important to note that the above limits to the magnetic field are estimated assuming that the density of the system is given by Equation (6); however, more realistic estimates of these limiting fields have to account for the contribution of the magnetic field to the mass–energy density (see below in Section 6) and the self-consistent value of the electron density accounting for the real number of Landau levels populated, which will be higher than one. The above microscopic limits to the magnetic field are higher than the maximal values allowed by the virial theorem. Therefore, the macroscopic dynamical instabilities appear to set in before both electron captures and pycnonuclear reactions.

6. GENERAL RELATIVISTIC EFFECTS

We now turn to show that for ultra high magnetic fields as the ones considered by Das & Mukhopadhyay (2013), general relativistic effects are relevant; therefore, a Newtonian treatment of the equations of equilibrium is not appropriate. First, we can calculate the contribution of an ultra high magnetic field, such as the ones considered in Das & Mukhopadhyay (2013), to the total energy density. For the maximum white dwarf mass in Das & Mukhopadhyay (2013), Equation (7), which is obtained for a magnetic field $B \approx 10^{18}$ G, the magnetic field contribution to the total energy density is $\rho_B \approx B^2/(8\pi c^2) \approx 4.4 \times 10^{13} \text{ g cm}^{-3}$. This value is indeed larger than the matter density of the configuration and cannot be therefore neglected in the energy–momentum tensor of the system. However, as we have shown such a large magnetic fields cannot be reached in the star; thus the real configurations of equilibrium

likely have a magnetic field energy density much smaller than the matter energy density, implying that the unmagnetized maximum mass, the Chandrasekhar mass $M_{\text{Ch}} \approx 1.44 M_{\odot}$, still applies.

On the other hand, when the maximum mass (Equation (7)) is approached for magnetic fields $B_D \gtrsim 10^4$, the central density of the system as given by Equation (6) is $\rho_c \gtrsim 4 \times 10^{12} \text{ g cm}^{-3}$. In particular, the maximum mass configuration would have a radius $R \approx 70 \text{ km}$ and therefore a central density $\rho_c \approx 1.2 \times 10^{13} \text{ g cm}^{-3}$, only one order of magnitude less than the nuclear saturation density. These values imply that the mass, radius, and density of the ultramagnetized objects considered by Das & Mukhopadhyay (2013) are much more similar to the parameters of neutron star rather than to the ones of a white dwarf. Therefore, it is natural to ask whether the compactness of the star is such to require a full general relativistic treatment. For the above star parameters close to the maximum mass configuration, it is obtained a compactness $GM/(c^2 R) \approx 0.05$, a value in clear contrast with a Newtonian treatment of the equilibrium equations.

In this line, our previous results (Rotondo et al. 2011) become relevant. We found there that in the case of carbon white dwarfs, general relativistic instability sets in at a density $\rho_{\text{crit}} \approx 2 \times 10^{10} \text{ g cm}^{-3}$ prior to the inverse β decay instability. Such a density is much lower than the densities of the ultramagnetized white dwarfs of Das & Mukhopadhyay (2013).

7. EVOLUTIONARY PATH

As a possible mechanism of formation of ultramagnetized white dwarfs, it was proposed in Das & Mukhopadhyay (2013) and further extended in Das et al. (2013) the traditional idea that the star by accretion could increase continuously its central density and its magnetic field owing to magnetic flux conservation. However, it is unlikely that such an accretion could bring the white dwarf to such extreme regimes without passing through all the instability channels analyzed in this work. It can be shown that the magnetic field, by flux conservation, cannot increase by orders of magnitude during the accretion process if we account for the stability limits and the realistic structure of the white dwarf. Flux conservation implies that for a uniform magnetic field as assumed by Das & Mukhopadhyay (2013), $B_f/B_0 = (R_0/R_f)^2$ where “0” and “f” stand for initial and final values. It is known that in the Newtonian treatment the critical mass is reached at infinite densities, so when the radius tends to zero, it causes an unphysical large increase of the above magnetic field when approaching the critical mass value. Therefore, it is essential to this computation to take into due account the general relativistic and microscopic instabilities leading to a finite critical density and radius for the critical mass configuration. For this purpose, we use the mass–radius relation obtained by Rotondo et al. (2011). If we start an accretion process on a carbon white dwarf with initial mass $M_0 \sim 1 M_{\odot}$ ($R_0 \approx 5587.43 \text{ km}$), typical of high magnetic field white dwarf population (see Ferrario et al. 2005 for details), we obtain that the magnetic field increases only a factor $B_f/B_0 \approx 28$ up to the final mass $M_f = M_{\text{crit}} \approx 1.39 M_{\odot}$ ($R_f \approx 1051.44 \text{ km}$). Indeed, the magnetic flux is $\Phi \sim B_0 R_0^2 \approx 3.1 \times 10^{25} (B_0/10^8) \text{ G cm}^2$, to be contrasted with much higher value of the frozen value $\Phi_{\text{frozen}} \approx 8.7 \times 10^{31} \text{ G cm}^2$, inferred in Section 3 for the maximum mass solution of Das & Mukhopadhyay (2013). This implies that the accretion will most likely, in due time, lead to the triggering of the white dwarf gravitational collapse to a neu-

tron star or to an ordinary Type Ia supernovae prior to reach a stage where the magnetic field causes appreciate changes to the EOS and to the structure of the star. One could think that the white dwarf already has a huge magnetic field ($\gtrsim 10^{15} \text{ G}$) before starting the accretion process. However, as we have shown in Section 3, the virial theorem imposes a limiting magnetic flux $\Phi_{\text{max}} \approx 1.1 \times 10^{30} \sqrt{4/(5-n)} (M/M_{\odot}) \text{ G cm}^2$, where n is the polytropic index, which limits the magnetic field of the initial configuration to lower values. In addition, huge seed magnetic fields in the interior of a solar mass white dwarf appear to be in contradiction with observations since the unmagnetized mass–radius relation reproduces with appreciable accuracy the observational data (see, e.g., Vauclair et al. 1997; Provencal et al. 1998).

8. RECENT DISCUSSION ON ULTRAMAGNETIZED WHITE DWARFS

Before concluding, it is worth mentioning that during the refereeing process of this work, several criticisms were raised about the new mass limit for white dwarfs presented by Das & Mukhopadhyay (2013). Some of the inconsistencies of the ultramagnetized super-Chandrasekhar white dwarf model, such as virial theorem violation, inverse β decay and pycnonuclear instabilities, breaking of spherical symmetry, and general relativistic effects have been analyzed here. We refer the reader to Chamel et al. (2013), Dong et al. (2014), and Nityananda & Konar (2014a, 2014b) for further details on some of the above points and for some others such as the neglected effect of the Lorentz force (magnetic field gradient).

Very recently, Das & Mukhopadhyay (2014) obtained new solutions for ultramagnetized, super-Chandrasekhar white dwarfs that take into account some of the above criticisms, leading to an improvement of the treatment. They solve the general relativistic equations of hydrostatic equilibrium within the assumption of spherical symmetry, including the magnetic pressure gradient. The effect of the magnetic field gradient was introduced through a phenomenological magnetic field profile. They solved the equations for two different conditions on the parallel pressure: (1) that the spherically averaged parallel pressure be positive throughout the star or (2) the parallel pressure be positive throughout. The total pressure of the system was assumed to be isotropic and increased by an *isotropized* magnetic field contribution $(1/3)B^2/(8\pi) = B^2/(24\pi)$. Clearly, this isotropic increase of the matter pressure could give, in principle, to systems with higher masses with respect to an unmagnetized case, as indeed Das & Mukhopadhyay (2014) obtained. They find that for the constraint (1), the maximum mass could be (for some choice of the phenomenological parameters of the magnetic field profile) as high as $M_{\text{max}} \approx 3.3 M_{\odot}$, and for the constraint (2), $M_{\text{max}} \approx 2.1 M_{\odot}$. The magnetic field at the center in these configurations is $B_{\text{center}} \approx 6.8 \times 10^{14} \text{ G}$. Those solutions, although interesting, use a phenomenological magnetic field profile not coming from the self-consistent solution of the Maxwell equations coupled to the Einstein equations. It is not clear that the self-consistent solution will have a distribution of the magnetic field similar to the one employed and with a value showing such a high excursion from the center to the surface. A good example for the latter is the self-consistent solution by Ferraro (1954), for which the magnetic field at the center is only five times larger than its value at the surface. Possibly a more self-consistent calculation has been recently performed by Bera & Bhattacharya (2014), which includes the break of the spherical symmetry and

the effect of the quantum pressure anisotropy. They obtain white dwarf masses as large as $1.9 M_{\odot}$. However, the maximum mass solution was obtained there for an electron Fermi energy that overcomes the limiting value for inverse β decay analyzed in this work and in Chamel et al. (2013).

As a positive support for their model, Das & Mukhopadhyay (2014) recalled the recent mathematical analysis by Federbush et al. (2014), who showed that there exist solutions for magnetic self-gravitating $n = 1$ polytropes for a specific ansatz of the current $J = \beta r \rho$, where r is the cylindrical coordinate, ρ is the matter density, and β a constant. For the case of constant density, the above ansatz reduces to the one introduced by Ferraro (1954). Federbush et al. (2014) proved that there exist solutions providing the constant β is properly bound by a sufficiently small value. However, the solutions found by Das & Mukhopadhyay (2013, 2014) do not conform such an ansatz of the current and therefore the analysis of Federbush et al. (2014) does not apply for such a specific solution. It is noteworthy that, in addition, Federbush et al. (2014) provides a simple proof on the non-existence of magnetic stars in the spherically symmetric case since the only possible solution has a magnetic field with a singularity at the center.

9. DISCUSSION AND CONCLUSIONS

We have shown that the ultramagnetized, $B \gtrsim 10^{15}$ G, massive, $M \gtrsim 2 M_{\odot}$ white dwarfs introduced in Das & Mukhopadhyay (2013) are unlikely to exist in nature since they are subjected to several macro and micro instabilities that would make a white dwarf either collapse or explode long before to reaching such a hypothetical structure. The construction of equilibrium configurations of a magnetized compact star needs the inclusion of several effects not accounted for in Das & Mukhopadhyay (2013) and therefore the acceptance of such ultramagnetized white dwarfs as possible astrophysical objects has to be considered with caution. On the contrary, sub-Chandrasekhar white dwarfs (or slightly exceeding the Chandrasekhar limiting value, e.g., by rotation) with surface magnetic fields in the observed range, i.e., $B \sim 10^6$ – 10^{10} G, can be safely described using an unmagnetized approximation for the calculation of the structure parameters such as mass and radius.

J.G.C. acknowledges the support by the International Cooperation Program CAPES-ICRANet financed by CAPES—Brazilian Federal Agency for Support and Evaluation of Graduate Education within the Ministry of Education of Brazil, and M.M. acknowledges the financial support of CNPq and FAPESP (São Paulo state agency, thematic project No. 2013/26258-4).

REFERENCES

- Barstow, M. A., Jordan, S., O’Donoghue, D., et al. 1995, *MNRAS*, **277**, 971
 Baym, G., Bethe, H. A., & Pethick, C. J. 1971, *NuPhA*, **175**, 225
 Bera, P., & Bhattacharya, D. 2014, arXiv:1405.2282
 Boshkayev, K., Izzo, L., Rueda Hernandez, J. A., & Ruffini, R. 2013a, *A&A*, **555**, A151
 Boshkayev, K., Rueda, J. A., Ruffini, R., & Siutsou, I. 2013b, *ApJ*, **762**, 117
 Chaichian, M., Masood, S. S., Pérez Martínez, A., & Pérez Rojas, H. 2000, *PhRvL*, **84**, 5261
 Chamel, N., Fantina, A. F., & Davis, P. J. 2013, *PhRvD*, **88**, 081301
 Chamel, N., Pavlov, R. L., Mihailov, L. M., et al. 2012, *PhRvC*, **86**, 055804
 Chandrasekhar, S., & Fermi, E. 1953, *ApJ*, **118**, 116
 Coelho, J. G., & Malheiro, M. 2013a, arXiv:1307.8158
 Coelho, J. G., & Malheiro, M. 2013b, arXiv:1303.0863
 Coelho, J. G., & Malheiro, M. 2014, *PASJ*, **66**, 1
 Das, U., & Mukhopadhyay, B. 2013, *PhRvL*, **110**, 071102
 Das, U., & Mukhopadhyay, B. 2014, *JCAP*, **06**, 050
 Das, U., Mukhopadhyay, B., & Rao, A. R. 2013, *ApJL*, **767**, L14
 Dong, J. M., Zuo, W., Yin, P., & Gu, J. Z. 2014, *PhRvL*, **112**, 039001
 Federbush, P., Luo, T., & Smoller, J. 2014, arXiv:1402.0265
 Ferrario, L., Wickramasinghe, D., Liebert, J., & Williams, K. A. 2005, *MNRAS*, **361**, 1131
 Ferraro, V. C. A. 1954, *ApJ*, **119**, 407
 Gasques, L. R., Afanasjev, A. V., Aguilera, E. F., et al. 2005, *PhRvC*, **72**, 025806
 Harrison, B. K., Thorne, K. S., Wakano, M., & Wheeler, J. A. 1965, *Gravitation Theory and Gravitational Collapse* (Chicago: Univ. Chicago Press)
 Harrison, B. K., Wakano, M., & Wheeler, J. A. 1958, *Onzieme Conseil de Physique de Solvay* (Brussels: Institut International de Physique Solvay)
 Hicken, M., Garnavich, P. M., Prieto, J. L., et al. 2007, *ApJL*, **669**, L17
 Howell, D. A., Sullivan, M., Nugent, P. E., et al. 2006, *Natur*, **443**, 308
 Ilkov, M., & Soker, N. 2012, *MNRAS*, **419**, 1695
 Kepler, S. O., Kleinman, S. J., Pelisoli, I., et al. 2010, in *AIP Conf. Proc.* 1273, 17th European White Dwarf Workshop, ed. K. Werner & T. Rauch (Melville, NY: AIP), **19**
 Kepler, S. O., Pelisoli, I., Jordan, S., et al. 2013, *MNRAS*, **429**, 2934
 Külebi, B., Jordan, S., Euchner, F., Gänsicke, B. T., & Hirsch, H. 2009, *A&A*, **506**, 1341
 Külebi, B., Jordan, S., Euchner, F., Gänsicke, B. T., & Hirsch, H. 2010a, *yCat*, **350**, 61341
 Külebi, B., Jordan, S., Nelan, E., Bastian, U., & Altmann, M. 2010b, *A&A*, **524**, A36
 Liebert, J., Schmidt, G. D., Green, R. F., Stockman, H. S., & McGraw, J. T. 1983, *ApJ*, **264**, 262
 Malheiro, M., Ray, S., Cuesta, H. J. M., & Dey, J. 2007, *IJMPD*, **16**, 489
 Malheiro, M., Rueda, J. A., & Ruffini, R. 2012, *PASJ*, **64**, 56
 Morini, M., Robba, N. R., Smith, A., & van der Klis, M. 1988, *ApJ*, **333**, 777
 Nityananda, R., & Konar, S. 2014a, arXiv:1405.4719
 Nityananda, R., & Konar, S. 2014b, *PhRvD*, **89**, 103017
 Ostriker, J. P., & Hartwick, F. D. A. 1968, *ApJ*, **153**, 797
 Paczynski, B. 1990, *ApJL*, **365**, L9
 Pérez Martínez, A., Pérez Rojas, H., & Mosquera Costa, H. J. 2003, *EPJC*, **29**, 111
 Pérez Martínez, A., Pérez Rojas, H., & Mosquera Costa, H. J. 2008, *IJMPD*, **17**, 2107
 Provencal, J. L., Shipman, H. L., Høg, E., & Thejll, P. 1998, *ApJ*, **494**, 759
 Rotondo, M., Rueda, J. A., Ruffini, R., & Xue, S.-S. 2011, *PhRvD*, **84**, 084007
 Rueda, J. A., Boshkayev, K., Izzo, L., et al. 2013, *ApJL*, **772**, L24
 Scalzo, R. A., Aldering, G., Antilogus, P., et al. 2010, *ApJ*, **713**, 1073
 Schmidt, G. D., Bergeron, P., Liebert, J., & Saffer, R. A. 1992, *ApJ*, **394**, 603
 Schmidt, G. D., West, S. C., Liebert, J., Green, R. F., & Stockman, H. S. 1986, *ApJ*, **309**, 218
 Shapiro, S. L., & Teukolsky, S. A. 1983, *Black Holes, White Dwarfs, and Neutron Stars: The Physics of Compact Objects* (New York: Wiley)
 Silverman, J. M., Ganeshalingam, M., Li, W., et al. 2011, *MNRAS*, **410**, 585
 Strickland, M., Dexheimer, V., & Menezes, D. P. 2012, *PhRvD*, **86**, 125032
 Suh, I.-S., & Mathews, G. J. 2000, *ApJ*, **530**, 949
 Taubenberger, S., Benetti, S., Childress, M., et al. 2011, *MNRAS*, **412**, 2735
 Tuli, J. K. 2011, *Nuclear Wallet Cards* (8th ed.; Upton, NY: Brookhaven National Laboratory)
 Vaclair, G., Schmidt, H., Koester, D., & Allard, N. 1997, *A&A*, **325**, 1055
 Yamanaka, M., Kawabata, K. S., Kinugasa, K., et al. 2009, *ApJL*, **707**, L118

HYPERCRITICAL ACCRETION, INDUCED GRAVITATIONAL COLLAPSE, AND BINARY-DRIVEN HYPERNOVAE

CHRIS L. FRYER¹, JORGE A. RUEDA^{2,3}, AND REMO RUFFINI^{2,3}

¹ CCS-2, Los Alamos National Laboratory, Los Alamos, NM 87545, USA

² ICRA, Piazza della Repubblica 10, I-65122 Pescara, Italy

³ Dipartimento di Fisica and ICRA, Sapienza Università di Roma, P.le Aldo Moro 5, I-00185 Rome, Italy

Received 2014 June 21; accepted 2014 August 30; published 2014 September 16

ABSTRACT

The induced gravitational collapse (IGC) paradigm has been successfully applied to the explanation of the concomitance of gamma-ray bursts (GRBs) with supernovae (SNe) Ic. The progenitor is a tight binary system composed of a carbon–oxygen (CO) core and a neutron star (NS) companion. The explosion of the SN leads to hypercritical accretion onto the NS companion, which reaches the critical mass, hence inducing its gravitational collapse to a black hole (BH) with consequent emission of the GRB. The first estimates of this process were based on a simplified model of the binary parameters and the Bondi–Hoyle–Lyttleton accretion rate. We present here the first full numerical simulations of the IGC phenomenon. We simulate the core-collapse and SN explosion of CO stars to obtain the density and ejection velocity of the SN ejecta. We follow the hydrodynamic evolution of the accreting material falling into the Bondi–Hoyle surface of the NS all the way up to its incorporation in the NS surface. The simulations go up to BH formation when the NS reaches the critical mass. For appropriate binary parameters, the IGC occurs in short timescales $\sim 10^2$ – 10^3 s owing to the combined effective action of the photon trapping and the neutrino cooling near the NS surface. We also show that the IGC scenario leads to a natural explanation for why GRBs are associated only with SNe Ic with totally absent or very little helium.

Key words: gamma-ray burst: general – stars: black holes – stars: neutron – supernovae: general

Online-only material: color figures

1. INTRODUCTION

Continued observations of massive stars have demonstrated that most, if not all, massive stars are in binary systems (e.g., Smith et al. 2004; Kobulnicky & Fryer 2007; Sana et al. 2012, and references therein). A large fraction (50%–75%) of these systems are in tight binaries that interact during evolution (e.g., mass transfer, common envelope phase). The high binary fraction has led to a growing consensus that most type Ib/Ic supernova progenitors are produced in interacting binary systems (Podsiadlowski et al. 1992; De Donder & Vanbeveren 1998; Fryer et al. 2007; Yoon et al. 2010). Since the type of SNe associated with long-duration gamma-ray bursts (GRBs) are of type Ic (Della Valle 2011), it is not surprising that binaries, often involving interactions of a massive star with a compact companion, have been invoked to produce GRB SNe to remove the hydrogen envelope, spin up the star, or both (Fryer & Woosley 1998; Fryer et al. 1999c, 2007; Fryer & Heger 2005; van den Heuvel & Yoon 2007; Woosley & Bloom 2006).

The induced gravitational collapse (IGC; Ruffini et al. 2008; Rueda & Ruffini 2012) model requires a tight binary (produced in a common envelope phase) between a massive CO star (a star that has lost its hydrogen envelope and helium shell) and a neutron star (NS) companion. In this scenario, the SN explosion and the GRB occur following a precise time sequence (see Figure 1): explosion of the CO core \rightarrow hypercritical accretion onto the NS \rightarrow the critical mass is reached \rightarrow gravitational collapse to a black hole (BH) is induced \rightarrow emission of the GRB. The theoretical framework and the first estimates of the hypercritical accretion onto the NS as a function of the nature of the binary parameters were first presented in Rueda & Ruffini (2012).

It has been clear since the analysis of GRB 090618 by Izzo et al. (2012) that the entire emission of what has been traditionally called a GRB, instead of being a single event, is actually a multi-episodic source whose understanding requires scrutiny of the time-resolved data. The IGC has been successfully applied to a class of energetic ($E_{\text{iso}} \sim 10^{52}$ – 10^{54} erg) GRB SNe. These systems, recently named binary-driven hypernovae (BdHNe; Ruffini et al. 2014b), evolve in a rapid sequence lasting a few hundreds of seconds in their rest frame. Up to now, the IGC has been verified in a dozen GRBs, all with cosmological redshift $z \leq 1$ (see Pisani et al. 2013 and references therein), and very recently in one of the farthest observed sources, GRB 090423, at $z = 8.2$ (Ruffini et al. 2014a). These systems are characterized by four distinct episodes, each with specific signatures in its spectrum and luminosity evolution.

Episode 1: the first part of the emission, presenting a soft X-ray spectrum with peak energies < 100 keV and generally time-separated from the rest of the emission. It shows a complex spectrum, which at times presents a thermal component. Physically, it has the imprint of the onset of the SN in a tight binary system with the companion NS. Its emission mainly originates from the hypercritical accretion, $\dot{M} \sim 10^{-2} M_{\odot} \text{ s}^{-1}$, of the SN ejecta onto the NS.

Episode 2: the second part of emission, observed with peak energies ~ 100 keV–1 MeV. It is the canonical GRB emission originated from the gravitational collapse of the NS to a BH. The dynamics of the evolution of the highly relativistic (Lorentz factor $\Gamma \gtrsim 10^2$) e^+e^- plasma, which engulfs baryonic matter and interacts with the circumburst medium (CBM), follows the fireshell model, which takes into account the special relativistic effects and the plasma rate equation (see Ruffini 2011 and references therein).

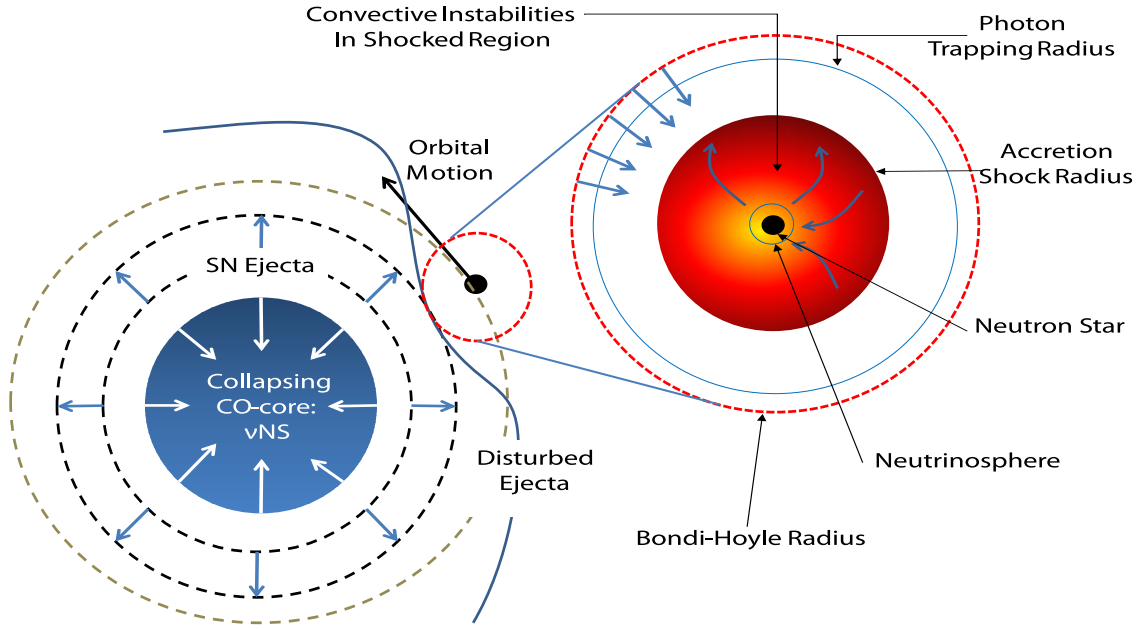


Figure 1. Induced gravitational collapse scenario.
(A color version of this figure is available in the online journal.)

Episode 3: the previously called afterglow emission, visible in optical and X-rays, and with a high energy component up to GeV energies, which observationally starts at the end of the GRB prompt emission. Independently from the features of Episode 2 and its energetics, Episode 3 appears to have a remarkable scaling law and a universal behavior for all the canonical GRBs. In the *Swift*/XRT light curve, it consists, starting at the end of the GRB prompt, of a steep decay followed by a plateau and a late power-law decay (Pisani et al. 2013). The late X-ray luminosities of BdHNe, in their rest-frame energy band 0.3–10 keV, evidence a common power-law behavior, $L_X \propto t^\alpha$, with a constant decay index clustered around $\alpha = -1.5 \pm 0.2$. Such a constant afterglow decay represents an authentic nested structure (Ruffini et al. 2014b) in the late X-ray emission of GRB SNe and it has been indicated as the qualifying feature for a GRB to be a BdHN family member. The identification of GRB 090423 at $z = 8.2$ as a BdHN (Ruffini et al. 2014a) implies that SN events, leading to NS formation, can occur already at 650 Myr after the Big Bang. The above opens the way to consider the late X-ray power law as a possible distance indicator.

Episode 4: the emergence of the SN emission after ~ 10 –15 days from the occurrence of the GRB, in the source rest frame. It has been observed for almost all the sources fulfilling the IGC paradigm with $z \sim 1$ for which current optical instrumentation allows their identification.

The first estimates of the IGC process (Rueda & Ruffini 2012; Izzo et al. 2012; Penacchioni et al. 2012, 2013; Pisani et al. 2013; Ruffini et al. 2013) were based on a simplified model of the binary parameters and the Bondi–Hoyle–Lyttleton accretion framework. The aim of this Letter is to better constrain the binary characteristics that lead to the IGC phenomenon (Episode 1) using more detailed supernova explosions coupled with models based on simulations of hypercritical accretion in supernova fallback (Fryer et al. 1996; Fryer 2009). We consider numerical simulations of collapsing CO cores leading to SNe Ic in order to calculate realistic profiles for the density and ejection velocity

of the SN outer layers. We follow the hydrodynamic evolution of the accreting material falling into the Bondi–Hoyle accretion region all the way up to its incorporation onto the NS surface.

2. BINARY PROGENITOR

The hypercritical accretion onto the NS from the SN ejecta in the IGC scenario can be estimated using the Bondi–Hoyle–Lyttleton formalism (Hoyle & Lyttleton 1939; Bondi & Hoyle 1944; Bondi 1952):

$$\dot{M}_{\text{BHL}} = 4\pi r_{\text{BHL}}^2 \rho (v^2 + c_s^2)^{1/2}, \quad (1)$$

where ρ is the density of the SN ejecta, v is the ejecta velocity in the rest frame of the NS (this includes a component from the ejecta velocity, v_{ej} , and another component from the orbital velocity of the NS, v_{orb}), c_s is the sound speed of the SN ejecta, and r_{BHL} is the Bondi radius:

$$r_{\text{BHL}} = \frac{GM_{\text{NS}}}{v^2 + c_s^2}, \quad (2)$$

where G is the gravitational constant and M_{NS} is the NS mass. Both the velocity components, v_{orb} and v_{ej} , are typically much higher than the sound speed. The ejecta velocity as a function of time is determined by the explosion energy and the nature of the SN explosion. The orbital velocity depends on the orbital separation, which in turn depends on the radius of the CO star and the binary interactions creating the tight-orbit binary just prior to the explosion of the CO core. The effect of the NS magnetic field can be neglected for $\dot{M} > 2.6 \times 10^{-8} M_\odot \text{ s}^{-1} = 0.8 M_\odot \text{ yr}^{-1}$ (Fryer et al. 1996; Rueda & Ruffini 2012).

The density evolution of the SN ejecta near the NS companion depends upon the SN explosion and the structure of the progenitor immediately prior to collapse. In Figure 2, we show the density profile for three different low-metallicity stars with initial zero-age main sequence masses of $M_{\text{ZAMS}} = 15, 20,$ and $30 M_\odot$ (Woosley et al. 2002). We designate the edge of the CO

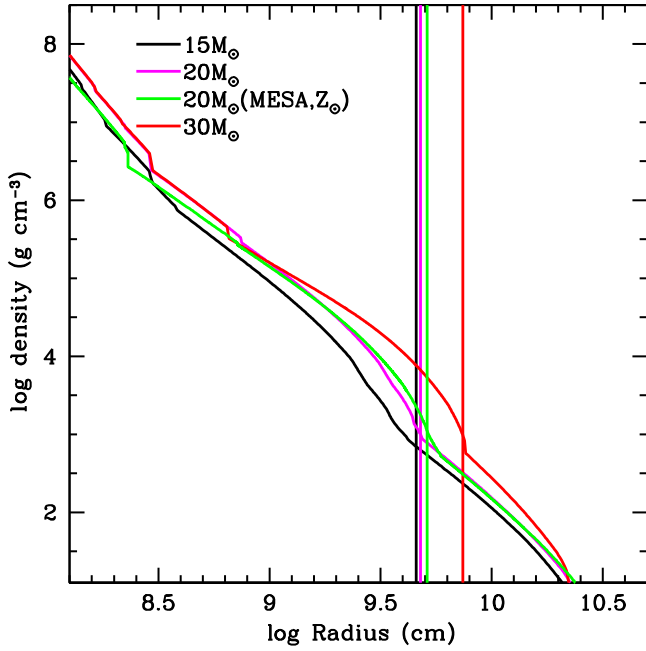


Figure 2. Density profile of different CO core progenitors with $M_{\text{ZAMS}} = 15$, 20, and $30 M_{\odot}$ for low-metallicity ($Z = 0.0001 Z_{\odot}$) stars using the Kepler stellar evolution code (Woosley et al. 2002). For comparison, we include the density structure of a solar metallicity star produced by the MESA code (S. Jones 2014, in preparation). The vertical lines show the radius of the CO core. As we shall see below, the accretion rate is extremely sensitive to the structure of the star.

(A color version of this figure is available in the online journal.)

core in all of these stars. The density profile depends on both on the initial conditions of the star (metallicity, initial mass, rotation) as well as the stellar evolution code used (in this case, KEPLER). The density profile of a $20 M_{\odot}$, solar metallicity star (S. Jones 2014, in preparation) is obtained using the MESA code. The IGC model assumes that both the hydrogen and helium layers are removed prior to collapse. There is a 3–4 order of magnitude pressure jump between the CO core and helium layer, indicating that the star will not expand significantly when the helium layer is removed. Comparisons of KEPLER models with the stripped CO cores from Moriya et al. (2010) suggest that, for some stellar evolution codes, the CO cores could be 1.5–2 times larger. We will discuss this effect on the accretion rate below.

The compactness of the CO core (see Figure 2) is such that there is no Roche lobe overflow⁴ prior to the SN explosion. For instance, for a CO core progenitor with $M_{\text{ZAMS}} = 15 M_{\odot}$ ($M_{\text{CO}} \approx 5 M_{\odot}$, $R_{\text{CO}} \approx 3 \times 10^9$ cm), no Roche lobe overflow occurs for binary periods $P \geq 2$ min or binary separation $a \geq 6 \times 10^9$ cm for an NS companion mass $M_{\text{NS}} \geq 1.4 M_{\odot}$.

3. BINARY-DRIVEN HYPERCRITICAL ACCRETION

To derive the hypercritical accretion onto the NS, we must implement an explosion model. Here, we take two approaches. The first is to assume a homologous outflow with a set explosion energy on the progenitor star structure. For comparison, we also use a second approach that follows the collapse, bounce, and explosion of the $20 M_{\odot}$ progenitor discussed above using the parameterized model developed to study a range of SN explosion

⁴ The Roche lobe radius is (Eggleton 1983)

$R_{\text{L,CO}} \approx 0.49q^{2/3} / [0.6q^{2/3} + \ln(1 + q^{1/3})]$, where $q = M_{\text{CO}}/M_{\text{NS}}$.

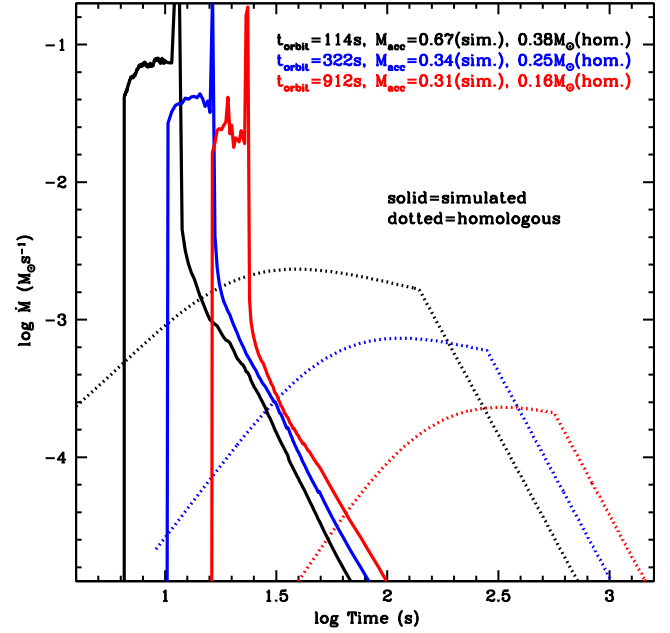


Figure 3. Hypercritical accretion for selected separation distances and for a star progenitor of $20 M_{\odot}$ using our two approaches for the explosive engine. The supernova shock increases the density of the outgoing material, producing a pileup at the shock that leads to a spike in the accretion rate over a brief (few second) period, a much sharper accretion profile than our $\gtrsim 100$ s accretion time for our homologous outflow models.

(A color version of this figure is available in the online journal.)

energies for fallback and SN light curves (Frey et al. 2013). The calculation uses a one-dimensional (1D) core-collapse code (Fryer et al. 1999a) to follow the collapse and bounce, and then injects energy just above the proto-NS to drive different SN explosions, mimicking the convective-engine paradigm. With this progenitor and explosion, we produce an example density and velocity evolution history at the position of the Bondi–Hoyle surface of our binary companion. Figure 3 shows the Bondi–Hoyle infall rate from both our homologous outflow and our simulated SN models for a range of orbital separations (the innermost separation is determined to be just high enough that the CO star does not overflow its Roche lobe). In our simulated explosion, the density piles up in the shock, producing a much sharper burst of accretion onto the NS. The accretion rate can be an order of magnitude higher in these models, but for a much shorter time, such that the total mass accreted is only less than two times higher.

This infall rate is well above the Eddington rate and will be reset to this rate if the assumptions of the Eddington accretion limit apply. The Eddington rate is derived assuming that the energy released when material accretes onto a compact object is released in photons and these photons exert pressure on the infalling material, reducing the accretion rate. The Eddington accretion limit, or critical accretion rate, makes a series of assumptions: the potential energy is released in the form of photons, the inflowing material and outflowing radiation is spherically symmetric, the photons are not trapped in the flow and can deposit momentum to the inflowing material, and the opacity is dominated by electron scattering. For a wide variety of accreting X-ray binaries, the Eddington limit seems to hold (at the order of magnitude level), but many of these assumptions break down for accretion rates as high as the ones achieved in the IGC scenario and these limits do not apply.

Table 1
Hypercritical Accretion Mass in the IGC scenario

Progenitor ZAMS Mass	$M_{\text{acc}}^a (M_{\odot}), t_{\text{acc}} \text{ (s)}$			
	$a_{\text{orbit}}/a_{\text{min}}^b = 1$	2	4	8
15 M_{\odot}	0.24, 160	0.15, 400	0.085, 600	0.042, 1300
20 M_{\odot}	0.38, 150	0.25, 250	0.16, 600	0.096, 1200
20 M_{\odot}^c	0.67, 5	0.34, 6	0.31, 7	0.17, 7
20 M_{\odot}^d	0.084, 150	0.058, 250	0.032, 600	0.001, 1200
30 M_{\odot}	0.62, 800	0.42, 2000	0.28, 3700	0.16, 8000

Notes.

^a Total accretion at super-Eddington rates in M_{\odot} .

^b a_{min} : minimum orbital separation such that the CO core does not fill its Roche lobe.

^c Simulated with the KEPLER code.

^d Solar metallicity star, simulated with the MESA code.

First and foremost, the photons in the hypercritical IGC accretion rates are almost certainly trapped in the flow. Chevalier (1989) derived the trapping radius where the photons emitted diffuse outward at a slower velocity than the infalling material flows inward:

$$r_{\text{trapping}} = \min[(\dot{M}_{\text{BHL}}\kappa)/(4\pi c), r_{\text{BHL}}], \quad (3)$$

where κ is the opacity (in $\text{cm}^2 \text{g}^{-1}$) and c is the speed of light. If the trapping radius is near or equal to the Bondi–Hoyle radius, the photons are trapped in the flow and the Eddington limit does not apply. This hypercritical accretion has been studied in detail for common envelope scenarios where κ is likely to be dominated by electron scattering. However, in SN fallback (Fryer et al. 1999b) and the IGC model, heavy elements are not completely ionized and lines can significantly increase the opacity. Following Colgan et al. (2013), we estimate for our CO core a Rosseland mean opacity of roughly $5 \times 10^3 \text{ cm}^2 \text{g}^{-1}$, a factor of $\sim 10^4$ higher than electron scattering. This means that the trapping radius is higher for the IGC model. Combined with our high accretion rates, it is clear that the Eddington limit does not apply in this scenario and hypercritical, largely Super-Eddington, accretion occurs. The inflowing material shocks as it piles up onto the NS, producing an atmosphere on top of the NS (for details, see Zel’dovich et al. 1972; Chevalier 1989; Houck & Chevalier 1991; Fryer et al. 1996). As the atmosphere compresses, it becomes sufficiently hot to emit neutrinos that cool the infalling material, allowing it to be incorporated into the NS. For details of the simulation of this process, we refer the reader to Ruffini & Wilson (1973), Fryer et al. (1996), and Fryer (2009).

Table 1 shows the total mass accreted (M_{acc}) for selected orbital separations and progenitor masses using different stellar evolution codes and different models (homologous versus simulated) of the SN explosion. We also indicate the time interval (t_{acc}) in which the accretion rate is integrated to obtain M_{acc} . For these systems, the accretion rate is largely hypercritical, exceeding $10^{-3} M_{\odot} \text{ s}^{-1}$, so we expect a fraction of these systems to push beyond the maximum NS mass and collapse to a BH. Note that for the helium star systems, the accretion rate is not high enough to produce an IGC. If the radius of the CO core was twice that of our models (see the discussion on the Moriya et al. 2010 models), our peak accretion rates would correspond to the $a_{\text{orbit}}/a_{\text{min}}^b = 2$ values.

As material piles onto the NS and the atmosphere radius, the accretion shock moves outward. The accretion shock weakens as it moves out and the entropy jump (derived from the shock

jump conditions) becomes smaller. This creates an atmosphere that is unstable to Rayleigh–Taylor convection. Simulations of these accretion atmospheres show that these instabilities can accelerate above the escape velocity, driving outflows from the accreting NS with final velocities approaching the speed of light, and ejecting up to 25% of the accreting material (Fryer et al. 2006; Fryer 2009). The entropy of the material at the base of our atmosphere, S_{bubble} , is given by (Fryer et al. 1996)

$$S_{\text{bubble}} = 38.7 \left(\frac{M_{\text{NS}}}{2 M_{\odot}} \right)^{7/8} \left(\frac{M_{\text{BHL}}}{0.1 M_{\odot} \text{ s}^{-1}} \right)^{-1/4} \left(\frac{r_{\text{NS}}}{10^6 \text{ cm}} \right)^{-3/8} k_B \text{ per nucleon} \quad (4)$$

where r_{NS} is the radius of the NS. The corresponding temperature of the bubble, T_{bubble} , is

$$T_{\text{bubble}} = 195 S_{\text{bubble}}^{-1} \left(\frac{r_{\text{NS}}}{10^6 \text{ cm}} \right)^{-1}. \quad (5)$$

For the typical hypercritical accretion conditions of the IGC, the temperature of the bubble when it begins to rise is $T_{\text{bubble}} \sim 5 \text{ MeV}$. If it rises adiabatically, expanding in all dimensions, its temperature drops to 5 keV at a radius of 10^9 cm , far too cool to observe. However, if it is ejected in a jet, as simulated by Fryer (2009), it may expand in the lateral direction but not in the radial direction, so $\rho \propto r^2$ and $T \propto r^{-2/3}$. In this scenario, the bubble outflow would have $T_{\text{bubble}} \sim 50 \text{ keV}$ at 10^9 cm and $T_{\text{bubble}} \sim 15 \text{ keV}$ at $6 \times 10^9 \text{ cm}$. This could explain the temperature and size evolution of the blackbody emitter observed in Episode 1 of several BdHNe (see, e.g., Izzo et al. 2012; Penacchioni et al. 2012, 2013; Pisani et al. 2013; Ruffini et al. 2013). For instance, the blackbody observed in Episode 1 of GRB 090618 (Izzo et al. 2012) evolves as $T \propto r^{-m}$ with $m = 0.75 \pm 0.09$, whose lower value is in striking agreement with the above simplified theoretical estimate. We are currently deepening our analysis of the possible explanation of the thermal emission observed in Episode 1 of BdHNe as being due to the convective instabilities in the accretion process. However, this is beyond the scope of this work and the results will be presented elsewhere.

4. DISCUSSION

While in this Letter we address simulations of Episode 1 of the IGC, let us shortly outline some recent progress in the understanding of the structure of Episode 3, which may become complementary to this work. (1) The scaling laws are remarkable in the X-ray luminosity in all BdHNe (see Pisani et al. 2013; Ruffini et al. 2014b for details). (2) The very high energy emission, all the way up to 100 GeV in GRB 130427A, as well as the optical one, follow a power-law behavior similar to the X-ray emission described above. The corresponding spectral energy distribution is also described by a power-law function with quite similar decay indexes (Ruffini et al. 2014c). These results clearly require a common origin for this emission process. (3) An X-ray thermal component has been observed in the early phases of Episode 3 of GRBs 060202, 060218, 060418, 060729, 061007, 061121, 081007, 090424, 100316D, 100418A, 100621A, 101219B, and 120422A (Page et al. 2011; Starling et al. 2012; Friis & Watson 2013). This feature has been clearly observed in GRB 090618 and GRB 130427A, implying a size of the emission region of 10^{12} – 10^{13} cm expanding at velocity $0.1 < v/c < 0.9$, and hence a bulk Γ Lorentz factor $\lesssim 2$ (Ruffini et al. 2014b, 2014c).

Recently, Ruffini et al. (2014b) raised the possibility of using the nuclear decay of ultra-heavy r -process nuclei, originated in

the close binary phase of Episode 1, as an energy source of Episode 3. These processes lead to power-law emission (see, e.g., Kasen et al. 2013) with a decay index similar to the one observed in Episode 3. The total energy emitted in the nuclear decays is also in agreement with the observations in Episode 3 of BdHNe. r -process avalanches in BdHNe could also originate from a mechanism similar to the one outlined by Fryer et al. (2006) in SN fallback. Additional possibilities for generating the scale-invariant power law in the luminosity evolution and spectrum are the type I and type II Fermi acceleration processes (Fermi 1949) during the evolution of the SN remnant. The application of the Fermi acceleration mechanisms has two clear advantages: the generation of the aforementioned power-law behaviors, and solving the longstanding problem, formulated by Fermi, of identifying the injection source in order to have his acceleration mechanism at work on astrophysical scales.

We have advanced our estimates of the NS accretion rate within the IGC model, which leads to BdHNe with all the above features. Our estimates assume that the Bondi–Hoyle–Lyttleton formalism is valid for our calculations. Although it has been shown that this formalism is valid in steady-state systems (see Edgar 2004, and references therein), the IGC model, with its time-variable conditions, may push the validity of these assumptions. Full accretion models are required in order to validate our results and/or to produce more reliable accretion rates.

It appears from observations that a condition necessary to produce a GRB SN is that the pre-SN core is fully absent of or has very little helium. We have shown that the IGC process provides a natural explanation for that condition: hypercritical accretion rates are favored by the presence of a compact CO core, since it leads to tighter binaries and produces higher opacities of the ejecta, which favors the photon trapping. We showed that helium cores do not trigger enough hypercritical accretion onto the NS companion to produce an IGC. A number of mechanisms have been proposed to remove this material (a common problem for most GRB scenarios): stellar winds (the difficulty with this model is removing just the helium layer and not a considerable portion of the CO core), mass transfer (only low-mass helium cores undergo a helium giant phase, so conditions for mass transfer or common envelope phases may be difficult to reproduce), and enhanced mixing, allowing fusion to consume the helium layer (Frey et al. 2013). Detailed simulations of the binary evolution, up to the formation of binary systems, conforming with the IGC conditions are needed in order to assess this fundamental question.

REFERENCES

- Bondi, H. 1952, *MNRAS*, **112**, 195
 Bondi, H., & Hoyle, F. 1944, *MNRAS*, **104**, 273
 Chevalier, R. A. 1989, *ApJ*, **346**, 847
 Colgan, J., Kilcrease, D. P., Magee, N. H., et al. 2013, *HEDP*, **9**, 369
 De Donder, E., & Vanbeveren, D. 1998, *A&A*, **333**, 557
 Della Valle, M. 2011, *IJMPD*, **20**, 1745
 Edgar, R. 2004, *NewAR*, **48**, 843
 Eggleton, P. P. 1983, *ApJ*, **268**, 368
 Fermi, E. 1949, *PhRv*, **75**, 1169
 Frey, L. H., Fryer, C. L., & Young, P. A. 2013, *ApJL*, **773**, L7
 Friis, M., & Watson, D. 2013, *ApJ*, **771**, 15
 Fryer, C. L. 2009, *ApJ*, **699**, 409
 Fryer, C. L., Benz, W., & Herant, M. 1996, *ApJ*, **460**, 801
 Fryer, C. L., Benz, W., Herant, M., & Colgate, S. A. 1999a, *ApJ*, **516**, 892
 Fryer, C. L., Colgate, S. A., & Pinto, P. A. 1999b, *ApJ*, **511**, 885
 Fryer, C. L., & Heger, A. 2005, *ApJ*, **623**, 302
 Fryer, C. L., Herwig, F., Hungerford, A., & Timmes, F. X. 2006, *ApJL*, **646**, L131
 Fryer, C. L., & Woosley, S. E. 1998, *ApJL*, **502**, L9
 Fryer, C. L., Woosley, S. E., & Hartmann, D. H. 1999c, *ApJ*, **526**, 152
 Fryer, C. L., Mazzali, P. A., Prochaska, J., et al. 2007, *PASP*, **119**, 1211
 Houck, J. C., & Chevalier, R. A. 1991, *ApJ*, **376**, 234
 Hoyle, F., & Lyttleton, R. A. 1939, *PCPS*, **35**, 405
 Izzo, L., Ruffini, R., Penacchioni, A. V., et al. 2012, *A&A*, **543**, A10
 Kasen, D., Badnell, N. R., & Barnes, J. 2013, *ApJ*, **774**, 25
 Kobulnicky, H. A., & Fryer, C. L. 2007, *ApJ*, **670**, 747
 Moriya, T., Tominaga, N., Tanaka, M., et al. 2010, *ApJ*, **719**, 1445
 Page, K. L., Starling, R. L. C., Fitzpatrick, G., et al. 2011, *MNRAS*, **416**, 2078
 Penacchioni, A. V., Ruffini, R., Bianco, C. L., et al. 2013, *A&A*, **551**, A133
 Penacchioni, A. V., Ruffini, R., Izzo, L., et al. 2012, *A&A*, **538**, A58
 Pisani, G. B., Izzo, L., Ruffini, R., et al. 2013, *A&A*, **552**, L5
 Podsiadlowski, P., Joss, P. C., & Hsu, J. J. L. 1992, *ApJ*, **391**, 246
 Rueda, J. A., & Ruffini, R. 2012, *ApJL*, **758**, L7
 Ruffini, R. 2011, *IJMPD*, **20**, 1797
 Ruffini, R., Bernardini, M. G., Bianco, C. L., et al. 2008, in *The Eleventh Marcel Grossmann Meeting*, ed. H. Kleinert, R. T. Jantzen, & R. Ruffini (Zurich: World Scientific), 368
 Ruffini, R., Izzo, L., Muccino, M., et al. 2013, arXiv:1311.7432
 Ruffini, R., Izzo, L., Muccino, M., et al. 2014a, arXiv:1404.1840
 Ruffini, R., Muccino, M., Bianco, C. L., et al. 2014b, *A&A*, **565**, L10
 Ruffini, R., Wang, Y., Kovacevic, M., et al. 2014c, arXiv:1405.5723
 Ruffini, R., & Wilson, J. 1973, *PhRvL*, **31**, 1362
 Sana, H., de Mink, S. E., de Koter, A., et al. 2012, *Sci*, **337**, 444
 Smith, N., Morse, J. A., Collins, N. R., & Gull, T. R. 2004, *ApJL*, **610**, L105
 Starling, R. L. C., Page, K. L., Pe’Er, A., Beardmore, A. P., & Osborne, J. P. 2012, *MNRAS*, **427**, 2950
 van den Heuvel, E. P. J., & Yoon, S.-C. 2007, *Ap&SS*, **311**, 177
 Woosley, S. E., & Bloom, J. S. 2006, *ARA&A*, **44**, 507
 Woosley, S. E., Heger, A., & Weaver, T. A. 2002, *RvMP*, **74**, 1015
 Yoon, S.-C., Woosley, S. E., & Langer, N. 2010, *ApJ*, **725**, 940
 Zel’dovich, Y. B., Ivanova, L. N., & Nadezhin, D. K. 1972, *SvA*, **16**, 209

Strangeness content of neutron stars with strong Σ^- -hyperon repulsion

M. Razeira¹, A. Mesquita², C.A.Z. Vasconcelos^{3,5,*}, R. Ruffini^{4,5,6}, J.A. Rueda^{4,5,6}, and R.O. Gomes^{3,7}

¹ Universidade Federal do Pampa (UNIPAMPA), Campus Caçapava do Sul, Av. Pedro Anunciação, s/n^o, Vila Batista, CEP 96570-000, Caçapava do Sul, RS, Brazil

² Universidade de Caxias do Sul (UCS), Campus Sede, Rua Francisco Getúlio Vargas, 1130, CEP 95070-560, Caxias do Sul, RS, Brazil

³ Instituto de Física, Universidade Federal do Rio Grande do Sul, Av. Bento Gonçalves 9500, CEP 91501-970, Porto Alegre, RS, Brazil

⁴ Sapienza Università di Roma, Piazzale Aldo Moro 5, 00185 Rome, Italy

⁵ ICRANet, P.zza della Repubblica 10, 65122 Pescara, Italy

⁶ ICRANet-Rio, Centro Brasileiro de Pesquisas Físicas, Rua Dr. Xavier Sigaud 150, Rio de Janeiro, RJ, 22290-180, Brazil

⁷ Frankfurt Institute for Advanced Studies, Johann Wolfgang Goethe Universität, Ruth-Moufang-Str. 1, 60438 Frankfurt am Main, Germany

Received 2014 Apr 30, accepted 2014 May 13

Published online 2014 Aug 01

Key words equation of state – stars: neutron – dense matter

A new constraint on the equation of state and composition of the matter on neutron stars has been provided by the measurement of the mass $2.01 \pm 0.04 M_{\odot}$ for PSR J0348+0432. In this contribution we investigate the role of many-body correlations in the maximum mass of neutron stars using the effective relativistic QHD-model with parameterized couplings. The complete expression of our QHD interaction Lagrangian exhausts the whole fundamental baryon octet (n , p , Σ^- , Σ^0 , Σ^+ , Λ , Ξ^- , Ξ^0) and includes many-body forces simulated by nonlinear self-couplings and meson-meson interaction terms involving scalar-isoscalar (σ , σ^*), vector-isoscalar (ω , ϕ), vector-isovector (ρ), and scalar-isovector (δ). We study the behavior of the asymmetry parameter, which describes the relative neutron excess in the system as well as the behavior of the strangeness asymmetry parameter, which specifies the strangeness content in the system and is strictly connected with the appearance of a particular hyperon species in the extreme case where the Σ^- experiences such a strong repulsion that it does not appear at all in nuclear matter.

© 2014 WILEY-VCH Verlag GmbH & Co. KGaA, Weinheim

1 Introduction

Neutron stars represent an excellent laboratory for the study of nuclear matter under extreme conditions of density and pressure. The pressure at the center of these stars is so high that many processes of generation of new particles and formation of new states of matter tend to occur, as for instance the generation of hyperon degrees of freedom, the deconfinement of quarks, the formation of a quark-gluon plasma and boson condensation such as kaon condensates and many others.

In addition there are theoretical predictions involving for example the formation of quark stars and strange matter, an absolutely stable composition of strange quarks, the content of hyperons. This prediction assumes that a neutron star would consist mostly of quarks up (u), down (d), and strange (s), surrounded by a thin nuclear crust. Hyperons, like Λ , Σ , Ξ , the K^- meson and the H-dibaryon, which play a vital role in the structure of neutron stars, may contain an s quark as one of their constituents. It therefore becomes

very important to study the presence of hyperons in nuclear matter and the strangeness content of neutron stars.

Hyperons are very unstable particles under terrestrial conditions, decaying into nucleons through the weak interaction. However, the equilibrium conditions in neutron stars allow the conversion of nucleons into hyperons to become energetically favorable. When the density of nuclear matter increases, the neutron chemical potential, μ_n , may exceed the mass of the Λ hyperon allowing this way the transformation of neutrons into Λ 's. These estimations are based on experimental hypernuclei constraints, assuming in general that the hyperon-nucleon and the hyperon-hyperon interactions in nuclear matter are similar in magnitude to the nucleon-nucleon interaction. To the extent that the nuclear density grows, additional hyperons as Σ and Ξ can then be generated originating a hyperon population as large as 20 % (Weber 2001).

Ambartsumyan & Saakyan (1960) were the first authors to suggest the appearance of hyperons in neutron stars. Since then, numerous studies have been performed in the search for a better understanding of the role of hyperons in the structure of the equation of state of neutron

* Corresponding author: cesarzen@cesarzen.com

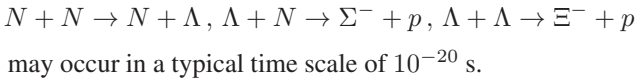
stars. For interesting discussions about this topic, see for instance Pandharipande (1971), Bethe & Johnson (1974), Moszkowski (1974), Glendenning (1985), Weber & Weigel (1989), Knorren, Prakash & Ellis (1995), Schaffner & Mishustin (1996), Huber et al. (1998), Glendenning (1982, 1985, 1996, 2000), Prakash et al. (1997), Balberg & Gal (1997), Baldo, Burgio & Schulze (1998), Schaffner-Bielich et al. (2002), Lackey, Nayyar & Owen (2005), Takatsuka et al. (2006), Djapo, Schaefer & Wambach (2010), Stone, Guichon & Thomas (2010), Blaschke, Klähn & Weber (2011), and Gupta & Arumugam (2013), among many others.

In the present contribution, special emphasis is placed on effects that can be attributed to the multi-species composition of neutron stars and the role of strangeness content of neutron stars with strong Σ^- -hyperon repulsion.

2 Equilibrium conditions

Assuming that hyperons (Λ , Σ , Ξ) appear in the core of neutron stars when the nucleon chemical potentials become large enough to compensate for the mass differences between nucleons and hyperons and that the threshold for the appearance of the hyperons is tuned by the strong interactions, most studies indicate that hyperons begin to appear at a density of about $2\rho_0$ with Fermi momentum greater than $k_F \sim 3 \text{ fm}^{-1}$ and $\rho_0 = 0.16 \text{ fm}^{-3}$ (Weber 2001).

In the high density domain, different strong interaction processes for hyperon formation such as



The equilibrium composition of neutron stars (Glendenning 1996; Prakash et al. 1997) requires chemical equilibrium of all weak interaction charge conservation processes: $B_i \rightarrow B_j + \ell + \bar{\nu}_\ell$ and $B_j + \ell \rightarrow B_i + \nu_\ell$, (1) in which B_i, B_j represent baryons, ℓ are leptons and ν and $\bar{\nu}$ denote respectively, neutrinos and anti-neutrinos on typical time scales of 10^{-10} s. These conditions for chemical equilibrium yields the ground state composition of neutron stars in beta equilibrium. We assume that neutron stars are transparent to neutrinos and anti-neutrinos on any relevant timescale; the chemical potentials of neutrinos and anti-neutrinos them obey the condition $\mu_\nu = \mu_{\bar{\nu}} = 0$. Under this assumption, the previous equilibrium conditions may then be summarized by the single generic equation

$$\mu_i = \mu_n - q_i \mu_e, \quad (2)$$

where μ_i and q_i represent, respectively, the chemical potential and electric charge of baryon species i , μ_n is the neutron chemical potential, and μ_e denotes the electron chemical potential. In the absence of neutrinos and anti-neutrinos, the equilibrium condition requires $\mu_e = \mu_n$, so muons start to appear in the system. Moreover, neutron and electron chemical potentials are constrained by the requirements of a constant total baryon number and electric charge neutrality

$$\sum_i \eta_{B_i} = 1 \text{ and } \sum_i q_i \eta_{B_i} + \sum_\ell q_\ell \eta_{B_\ell} = 0, \quad (3)$$

where $\eta_{B_i} = \rho_{B_i}/\rho_B$ and $\eta_{B_\ell} = \rho_{B_\ell}/\rho_B$ represent respectively the relative species of baryons and leptons as a function of the total baryon density ρ_B . The appearance of muons reduces the number of protons and affects this way the proton fraction. The resulting neutron excess is described by the isospin asymmetry parameter

$$f_{ia} = \frac{\mathcal{N}_n - \mathcal{N}_p}{\mathcal{N}_T}, \quad (4)$$

where \mathcal{N}_n and \mathcal{N}_p represent respectively the number of neutrons and protons with $\mathcal{N}_T = \mathcal{N}_n + \mathcal{N}_p$. Similarly, taking into account that strangeness is not conserved during the weak interactions, we introduce the strangeness asymmetry parameter

$$f_{sa} = \frac{\mathcal{N}_\Lambda + \mathcal{N}_\Sigma + 2\mathcal{N}_\Xi}{\mathcal{N}_\Lambda + \mathcal{N}_\Sigma + \mathcal{N}_\Xi + \mathcal{N}_T}, \quad (5)$$

where \mathcal{N}_Λ , \mathcal{N}_Σ , and \mathcal{N}_Ξ represent respectively the number of the Λ , Σ and Ξ hyperon species. The f_{sa} parameter specifies the strangeness content in the system and is strictly connected with the appearance of a particular hyperon species.

Qualitatively, typical calculations which take into account attractive nucleon-hyperon potentials (see, for instance, Glendenning 2001), the first hyperon species that appears is the Σ^- closely followed by the Λ and the Σ^+ . Then, the other hyperon species follow at higher densities, Σ^0 , Σ^+ , and Ξ^- . The appearance of negatively charged hyperons at high densities allows deleptonization processes to occur in the core of neutron stars, i.e, the loss of lepton content, and thus charge neutrality tends to be guaranteed without lepton contributions.

As already stressed by Glendenning (2001), the uncertainties of hyperon couplings, in particular, that of Σ^- in dense matter raises questions about the behavior of the electrochemical potential, a crucial quantity for the possible presence of a kaon condensed phase in the core of neutron stars. As most often assumed, regardless the uncertainties, we consider that hyperon couplings are constrained by the hyperon binding in nuclear matter. Kaon condensation in turn is not taken into account in this study. In the following we consider the extreme case where the Σ^- experiences such a strong repulsion that it does not appear at all in nuclear matter.

3 Lagrangian density

We consider in the following an effective relativistic model with parameterized couplings. As a guideline for the strengths of the various couplings the concept of naturalness has been adopted. (Vasconcellos et al. 2014a). The interaction Lagrangian density is

$$\mathcal{L}_{\text{int}} = - \sum_B \bar{\psi}_B \left[\gamma_\mu \Sigma_B^\mu \xi(\sigma, \sigma^*, \delta, \omega) + \gamma_\mu \tau \cdot \Sigma_{B\kappa}^\mu(\sigma, \sigma^*, \delta, \varrho) + \gamma_\mu \Sigma_{B\eta}^\mu(\sigma, \sigma^*, \delta, \phi) + \Sigma_{B\zeta}^s(\sigma, \sigma^*, \delta) \right] \psi_B. \quad (6)$$

In this expression, one can identify the following self-energy insertions:

$$\Sigma_{B\xi}^{\mu}(\sigma, \sigma^*, \delta, \omega) = g_{\omega B\xi}^* \omega^{\mu}, \quad \Sigma_{B\kappa}^{\mu}(\sigma, \sigma^*, \delta, \varrho) = \frac{1}{2} g_{\varrho B\kappa}^* \varrho^{\mu}$$

$$\Sigma_{B\eta}^{\mu}(\sigma, \sigma^*, \delta, \phi) = g_{\phi B\eta}^* \phi^{\mu}, \quad \Sigma_{B\zeta}^s(\sigma, \sigma^*, \delta) = M_B \Sigma_{B\zeta}^s, \quad (7)$$

where $B = n, p, \Sigma^-, \Sigma^0, \Sigma^+, \Lambda, \Xi^-, \Xi^0$, and with the effective parameterized baryon-meson coupling constants g_{Φ}^* ($\Phi = \omega, \phi, \varrho$), defined as $g_{\omega B\xi}^* = g_{\omega B} m_{B\xi}^*$, $g_{\varrho B\kappa}^* = g_{\varrho B} m_{B\kappa}^*$, $g_{\phi B\eta}^* = g_{\phi B} m_{B\eta}^*$, and with $\Sigma_{B\zeta}^s = m_{B\zeta}^*$, where

$$m_{B\alpha}^* \equiv \left(1 + \frac{g_{\sigma B} \sigma + g_{\sigma^* B} \sigma^* + \frac{1}{2} g_{\delta B} \tau \cdot \delta}{\alpha M_B} \right)^{-\alpha}, \quad (8)$$

with $\alpha = (\xi, \kappa, \eta, \zeta)$.

The effective parameterized baryon mass $M_{B\zeta}^* = M_B \Sigma_{B\zeta}^s = M_B m_{B\zeta}^*$, for $(\frac{g_{\sigma B} \sigma_0}{\zeta M_B}, \frac{g_{\sigma^* B} \sigma_0^*}{\zeta M_B}, \frac{g_{\delta B} \delta_{03}}{\zeta M_B}) \ll 1$, in the mean field approximation, becomes

$$M_{B\zeta}^* = M_B - M_B \left(\frac{g_{\sigma B} \sigma_0 + g_{\sigma^* B} \sigma_0^* + \frac{1}{2} g_{\delta B} \langle \tau_3 \rangle \delta_{03}}{M_B} \right)$$

$$+ \left(\frac{\zeta}{2} \right) \left(\frac{g_{\sigma B} \sigma_0 + g_{\sigma^* B} \sigma_0^* + \frac{1}{2} g_{\delta B} \langle \tau_3 \rangle \delta_{03}}{\zeta M_B} \right)^2$$

$$+ \mathcal{O}(3), \quad (9)$$

with $\left(\frac{\zeta}{2} \right)$ representing the generalized binomial coefficients of the expansion (Taurines et al. 2001; Vasconcellos et al. 2012). Properties of the fields considered in our formulation are presented in Table 1.

For certain values of the parameters of the model, the treatment adopted in this work reproduces the same predictions for global properties of neutron stars as most of the models based on Yukawa-type couplings involving the σ , ω and ϱ mesons. This can be easily understood looking at the simplifications shown in Table 2. For other choices of the model parameters, our approach allows the description of the effects of self-density-correlations of higher orders involving the extended scalar sector of the strong interaction on global properties of neutron stars.

Table 1 Properties of the fields considered in our formulation. In what follows, we use the abbreviations ISS: isoscalar-scalar; IVS: isovector-scalar; ISV: isoscalar-vector; IVV: isovector-vector.

Fields	Classification	Particles	Coupling Constants	Mass (MeV)
ψ_B	Baryons	N, Λ , Σ , Ξ	N/A	939, 1116, 1193, 1318
ψ_l	Leptons	e^- , μ^-	N/A	0.5, 106
σ	ISS-meson	σ	$g_{\sigma B}^*$	550
δ	IVS-meson	a_0	$g_{\delta B}^*$	980
ω_{μ}	ISV-meson	ω	$g_{\omega B}^*$	782
ϱ_{μ}	IVV-meson	ϱ	$g_{\varrho B}^*$	770
σ^*	ISS-meson	f_0	$g_{\sigma^* B}^*$	975
ϕ_{μ}	ISV-meson	ϕ	$g_{\phi B}^*$	1020

Table 2 Examples of parameterizations of our model. S: scalar model; SIV: scalar-isoscalar-vector model; SIIV: scalar-isoscalar-vector-isovector-vector model. Model II differs from I due to the presence of the ϕ meson.

Model	ζ	ξ	κ	η
S	$\neq 0$	0	0	0
SIV	$\neq 0$	$\neq 0$	0	0
SIIV-I	$\neq 0$	$\neq 0$	$\neq 0$	0
SIIV-II	$\neq 0$	$\neq 0$	$\neq 0$	$\neq 0$

4 Coupling constants

In the following, the values of the sets of parameters $(\zeta, \xi, \kappa, \eta)$ have been chosen to allow the model to reproduce nuclear properties at saturation, like for example the compressibility modulus of nuclear matter smaller than 300 MeV. We assume for the saturation density of nuclear matter $\rho_0 = 0.17 \text{ fm}^{-3}$ and for the binding energy of nuclear matter $\epsilon_B = -16.0 \text{ MeV}$. The isovector coupling constant g_{ϱ} is constrained to the symmetry energy coefficient $a_{\text{asym}} = 32.5 \text{ MeV}$ (Haensel et al. 2007). In the high density regime, the intensity of the couplings of scalar mesons with hyperons is chosen by determining the depth of the hyperon-nucleon interaction potential on saturated nuclear matter. For the details of this part of the calculation see the contribution to this issue (Vasconcellos et al. 2014b).

5 TOV equations and gravitational binding energy

We have calculated the EoS, population profiles and, by solving the Tolman-Oppenheimer-Volkoff (TOV) equations (Tolman 1939; Oppenheimer & Volkoff 1939), we have determined the mass-radius relation for families of neutron stars with hyperon content. Our results for different values of the set of parameter $(\zeta, \xi, \kappa, \eta)$ are illustrated in Figs. 1–10, where each set of parameters generates a sequence of neutrons stars with different equations of state, particle populations, central densities, and maximum masses.

The gravitational mass of a neutron stars is given by one of the TOV equations,

$$M_{*G} = 4\pi \int_0^R \epsilon(r) r^2 dr, \quad (10)$$

where ϵ represents the internal density energy of the star. The quantity M_{*G} represents the mass that is measured by Keplers law when a satellite orbits the star.

The baryon mass of the star, M_{*B} , is given by the volume integral of the baryon number density n times the baryon mass M_{*B} :

$$M_{*B} = N M_B = \int_0^R dV$$

$$= 4\pi \int_0^R n dr r^2 \left(1 - \frac{2GM(r)}{c^2 r} \right)^{-1/2}, \quad (11)$$

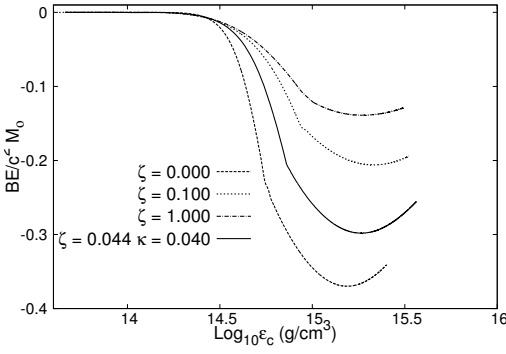


Fig. 1 Gravitational binding energy as a function of the central energy density of the stars. For comparison, the curves labelled with $\zeta = 0.000$ and $\zeta = 1.000$ represent the results of our model corresponding respectively to the Serot & Walecka (1997) and ZM (Zimanyi & Moszkowski 1990) models. The remaining curves labelled with $\zeta = 0.100$ and $\zeta = 0.044$, $\kappa = 0.040$ represent particular combinations of the parameters of our model. This last result of our model represents one of the most stable gravitational binding energy curve that reproduces nuclear phenomenology (as for instance the compressibility of nuclear matter) and allows, through the calculation of the TOV equations (Tolman 1939; Oppenheimer & Volkoff 1939) to obtain a maximum mass of neutron stars in good agreement with recent experimental observations (Demorest et al. 2010). The remaining model parameters, not shown in the curves, are set equal to zero.

where $dV = 4\pi dr r^2 \left(1 - \frac{2GM(r)}{c^2 r}\right)^{1/2}$ is the volume element in Schwarzschild coordinates, N represents the star baryon number, and $M(r)$ is the internal neutron star mass. The difference between M_{*G} and M_{*B} corresponds to the binding energy

$$E_{* \text{bin}} = (M_{*G} - M_{*B}) c^2. \quad (12)$$

The behavior of the gravitational energy as a function of the central density of neutron stars is crucial for determining the most stable configurations of families of stars.

6 Results

Our calculation indicate that many-body correlations shield the attractive part of the strong interaction, and intensify this way the corresponding repulsive part, favoring in this way the stiffening of the EoS. On the other hand, the effective masses of baryons increase as the shielding of the attractive part of the strong interaction increase, as shown in Eq. (4). This favors the growth of the internal pressure of the system and the stiffening of the EoS.

On the other hand, our predictions for the particle population show that the threshold equation for a given species (Glendenning 1996) is also affected by the presence of many-body correlations (see Eq. 8):

$$\begin{aligned} \mu_n - q_B \mu_e \geq & g_{\omega B} f_{\sigma\sigma^*} \delta \xi \omega_0 + g_{\rho B} f_{\sigma\sigma^*} \delta \kappa \rho_{03} I_{3B} \\ & + g_{\phi B} f_{\sigma\sigma^*} \delta \eta \phi_0 + f_{\sigma\sigma^*} \delta \zeta M_B. \end{aligned} \quad (13)$$

In this expression, μ_n and μ_e represent respectively the neutron and electron chemical potential, and q_B is the baryon

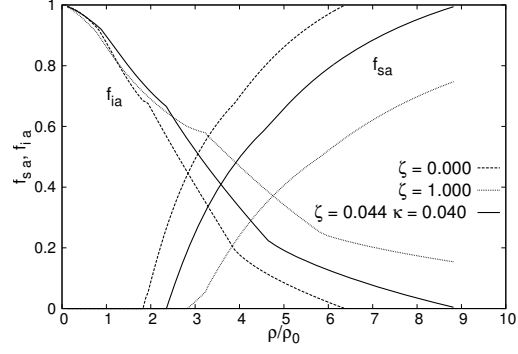


Fig. 2 Isospin asymmetry f_{ia} and strangeness asymmetry f_{sa} of nuclear matter as a function of the ratio between the baryon density ρ_B and the nuclear saturation density ρ_0 . The meaning of the labels is similar to the previous figure.

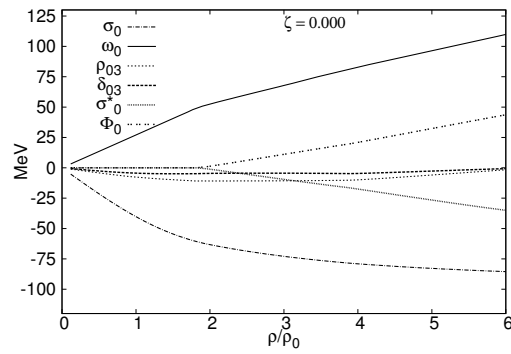


Fig. 3 The meson fields condensates as functions of the ratio between the baryon density ρ and the nuclear saturation density ρ_0 for a given parameter set which corresponds to the Serot and Walecka (1997) model. The remaining model parameters, not shown in the figure, are set equal to zero.

charge. The sign of $g_{\rho B} \rho_{03} I_{3B}$ is determined by the net isospin density of the star. This term determines whether a given baryon configuration is isospin favored or unfavored. Similarly, the term $q_B \mu_e$ determines whether a given baryon state is charge favored or unfavored. Moreover, in this expression

$$\begin{aligned} f_{\sigma\sigma^*} \delta \alpha = & 1 - \left(\frac{g_{\sigma B} \sigma_0 + g_{\sigma^* B} \sigma_0^* + \frac{1}{2} g_{\delta B} \langle \tau_3 \rangle \delta_{03}}{M_B} \right) \\ & + \left(\frac{\alpha}{2} \right) \left(\frac{g_{\sigma B} \sigma_0 + g_{\sigma^* B} \sigma_0^* + \frac{1}{2} g_{\delta B} \langle \tau_3 \rangle \delta_{03}}{\alpha M_B} \right)^2 \\ & + \mathcal{O}(3), \end{aligned} \quad (14)$$

with $\alpha = \xi, \kappa, \eta, \zeta$. These equation show that the population of hyperons is affected by many-body correlations, which shift the critical density for hyperon saturation to higher densities.

Following recent experimental results (Zhao & Zhang 2013; see also Bednarek, Keska & Manka 2003), we have considered in our calculations the extreme case where the Σ^- experiences such a strong repulsion that it does not appear at all in nuclear matter for densities exceeding those found in neutron stars. The first hyperon species that ap-

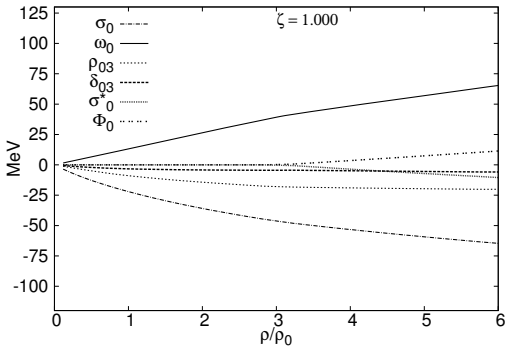


Fig. 4 The meson fields condensates as functions of the ratio between the baryon density ρ and the nuclear saturation density ρ_0 for a given parameter set which corresponds to the ZM (Zimanyi & Moszkowski 1990) model. The remaining model parameters, not shown in the figure, are set equal to zero.

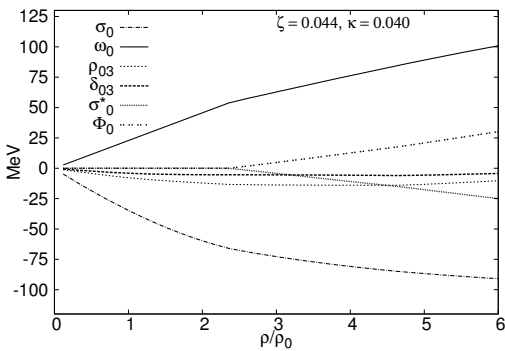


Fig. 5 The meson fields condensates as functions of the ratio between the baryon density ρ and the nuclear saturation density ρ_0 for a given parameter set of our model which reproduces nuclear phenomenology (as for instance the compressibility of nuclear matter) and allows, through the calculation of the TOV equations (Tolman 1939; Oppenheimer & Volkoff 1939) to obtain a maximum mass of neutron stars in good agreement with recent experimental observations (Demorest et al. 2010). The remaining model parameters, not shown in the figure, are set equal to zero.

appears is the Λ : free of isospin-dependent forces, as the density increases, the Λ hyperon continues to accumulate until short-range repulsion forces cause them to saturate. Other hyperon species follow at higher densities.

Our model originates moreover an anti-correlation between the amount of hyperons: for certain values of the parameters, according to Eqs. (13) and (14), an anti-correlation associated with the predominance of the scalar part occurs. This means that hyperon degrees of freedom become more numerous to the extent that the attractive sector is favored in comparison with the repulsive part, thus favoring smaller neutron star masses. However, the absence of the Σ^- hyperon reduces this effect.

When considering simultaneously both shielding effects involving the attractive and repulsive contributions of the strong interaction, one would expect that, – since the repulsive part of the strong interaction is more effective in nuclear matter at high densities, on the average, than the attractive

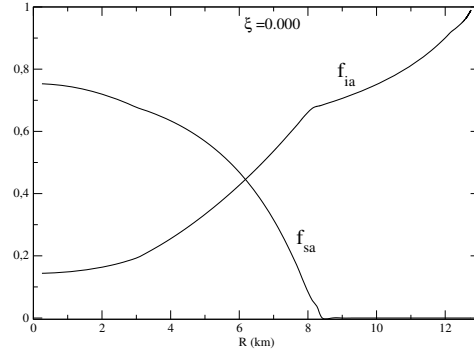


Fig. 6 Isospin asymmetry f_{ia} and strangeness asymmetry f_{sa} of nuclear matter in the configuration for maximum mass for a set of parameters corresponding to the Serot & Walecka (1997) model as a function of the star radius. In this configuration the maximum star mass is approximately equal to $2.2 M_\odot$, and the star radius is ~ 12.8 km.

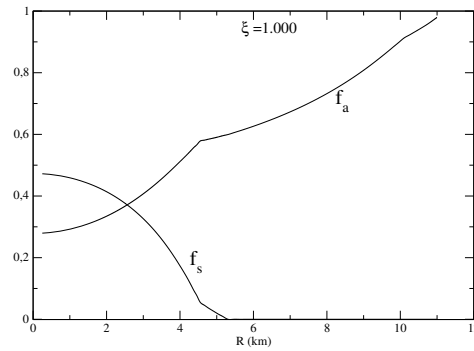


Fig. 7 Isospin asymmetry f_{ia} and strangeness asymmetry f_{sa} of nuclear matter in the configuration for maximum mass for a set of parameters corresponding to the ZM (Zimanyi & Moszkowski 1990) model as a function of the star radius. In this configuration the maximum star mass is approximately equal to $1.6 M_\odot$, and the star radius is ~ 11 km.

sector –, that the shielding of the strong interaction would favor the attractive part, contributing this way to the reduction of the mass of the neutron star. However, our results indicate that the combination of these effects with the others previously reported favors the stiffening of the EoS. In other words, the shielding of the attractive part of the strong interaction combined with the increase of the effective mass of baryons and the absence of the Σ^- hyperon, are dominant when compared with those effects favoring the softening of the EoS, i.e., the shielding of the repulsive part of the strong interaction and the increase on the population of the remaining hyperons beyond the Σ^- .

7 Conclusions

The main result of our study is that our predictions for the properties of neutron stars show a better agreement with experimental observations when compared with the predictions of other known models found in the literature. In particular, our predictions for the masses of neutron stars are in

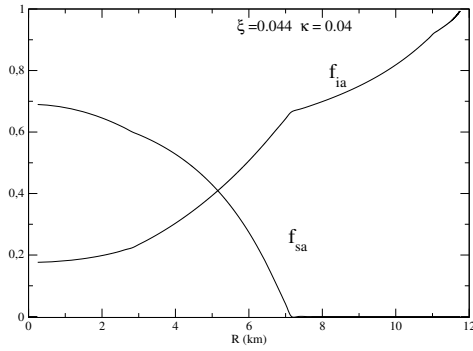


Fig. 8 Isospin asymmetry f_{ia} and strangeness asymmetry f_{sa} of nuclear matter in the configuration for maximum mass for a set of parameters of our model. In this configuration, the maximum star mass is approximately equal to $1.95 M_{\odot}$, in good agreement with recent experimental observations (Demorest et al. 2010), and the star radius is ~ 11.8 km.

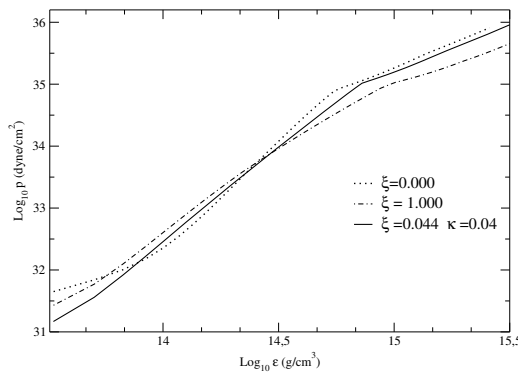


Fig. 9 The EoS of nuclear matter. Dotted, dashed, and straight lines represent model parameters for given sets corresponding to the Serot & Walecka (1997) model, to the ZM (Zimanyi & Moszkowski 1990) model, and to our model, respectively.

very good agreement with recent experimental observations (Demorest et al. 2010)

It is worth to recall that in this work we have constructed the neutron star configurations through the spherically symmetric equations of equilibrium given by the TOV equations which assume the condition of local charge neutrality of the system; see Eq. (3). It is therefore important to scrutinize the effects found in (Belvedere et al 2012, and references therein), where it was shown a more general picture of the equilibrium inside a neutron star, ensuring global but not local charge neutrality. A more general system of equilibrium equations including effects of gravito-polarization throughout the star, the Einstein-Maxwell-Thomas-Fermi equations, were shown to supersede the TOV ones. The appearance of other charged degrees of freedom besides proton and electrons presented here, will certainly change at least quantitatively, the electric fields inside the neutron star.

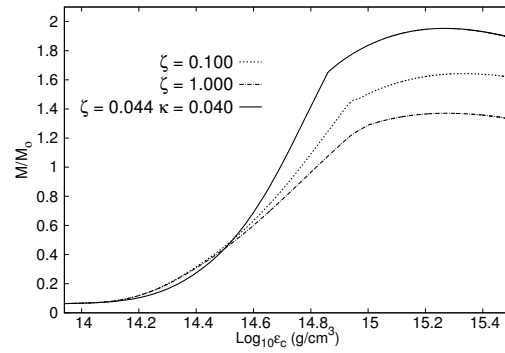


Fig. 10 Maximum masses as functions of the central density of neutron stars for a given set of parameters of our model. The meaning of the labels is similar to the previous figure.

References

- Ambartsumyan, V.A., Saakyan, & G.S. 1960, *Soviet Astron.*, 4, 187
- Babaev, E. 2009, *Phys. Rev. Lett.*, 103, 231101
- Balberg, S., & Gal, A. 1997, *Nucl. Phys. A*, 625, 435
- Baldo, M. Burgio, G.F., & Schulze, H.J. 1998, *Phys. Rev. C*, 58, 3688
- Belvedere R., Pugliese D., Rueda J. A., Ruffini R., & Xue S.-S. 2012, *Nucl. Phys. A*, 883, 1
- Blaschke, D., Klähn, S., & Weber, F. 2011, in *The Compressed Baryonic Matter Physics Book*, *Lect. Notes in Phys.*, 814, 158
- Bethe, H.E., & Johnson, M.B. 1974, *Nucl. Phys. A*, 230, 1
- Djapo, H., Schaefer, B.J., & Wambach, J. 2010, *Phys. Rev. C*, 81, 035803
- Glendenning, N.K. 1982, *Phys. Rev. D*, 46, 1274; 1985, *ApJ*, 293, 470; 1996, *Compact Stars* (New York: Springer); 2000, *Phys. Rev. C*, 64, 025801; 2001, *Phys. Rev. C*, 64, 025801
- Gupta, N., & Arumugam, P. 2013, *Phys. Rev. C*, 88 1, 015803
- Huber, H., Weber, F., Weigel, M.K., & Schaab, Ch. 1998, *Int. J. Mod. Phys. E*, 7, 301
- Kantor, E.M., & Gusakov, M.E. 2009, *Phys. Rev. D*, 79, 043004
- Knorren, R., Prakash, M., & Ellis, P.J. 1995, *Phys. Rev. C*, 52, 3470
- Lackey, B.D., Nayyar, M., & Owen, B.J. 2005, *Phys. Rev. D*, 73, 024021
- Moszkowski, S.A. 1974, *Phys. Rev. D*, 9, 1613
- Pandharipande, V.R. 1971, *Nucl. Phys. A*, 178, 123
- Prakash, M., et al. 1997, *Phys. Rep.*, 280, 1
- Schaffner-Bielich, J., Hanauske, M., Stoeker, H., & Greiner, W. 2002, *Phys. Rev. Lett.* 89, 171101
- Schaffner-Bielich, J., & Mishustin, I.N. 1996, *Phys. Rev. C*, 53, 1416
- Stone, J.R., Guichon, P.A.M., & Thomas, A.W. 2010, *arXiv:1012.2919*, [nucl-th]
- Takatsuka, T., Nishizaki, S., Yamamoto, Y., & Tamagaki, R. 2006, *Prog. Theor. Phys.*, 115, 355
- Serot, B.D., Walecka, J.D., 1997 *Int. J. Mod. Phys. E*, 515, 6; Serot, B.D., Walecka, J.D. 1986, in *The Relativistic Nuclear Many-Body Problem*, eds. J.W. Negele, & E. Vogt, *Adv. Nucl. Phys.*, 16, 1.
- Weber, F., & Weigel, M.K. 1989, *Nucl. Phys. A*, 505, 779
- Weber, F. 2001, *J. Phys. G*, 27, 465

Effective field theory for neutron stars with strong Σ^- -hyperon repulsion

M. Razeira^{1,*}, A. Mesquita², C.A.Z. Vasconcellos^{3,5}, R. Ruffini^{3,4,5}, J.A. Rueda^{3,4,5}, and R.O. Gomes³

¹ Universidade Federal do Pampa (UNIPAMPA), Campus Caçapava do Sul, Av. Pedro Anunciação, s/n^o, Vila Batista, CEP 96570-000, Caçapava do Sul, RS, Brazil

² Universidade de Caxias do Sul (UCS), Campus Sede, Rua Francisco Getúlio Vargas, 1130, CEP 95070-560, Caxias do Sul, RS, Brazil

³ Instituto de Física, Universidade Federal do Rio Grande do Sul, Av. Bento Gonçalves 9500, CEP 91501-970, Porto Alegre, RS, Brazil

⁴ Sapienza Università di Roma, Piazzale Aldo Moro 5, 00185 Rome, Italy

⁵ ICRANet, P.zza della Repubblica 10, 65122 Pescara, Italy

⁶ ICRANet-Rio, Centro Brasileiro de Pesquisas Físicas, Rua Dr. Xavier Sigaud 150, Rio de Janeiro, RJ, 22290-180, Brazil

⁷ Frankfurt Institute for Advances Studies, Ruth-Moufang-Strasse 1 60438 Frankfurt am Main

Received 2014 Apr 30, accepted 2014 May 13

Published online 2014 Aug 01

Key words elementary particles – equation of state – stars: neutron

We investigate the role of many-body correlations in the maximum mass of neutron stars using the effective relativistic QHD-model with parameterized couplings which represents an extended compilation of other effective models found in the literature. Our model exhausts the whole fundamental baryon octet (n , p , Σ^- , Σ^0 , Σ^+ , Λ , Ξ^- , Ξ^0) and simulates corrections to the minimal Yukawa couplings by considering many-body nonlinear self-couplings and meson-meson interaction terms involving scalar-isoscalar (σ , σ^*), vector-isoscalar (ω , ϕ), vector-isovector (ρ) and scalar-isovector (δ). Following recent experimental results, we consider in our calculations the extreme case where the Σ^- experiences such a strong repulsion that it does not appear at all in nuclear matter.

© 2014 WILEY-VCH Verlag GmbH & Co. KGaA, Weinheim

1 Introduction

The knowledge of the equation of state (EoS) of nuclear matter at high densities, such as those found in neutron stars and pulsars, is still an open problem in physics. The formal complexity of Quantum Chromodynamics (QCD), the fundamental theory of the strong interaction physics, has led nuclear physicists to search for alternative effective models for the description of properties of nuclear matter.

In 1977, one of the most popular formulations for the problem, the effective relativistic quantum field theory known as Quantum Hadrodynamics (QHD), was proposed by Walecka & Serot (1997). QHD considers nucleons as effective fields and assumes that the interaction terms involving nucleons and meson fields is described by Yukawa-type minimal couplings which involve the exchange of the long-range (attractive) and short-range (repulsive) components of the nuclear force represented, respectively, by the scalar-isoscalar σ -meson and the vector-isoscalar ω -meson. The model is linearized by using the mean-field approximation.

To address a few of the shortcomings of the Walecka model with Yukawa minimal couplings, alternative approaches have been proposed. Among these we mention the

nonlinear model of Boguta & Bodmer (1997) who considered a correction to the Yukawa minimal coupling in the scalar sector, by taking into account the leading third- and fourth-orders of the σ meson self-interaction terms to simulate density-dependent correlations in the “in-medium” nucleon-nucleon interaction.

Another important effective model, proposed by Zimanyi & Moszkowski (1990), replaces the Yukawa’s minimum coupling involving the scalar-isoscalar meson σ and the nucleon by a derivative coupling allowing self-interaction density-dependent correlation terms of higher orders than the leading third and fourth ones. We also mention the model of Glendenning (1996), who introduced hyperon degrees of freedom into the original versions of the QHD formalism.

It has been found by many authors that hadronic masses of the various SU(3) multiplets, including hyperon fields, and the nuclear matter equation of state can be described reasonably well within QHD models respecting chiral symmetry (see, for instance, Papazoglou et al. 1998; Massot, Margueron & Chanfray 2012). However, it has been also shown that the central potentials of hyperon degrees of freedom come out too large in such descriptions. These studies also show that such too high central potentials for hyperon fields cannot be corrected within a model with con-

* Corresponding author: mrazeira@gmail.com

ventional Yukawa-type baryon-meson interactions. The reasons for this ‘‘pathology’’ may be synthesized as follows: linear realization of chiral symmetry restricts interaction coupling terms involving spin-0 meson fields and baryons to be symmetric (d-couplings), while the couplings involving spin-1 meson field to baryons must be antisymmetric (f-couplings); this way, the balance between nuclear repulsive contributions due to vector short range potentials and attractive contributions owing to scalar long range potentials is destroyed. There are other arguments that support this assertion but will not be mentioned here because they are outside the scope of this study; see, for instance, Papazoglou et al. 1998; Massot, Margueron & Chanfray 2012). Note that these issues are not present if the non-linear realization of the sigma model is considered instead (Papazoglou et al. 1999; Dexheimer & Schramm 2008).

In this work, we focus on the role of non-Yukawa couplings involving baryons and meson fields on the equation of state (EoS) of neutron stars. Particularly, we focus on the effects of many-body correlations on the polarization of baryon masses due to the background field fluctuations of scalar meson fields, induced by a strong interaction scalar response of the nuclear medium. These polarization effects are particularly responsible for non Yukawa-type density correlations on the scalar sector of the strong interaction.

2 Lagrangian density

We consider in the following an effective relativistic model with parameterized couplings which takes into account, as a conventional way of classifying and organizing the interaction strengths of the various couplings of the Lagrangian density \mathcal{L}_{int} , the concept of naturalness (Vasconcellos et al. 2014):

$$\mathcal{L}_{int} = - \sum_B \bar{\psi}_B \left[\gamma_\mu \Sigma_B^\mu(\sigma, \sigma^*, \delta, \omega) \gamma_\mu \boldsymbol{\tau} \cdot \boldsymbol{\Sigma}_{B\kappa}^\mu(\sigma, \sigma^*, \delta, \boldsymbol{\rho}) + \gamma_\mu \Sigma_{B\eta}^\mu(\sigma, \sigma^*, \delta, \phi) + \Sigma_{B\zeta}^s(\sigma, \sigma^*, \delta) \right] \psi_B. \quad (1)$$

In this expression, one can identify the following self-energy insertions:

$$\begin{aligned} \Sigma_{B\xi}^\mu(\sigma, \sigma^*, \delta, \omega) &= g_{\omega B\xi}^* \omega^\mu; \quad \Sigma_{B\kappa}^\mu(\sigma, \sigma^*, \delta, \boldsymbol{\rho}) = \frac{1}{2} g_{\rho B\kappa}^* \boldsymbol{\rho}^\mu \\ \Sigma_{B\eta}^\mu(\sigma, \sigma^*, \delta, \phi) &= g_{\phi B\eta}^* \phi^\mu; \quad \Sigma_{B\zeta}^s(\sigma, \sigma^*, \delta) = M_B \Sigma_{B\zeta}^s, \quad (2) \end{aligned}$$

where $B = n, p, \Sigma^-, \Sigma^0, \Sigma^+, \Lambda, \Xi^-, \Xi^0$, and with the effective parameterized baryon-meson coupling constants g_Φ^* ($\Phi = \omega, \phi, \rho$), defined as $g_{\omega B\xi}^* = g_{\omega B} m_{B\xi}^*$, $g_{\rho B\kappa}^* = g_{\rho B} m_{B\kappa}^*$, $g_{\phi B\eta}^* = g_{\phi B} m_{B\eta}^*$, and with $\Sigma_{B\zeta}^s = m_{B\zeta}^*$, where

$$m_{B\alpha}^* \equiv \left(1 + \frac{g_{\sigma B} \sigma + g_{\sigma^* B} \sigma^* + \frac{1}{2} g_{\delta B} \boldsymbol{\tau} \cdot \boldsymbol{\delta}}{\alpha M_B} \right)^{-\alpha}, \quad (3)$$

with $\alpha = (\xi, \kappa, \eta, \zeta)$.

The effective parameterized baryon mass

$$M_{B\zeta}^* = M_B \Sigma_{B\zeta}^s = M_B m_{B\zeta}^*, \quad (4)$$

for

$$\left(\frac{g_{\sigma B} \sigma_0}{\zeta M_B}, \frac{g_{\sigma^* B} \sigma_0^*}{\zeta M_B}, \frac{g_{\delta B} \delta_{03}}{\zeta M_B} \right) \ll 1,$$

in the mean field approximation becomes

$$\begin{aligned} M_{B\zeta}^* &= M_B - M_B \left(\frac{g_{\sigma B} \sigma_0 + g_{\sigma^* B} \sigma_0^* + \frac{1}{2} g_{\delta B} \langle \tau_3 \rangle \delta_{03}}{M_B} \right) \\ &+ \binom{\zeta}{2} \left(\frac{g_{\sigma B} \sigma_0 + g_{\sigma^* B} \sigma_0^* + \frac{1}{2} g_{\delta B} \langle \tau_3 \rangle \delta_{03}}{\zeta M_B} \right)^2 \\ &+ \mathcal{O}(3), \quad (5) \end{aligned}$$

with $\binom{\zeta}{2}$ representing the generalized binomial coefficients of the expansion (Taurines et al. 2001; Vasconcellos et al. 2012). Properties of the fields considered in our formulation are presented in Table 1.

For certain values of the parameters of the model, the treatment adopted in this work reproduces the same predictions for global properties of neutron stars as most of the models based on Yukawa-type couplings involving the σ , ω , and ρ mesons. This can be easily understood looking at the simplifications shown in Table 2. For other choices of the model parameters, our approach allows the description of the effects of self-density-correlations of higher orders involving the extended scalar sector of the strong interaction on global properties of neutron stars.

3 Coupling constants

In the following, the values of the sets of parameters $(\zeta, \xi, \kappa, \eta)$ have been chosen to allow the model to reproduce nuclear properties at saturation, like for example the compressibility modulus of nuclear matter smaller than 300 MeV. We assume for the saturation density of nuclear matter $\rho_0 = 0.17 \text{ fm}^{-3}$ and for the binding energy of nuclear matter $\epsilon_B = -16.0 \text{ MeV}$. The isovector coupling constant g_ρ is constrained to the symmetry energy coefficient $a_{\text{asym}} = 32.5 \text{ MeV}$ (Haensel et al. 2007).

In the high density regime, hyperon degrees of freedom must be taken into account. In most models found in the literature, hyperon degrees of freedom appear in nuclear matter at around two times the nuclear saturation density ρ_0 , as for instance, in relativistic mean-field models (Wang et

Table 1 Properties of the fields considered in our formulation. In what follows, we use the abbreviations ISS: isoscalar-scalar; IVS: isovector-scalar; ISV: isoscalar-vector; IVV: isovector-vector.

Fields	Classification	Particles	Coupling Constants	Mass (MeV)
ψ_B	Baryons	N, Λ , Σ , Ξ	N/A	939, 1116, 1193, 1318
ψ_l	Leptons	e^- , μ^-	N/A	0.5, 106
σ	ISS-meson	σ	$g_{\sigma B}^*$	550
δ	IVS-meson	a_0	$g_{\delta B}^*$	980
ω_μ	ISV-meson	ω	$g_{\omega B}^*$	782
$\boldsymbol{\rho}_\mu$	IVV-meson	ρ	$g_{\rho B}^*$	770
σ^*	ISS-meson	f_0	$g_{\sigma^* B}^*$	975
ϕ_μ	ISV-meson	ϕ	$g_{\phi B}^*$	1020

Table 2 Examples of parameterizations of our model. S: scalar model; SIV: scalar-isoscalar-vector model; SIIV: scalar-isoscalar-vector-isovector-vector model. Model II differs from I due to the presence of the ϕ meson.

Model	ζ	ξ	κ	η
S	$\neq 0$	0	0	0
SIV	$\neq 0$	$\neq 0$	0	0
SIIV-I	$\neq 0$	$\neq 0$	$\neq 0$	0
SIIV-II	$\neq 0$	$\neq 0$	$\neq 0$	$\neq 0$

al. 2006), in non-relativistic potential models (Dabrowski & Rozynek 2010), in the quark-meson coupling model (Whittembury et al. 2013), in relativistic Hartree-Fock models (Huber et al. 1998), in Brueckner-Hartree-Fock calculations (Shternin, Baldo & Haensel 2013), and within chiral effective Lagrangian (Banik et al. 2004). Nevertheless, the details of the hyperon composition of neutron star matter are rather sensitive to the chosen hyperon potentials.

The intensity of the couplings of scalar mesons with hyperons can be obtained by determining the depth of the hyperon-nucleon interaction potential on saturated nuclear matter

$$U_H^N(\rho_0) = -g_{\sigma H}\sigma_0 + g_{\omega H}\omega_0, \quad (6)$$

where $H = \Lambda, \Sigma, \Xi$, and

$$-g_{\sigma N}\sigma_0 = \sum_N \left(\frac{g_{\sigma N}}{m_\sigma} \right)^2 \left[(\zeta - 1)m_{N\zeta}^* - \zeta(m_{N\zeta}^*)^{\frac{\zeta+1}{\zeta}} \right] \rho_{SN} - \sum_N \left(\frac{g_{\sigma N}}{m_\sigma} \right)^2 g_{\omega N} \frac{m_{\xi N}^*}{M_N} \frac{\xi+1}{\xi} \rho_N, \quad (7)$$

and

$$g_{\omega N}\omega_0 = \sum_N \left(\frac{g_{\omega N}}{m_\omega} \right)^2 m_{\xi N}^* \rho_N; \quad (8)$$

in these expressions, ρ_{SN} and ρ_N represent respectively the scalar and baryonic densities. We adopt the following values for the depth of the hyperon-nucleus potential: $U_\Lambda^N(\rho_0) = -28$ MeV; $U_\Sigma^N(\rho_0) = 20$ MeV, $U_\Xi^N(\rho_0) = -18$ MeV (Bart et al. 1999; Batty, Friedman & Gal 1994). Here and in what follows, other symbols follow the usual convention used in most of the literature. Tables 3 and 4 show the coupling constants and the corresponding ratios $\chi_{\Phi H} \equiv \frac{g_{\Phi H}}{g_{\Phi N}}$. Due to the scarcity of data, some coupling constants (marked with the symbol †) are determined by the SU(3) symmetry.

The Λ -hyperon is a singlet (it has zero isospin) and therefore it does not couple to the ϱ -meson. As an example of our results, Table 5 shows a particular set of values

Table 3 Ratios $\chi_{\Phi H} \equiv \frac{g_{\Phi H}}{g_{\Phi N}}$ with $\Phi = \omega, \varrho$ and $H = \Lambda, \Sigma, \Xi$.

$\chi_{\phi\Lambda}^\dagger$	$\chi_{\phi\Sigma}^\dagger$	$\chi_{\phi\Xi}^\dagger$	$\chi_{\varrho\Lambda}^\dagger$	$\chi_{\varrho\Sigma}^\dagger$	$\chi_{\varrho\Xi}^\dagger$
$\frac{2}{3}$	$\frac{2}{3}$	$\frac{1}{3}$	0.0	2.0	1.0

Table 4 Ratios $\chi_{\Phi H} \equiv \frac{g_{\Phi H}}{g_{\Phi N}}$ with $\Phi = \phi, \sigma^*$ and $H = \Lambda, \Sigma, \Xi$.

$\chi_{\phi\Lambda}^\dagger$	$\chi_{\phi\Sigma}^\dagger$	$\chi_{\phi\Xi}^\dagger$	$\chi_{\sigma^*\Lambda}^\dagger$	$\chi_{\sigma^*\Sigma}^\dagger$	$\chi_{\sigma^*\Xi}^\dagger$
$\frac{2\sqrt{2}}{6}$	$\frac{2\sqrt{2}}{6}$	$\frac{2\sqrt{2}}{3}$	$\frac{2\sqrt{2}}{6}$	$\frac{2\sqrt{2}}{6}$	$\frac{2\sqrt{2}}{3}$

Table 5 Coupling constants using $g_{\delta N} = 3.1$. We only show the non-zero parameters.

Model	$g_{\sigma N}$	$g_{\omega N}$	$g_{\rho N}$	$g_{\sigma\Lambda}$	$g_{\sigma\Sigma}$	$g_{\sigma\Xi}$
$\zeta = 0.044$	9.893	10.719	8.657	5.343	3.832	2.719
$\zeta = 0.044$						
$\kappa = 0.040$	9.893	10.719	8.657	5.343	3.832	2.719
$\zeta = \xi =$						
$\eta = 0.100$	11.857	14.520	8.177	9.680	5.764	3.653

Table 6 Saturation properties of nuclear matter and global properties of families of neutron stars corresponding to the set of coupling constants shown in Table 4. ρ_c is the central baryon density, M_* is the maximum star mass, and R_* is the star radius corresponding to the maximum mass. Only the non-zero parameters are shown.

Model	$\frac{M_*^*}{M_N}$	K (MeV)	M_* (M_\odot)	R_* (km)	$\frac{\rho_c}{\rho_0}$
$\zeta = 0.044$	0.66	297	1.92	12.19	4.96
$\zeta = 0.044$					
$\kappa = 0.040$	0.66	297	1.95	11.96	5.20
$\zeta = \xi =$					
$\kappa = \eta = 0.100$	0.58	360	2.02	12.10	5.05

of the coupling constants, and Table 6 shows the corresponding equilibrium properties of nuclear matter and the results for global properties of families of neutron stars which are in good agreement with recent observation results (Demorest et al. 2010).

4 Results

We have calculated the EoS, population profiles and, by solving the Tolman-Oppenheimer-Volkoff (TOV) equations (Tolman 1939; Oppenheimer & Volkoff 1939), we have determined the mass-radius relation for families of neutron stars with hyperon content. Our results for different values of the set of parameter (ζ, ξ, κ, η) are illustrated in Figs. 1–5, where each set generates a sequence of neutrons stars with different equations of state, particle populations, central densities, and maximum masses for neutron stars.

The analysis of these results demands first to remember that a stiffer, or equivalently, more rigid equation of state of nuclear matter is related to higher values of the internal pressure of the system and, accordingly, to higher values of the compressibility modulus $|K_{\text{sym}}|$ of nuclear matter. This in turn requires stronger contributions from repulsive components of the nuclear force when compared to the attractive

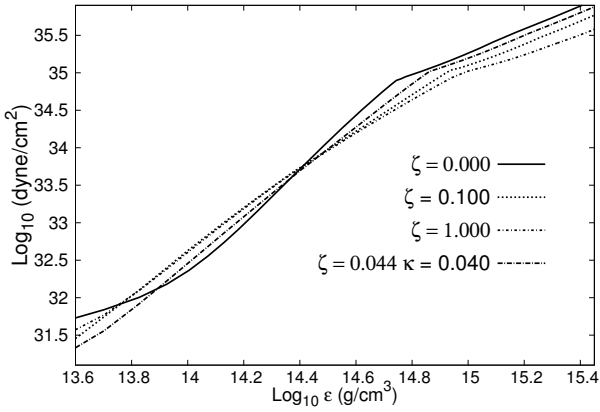


Fig. 1 Equation of state for a set of parameters. For comparison, the curves labelled with $\zeta = 0.000$ and $\zeta = 1.000$ represent the results of our model corresponding respectively to the Serot & Walecka (1997) and ZM (Zimanyi & Moszkowski 1990) models. The remaining curves labelled with $\zeta = 0.100$ and $\zeta = 0.044, \kappa = 0.040$ represent a particular combination of the parameters of our model. This last result allows, through the calculation of the TOV equations (Tolman 1939; Oppenheimer & Volkoff 1939) to a maximum mass of neutron stars in good agreement with recent experimental observations (Demorest et al. 2010). The remaining model parameters, not shown in the curves, are set equal to zero.

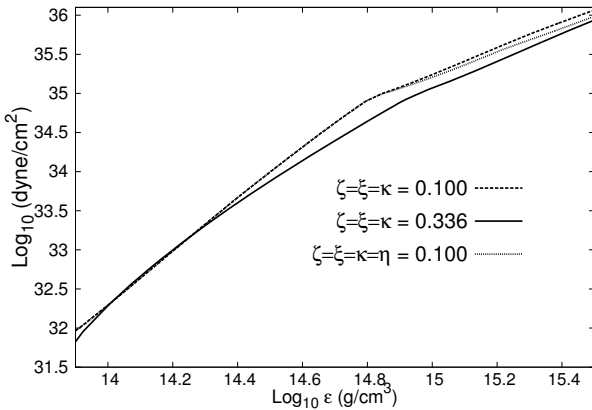


Fig. 2 For comparison, the curves show the predictions of our model for the equation of state for a particular set of parameters. The remaining model parameters, not shown in the curves, are set equal to zero.

ones. In our general approach, however, many body forces (density correlations) lower the intensities both of attractive and repulsive interaction terms due to *shielding effects*, which result in higher (lower) values of the compressibility modulus $|K_{\text{sym}}|$ of nuclear matter in the case of higher (lower) relative reduction of the attractive (repulsive) contributions.

In this sense, when many-body correlations shield the attractive part of the strong interaction, they intensify the corresponding repulsive part, favoring in this way the stiffening of the EoS. On the other hand, the effective masses of baryons increase as the shielding of the attractive part of

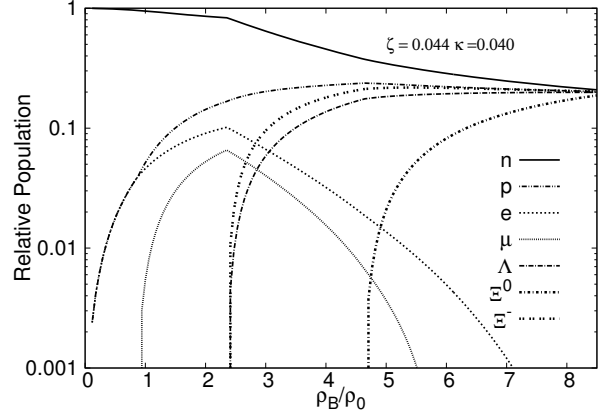


Fig. 3 Population profiles as a function of the baryon density for the particular set of parameters $\zeta = 0.044, \kappa = 0.040$ which allows, through the calculation of the TOV equations (Tolman 1939; Oppenheimer & Volkoff 1939) to a maximum mass of neutron stars in good agreement with recent experimental observations (Demorest et al. 2010). The remaining model parameters, not shown in the curves, are set equal to zero.

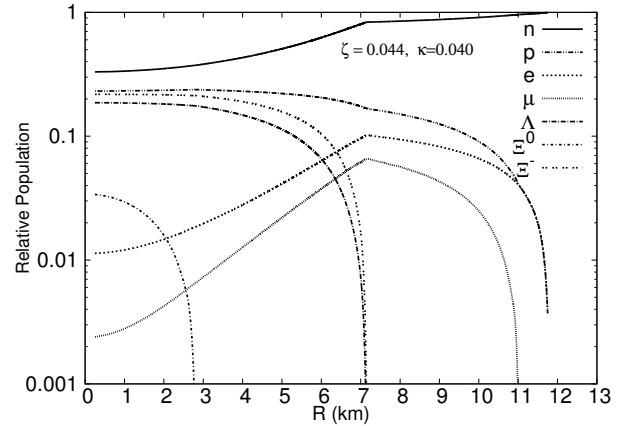


Fig. 4 Population profile as a function of the stellar radius for the particular set of parameters shown in the previous figure.

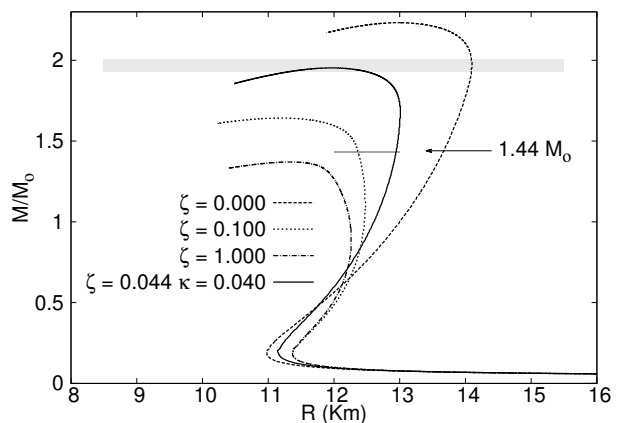


Fig. 5 Mass-radius relation for different sets of parameters and different versions of the model. The highlighted region determine the observational threshold for the maximum mass $1.97 \pm 0.04 M_{\odot}$ (Demorest et al. 2010). The thin horizontal line corresponds to a canonical $1.44 M_{\odot}$ neutron star with radius 12.5 ± 0.5 km (Erler et al. 2013).

the strong interaction increase, as shown in Eq. (4). This favors the growth of the internal pressure of the system and the stiffening of the EoS.

There is another important effect to be considered, the presence of hyperons. Our predictions for the particle population show that the threshold equation for a given species (Glendenning 1996) is also affected by the presence of many-body correlations (see Eq. 3):

$$\mu_n - q_B \mu_e \geq g_{\omega B} f_{\sigma\sigma^* \delta\xi} \omega_0 + g_{\rho B} f_{\sigma\sigma^* \delta\kappa} \rho_{03} I_{3B} + g_{\phi B} f_{\sigma\sigma^* \delta\eta} \phi_0 + f_{\sigma\sigma^* \delta\zeta} M_B. \quad (9)$$

In this expression, μ_n and μ_e represent respectively the neutron and electron chemical potential, and q_B is the baryon charge. The sign of $g_{\rho B} \rho_{03} I_{3B}$ is determined by the net isospin density of the star. This term determines whether a given baryon configuration is isospin favored or unfavored. Similarly, the term $q_B \mu_e$ determines whether a given baryon state is charge favored or unfavored. Moreover, in this expression

$$f_{\sigma\sigma^* \delta\alpha} = 1 - \left(\frac{g_{\sigma B} \sigma_0 + g_{\sigma^* B} \sigma_0^* + \frac{1}{2} g_{\delta B} \langle \tau_3 \rangle \delta_{03}}{M_B} \right) + \left(\frac{\alpha}{2} \right) \left(\frac{g_{\sigma B} \sigma_0 + g_{\sigma^* B} \sigma_0^* + \frac{1}{2} g_{\delta B} \langle \tau_3 \rangle \delta_{03}}{\alpha M_B} \right)^2 + \mathcal{O}(3), \quad (10)$$

with $\alpha = \xi, \kappa, \eta, \zeta$. These equation show that the population of hyperons is affected by many-body correlations, which shift the critical density for hyperon saturation to higher densities.

Following recent experimental results (Zhao & Zhang 2013; see also Bednarek, Keska & Manka 2003), we have considered in our calculations the extreme case where the Σ^- experiences such a strong repulsion that it does not appear at all in nuclear matter for densities exceeding those found in neutron stars. The first hyperon species that appears is the Λ : free of isospin-dependent forces, as the density increases, the Λ hyperon continues to accumulate until short-range repulsion forces cause them to saturate. Other hyperon species follow at higher densities.

Our model originates moreover an anti-correlation between the amount of hyperons: for certain values of the parameters, according to Eqs. (9) and (10) an anti-correlation associated with the predominance of the scalar part occurs. This mean that hyperon degrees of freedom become more numerous to the extent that the attractive sector is favored in comparison with the repulsive part, thus favoring smaller neutron star masses. However, the absence of the Σ^- hyperon reduces this effect.

When considering simultaneously both shielding effects involving the attractive and repulsive contributions of the strong interaction, one would expect that, – since the repulsive part of the strong interaction is more effective in nuclear matter at high densities, on the average, than the attractive sector –, that the shielding of the strong interaction would favor the attractive part, contributing this way to the reduction of the mass of the neutron star. However, our results

indicate that the combination of these effects with the others previously reported favors the stiffening of the EoS. In other words, the shielding of the attractive part of the strong interaction combined with the increase of the effective mass of baryons and the absence of the Σ^- hyperon, are dominant when compared with those effects favoring the softening of the EoS, i.e., the shielding of the repulsive part of the strong interaction and the increase on the population of the remaining hyperons beyond the Σ^- .

5 Conclusions

One of the most controversial and intriguing questions in modern astrophysics concerns the existence of a maximum mass of a neutron star. The establishment of this threshold and the controversies correlated with this conception followed historically a logical line of thought quite similar to the corresponding determination of the maximum mass of another type of compact star, the white dwarf. For interesting discussions on this topic, see Yakovlev et al. (2010).

Stoner (1929) was the first scientist to predict the existence of a maximum mass for a white dwarf. In doing this, Stoner calculated the equation of state of a relativistic Fermi gas and applied it to stellar configurations of white dwarfs of uniform density (incompressible matter). A little later, Chandrasekhar (1931) improved the stellar mass limit of Stoner by allowing the internal density to vary (compressible matter) within a polytropic model, based on the solutions of the Lane-Emden equation. Chandrasekhar considered in his calculations non-rotating white dwarf stars composed of a fully ionized plasma of nuclei and electrons with a net concentration Y_e of electrons per nucleon (lepton fraction). In his studies, he assumed that the nuclei do not contribute to the internal pressure of the plasma and that the electrons could be described by an ideal Fermi gas. Moreover, taking into account that electrons become relativistic in the high density domain and assuming that the electron degeneracy pressure resists gravitational collapse, the result so obtained, now known as the Chandrasekhar limit, provided that the maximum mass of a stable white dwarf, M_{WD} , is about $1.4 M_\odot$.

Independently, Landau (1932) mentioned the possible existence of dense stars which look like giant nuclei which can be regarded as an early theoretical prediction or anticipation of neutron stars, prior to the discovery of the neutron. He showed that hydrostatic equilibria of stars supported by the pressure of degenerate electrons only exist if the mass of the star do not exceed $1.5 M_\odot$. However, his predictions in this regard occurred before the discovery of the neutron by Chadwick (1932). Landau assumed that protons and electrons constitute atomic nuclei and do not annihilate because his ideas was conceived before the discovery of the neutron. However, his suggestion that sources of stellar energy were located in pathological cores was convenient, but at the same time naive (Yakovlev et al. 2010). After the discovery

of the neutron an adaptation of his calculation provides a limit of $1.8 M_{\odot}$.

In 2010, Paul Demorest and colleagues (Demorest et al. 2010), using the Shapiro delay, measured the mass of the millisecond pulsar PSR J1614–2230. The result obtained was $1.97 \pm 0.04 M_{\odot}$, a value substantially higher than any previously measured neutron star mass, placing this way strong constraints on the interior composition of neutron stars. Moreover, in 2013, Antoniadis and colleagues (Antoniadis et al. 2013) measured the mass of the millisecond pulsar PSR J0348+0432 to be $2.01 \pm 0.04 M_{\odot}$. This confirmed the existence of such massive stars using a different method. Furthermore, this allowed, for the first time, a test of general relativity using such a massive neutron star.

In Fig. 5, the curves labelled with $\zeta = 0.000$ and $\zeta = 1.000$ represent the results of our model for the mass-radius relationship of neutrons stars corresponding to the Serot & Walecka (1997) and ZM (Zimanyi & Moszkowski 1990) models, respectively. The remaining curves labelled with $\zeta = 0.100$ and $\zeta = 0.044$, $\kappa = 0.040$ represent a particular combination of the parameters of our model. This last result allows, through the calculation of the TOV equations (Tolman 1939; Oppenheimer & Volkoff 1939) to a maximum mass of neutron stars in good agreement with recent experimental observations (Demorest et al. 2010). The remaining model parameters, not shown in the curves, are set equal to zero.

Our results also indicate that, to compensate the absence of the Σ^- to bring about charge neutrality and chemical equilibrium, as well as the requirements of the Pauli principle and the rearrangement of Fermi populations to minimize energy, the Λ and Ξ^- thresholds have been reduced. This last reduction is charge favored, replacing a neutron and electron at the top of their Fermi seas, although both Σ^- and Ξ^- are isospin unfavored.

Interesting issues for future studies will be the role of finite temperature, neutrino trapping, and strong magnetic effects in neutron stars. Work along these lines is in progress.

References

- Antoniadis, J., Freire, P.C.C., Wex, N., et al. 2013, *Science*, 340, 6131, 448
- Bandyopadhyay, D., & Greiner, W. 2004, *Phys.Rev. D*, 70, 123004
- Banik, S., Hanauske, M., Bandyopadhyay, D., & Greiner, W. 2004, *Phys.Rev. D*, 70, 123004
- Bart, S., Chrien, R.E., Franklin, W.A., et al. 1999, *Phys. Rev. Lett.* 83, 5238
- Batty, C.J., Friedmanm E., & Gal, A. 1994, *Phys. Lett. A*, 335, 273
- Bednarek, I., Keska, M., & Manka, R. 2003, *Phys. Rev. C*, 68, 035805
- Boguta, J., Bodmer, A. R. 1997, *Nucl. Phys. A* 292, 413
- Chadwick, J. 1932, *Proc.Royal Soc.London A*, 136, 692
- Chamel, N., Haensel, P., Zdunik, J.L., & Fantina. A.F. 2013, *Int. J. Mod. Phys. E*, 22, 1330018
- Chandrasekhar, S. 1931, *ApJ*, 74, 81
- Dabrowski, J., & Rozynek, J. 2010, *Acta Phys. Polon. B*, 41, 357
- Demorest, P., Pennucci, T., Ransom, S., Roberts, M., & Hessels, J. 2010, *Nature*, 467, 1081
- Dexheimer, V., & Schramm, S. 2008, arxiv.org/pdf/08021999
- Erler, J., Horowitz, C.J., Nazarewicz, W., Rafalski, M., & Reinhard, P.-G. 2013, *Phys. Rev. C*, 86, 044320
- Glendenning, N. K. 1996, *Compact Stars*, (Springer Verlag, Berlin)
- Haensel, P., Potekhin, A.Y., & Yakovlev, D.G. 2007, *Neutron Stars I – Equation of State and Structure*, (Springer Verlag, Berlin)
- Huber, H., Weber, F., Weigel, M.K., & Schaab, C. 1998, *Int. J. Mod. Phys. E*, 7, 301
- Landau, L.D.1932, *Phys. Z. Sowjetunion*, 1, 285
- Lattimer, J.M. 2013, *Annu. Rev. Nucl. Part. Sci.*, 62, 485
- Massot, E., Margueron, J., & Chanfray, G. 2012, *Europhys.Lett.*, 97, 39002
- Papazoglou, P., Zschieche, D., Schramm, S., Schaffner-Bielich, J., Stoecker, H., & Greiner, W. 1998, *Phys. Rev. C*, 57, 2576
- Papazoglou, P., Zschieche, D., Schramm, S., Schaffner-Bielich, J., Stoecker, H., & Greiner, W.1999, *Phys. Rev. C*, 59, 411
- Oppenheimer, J., & Volkoff, G. 1939, *Phys.Rev.*, 55, 374
- Schaffner, J., Dover, C.B., Gal, A., Millener, D.J., Greiner, C., & Stoecker, H. 1994, *Ann. Phys.*, 235, 35
- Serot, B.D., Walecka, J.D. 1997, *Int. J. Mod. Phys. E*, 515, 6; Serot, B.D., Walecka, J.D. 1986, *The Relativistic Nuclear Many-Body Problem*, in: J.W. Negele, E. Vogt (eds.) *Adv. Nucl. Phys.*, 16, 1.
- Shternin, P.S., Baldo, M., & Haensel, P. 2013, [arXiv: 1311.4278](https://arxiv.org/abs/1311.4278) [astro-ph.SR]
- Stoner, E.C. 1929, *The Limiting Density in White Dwarfs*, *Philosophical Magazine* vii, 63
- Taurines, A., Vasconcellos, C.A.Z., Malheiro, M., & Chiapparini, M. 2001, *Phys.Rev. C*, 63, 065801
- Tolman, R.C. 1939, *Phys.Rev.*, 55, 364
- Vasconcellos, C.A.Z., Horvath, J., Hadjimichef, D., Gomes, R.O. 2012, *Int. J. Mod. Phys. Conf. Ser.*, 18, 182
- Vasconcellos, C.A.Z., Gomes, R.O, Dexheimer, V., Negreiros, R.P., Horvath, J., & Hadjimichef, D. 2014, this volume
- Wang, Q.L., Dang, L., Zhong, X.H., & Ning, P.Z. 2006, *Europhys. Lett.*, 75, 36
- Whittenbury, D.L., Carroll, J.D., Thomas, A.W., Tsushima, K., & Stone, J.R. 2013, ADP-13-17-T837 e-Print: [arXiv:1307.4166](https://arxiv.org/abs/1307.4166)
- Zhao, X.F., & Zhang, L. 2013, *Int. J. Theor. Phys.*, 52, 429
- Yakovlev, D.G., Haensel, P., Baym, G., & Pethick, C.J. 2013, *Physics Uspekhi*, 56, 289; 2012, [arXiv:1210.0682](https://arxiv.org/abs/1210.0682) [physics.hist-ph]
- Zimanyi, J, Moszkowski, S.A. 1990, *Phys. Rev. C*, 42, 1416

Induced gravitational collapse at extreme cosmological distances: the case of GRB 090423

R. Ruffini^{1,2,3,4}, L. Izzo^{1,2}, M. Muccino¹, G. B. Pisani^{1,3}, J. A. Rueda^{1,2,4}, Y. Wang¹, C. Barbarino^{1,5}, C. L. Bianco^{1,2},
M. Enderli^{1,3}, and M. Kovacevic^{1,3}

¹ Dip. di Fisica and ICRA, Sapienza Università di Roma, P.le Aldo Moro 5, 00185 Rome, Italy
e-mail: Ruffini@icra.it

² ICRA-Net, Piazza della Repubblica 10, 65122 Pescara, Italy

³ Université de Nice-Sophia Antipolis, Cedex 2, Grand Château Parc Valrose, Nice, France

⁴ ICRA-Net-Rio, Centro Brasileiro de Pesquisas Físicas, Rua Dr. Xavier Sigaud 150, 22290-180 Rio de Janeiro, RJ, Brazil

⁵ INAF-Napoli, Osservatorio Astronomico di Capodimonte, Salita Moiariello 16, 80131 Napoli, Italy

Received 17 January 2014 / Accepted 25 May 2014

ABSTRACT

Context. The induced gravitational collapse (IGC) scenario has been introduced in order to explain the most energetic gamma ray bursts (GRBs), $E_{\text{iso}} = 10^{52} - 10^{54}$ erg, associated with type Ib/c supernovae (SNe). It has led to the concept of binary-driven hypernovae (BdHNe) originating in a tight binary system composed by a FeCO core on the verge of a SN explosion and a companion neutron star (NS). Their evolution is characterized by a rapid sequence of events: 1) the SN explodes, giving birth to a new NS (ν NS). The accretion of SN ejecta onto the companion NS increases its mass up to the critical value; 2) the consequent gravitational collapse is triggered, leading to the formation of a black hole (BH) with GRB emission; 3) a novel feature responsible for the emission in the GeV, X-ray, and optical energy range occurs and is characterized by specific power-law behavior in their luminosity evolution and total spectrum; 4) the optical observations of the SN then occurs.

Aims. We investigate whether GRB 090423, one of the farthest observed GRB at $z = 8.2$, is a member of the BdHN family.

Methods. We compare and contrast the spectra, the luminosity evolution, and the detectability in the observations by *Swift* of GRB 090423 with the corresponding ones of the best known BdHN case, GRB 090618.

Results. Identification of constant slope power-law behavior in the late X-ray emission of GRB 090423 and its overlapping with the corresponding one in GRB 090618, measured in a common rest frame, represents the main result of this article. This result represents a very significant step on the way to using the scaling law properties, proven in Episode 3 of this BdHN family, as a cosmological standard candle.

Conclusions. Having identified GRB 090423 as a member of the BdHN family, we can conclude that SN events, leading to NS formation, can already occur, namely at 650 Myr after the Big Bang. It is then possible that these BdHNe stem from 40–60 M_{\odot} binaries. They are probing the Population II stars after the completion and possible disappearance of Population III stars.

Key words. gamma-ray burst: general – gamma-ray burst: individual: GRB 090423 – black hole physics

1. Introduction

The induced gravitational collapse (IGC) paradigm (Ruffini 2011; Rueda & Ruffini 2012; Izzo et al. 2012b) has been proposed to explain a class of very energetic ($E_{\text{iso}} \sim 10^{52} - 10^{54}$ erg) long gamma ray bursts (GRBs) associated with supernovae (SNe). A new class of systems, with progenitor a tight binary composed by a FeCO core and a companion neutron star (NS), has been considered. These systems evolve in a very rapid sequence lasting a few hundred seconds in their rest frame: 1) the SN explodes giving birth to a new NS (ν NS); 2) the accretion of the SN ejecta onto the companion NS increases its mass, reaching the critical value; 3) the gravitational collapse is triggered, leading to the formation of a black hole (BH) with GRB emission. Such systems have been called binary-driven hypernovae (BdHN Ruffini et al. 2014a).

Observationally, this authentic cosmic matrix is characterized by four distinct episodes, with the “in” state represented

by a FeCO core and a NS and the “out” state by a ν NS and a BH. Each episode contains specific signatures in its spectrum and luminosity evolution. Up to now, the IGC paradigm has been verified in a dozen GRBs, all with redshift up to $z \sim 1$ (Izzo et al. 2012a; Penacchioni et al. 2012, 2013; Pisani et al. 2013; Ruffini et al. 2013).

Various approaches have been followed to reach an understanding of long GRBs. One of these has been the use of statistical tools to obtain general results that examine the most complete source catalog (see, e.g., Nousek et al. 2006; Kann et al. 2011; Salvaterra et al. 2012; Margutti et al. 2013, and references therein).

We follow a different approach here. We first identified the specific class of BdHNe of GRBs related to SNe, as mentioned above, widely tested at $z \approx 1$. We furthermore explore the members of this class by extending our analysis to higher values of the cosmological redshifts. We do that by taking the scaling laws for the cosmological transformations into account, as well as the

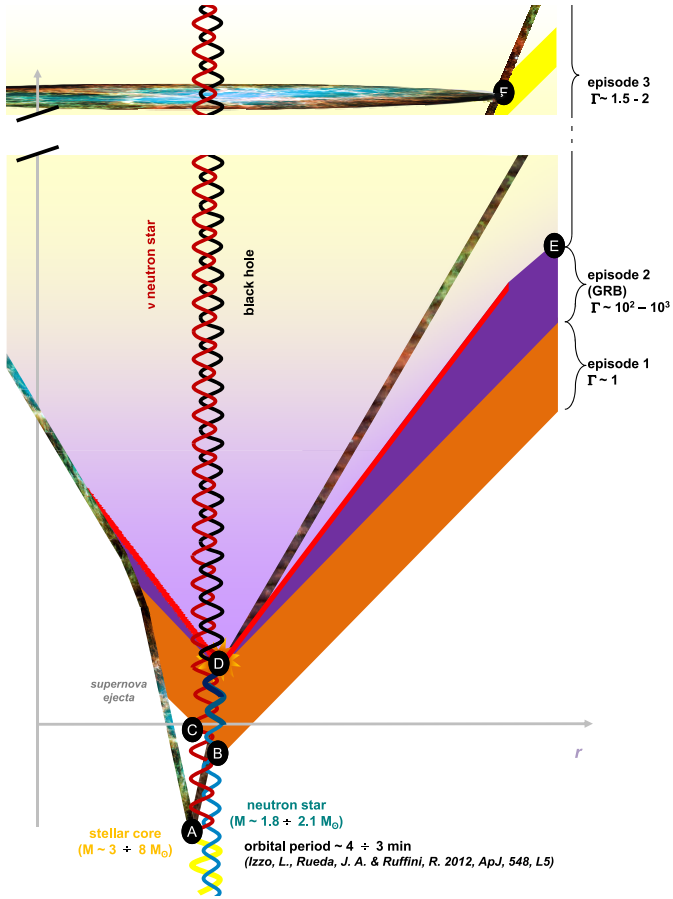


Fig. 1. Space-time diagram of the induced gravitational collapse applied to GRB 090618 (Enderli 2013; Ruffini 2013). The sequence is summarized as follows: A) the explosion as a SN of the evolved FeCO core which creates a ν -NS and its remnant; B) the beginning of the accretion of the SN ejecta onto the companion NS, emitting Episode 1; C) a prolonged interaction between the ν -NS and the NS binary companion; D) the companion NS reaches its critical mass by accretion, and a BH is formed with the consequent emission of a GRB; E) the arrival time at the separatrix between Episodes 2 and 3; F) the optical emission of the SN due to the decay of ^{56}Ni after $t_a^d \sim 10(1+z)$ days in the observer frame (Episode 4).

specific sensitivities of the GRB detectors (in this case *Swift*, Gehrels et al. 2005; and *Fermi*, Meegan et al. 2009).

Our aim is to verify that such BdHNe, originating in a SN and a companion NS, did form in the earliest phases of the universe. If this is confirmed, we go on to examine the possibility that all GRBs with $E_{\text{iso}} \sim 10^{52} - 10^{54}$ erg are indeed associated to SN and belong to the BdHN family independently of their space and time location.

2. The four episodes of BdHNe sources

In order to achieve this goal, we recall the four above-mentioned episodes, present in the most general BdHN (see Fig. 1):

Episode 1 has the imprint of the onset of a SN in the tight binary system with the companion neutron star (NS; see Fig. 2). It stemmed from the hyper-critical accretion of the SN matter ejecta ($\sim 10^{-2} M_{\odot} \text{ s}^{-1}$) (Rueda & Ruffini 2012). Decades of conceptual progress have passed from the original work of Bondi & Hoyle (1944) and Bondi (1952) to the problem of a “hypercritical” accretion rate. This problem has acquired growing scientific interest as it moved from the classical astronomical field to the

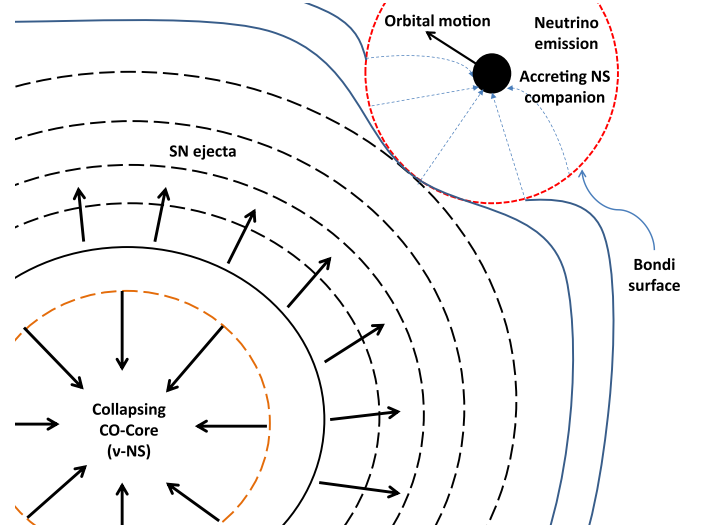


Fig. 2. Sketch (not in scale) of the accretion induced gravitational collapse (IGC) scenario.

domain of the relativistic astrophysics. The crucial role of neutrino cooling, earlier considered by Zel’dovich et al. (1972) and later on by Bisnovaty-Kogan & Lamzin (1984) in SN fallback, has been recognized to play a crucial role in describing binary common envelope systems by Chevalier (1989, 1993). In the work by Fryer et al. (1996), and more recently in Fryer (2009), it was clearly shown that an accretion rate $\dot{M} \sim 10^{-2} M_{\odot} \text{ s}^{-1}$ onto a neutron star (NS) could lead in a few seconds to the formation of a black hole (BH), when neutrino physics in the description of the accreting NS is taken into due account. The data acquired in Episode 1 of GRB 090618 (Izzo et al. 2012a), as well as the one in GRB 101023 (Penacchioni et al. 2012), GRB 110709B (Penacchioni et al. 2013), and GRB 970828 (Ruffini et al. 2013), give for the first time the possibility to probe the Bondi-Hoyle hypercritical accretion and possibly the associated neutrino emission, which was theoretically considered by Zel’dovich et al. (1972); Chevalier (1993); Fryer et al. (1996), and Fryer (2009).

Episode 2 is the canonical GRB emission, which originated in the collapse of the companion NS, which reached its critical mass by accretion of the SN ejecta and then collapsed to a black hole (BH), indeed emitting the GRB.

Episode 3 observed in X-rays by *Swift*-XRT, shows very precise behavior consisting of steep decay, starting at the end point of the prompt emission, and then a plateau phase followed by a late power-law decay (see Pisani et al. 2013 and also Fig. 3). The late X-ray luminosities of BdHNe, in their rest-frame energy band 0.3–10 keV, show a common power-law behavior with a constant decay index clustering around $\alpha = -1.5 \pm 0.2$. The occurrence of such a constant afterglow decay has been observed in all the BdHN sources examined. For example, see in Fig. 4 the data for GRB 130427A, GRB 061121, GRB 060729, respectively. It appears an authentic nested structure, in the late X-ray emission of GRBs associated to SNe, and it has indeed to be indicated as the qualifying feature for a GRB to be a member of the BdHNe family (Ruffini et al. 2014a). It is clear that such a phenomenon offers a strong challenge for explaining by any GRB model.

In addition to these X-ray features, the observations of GRB 130427A by the *Swift*, *Fermi*, and *Konus-WIND* satellites and a large number of optical telescopes have led to the evidence of such power laws at very high energies, in γ -rays and

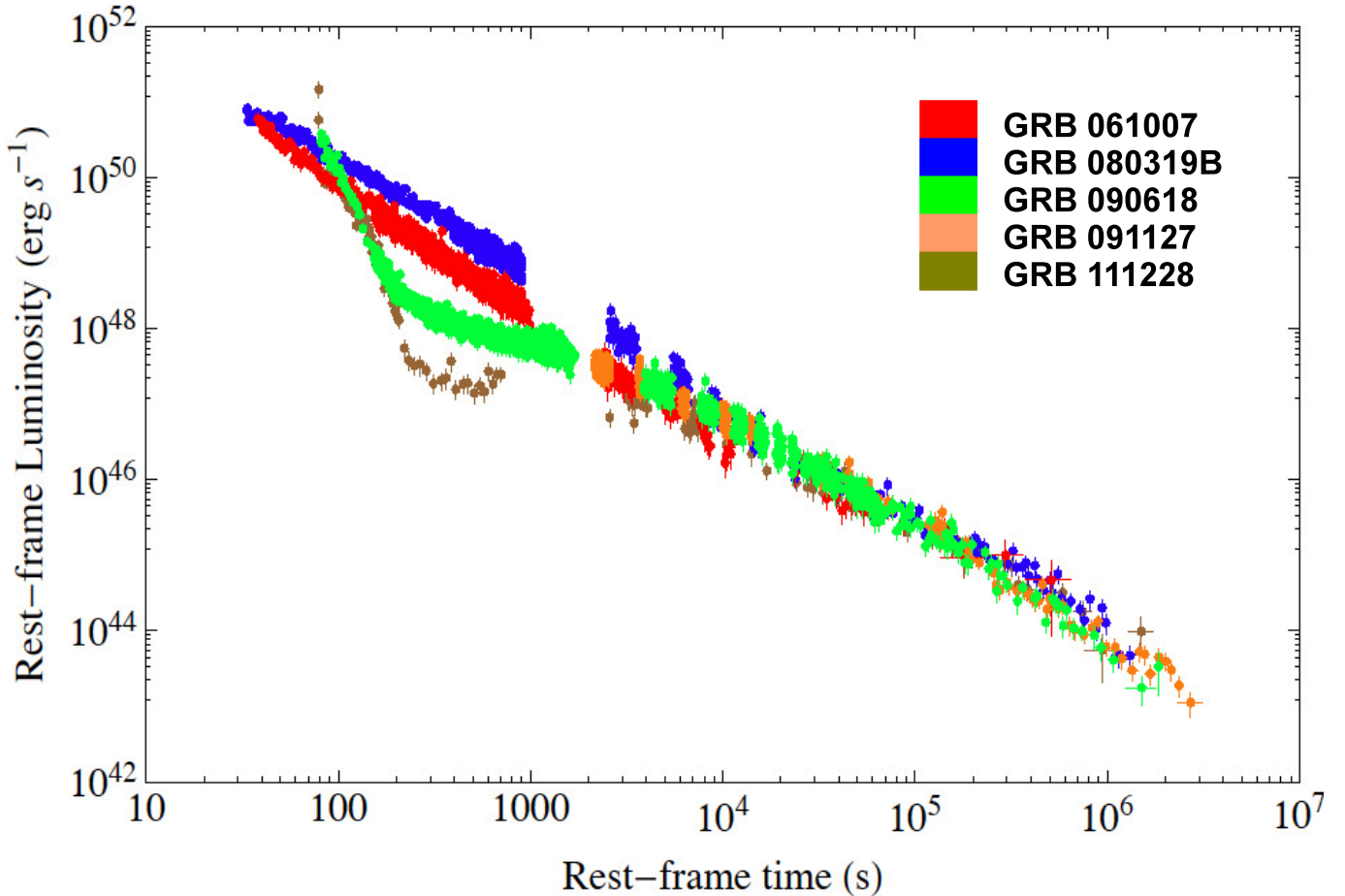


Fig. 3. Rest-frame, X-ray afterglow, luminosity light curves of some IGC GRBs-SNe belonging to the “golden sample” described in Pisani et al. (2013). The overlapping after 10^4 s is clearly evident, confirming the presence of an Episode 3 in this GRB.

at the optical wavelengths (Fermi-LAT collaboration & Fermi-GBM collaboration 2014; Melandri et al. 2014; see also Ruffini et al. 2014b).

Episode 4 is characterized by the emergence of the SN emission after about 10–15 days from the occurrence of the GRB in the rest frame of the source, which has been observed for almost all the sources fulfilling the IGC paradigm with $z \sim 1$.

3. GRB 090423 compared and contrasted with GRB 090618

We first consider the data of GRB 090423, one of the farthest GRB ever observed at $z = 8.2$ (Salvaterra et al. 2009; Tanvir et al. 2009), with the prototypical member of the BdHNe class, namely GRB 090618, and its associated SN (Izzo et al. 2012a). In other words we proceed with a specific ansatz: we verify that GRB 090423, at $z = 8.2$, presents analogous intrinsic features to GRB 090618, which was observed at $z = 0.54$.

We proceed by examining (see Sect. 4) each one of the above episodes for both sources, by a detailed spectral analysis and simulations. We first verify that Episode 1 of GRB 090618 transposed at redshift $z = 8.2$ should not have triggered the *Swift*-BAT detector. Indeed, no precursor in the light curve of GRB 090423 was detected. Consequently, we do not address any theoretical considerations of the hypercritical accretion in Episode 1 of GRB 090423, since it is not observable in this source (see Sect. 5). We also notice that the distance of

GRB 090423 prevents any possible detection of a SN associated with this GRB, and therefore Episode 4 cannot be observed in GRB 090423.

For Episode 2, we have found that indeed the transposed emission of GRB 090618 should provide a positive trigger: we show in Sect. 6 that the duration, the observed luminosity and the spectral emission of Episode 2 in GRB 090423 present analogous intrinsic features to the transposed ones of GRB 090618 and differ only in the spectral energy distribution due to different circumburst medium properties.

For Episode 3, the crucial result, probing the validity of the above ansatz, is that the late X-ray emission in GRB 090423, computed in the rest frame of the burst at $z = 8.2$, precisely coincides (overlaps) with the corresponding late X-ray emission in GRB 090618, as evaluated in the rest frame of the source at $z = 0.54$, see Sect. 7. The occurrence of this extraordinary coincidence in Episode 3 proves that GRB 090423 is indeed a member of the BdHN family. This in particular opens the possibility of elaborating a role for the late X-ray emission in BdHNe as a standard candle.

4. The data

GRB 090423 was discovered on 23 April 2009, 07:55:19 UT, T_0 from here, by the *Swift* Burst Alert Telescope (BAT; Krimm et al. 2009), at coordinates RA = $09^{\text{h}} 55^{\text{m}} 35^{\text{s}}$, Dec = $+18^{\circ} 09' 37''$ (J2000.0; $3'$ at 90% containment radius). The

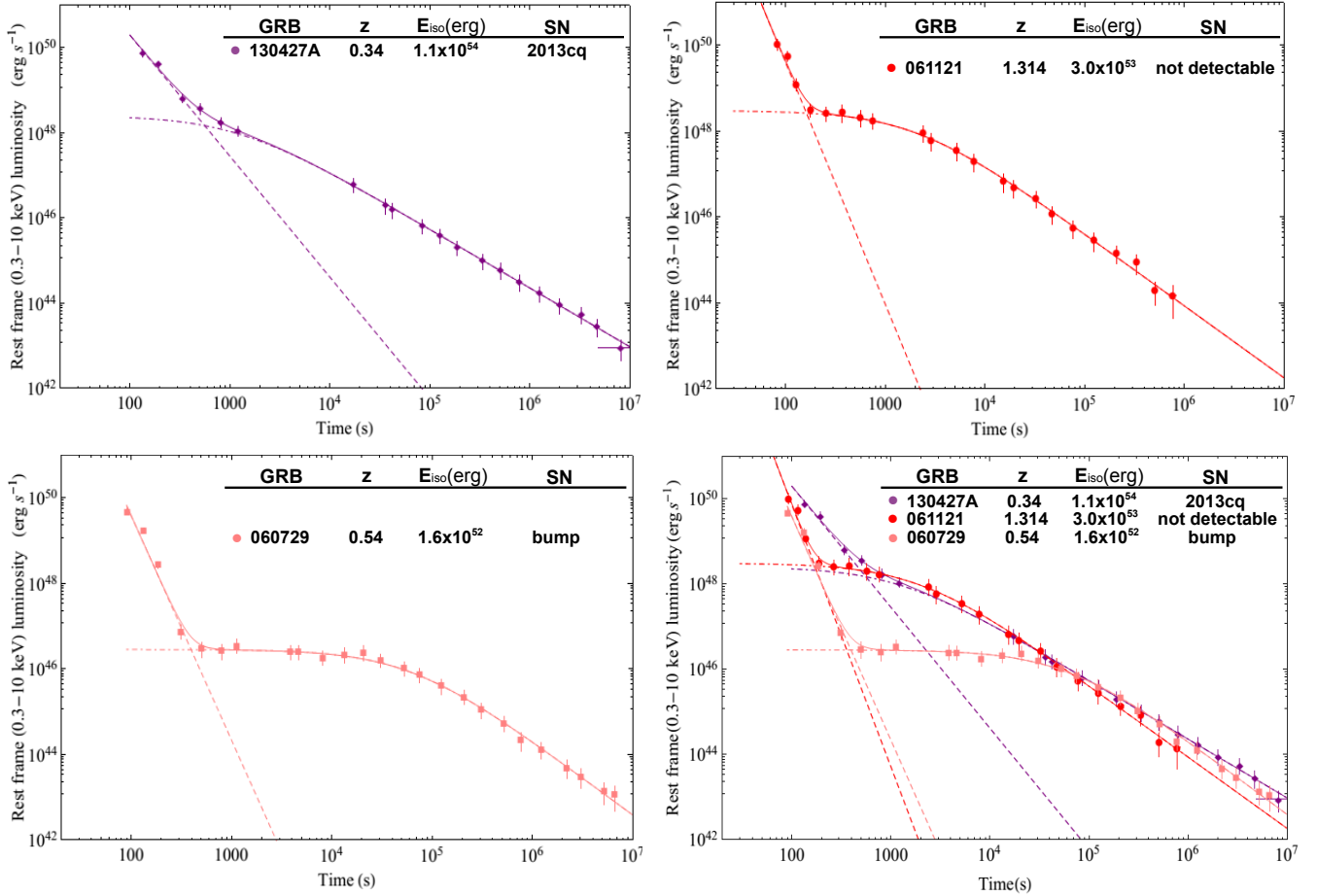


Fig. 4. Rest-frame, (0.3–10) keV, and re-binned luminosity light curves of GRB 130427A (*upper left*), GRB 061121 (*upper right*), GRB 060729 (*lower left*) and a combined picture (*lower right*). The fits to their emission is done using a power-law function for the early steep decay and a phenomenological function for the following emission, which is described well in [Ruffini et al. \(2014a\)](#).

Swift-BAT light curve showed a double-peaked structure with a duration of about 20 s. The X-ray Telescope (XRT; [Burrows et al. 2005](#)) on board the same spacecraft started to observe GRB 090423 72.5 s after the initial trigger, finding a fading source and providing enhanced coordinates for the follow-up by on-ground telescopes that have allowed the discovery of its redshift ($z = 8.2$, [Salvaterra et al. 2009](#); [Tanvir et al. 2009](#)). The light curve is characterized by an intense and long flare peaking at about $T_0 + 180$, followed by a power-law decay, observed from the second orbit of *Swift* ([Stratta & Perri 2009](#)). The prompt emission from GRB 090423 was also detected by the *Fermi* Gamma-Ray Burst Monitor (GBM, trigger 262166127/090423330; [von Kienlin 2009a](#)), whose on-ground location was consistent with the *Swift* position. The Large Area Telescope (LAT) on-board the *Fermi* satellite did not detect any signal from GRB 090423. The GBM light curve showed a single-structured peak with a duration of about 12 s, whose spectral energy distribution was best fit with a power law with an exponential cut-off energy, parameterized as $E_{\text{peak}} = (82 \pm 15)$ keV. The observed fluence was computed from *Fermi* data to be $S_\gamma = 1.1 \times 10^{-6}$ ergs/cm² that, considering the standard Λ CDM cosmological model, corresponds to an isotropic energy emitted of $E_{\text{iso}} = 1.1 \times 10^{53}$ ergs for the spectroscopic redshift $z = 8.2$ ([von Kienlin 2009b](#)). With these values for E_{peak} and E_{iso} , GRB 090423 satisfies the Amati relation, which is only valid for long GRBs ([Amati et al. 2002](#)).

5. The impossibility of detecting Episode 1

It has become natural to ask if observations of Episodes 1 and 2 in the hard X-ray energy range could be addressed for the case of GRB 090423. We have first analyzed a possible signature of Episode 1 in GRB 090423. Since the *Swift*-BAT, (15–150) keV, light curve is a single-structured peak with duration of ~ 19 s, as detected by *Swift*-BAT, with no thermal emission in its spectrum and no detection of any emission from a precursor in the *Swift* and *Fermi* data, we have considered the definite possibility that Episode 1 was not observed at all. In this light, the best way to check this possibility consists in verifying that the Episode 1 emission is below the threshold of the *Swift*-BAT detector, consequently, it could have not triggered the *Swift*-BAT. We have considered the prototype of Episode 1 as the one observed in GRB 090618 ([Izzo et al. 2012b](#)), which is at redshift $z = 0.54$, and then we transposed it at redshift $z = 8.2$, simulating the observed emission of GRB 090618 as if it had been observed at this large distance. Then, we performed a time-resolved spectral analysis of Episode 1 in GRB 090618, using a Band function as spectral model, and finally we translated the specific photon spectra obtained from the analysis at the redshift of GRB 090423. This last operation consists in two transformations, concerning the peak energy E_{peak} of the Band function and the normalization value K_{Band} . The new value of the peak energy is simply given by $E_{\text{peak},8} = E_{\text{peak}} (1 + 0.54)/(1 + 8.2)$, while the

normalization, which corresponds to the specific photon flux at 1 keV, requires knowledge of the luminosity distances of the two bursts, $d_l(z)$:

$$K_{\text{Band},8} = K_{\text{Band}} \left(\frac{1 + 8.2}{1 + 0.54} \right)^2 \left(\frac{d_l(0.54)}{d_l(8.2)} \right)^2. \quad (1)$$

Another transformation concerns the observational time of Episode 1 of GRB 090618 at redshift $z = 8.2$. At large distances, any astrophysical event will be dilated in time by the cosmological redshift effect, which in the current case modifies the time interval by a quantity $(1 + 8.2)/(1 + 0.54) = 5.97$. The knowledge of this time interval is fundamental since it represents the exposure of a simulated spectrum translated at $z = 8.2$. We considered Fermi GBM data for analyzing the time-resolved spectra of GRB 090618, as described by Izzo et al. (2012b). The wide energy range of Fermi GBM NaI detectors, (8–1000) keV, allows a more accurate determination of the Band parameters, which are used as input values for the simulated spectra. We also rebinned the Fermi data considering a signal-to-noise ratio (SNR) = 10, and finally performed our spectral analysis. The next step consisted in transforming the peak energy of the Band function and of the normalization of all these time-resolved photon spectra $N(E)$, as described above.

Following the work of Band (2003), the sensitivity of an instrument to detect a burst depends on its burst trigger algorithm. The *Swift*-BAT trigger algorithm, in particular, looks for excesses in the detector count rate above expected background and constant sources. There are several criteria for determining the correct BAT threshold significance σ_0 for a single GRB (Barthelmy et al. 2005), but in this work we have considered the treatment given in Band (2003). Recently, the threshold of *Swift*-BAT has been modified to allow detecting of subthreshold events, but since GRB 090423 was detected before, the Band (2003) analysis is still valid for our purposes. The preset threshold significance for *Swift*-BAT can be expressed by the following formula:

$$\sigma_0 = \frac{A_{\text{eff}} f_{\text{det}} f_{\text{mask}} \Delta t \int_{15}^{150} \epsilon(E) N(E) dE}{\sqrt{A_{\text{eff}} f_{\text{det}} \Delta t \int_{15}^{150} B(E) dE}}, \quad (2)$$

where A_{eff} is the effective area of the detector, f_{det} the fraction of the detector plane that is active, f_{mask} the fraction of the coded mask that is open, Δt the exposure of the photon spectrum $N(E)$, $\epsilon(E)$ the efficiency of the detector, and $B(E)$ the background. We considered the values for these parameters as the ones given in the Band work (with the exception of the detecting area, assumed to be $A_{\text{eff}} = 5200 \text{ cm}^2$), while the efficiency and the background were obtained from the *Swift*-BAT integrated spectrum of GRB 090423 using the XSPEC fitting package. Then we considered as input photon spectra $N(E)$ the ones obtained from the Fermi GBM analysis of Episode 1 of GRB 090618 and translated for the redshift $z = 8.2$. It is appropriate to note that the transformations of spectra presented above are the correct ones: since the sensitivity of *Swift*-BAT strongly depends on the peak energy of the photon flux of the single spectra of the GRB (for the *Swift*-BAT case, see e.g. Fig. 7 of Band 2003), we find that at $z = 8.2$ the observed peak energies of any spectrum will be lowered by a factor $(1 + 0.54)/(1 + 8.2)$. Our procedure also takes this further effect of the cosmological redshift into account.

Since the threshold significance of *Swift*-BAT is variable from a minimum value of $\sigma_0 = 5.5$ up to a maximum value of 11¹, with an average value of $\sigma_0 = 6.7$, the results of this

¹ http://swift.gsfc.nasa.gov/about_swift/bat_desc.html

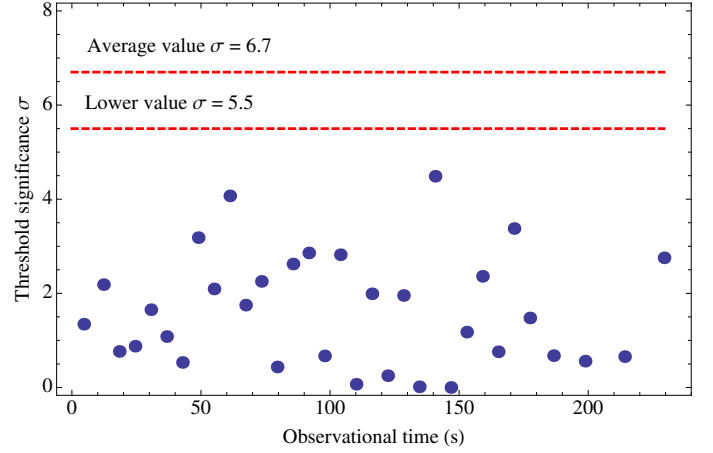


Fig. 5. Threshold significance σ_0 computed using the treatment of Band (2003) for any single time-resolved spectra of the first emission episode in GRB 090618, as if they were emitted at redshift 8.2. The dashed lines correspond to the values for the threshold significance of $\sigma_0 = 5.5$ and $\sigma_0 = 6.7$.

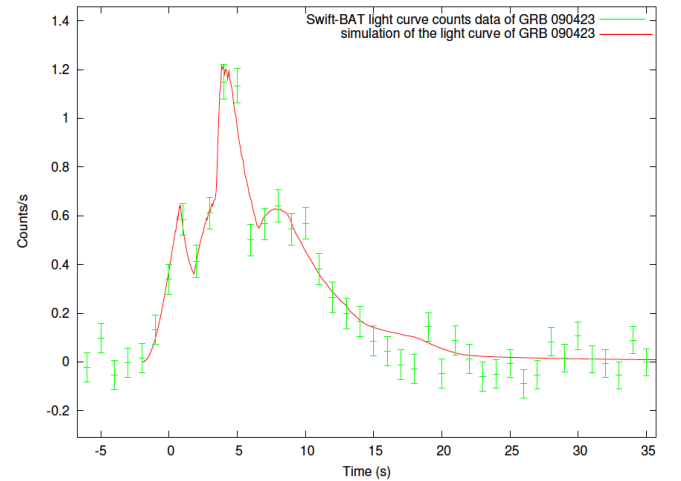


Fig. 6. *Swift*-BAT (15–150 keV) light curve emission of GRB 090423. The red line corresponds to the simulation of the GRB emission in the fireshell scenario (Izzo et al. 2010).

first analysis suggest that an Episode 1 similar to the one of GRB 090618 would not have been detected in GRB 090423 (see Fig. 5).

6. Detection of Episode 2 and its analysis

Episode 2 emission of GRB 090423, detected by *Swift*-BAT, was examined in the context of the fireshell scenario (Izzo et al. 2010; Ruffini 2011). A Lorentz Gamma factor of $\Gamma \sim 1100$ and a baryon load $B = 8 \times 10^{-4}$ were obtained. The simulations of the observed spikes in the observed time interval (0–440) s lead to homogeneous circumburst medium ($\mathcal{R} = 10^{-8}$, see Bianco & Ruffini 2005 for a complete description), and an average density of 10^{-1} particles cm^{-3} . The simulation of the GRB 090423 emission is shown in Fig. 6.

We can now compare and contrast the emission observed in GRB 090423, expressed at $z = 8.2$ (see Fig. 6, Izzo et al. 2010), and the portion of the emission of GRB 090618 if observed at $z = 8.2$, (see Fig. 7, Izzo et al. 2012a). In view of the *Swift*-BAT threshold, only the dashed region in Fig. 8, lasting 6 s, would be

Table 1. Results of the spectral fits of the T_{90} duration of GRB 090423 and of the $\Delta t_{A,obs}$ time interval for GRB 090618.

	α	β (keV)	$E_{p,i}$ (keV)	norm. (ph/cm ² /s/keV)	χ^2	Δt_{obs} (s)
090618	-0.66 ± 0.57	-1.99 ± 0.05	284.57 ± 172.10	0.3566 ± 0.16	0.924	6.1
090423	-0.78 ± 0.34	-3.5 ± 0.5	433.6 ± 133.5	0.015 ± 0.010	0.856	10.4

Notes. The latter is computed in a time interval corresponding to the one expected to be observed if GRB 090618 is transposed at the redshift $z = 8.2$, and in the observed energy range (89.6–896) keV.

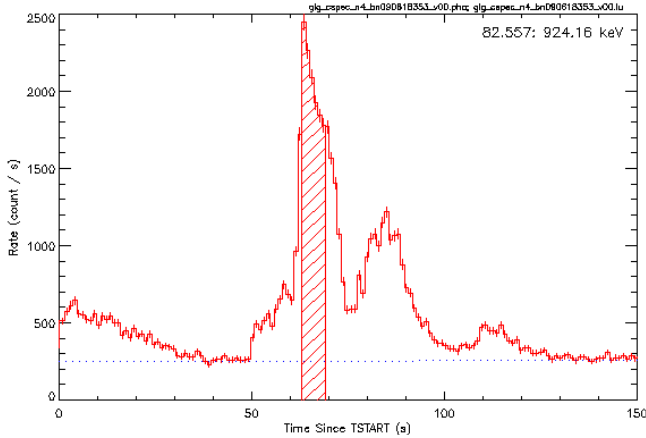


Fig. 7. Light curve of Episode 2 in GRB 090618, ranging from 50 to 150 s. The dashed region represents the portion which would have triggered the *Swift*-BAT if this GRB had been at the redshift $z = 8.2$. The observed duration of that interval is approximately $\Delta t \approx 6$ s. The results obtained in Fig. 6, when scaled to $z = 0.54$, provide $\Delta T \approx 3$ s.

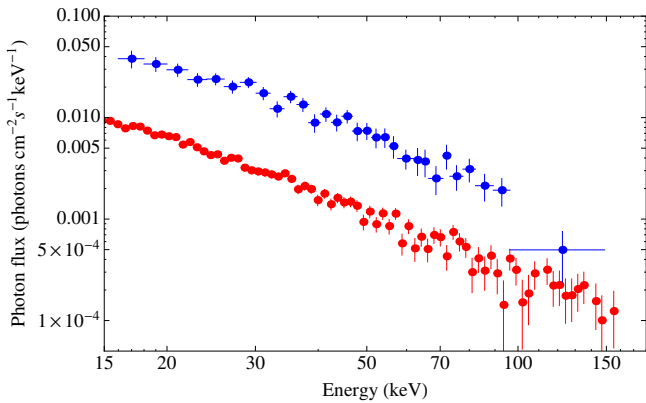


Fig. 8. Spectra of GRB 090423 (blue data) and of the spectrum of the emission of GRB 090618 (red data) considered as possible Episode 2 if GRB 090618 had been observed at $z = 8.2$. The low-energy photon index is ≈ -0.8 , which corresponds to the expectations from the Fireshell scenario (Ruffini 2011; Patricelli et al. 2012).

detectable. The observed flux in Fig. 6 and the one of the dashed region in Fig. 8 will be similar when compared in a common frame.

For the above considerations, the analysis presented in the previous section can be applied to Episode 2 of GRB 090618. Assuming a detector threshold for *Swift*-BAT of $\sigma_0 = 6.7$, see Eq. (2), only the dashed region in Fig. 7 is detectable when transposing GRB 090618 at $z = 8.2$. In the observer frame, this emission corresponds to the time interval ($T_{0,G} + 63.0$, $T_{0,G} + 69.1$) s, with $T_{0,G}$ the trigger time of Fermi GBM data

of GRB 090618. This time interval, at $z = 8.2$, has a duration $\Delta t_{A,obs} = \Delta t_{obs} \times 5.97 = 36.4$ s, owing to the time dilation by the cosmological redshift z (see Fig. 6). The remaining emission of GRB 090618 is unobservable, since below the threshold of the *Swift*-BAT detector. We note that $\Delta t_{A,obs}$ is quite comparable to the observed duration of GRB 090423 (see Fig. 6).

We turn now to comparing and contrasting the spectral energy distributions in the rest frame of the two GRBs. We consider the spectrum of GRB 090618 in the energy range (89.6–896) keV, which corresponds to the *Swift*-BAT band (15–150) keV in the rest frame of GRB 090423. As for the time interval in GRB 090423, we consider the observational time interval (63.0–69.1) s, determined from applying Eq. (2) to the entire Episode 2 of GRB 090618 (see the dashed region in Fig. 7). We fitted the spectral emission observed in GRB 090423 with a Band function (Band et al. 1993), and the results provide an intrinsic peak energy $E_{p,i} = (284.57 \pm 172.10)$ keV (see Table 1). The same model provides for the spectral emission of GRB 090423, in the T_{90} time duration, an intrinsic peak energy of $E_{p,i} = (433.6 \pm 133.5)$ keV. However, the break in GRB 090423 is steeper, while in GRB 090618 it is more shallow. This is clear in Fig. 8, where we show the spectra of both GRBs that are transformed to a common frame, which is the one at redshift $z = 8.2$. Very likely, the difference in the steepening at high energies is related to the structure of the circumburst medium (CBM): the more fragmented the CBM, the larger the cutoff energy of the fireshell spectrum (Bianco & Ruffini 2005). Another important result is that the low energy index α is quite similar in both GRBs. This agrees with the expectation from the fireshell scenario, where a photon index of ≈ -0.8 is expected in the early emission of a GRB (Patricelli et al. 2012).

The isotropic energy emitted in the time interval delineated by the dashed region in Fig. 7 has been computed to be $E_{iso} = 3.49 \times 10^{52}$ erg, which is very similar to the one computed for the T_{90} duration, in the same energy range, for GRB 090423, $E_{iso} = 4.99 \times 10^{52}$ erg.

7. Striking observations of Episode 3

That in long GRBs the X-ray emission, observed by *Swift*-XRT in energy range 0.3–10 keV, presents a typical structure composed of a steep decay, a plateau phase and a late power-law decay, was clearly expressed by Nousek, Zhang and their collaborators (Nousek et al. 2006; Zhang et al. 2006). This structure acquires a special meaning when examined in the most energetic sources, $E_{iso} = 10^{52}$ – 10^{54} erg, and leads to the fundamental proof that GRB 090423 is a BdHN source.

It has only been after applying the IGC paradigm to the most energetic long GRBs associated to SNe that we noticed the most unique characterizing property of the BdHN sources: while the steep decay and the plateau phase can be very different from source to source, the late X-ray power-law component overlaps,

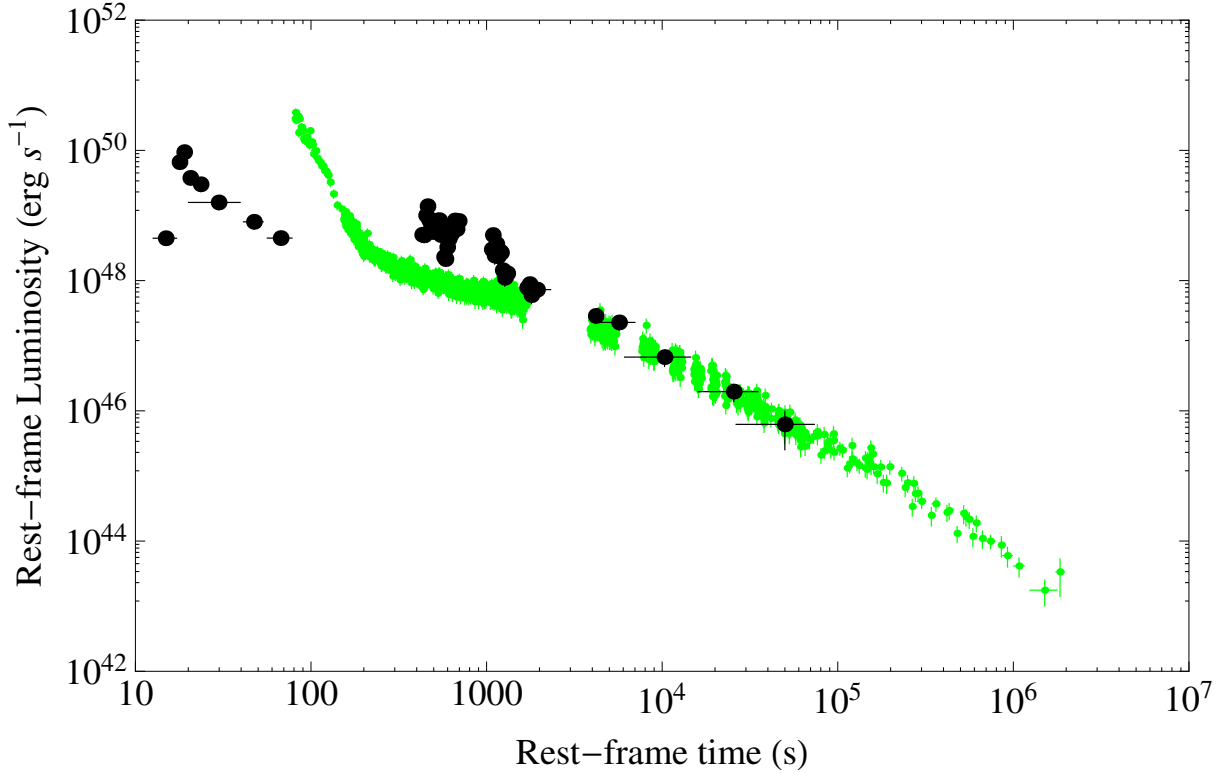


Fig. 9. Behavior of the Episode 3 luminosity of GRB 090423 (black dots) compared with the prototype case of GRB 090618 (green data).

when computed in the cosmological rest-frame (see [Pisani et al. 2013](#) and [Fig. 3](#)). This has become the crucial criterion for asserting membership of a GRB in the BdHN family. Indeed, when we report the late X-ray emission of Episode 3 in GRB 090423 at $z = 8.2$, and GRB 090618 at $z = 0.54$, we observe a complete overlapping at times longer than 10^4 s, see [Fig. 9](#).

7.1. Recent progress in understanding the nature of Episode 3

We recall:

- that the X-ray luminosity of Episode 3 in all BdHN sources presents precise scaling laws (see, e.g., [Fig. 3](#));
- that the very high energy emission all the way, up to 100 GeV, in GRB 130427A, as well as the optical one, follows a power-law behavior similar to the one in the X-ray emission described above. The corresponding spectral energy distribution is also described by a power-law function ([Kouveliotou et al. 2013](#); [Ruffini et al. 2014b](#)). These results clearly require a common origin for this emission process in Episode 3;
- that an X-ray thermal component has been observed in the early phases of Episode 3 of GRB 060202, 060218, 060418, 060729, 061007, 061121, 081007, 090424, 100316D, 100418A, 100621A, 101219B, and 120422A ([Page et al. 2011](#); [Starling et al. 2012](#); [Friis & Watson 2013](#)). In particular, this feature has been clearly observed in GRB 090618 and GRB 130427A ([Ruffini et al. 2014b](#)). This implies an emission region size of 10^{12-13} cm in these early phases of Episode 3, with an expansion velocity of $0.1 < v/c < 0.9$, with a bulk Lorentz Γ factor $\lesssim 2$ ([Ruffini et al. 2014a](#)).

The simultaneous occurrence of these three features imposes very stringent constraints on any possible theoretical models. In

particular, the traditional synchrotron ultra-relativistic scenario of the Collapsar jet model ([Woosley 1993](#); [Meszaros & Rees 2000](#)) does not appear suitable for explaining these observational facts.

In [Ruffini et al. \(2014a\)](#), we have recently pointed out the possibility of using the nuclear decay of ultra-heavy nuclei originally produced in the close binary phase of Episode 1 by r-process as an energy source of Episode 3. There is the remarkable coincidence that this set of processes leads to the value of the power-law emission with decay index α , similar to the one observed and reported in [Metzger et al. \(2010\)](#). The total energy emitted in the decay of these ultra-heavy elements agrees with the observations in Episode 3 of BdHN sources ([Ruffini et al. 2014a](#)). An additional possibility of process-generating a scale-invariant power law in the luminosity evolution and spectrum are the ones expected from type-I and type-II Fermi acceleration mechanisms ([Fermi 1949](#)). The application of these acceleration mechanisms to the BdHN remnant has two clear advantages: 1) for us, to fulfill the above-mentioned power laws, both for the luminosity and the spectrum; and 2) for Fermi, to solve the long-standing problem, formulated by Fermi in his classic paper, of identifying the injection source to make his acceleration mechanism operational on an astrophysical level.

8. Conclusions

The ansatz that GRB 090423 is the transposed of GRB 090618 at $z = 8.2$ has passed scrutiny. It is viable with respect to Episodes 1 and 4 and has obtained important positive results from the analysis of Episodes 2 and 3:

- Episodes 1 and 4 have not been detected in GRB 090423. This is consistent with the fact that the flux of Episodes 1 and 4 of GRB 090618 should not be observed by the

Swift-BAT detector or by the optical telescopes, owing to the very high redshift of the source and the current sensitivities of X-ray and optical detectors;

- Episode 2 of GRB 090423 has definitely been observed by *Swift*-BAT: its observed emission is comparable 1) to energy emitted (3.49×10^{52} erg for GRB 090618 and 4.99×10^{52} erg for GRB 090423); 2) to the observed time duration (34 s for the observable part of GRB 090618 when transposed to $z = 8.2$ and 19 s for GRB 090423); and 3) to the spectral energy distribution: the low energy part of the spectra of both GRBs is consistent with the expectation of the fireshell model (Patricelli et al. 2012). There is a significant difference only in the high energy part of the spectrum of GRB 090423, where a cutoff is observed at lower energy than the one in GRB 090618. This can be explained, in the fireshell scenario, by the existence of a dense and homogeneous CBM (Bianco & Ruffini 2005), which is expected for bursts at high redshifts;
- Episode 3 shows the striking feature of the overlapping of the late X-ray luminosities of Episode 3 in GRB 090618 and GRB 090423, when compared in their cosmological rest frames (see Fig. 9). This result confirms the extension of the relation presented in Pisani et al. (2013) for $z \leq 1$, all the way up to $z = 8.2$.

From an astrophysical point of view, all the above results clearly indicate that

- a) GRB 090423 is fully consistent with being a member of the BdHN family, and the associated SN did occur already at $z = 8.2$: the possibility of having an evolved binary system about 650 Myr after the Big Bang is not surprising, since the lifetime of massive stars with a mass up to $30 M_{\odot}$ is ~ 10 Myr (Woosley et al. 2002), which is similar to expectations from normal Population II binary stars also at $z = 8.2$, as pointed out by Belczynski et al. (2010);
- b) the FeCO core and the NS companion occurring at $z = 8.2$ also implies the existence, as the progenitor, of a massive binary $\sim 40\text{--}60 M_{\odot}^2$. Such massive binaries have recently been identified in η Carinae (Damineli et al. 2000). The very rapid evolution of such very massive stars will lead first to a binary X-ray source, like Cen-X3 (see, e.g., Gursky & Ruffini 1975) and Giacconi & Ruffini (1978), which will further evolve in the FeCO with the binary NS companion. A similar evolution starting from a progenitor of two very massive stars was considered by Fryer et al. (1999) and by Bethe & Brown (1998), leading to the formation of binary NSs or postulating the occurrence of GRBs. They significantly differ from the IGC model and also differ in their final outcomes;
- c) the results presented in this article open the way to considering the late X-ray power-law behavior in Episode 3 as a distance indicator and represents a significant step toward formulating a cosmological standard candle based on Episode 3 of these BdHN sources.

We turn now to fundamental issues in physics.

- 1) The traditional fireball jet model (Meszaros 2006) describes GRBs as a single phenomenon, originating in a collapsar (Woosley 1993) and characterized by jet emission moving at Lorentz Γ factor in the range $\approx 200\text{--}2000$. This contrasts with the BdHN model where the GRB is actually composed

of three different episodes that are conceptually very different among each other (see Fig. 1): Episode 1 is non-relativistic, and Episode 2 is ultra-relativistic with Lorentz Γ factor $\approx 200\text{--}2000$, Episode 3 is mildly relativistic, with $\Gamma \approx 2$.

- 2) The description of Episode 1, see Fig. 2, proposes the crucial role of the Bondi-Hoyle hypercritical accretion process of the SN ejecta onto the NS companion. This requires an urgent analysis of the neutrino emission pioneered in the classic papers of Zel'dovich et al. (1972); Chevalier (1993); Fryer et al. (1996), and (Fryer 2009).
- 3) The binary nature of the progenitors in the BdHN model and the presence of the specific scaling power laws in the luminosity in Episode 3 of GRB 090423, as well as in all the other sources of the “golden sample” (see Fig. 3; Pisani et al. 2013), has led us to consider the decay of heavy nuclear material originating in r -processes (Ruffini et al. 2014a), as well as type-I and type-II Fermi acceleration mechanism as possible energy sources of the mildly relativistic Episode 3 (Ruffini et al. 2014b).

Acknowledgements. We are very grateful to the referee for the very thoughtful considerations and advices which greatly improved the presentation of our manuscript. We thank David W. Arnett for fruitful discussions and support. We are also grateful to Elena Zaninoni and Gennaro De Tommaso for their comments on the manuscript. This work made use of data supplied by the UK *Swift* Science Data Centre at the University of Leicester. G.B.P., M.E., and M.K. are supported by the Erasmus Mundus Joint Doctorate Program by grant Nos. 2011-1640, 2012-1710, and 2013-1471, respectively, from the EACEA of the European Commission.

References

- Amati, L., Frontera, F., Tavani, M., et al. 2002, A&A, 390, 81
 Band, D. L. 2003, ApJ, 588, 945
 Band, D., Matteson, J., Ford, L., et al. 1993, ApJ, 413, 281
 Barthelmy, S. D., Barbier, L. M., Cummings, J. R., et al. 2005, Space Sci. Rev., 120, 143
 Belczynski, K., Holz, D. E., Fryer, C. L., et al. 2010, ApJ, 708, 117
 Bethe, H. A., & Brown, G. E. 1998, ApJ, 506, 780
 Bianco, C. L., & Ruffini, R. 2005, ApJ, 620, L23
 Bisnovatyi-Kogan, G. S., & Lamzin, S. A. 1984, Sov. Astron., 28, 187
 Bondi, H. 1952, MNRAS, 112, 195
 Bondi, H., & Hoyle, F. 1944, MNRAS, 104, 273
 Burrows, D., Hill, J., Nousek, J., et al. 2005, Space Sci. Rev., 120, 165
 Chevalier, R. A. 1989, ApJ, 346, 847
 Chevalier, R. A. 1993, ApJ, 411, L33
 Damineli, A., Kaufer, A., Wolf, B., et al. 2000, ApJ, 528, L101
 Enderli, M. 2013, 27th Texas Symp. on Relativistic Astrophysics, Dallas, TX (USA), December 8–13
 Fermi, E. 1949, Phys. Rev., 75, 1169
 Fermi-LAT collaboration, & Fermi-GBM collaboration. 2014, Science, 343, 42
 Friis, M., & Watson, D. 2013, ApJ, 771, 15
 Fryer, C. L. 2009, ApJ, 699, 409
 Fryer, C. L., Benz, W., & Herant, M. 1996, ApJ, 460, 801
 Fryer, C. L., Woosley, S. E., & Hartmann, D. H. 1999, ApJ, 526, 152
 Gehrels, N., Sarazin, C. L., O’Brien, P. T., et al. 2005, Nature, 437, 851
 Giacconi, R., & Ruffini, R. 1978, Physics and astrophysics of neutron stars and black holes (Amsterdam: North Holland Publishing)
 Gursky, H., & Ruffini, R. 1975, Neutron stars, black holes and binary X-ray sources; Proceedings of the Annual Meeting, San Francisco, Calif., February 28, 1974, (Dordrecht: D. Reidel Publishing), Astrophys. Space Sci. Lib. 48
 Izzo, L., Bernardini, M. G., Bianco, C. L., et al. 2010, JKPS, 57-3, 551
 Izzo, L., Rueda, J. A., & Ruffini, R. 2012a, A&A, 548, L5
 Izzo, L., Ruffini, R., Penacchioni, A. V., et al. 2012b, A&A, 543, A10
 Kann, D. A., Klose, S., Zhang, B., et al. 2011, ApJ, 734, 96
 Kouveliotou, C., Granot, J., Racusin, J. L., et al. 2013, ApJ, 779, L1
 Krimm, H. A., Beardmore, A. P., Evans, P. A., et al. 2009, GRB Coordinates Network, 9198, 1
 Margutti, R., Zaninoni, E., Bernardini, M. G., et al. 2013, MNRAS, 428, 729

² <http://nsm.utdallas.edu/texas2013/proceedings/3/1/Ruffini.pdf>

- Meegan, C., Lichti, G., Bhat, P. N., et al. 2009, *ApJ*, 702, 791
- Melandri, A., Pian, E., D'Elia, V., et al. 2014, *A&A*, 567, A29
- Meszáros, P. 2006, *Rep. Prog. Phys.*, 69, 2259
- Meszáros, P., & Rees, M. J. 2000, *ApJ*, 530, 292
- Metzger, B. D., Martínez-Pinedo, G., Darbha, S., et al. 2010, *MNRAS*, 406, 2650
- Nousek, J. A., Kouveliotou, C., Grupe, D., et al. 2006, *ApJ*, 642, 389
- Page, K. L., Starling, R. L. C., Fitzpatrick, G., et al. 2011, *MNRAS*, 416, 2078
- Patricelli, B., Bernardini, M. G., Bianco, C. L., et al. 2012, *ApJ*, 756, 16
- Penacchioni, A. V., Ruffini, R., Izzo, L., et al. 2012, *A&A*, 538, A58
- Penacchioni, A. V., Ruffini, R., Bianco, C. L., et al. 2013, *A&A*, 551, A133
- Pisani, G. B., Izzo, L., Ruffini, R., et al. 2013, *A&A*, 552, L5
- Rueda, J. A., & Ruffini, R. 2012, *ApJ*, 758, L7
- Ruffini, R. 2011, *Int. J. Mod. Phys. D*, 20, 1797
- Ruffini, R. 2013, 27th Texas Symposium on Relativistic Astrophysics, Dallas, TX (USA), December 8–13
- Ruffini, R., Izzo, L., Muccino, M., et al. 2013, [[arXiv:1311.7432](https://arxiv.org/abs/1311.7432)]
- Ruffini, R., Muccino, M., Bianco, C. L., et al. 2014a, *A&A*, 565, L10
- Ruffini, R., Wang, Y., Kovacevic, M., et al. 2014b, *ApJ*, submitted [[arXiv:1405.5723](https://arxiv.org/abs/1405.5723)]
- Salvaterra, R., Della Valle, M., Campana, S., et al. 2009, *Nature*, 461, 1258
- Salvaterra, R., Campana, S., Vergani, S. D., et al. 2012, *ApJ*, 749, 68
- Starling, R. L. C., Page, K. L., Pe'Er, A., Beardmore, A. P., & Osborne, J. P. 2012, *MNRAS*, 427, 2950
- Stratta, G., & Perri, M. 2009, *GRB Coordinates Network*, 9212, 1
- Tanvir, N. R., Fox, D. B., Levan, A. J., et al. 2009, *Nature*, 461, 1254
- von Kienlin, A. 2009a, *GRB Coordinates Network*, 9229, 1
- von Kienlin, A. 2009b, *GRB Coordinates Network*, 9251, 1
- Woosley, S. E. 1993, *ApJ*, 405, 273
- Woosley, S. E., Heger, A., & Weaver, T. A. 2002, *Rev. Mod. Phys.*, 74, 1015
- Zel'dovich, Y. B., Ivanova, L. N., & Nadezhin, D. K. 1972, *Sov. Astron.*, 16, 209
- Zhang, B., Fan, Y. Z., Dyks, J., et al. 2006, *ApJ*, 642, 354



On the black hole mass decomposition in nonlinear electrodynamics



Jonas P. Pereira^{a,b,d}, Herman J. Mosquera Cuesta^{a,e,c}, Jorge A. Rueda^{a,b,c,*}, R. Ruffini^{a,b,c,d}

^a ICRANet, Piazza della Repubblica 10, I-65122 Pescara, Italy

^b Dip. di Fisica and ICRA, Sapienza Università di Roma, P.le Aldo Moro 5, I-00185 Rome, Italy

^c ICRANet-Rio, Centro Brasileiro de Pesquisas Físicas, Rua Dr. Xavier Sigaud 150, Rio de Janeiro, RJ, 22290-180, Brazil

^d Université de Nice Sophia Antipolis, 28 Av. de Valrose, 06103 Nice Cedex 2, France

^e Instituto Federal de Educação, Ciência e Tecnologia do Ceará, Avenida Treze de Maio, 2081, Benfica, Fortaleza/CE, CEP 60040-531, Brazil

ARTICLE INFO

Article history:

Received 25 July 2013

Received in revised form 4 April 2014

Accepted 25 April 2014

Available online 30 April 2014

Editor: S. Dodelson

ABSTRACT

In the weak field limit of nonlinear Lagrangians for electrodynamics, i.e. theories in which the electric fields are much smaller than the scale (threshold) fields introduced by the nonlinearities, a generalization of the Christodoulou–Ruffini mass formula for charged black holes is presented. It proves that the black hole outer horizon never decreases. It is also demonstrated that reversible transformations are, indeed, fully equivalent to constant horizon solutions for nonlinear theories encompassing asymptotically flat black hole solutions. This result is used to decompose, in an analytical and alternative way, the total mass-energy of nonlinear charged black holes, circumventing the difficulties faced to obtain it via the standard differential approach. It is also proven that the known first law of black hole thermodynamics is the direct consequence of the mass decomposition for general black hole transformations. From all the above we finally show a most important corollary: for relevant astrophysical scenarios nonlinear electrodynamics decreases the extractable energy from a black hole with respect to the Einstein–Maxwell theory. Physical interpretations for these results are also discussed.

© 2014 The Authors. Published by Elsevier B.V. This is an open access article under the CC BY license (<http://creativecommons.org/licenses/by/3.0/>). Funded by SCOAP³.

1. Introduction

Black hole solutions to the Einstein equations have always attracted the attention of researchers, not only due to their unusual properties, but also from the discovery that they could be one of the most abundant sources of energy in the Universe.

From conservation laws, R. Penrose [1] showed how energy could be extracted from a black hole [2]. D. Christodoulou [3] and D. Christodoulou and R. Ruffini [4], through the study of test particles in Kerr and Kerr–Newman spacetimes [5], quantified the maximum amount of energy that can be extracted from a black hole. These works deserve some comments. First, this maximum amount of energy can be obtained only by means of the there introduced, *reversible processes*. Such processes are the only ones in which a black hole can be brought back to its initial state, after convenient interactions with test particles. Therefore, reversible transformations constitute the most efficient processes of energy extraction from a black hole. Furthermore, it was also introduced in Refs. [3,4] the concept of *irreducible mass*. This mass can never be diminished by any sort of processes and hence would constitute an intrinsic property of the system, namely the *fundamental*

energy state of a black hole. This is exactly the case of Schwarzschild black holes. From this irreducible mass, one can immediately verify that the area of a black hole never decreases after any infinitesimal transformation performed on it. Moreover, one can write down the total energy of a black hole in terms of this quantity [4].

Turning to effective nonlinear theories of electromagnetism, their conceptual asset is that they allow the insertion of desired effects such as quantum-mechanical, avoidance of singular solutions, and others e.g. via classical fields [6]. As a first approach, all of these theories are built up in terms of the two local invariants constructed out of the electromagnetic fields [7,8]. Notice that the field equations of nonlinear theories have the generic problem of not satisfying their hyperbolic conditions for all physical situations (see e.g. [9,10]). The aforementioned invariants are assumed to be functions of a four-vector potential in the same functional way as their classic counterparts, being therefore also gauge independent invariants. We quote for instance the Born–Infeld Lagrangian [11], conceived with the purpose of solving the problem of the infinite self-energy of an electron in the classic theory of electromagnetism. The Born–Infeld Lagrangian has gained a renewal of interest since the effective Lagrangian of string theory in its low energy limit has an analog form to it [12]. It has also been minimally coupled to general relativity, leading to an exact

* Corresponding author.

solution [13,14] and this coupling has been studied in a variety of problems [15–17]. Another worthwhile example of nonlinear electromagnetic theory is the Euler–Heisenberg Lagrangian [18, 19]. This Lagrangian allows one to take effectively into account one-loop corrections from the Maxwellian Lagrangian coming from Quantum Electrodynamics (QED), and it has been extensively studied in the literature [6]. Nonlinear theories of electromagnetism have also been investigated in the context of astrophysics. For instance, they could play an important role in the description of the motion of particles in the neighborhood of some astrophysical systems [20], as a simulacrum to dark energy and as a simulacrum of dark energy [21].

In connection with the above discussion, the thermodynamics of black holes [22] in the presence of nonlinear theories of electromagnetism has also been investigated. The zeroth and first laws (see Section 7) have been studied in detail [12,23], allowing the raise of other important issues. We quote for example the difficulty in generalizing the so-called Smarr mass [24,25] (a parametrization of the Christodoulou–Ruffini mass [4]) for nonlinear theories [12]. Many efforts have been pursued in this direction, through the suggestion of systematic ways to write down this mass, which has led to some inconsistencies (see e.g. Ref. [26]). For some specific nonlinear Lagrangians, this problem has been circumvented [27].

We first deal with static spherically symmetric electrovacuum solutions to the Einstein equations minimally coupled to Abelian nonlinear theories of electromagnetism, i.e. nonlinear charged black holes, for electric fields that are much smaller than the scale fields introduced by the nonlinearities, i.e. *weak field* nonlinear Lagrangians. We decompose the total mass-energy of a charged black hole in terms of its characteristic parameters: charge, irreducible mass, and nonlinear scale parameter. We also show the constancy of the black hole outer horizon in the case of reversible transformations. We then generalize the previous results for a generic nonlinear theory leading to an asymptotically flat black hole solution. As an immediate consequence of this general result, we show that the first law of black hole thermodynamics (or mechanics) in the context of nonlinear electrodynamics [12] is a by-product of this mass decomposition. These results also allow us to investigate the extraction of energy from charged black holes in the framework of nonlinear theories of electromagnetism.

The article is organized as follows. In Section 2 the notation is established and the field equations are stated and solved formally in the spherically symmetric case for nonlinear electromagnetic theories that lead to null fields at infinity. In Section 3, reversible transformations are investigated. In Section 4 the field equations are solved for the weak field limit of nonlinear theories of electromagnetism. Section 5 is devoted to the deduction of the total mass-energy of a charged black hole in terms of irreducible and extractable quantities, when reversible transformations are taken into account. In Section 6 variations of the outer horizon associated with the capture of test particles in nonlinear theories of electromagnetism are analyzed. In Section 7, we shall present the way to decompose the energy of a black hole within nonlinear theories of electromagnetism and show that it leads automatically to the first law of black hole mechanics. Finally, in Section 8 we discuss the results of this work. We use geometric units with $c = G = 1$, and metric signature -2 .

2. Field equations

The minimal coupling between gravity and nonlinear electrodynamics that depends only on the local invariant F can be stated mathematically through the action

$$S = \int d^4x \sqrt{-g} \left(-\frac{R}{16\pi} + \frac{L_{em}(F)}{4\pi} \right) \doteq S_g + \frac{S_{em}}{4\pi}, \quad (1)$$

where $F \doteq F^{\mu\nu}F_{\mu\nu}$, $F_{\mu\nu} = \nabla_\mu A_\nu - \nabla_\nu A_\mu = \partial_\mu A_\nu - \partial_\nu A_\mu$, A_μ is the electromagnetic four-potential, R is the Ricci scalar, S_g is the action for the gravitational field, S_{em} is the action of the electromagnetic theory under interest, and g the determinant of the metric $g_{\mu\nu}$ of the spacetime. Under the variation of Eq. (1) with respect to $g^{\mu\nu}$, and applying the principle of least action, one obtains (see e.g. Ref. [8])

$$R_{\mu\nu} - \frac{1}{2}Rg_{\mu\nu} = 8\pi T_{\mu\nu}^{(em)}, \quad (2)$$

with $R_{\mu\nu}$ the Ricci tensor and $T_{\mu\nu}^{(em)}$ the energy–momentum tensor of the electromagnetic field, defined as

$$4\pi T_{\mu\nu}^{(em)} \doteq \frac{2}{\sqrt{-g}} \frac{\delta S_{em}}{\delta g^{\mu\nu}} = 4L_F^{(em)} F_{\mu\alpha} F_{\nu\beta} g^{\alpha\beta} - L^{(em)} g_{\mu\nu}, \quad (3)$$

where $L_F^{(em)} \doteq \partial L^{(em)} / \partial F$.

Application of the principle of least action in Eq. (1) with respect to $A_\mu(x^\beta)$ gives

$$\nabla_\mu (L_F^{(em)} F^{\mu\nu}) = 0, \quad (4)$$

since we are interested in solutions to general relativity in the absence of sources.

In the static spherically symmetric case, it is possible to solve the Einstein equations minimally coupled to nonlinear electromagnetic theories [see Eqs. (2) and (4)] and due to the form of the energy–momentum tensor in this case the metric must be of the form

$$ds^2 = e^\nu dt^2 - e^{-\nu} dr^2 - r^2 d\theta^2 - r^2 \sin^2 \theta d\varphi^2, \quad (5)$$

with [8,23]

$$e^\nu = 1 - \frac{2M}{r} + \frac{8\pi}{r} \int_r^\infty r'^2 T_0^0(r') dr', \quad (6)$$

where the integration constant M stands for the total mass-energy of the black hole as measured by observers at infinity.

Eq. (4) in this special spherically symmetric case reduce to

$$L_F^{(em)} E_r r^2 = -\frac{Q}{4}, \quad (7)$$

where Q is an arbitrary constant representing physically the total charge of the black hole.

If one defines

$$E_r \doteq -\frac{\partial A_0}{\partial r} \quad \text{and} \quad \frac{\partial \mathcal{F}}{\partial r} \doteq -L^{(em)} r^2, \quad (8)$$

and take into account Eqs. (4), (5) and (7), then Eq. (6) can be rewritten as

$$e^\nu = 1 - \frac{2M}{r} + \frac{2Q A_0}{r} - \frac{2\mathcal{F}}{r}, \quad (9)$$

where it has been imposed a gauge such that the scalar potential A_0 goes to zero when the radial coordinate goes to infinity, which also holds to \mathcal{F} . These conditions guarantee that the associated nonlinear black holes are asymptotically flat (Minkowskian). In this work we are not interested in Lagrangian densities which do not fulfill this condition.

The black hole horizons are given by the solutions to

$$g_{00}(r_h) = e^{\nu(r_h)} = 0. \quad (10)$$

3. Reversible and irreversible transformations

A way to investigate the motion of test particles in a static spherically symmetric spacetime is through the solution to the Hamilton–Jacobi equation. The trajectories of the test particles can be obtained in the traditional way (see e.g. Ref. [28]) through the particle constants of motion (energy E , orbital angular momentum L , and the Carter constant) [5,29]. The energy of the test particle is given by [3–5,29]

$$E = qA_0 + \sqrt{\frac{e^v}{r^2} \left[r^4 (p^\theta)^2 + \frac{L^2}{\sin^2 \theta} + m^2 r^2 \right]} + (p^r)^2, \quad (11)$$

where $p^\mu \doteq dx^\mu/d\tau$, τ an affine parameter along the worldline of the particle and q its charge. The “+” sign has been chosen in Eq. (11), because we are interested just in particles traveling to the future [29,30].

If the worldline of an arbitrary test particle intersects the outer horizon, i.e. the largest solution to Eq. (10), then the changes in the energy and charge of the black hole (which lead to another black hole configuration infinitesimally close to the initial one) reads: $\delta M = E$ and $\delta Q = q$ [29], respectively.

From Eq. (11), one can see that the only way to apply a reversible transformation in the sense of Christodoulou–Ruffini [3,4,6] to a black hole interacting with a test particle is by demanding that its square root term is null. It guarantees that a nonlinear black hole can always be restored to its initial configuration, as demanded by reversible transformations, see Section 1, after a test particle has crossed the horizon. Hence, from Eq. (11) and the aforementioned conservation laws, reversible transformations select geodesics whose changes to the black hole masses are minima and are given by

$$\delta M_{min} = qA_0(r_+) = \delta Q A_0(r_+). \quad (12)$$

Clearly, Eq. (12) is the mathematical expression for the physical case where $|p^r(r_+)|$ is much smaller than $|qA_0(r_+)|$, that is, when irreversible processes are negligible. Reversible transformations are important processes since like the internal energy of a thermodynamical system, the energy M of a black hole is assumed to be an exact differential. This therefore allows one to describe intrinsic properties of the spacetime by using test particles; see Eq. (12).

For the sake of completeness, in the case of general black hole transformations one has

$$\delta M \geq qA_0(r_+). \quad (13)$$

4. Weak field nonlinear Lagrangians

An interesting and convenient limit for investigating nonlinear properties of Lagrangians is when their electric fields are small compared to their scale or threshold fields, set defined off by the nonlinearities [21]. In this limit, one expects that their leading term be the Maxwell Lagrangian [23]. In this line, assuming the nonexistence of magnetic charges, let us first investigate Lagrangian densities given by

$$L^{(em)} = -\frac{F}{4} + \frac{\mu}{4} F^2, \quad (14)$$

where μ is related to the scale field of the theory under interest, and as a necessary condition to avoid any violation of the most experimentally tested physical theory, the Maxwell theory, this nonlinear term is assumed such that it must be much smaller than the Maxwell one. This means we are generically interested in electric fields that satisfy

$$E_r \ll \frac{1}{\sqrt{\mu}}. \quad (15)$$

Physically speaking, the second term of Eq. (14) is a first order correction to the Maxwell theory. For instance, in the case of the Euler–Heisenberg Lagrangian, the nonlinearities are related to quantum corrections, whose scale field is $E_c = m_e^2 c^3 / (e\hbar) \approx 10^{18}$ V/m, where m_e is the electron rest-mass, e is the fundamental charge, and \hbar is the reduced Planck constant (see e.g. [6], and references therein). Hence, in virtue of this limit a perturbative analysis could be carried out. The sign of μ in principle could be arbitrary. Nevertheless, from the inspection of the Euler–Heisenberg Lagrangian, for instance, this constant turns out to be positive [19]. The same behavior happens if one expands perturbatively the Born–Infeld Lagrangian [6,11–15,21]. It is worth to stress that the weak field analysis is however not very restrictive in terms of the strength of the fields. Note for instance that for the Euler–Heisenberg and Born–Infeld theories, our analysis is indeed meaningful for electric fields $E_r \sim 10^{18}$ V/m (see Section 8).

When one interprets nonlinear Lagrangians as the ones related to effective media [11], then one expects that their associated electric field solutions should be reduced. This constrains the sign of μ , as we shall show below. Nevertheless, it is not ruled out in principle Lagrangians where the associated electric field could increase.

By substituting Eq. (14) into Eq. (7) and the first term of Eq. (8), solving exactly and then expanding perturbatively (or by directly working perturbatively), one can easily show that

$$E_r(r) = \frac{Q}{r^2} \left(1 - \frac{4\mu Q^2}{r^4} \right), \quad A_0(r) = \frac{Q}{r} \left(1 - \frac{4\mu Q^2}{5r^4} \right). \quad (16)$$

Expressions (16) are just meaningful if the characteristic distances of the system are such that

$$r \gg r_c, \quad r_c^4 = |\mu| M^2 \xi^2, \quad \xi \doteq \frac{Q}{M}. \quad (17)$$

As we pointed out before, when $\mu > 0$, the modulus of the electric field diminishes in comparison to the pure Maxwellian case, while the opposite happens when $\mu < 0$. The former case is exactly what happens in usual media [31], while the latter could happen in the so-called metamaterials (see e.g. Refs. [32,33]).

From Eq. (14), the second term of Eq. (8) and Eq. (16), and assuming that the constraint in Eq. (17) is fulfilled, it is also readily shown that

$$\mathcal{F} = \frac{Q^2}{2r} \left(1 - \frac{6\mu Q^2}{5r^4} \right). \quad (18)$$

When Eqs. (16) and (18) are substituted in the expression for the g_{00} component of the metric, Eq. (9), one obtains

$$e^v = 1 - \frac{2M}{r} + \frac{Q^2}{r^2} - \frac{2\mu Q^4}{5r^6}. \quad (19)$$

The above result agrees with the one obtained in Ref. [34], for the Euler–Heisenberg Lagrangian density, in the corresponding units. Notice that when $\mu = 0$, i.e., for the Maxwell Lagrangian [see Eq. (14)], Eq. (19) gives the well-known Reissner–Nordström solution (see e.g. Ref. [29]).

The outer horizon can be found perturbatively from Eqs. (10) and (19) and the result is

$$r_+ = \mathcal{R}_+ \left(1 + \frac{\mu Q^4}{5(\mathcal{R}_+)^5 \sqrt{M^2 - Q^2}} \right), \quad (20)$$

where we defined

$$\mathcal{R}_+ \doteq M + \sqrt{M^2 - Q^2}, \quad (21)$$

functionally the same as the outer horizon in the Reissner–Nordström solution. Besides, in Eq. (20), it was understood that the second term in the parenthesis is much smaller than one. These latter equations are not valid in the case $Q = M$, and up to what extent the above perturbative analysis is meaningful in the proximity of this limit is dictated by the value μ/M^2 . Namely, the smaller the μ/M^2 , the closer one can approach $Q = M$ using perturbative theory. For the sake of reference, in Euler–Heisenberg and standard Born–Infeld theories, $\mu \sim 10^{-33} \text{ (e.s.u.)}^{-2}$ [6,11], hence for objects of masses around $M \sim 10^5 M_\odot$, μ/M^2 when brought to geometrical units ($\mu [\text{cm}^2] = \mu [(\text{e.s.u.})^{-2}]c^4/G$ and $M [\text{cm}] = M [\text{g}]G/c^2$), would be approximately 10^{-4} . In this specific example, the limit $Q = M$ can be therefore approached with a precision of up to four decimals within the perturbative analysis presented here.

For the classic extreme value $Q = M$, the perturbative solution to the outer horizon is

$$r_+^{Q=M} = M \left\{ 1 + \sqrt{\frac{2\mu}{5M^2}} - \frac{4\mu}{5M^2} + \mathcal{O}\left[\left(\frac{\mu}{M^2}\right)^{\frac{3}{2}}\right] \right\}, \quad (22)$$

and there exist inner horizons given by

$$r_-^{Q=M} = M \left\{ 1 - \sqrt{\frac{2\mu}{5M^2}} - \frac{4\mu}{5M^2} + \mathcal{O}\left[\left(\frac{\mu}{M^2}\right)^{\frac{3}{2}}\right] \right\} \quad (23)$$

$$r_{ncl}^{Q=M} = M \left\{ \left(\frac{2\mu}{5M^2}\right)^{\frac{1}{4}} + \left(\frac{\mu}{10M^2}\right)^{\frac{1}{2}} + \mathcal{O}\left[\left(\frac{\mu}{M^2}\right)^{\frac{3}{4}}\right] \right\}, \quad (24)$$

where $r_-^{Q=M}$ in Eq. (23) is the nonlinear version of the inner horizon in Reissner–Nordström solution, and the solution given by Eq. (24) has no classical (ncl) counterpart, being intrinsically due to corrections to the Maxwell theory, e.g. quantum. Notice that when $\mu \neq 0$ the inner and outer horizons are never equal in an arbitrary nonlinear theory given by Eq. (14) in the case $Q = M$. Hence, as we expect, when corrections are added to Maxwell theory, the degeneracy in the case $Q = M$, is broken. Nevertheless, due to the continuity of the metric, there always exists a value of $|\xi|$ where the horizons degenerate, depending now on μ/M^2 . We stress that Eq. (24) is just a mathematical solution to Eqs. (19) and (10), being physically meaningless, as the following analysis shows. Assume that the charge of the black hole is comparable with its mass (minimum value for being relevant the *nonclassical horizon*), that is $Q^2 \sim M^2$. From Eq. (24), however, one has $r_{ncl}^{Q=M} \sim (\mu M^2)^{1/4} = r_c$. Since just distances much larger than r_c are physically meaningful in the realm of our perturbative calculations; see Eq. (17), it is proved that $r_{ncl}^{Q=M}$ is not physically relevant. The above reasoning implies that perturbative changes in the Maxwell Lagrangian just lead to corrections in the Reissner–Nordström horizons. This means that naked singularities still rise in such theories, but now for values of $|\xi|$ slightly larger or smaller than one, depending upon the sign and absolute value of μ/M^2 .

5. The weak field black hole mass decomposition

Assume a test particle being captured by a black hole under a reversible transformation. In mathematical terms, this means that the equality in Eq. (13) is to be taken into account and the changes can be considered as infinitesimals. By taking into account the second term in Eq. (16) and Eq. (20), one ends up to first order approximation with

$$\frac{dM}{dQ} = \frac{Q}{\mathcal{R}_+} - \frac{\mu Q^3}{5(\mathcal{R}_+)^5} \left[\frac{Q^2}{\mathcal{R}_+ \sqrt{M^2 - Q^2}} + 4 \right]. \quad (25)$$

Since we are supposing that the second term of the above equation is much smaller than the first one, the method of successive approximations can be used. We shall suppose that

$$M(Q) = M^{(0)}(Q) + \mu M^{(1)}(Q), \quad (26)$$

where the second term of the above expression is thought of as a perturbation. At the zeroth order approximation, $M^{(0)}$ satisfies the differential equation

$$\frac{dM^{(0)}}{dQ} = \frac{Q}{M^{(0)} + \sqrt{(M^{(0)})^2 - Q^2}}. \quad (27)$$

As it is known, the solution to the above equation is [4]

$$M^{(0)}(Q) = M_{irr} + \frac{Q^2}{4M_{irr}}, \quad (28)$$

where M_{irr} is a constant of integration known as the irreducible mass and it accounts for the total energy of the system when the charge of the black hole is zero. Expression (28) is the Christodoulou–Ruffini black hole mass formula valid for a classical spherically symmetric charged black hole. By substituting this expression into Eq. (21) one obtains $\mathcal{R}_+ = 2M_{irr}$ and then it follows that $Q^2/(2\mathcal{R}_+) \leq M/2$, where the equality is valid in the case $Q = M$. Hence, up to 50% of the total mass of a black hole is due to the electromagnetic energy contribution $Q^2/(4M_{irr})$.

Substituting Eq. (26) into Eq. (25) and working now up to first order approximation, using Eqs. (27) and (28) we have

$$\begin{aligned} \frac{dM^{(1)}}{dQ} = & -\frac{Q}{2M_{irr}[M_{irr} - Q^2/(4M_{irr})]} \left[M^{(1)} + \frac{Q^4}{160M_{irr}^5} \right] \\ & - \frac{Q^3}{40M_{irr}^5} \end{aligned} \quad (29)$$

from which we obtain

$$M^{(1)}(Q) = -\frac{Q^4}{160M_{irr}^5}. \quad (30)$$

The above equation is obtained by imposing $M^{(1)}(0) = 0$, which is physically clear from our previous considerations. Since energy could be extracted from black holes only when it is charged [see Eq. (13)], the extractable energy, M_{ext} , or the *blackholic energy* [6], in weak fields nonlinear theories of electromagnetism given by Eq. (14) is

$$M_{ext}(Q) = \frac{Q^2}{4M_{irr}} - \frac{\mu Q^4}{160M_{irr}^5}. \quad (31)$$

As it can be checked easily, the above equation is exactly the electromagnetic energy $E^{(em)}$ [35,36] stored in the electric field in the spacetime given by Eq. (19) viz.,

$$E^{(em)} = 4\pi \int_{r_+}^{\infty} T_0^0 r^2 dr = \int_{r_+}^{\infty} \int_{2\pi}^0 \int_{\pi}^0 T_0^0 \sqrt{g} d\theta d\varphi dr, \quad (32)$$

where g is the determinant of the metric, that in Schwarzschild coordinates is given by $r^2 \sin^2 \theta$; see Eq. (5). Notice that even in the case where corrections to the Maxwell Lagrangian are present (e.g. quantum), $r_+ = 2M_{irr}$, as is clear from Eqs. (20), (21), (26), (28) and (30).

From Eq. (31), one clearly sees that the total amount energy that can be extracted from a nonlinear charged black hole is reduced if $\mu > 0$, in relation to the Maxwell counterpart. The positiveness of μ is valid both to the Euler–Heisenberg effective

nonlinear Lagrangian to one-loop QED as well as to the standard Born–Infeld Lagrangian, as we pointed out earlier. Hence, in these theories, the extractable energy is always smaller than 50% of the total energy. More precisely, from Eqs. (20), (21), (26), (28) and (30),

$$M_{ext} \leq \frac{M}{2} - \frac{\mu Q^4}{320M_{irr}^4 \sqrt{M^2 - Q^2}}, \quad (33)$$

the equality in this case being true only when $\mu = 0$.

6. Transformations in the outer horizon

Under the capture of a test particle of energy E and charge q , one has that the black hole undergoes the (infinitesimal) given changes $\delta M = E$ and $\delta Q = q$, satisfying Eq. (13). Since the outer horizon of this black hole is dependent upon M and Q , it would also undergo a change. Such a change can be obtained in the scope of the perturbative description we are carrying out and the basic equation for doing so is Eq. (20).

By using Eqs. (20), (21), (13) and the second term of Eq. (16), one can easily show that

$$\delta r_+ \geq -\frac{\mu Q^4 \delta \mathcal{R}_+}{5(\mathcal{R}_+)^5 (M^2 - Q^2)} [\mathcal{R}_+ + 3\sqrt{M^2 - Q^2}]. \quad (34)$$

As it can be seen from Eqs. (21), (26), (28) and (30), $\delta \mathcal{R}_+ \sim \mathcal{O}(\mu)$, then, up to first order in μ , we have $\delta r_+ \geq 0$. This result can be easily understood if one notices that up to first order approximation in μ , based on the two last sections, $r_+ = 2M_{irr}$. Under irreversible transformations, however, Eq. (34) shows that the outer horizon increases. Notice that the above results are just valid for $Q/M < 1$.

Another way of realizing whether or not there is an increase of the outer horizon due to the capture of a test particle is to search for the solutions to Eqs. (10) and (19) when one performs the changes $M \rightarrow M + \delta M$ and $Q \rightarrow Q + \delta Q$, satisfying Eq. (13). If one defines generally r_+ as the largest solution to Eqs. (10) and (19), then it is simple to verify that $\delta r_+ = 0$ for reversible transformations. For irreversible transformations, $\delta r_+ > 0$. Hence, generically, one has $\delta r_+ \geq 0$ for an arbitrary infinitesimal transformation undergone by the black hole in nonlinear weak field electromagnetism.

7. Energy decomposition for asymptotically flat nonlinear black holes

Weak field nonlinear Lagrangians suggest that the outer horizon of spherically symmetric $L(F)$ theories are $r_+ = 2M_{irr}$ when reversible transformations are considered, for any range of the electric field, and not only for the one where $E_r \ll 1/\sqrt{\mu}$. Now we shall show that indeed this is the case. This means that it is possible to obtain the total mass-energy of spherically symmetric, asymptotically flat, nonlinear black holes in an algebraic way, overcoming the problems in solving differential equations coming from the thermodynamical approach. Also, it gives us the extractable energy from nonlinear black holes.

Assume that the invariant $F = -2E_r^2$ is such that $F = F(r, Q)$. From Eqs. (7)–(9), it follows that

$$Q \frac{\partial A_0}{\partial Q} = \frac{\partial \mathcal{F}}{\partial Q}. \quad (35)$$

Assume now that $r_+ = C = \text{constant}$, that is, the outer horizon is an intrinsic property of the system. From Eqs. (10) and (35), one shows immediately that

$$\delta M = \delta Q A_0|_{r_+=C}. \quad (36)$$

It can be checked that the above equation is valid only when $r_+ = C$. We recall that we assumed Eq. (36) as the law for reversible transformations (energy conservation). Thereby, we showed that reversible transformations are fully equivalent to having constant horizons in spherically symmetric black hole solutions to general relativity. Since Eq. (36) is valid for any stage of the sequence of reversible transformations for any theory satisfying the conditions mentioned before, it is even so when $Q = 0$ and hence, $C = 2M_{irr}$. So, horizons for reversible transformations are dependent just upon the fundamental energy states black holes, $2M_{irr}$. Even more remarkable is that we already know the solution to Eq. (36), which from Eqs. (6), (10) and (9) is

$$\begin{aligned} M &= M_{irr} + Q A_0|_{r=2M_{irr}} - \mathcal{F}|_{r=2M_{irr}} \\ &= M_{irr} + 4\pi \int_{2M_{irr}}^{\infty} r'^2 T_0^0(r') dr'. \end{aligned} \quad (37)$$

The above equation is the generalization of the Christodoulou–Ruffini black hole mass decomposition formula to $L(F)$ theories that do not depend upon M . If this is not the case, one then have an algebraic equation to solve. The extractable energy $M - M_{irr}$ from $L(F)$ can be read off immediately from Eq. (37) and as we expect, it is the same as Eq. (32); it can also be checked that Eq. (37) is in total agreement with the results for the weak field Lagrangians in terms of the differential approach.

It is worth to notice that Eq. (37) could be also obtained from Eq. (30) of Ref. [23], by replacing there the relation $r_h = 2M_{irr}$. However, following the purely mathematical approach in [23], this latter assumption does not find a clear physical justification. Our approach in this work is completely different from [23]: it is based on physical requirements of energy and charge conservation laws and reversible transformations. As a consequence of these physical requirements, we actually showed that the horizon is indeed a constant of integration, hence an independent quantity.

Since in the present case the horizon area is $A = 4\pi r_+^2$, Eq. (37) can as well be written in terms of it. As we showed above, for reversible transformations the outer horizon must be kept constant and the mass change must be given by Eq. (36). Nevertheless, intuitively, one would expect the total mass of a given black hole to have a definite meaning. In this sense, Eq. (37) in terms of the black hole area should be the expression for the mass even in the case A changes. Such a general statement is reinforced by the fact that it is true for black holes described by the Maxwell Lagrangian.¹ As we show now, this is precisely the case also in nonlinear electrodynamics. Initially we recall that the surface gravity [22] in spherically symmetric solutions in the form [37]

$$\kappa = \frac{(e^\nu)'|_{r_+}}{2} \quad (38)$$

where the prime means differentiation with respect to the radial coordinate and from Eqs. (9) and (10) the above equation can be cast as

$$\kappa = \frac{1}{2r_+} \left[1 + 2Q \frac{\partial A_0}{\partial r_+} - 2 \frac{\partial \mathcal{F}}{\partial r_+} \right]. \quad (39)$$

From Eqs. (10) and (35), one can see in the general case that

$$\delta M = A_0 \delta Q + \frac{\kappa}{8\pi} \delta A, \quad (40)$$

¹ This can be seen in Refs. [24,25] when one works with its final mass expression, M , and check it is exactly the same as Eq. (2) of Ref. [4] in the context of reversible transformations.

where Eq. (39) was used. Nevertheless, this is nothing but the generalized first law of black hole mechanics for nonlinear electrodynamics [12]. Since M as given in Eq. (37) was derived from Eqs. (10) and (35), it is assured its variation satisfies Eq. (40). Hence, it is the generalization under the physical approach of the parametrization done by Smarr [24,25] for the classical Christodoulou–Ruffini black hole mass formula in the context of nonlinear electrodynamics. We would like to stress that all the previous reasoning is a direct consequence of having M as an exact differential. Besides, Eq. (37) can be written in the suggestive way as

$$M = Q A_0(r_+) + \frac{A}{8\pi r_+} \left[1 - 2 \frac{\mathcal{F}(r_+)}{r_+} \right]. \quad (41)$$

From Eq. (39), we see that in general the term in the square brackets of the above equation does not coincide with $2\kappa r_+$. This could be easily seen in the scope of weak field nonlinear theories described by Eq. (14) analyzed previously. Nevertheless, for the case of the Maxwell Lagrangian, the term inside the square brackets of Eq. (41) is exactly $2\kappa r_+$. It implies that the generalized Christodoulou–Ruffini black hole mass formula does not keep the same functional form in nonlinear electrodynamics as in the classic Maxwellian case.

8. Discussion

As we have shown above, in the weak field limit of nonlinear Lagrangians, a generalization of the Christodoulou–Ruffini black hole mass decomposition formula can always be obtained; see Eqs. (26), (28) and (30).

Indeed, the weak field limit of nonlinear theories of electromagnetism lead to the constancy of the outer horizon when reversible transformations are taken into account ($2M_{irr}$, exactly as the horizon in the Schwarzschild theory). For irreversible transformations, it always increases. We have also shown that these results actually are valid for any nonlinear asymptotically flat black hole, once it is the only way to lead to the equation coming from the laws of energy and charge conservation for reversible transformations; see the equality in Eq. (13). As a by-product, it allowed us to write down the total mass and the extractable energy (upper limit) of nonlinear spherically symmetric black holes in terms of their charge, outer horizon areas and the scale parameters coming from the electrodynamic theory under interest. When irreversible transformations are present, for each transformation, $\delta r_+ > 0$ iff $(1 - 8\pi T_0^0|_{r_+, r_+^2}) > 0$, as it can be seen from Eq. (6). From the same equation, it can be checked that this is always valid when there exists an outer horizon. Hence, for $L(F)$, the areas of the outer horizons never decrease for irreversible processes. With this generalized Christodoulou–Ruffini black hole mass formula, one can notice that the known first law of black hole mechanics [12] is just its direct consequence and hence one could say that it defines such a law. In general such a mass is not functionally the same as the one obtained in the case of the classic Maxwell electrodynamics. If the entropy of a black hole is proportional to its horizon area, the approach of reversible and irreversible transformations lead to the conclusion it can never decrease even in the context of nonlinear electrodynamics.

Turning to astrophysics, it is important to discuss the specific sign of the nonlinear correction parameter, μ . Its positiveness is indeed in agreement with very well-founded nonlinear Lagrangians, such as the Euler–Heisenberg and the Born–Infeld Lagrangians. We have shown that $\mu > 0$ implies that the extractable energy of a black hole described by weak field nonlinear Lagrangian is always smaller than the one associated with the Maxwell Lagrangian; see Eqs. (31) and (33). Hence, due to a continuity argument, we are

led to a most important corollary of this work: nonlinear theories of the electromagnetism reduce the amount of extractable energy from a black hole with respect to the classical Einstein–Maxwell case. It means that the extractable energy from nonlinear black holes are always smaller than half of their total mass, which is the largest amount of extractable energy obtained from the Christodoulou–Ruffini black hole mass formula. This result might, in principle, be relevant in the context of gamma-ray bursts (see e.g. [38] and references therein) since their energy budget, as shown by Damour & Ruffini [39], comes from the electromagnetic energy of the black hole extractable by the electron–positron pair creation process à la Sauter–Heisenberg–Euler–Schwinger. However, it is important to keep in mind that for quantitative estimates the perturbative analysis presented in this work is valid only if the condition (15) is satisfied. In the case of the Euler–Heisenberg Lagrangian ($1/\sqrt{\mu} \approx 200E_c$) and for a black hole mass $M \sim 3M_\odot$, as expected from the gravitational collapse of a neutron star to a black hole, $\mu/M^2 \approx 8.2 \times 10^5$, so for a charge to mass ratio $\xi = 5 \times 10^{-4}$ (at the outer horizon $r = r_+$, $E_r/E_c \approx 21$), the reduction of the extractable energy is of only 0.5% with respect to the Maxwell case. For supermassive black holes in active galactic nuclei, e.g. $M \sim 10^9 M_\odot$ ($\mu/M^2 \approx 7.4 \times 10^{-12}$), we obtain for $\xi = 0.9999$ (at r_+ , $E_r/E_c \approx 5 \times 10^{-4}$) an extractable energy reduced only by $10^{-8}\%$ with respect to the Maxwell case.

Acknowledgements

J.P.P. acknowledges the support given by the International Relativistic Astrophysics PhD Program through the Erasmus Mundus Grant 2011–1640 from EACEA of the European Commission. H.J.M.C. acknowledges the ICRANet Coordinating Headquarters in Pescara, Italy, for hospitality, and the support by the International Cooperation Program CAPES-ICRANet through the Sabbatical Grant 0153-14-1, financed by CAPES – Brazilian Federal Agency for Support and Evaluation of Graduate Education within the Ministry of Education of Brazil. We thank the anonymous referee for the comments and suggestions which helped us to improved the presentation of the results of this research.

References

- [1] R. Penrose, Gravitational collapse: the role of general relativity, *Nuovo Cimento Rivista Ser. 1* (1969) 252.
- [2] R. Ruffini, The ergosphere and dyadosphere of black holes, in: D.L. Wiltshire, M. Visser, S. Scott (Eds.), *The Kerr Spacetime*, Cambridge University Press, 2009.
- [3] D. Christodoulou, Reversible and irreversible transformations in black-hole physics, *Phys. Rev. Lett.* 25 (1970) 1596–1597, <http://dx.doi.org/10.1103/PhysRevLett.25.1596>.
- [4] D. Christodoulou, R. Ruffini, Reversible transformations of a charged black hole, *Phys. Rev. D* 4 (1971) 3552–3555, <http://dx.doi.org/10.1103/PhysRevD.4.3552>.
- [5] B. Carter, Global structure of the Kerr family of gravitational fields, *Phys. Rev.* 174 (1968) 1559–1571, <http://dx.doi.org/10.1103/PhysRev.174.1559>.
- [6] R. Ruffini, G. Vereshchagin, S. Xue, Electron–positron pairs in physics and astrophysics: from heavy nuclei to black holes, *Phys. Rep.* 487 (2010) 1–140, <http://dx.doi.org/10.1016/j.physrep.2009.10.004>, arXiv:0910.0974.
- [7] W. Dittrich, H. Gies, Light propagation in nontrivial QED vacua, *Phys. Rev. D* 58 (2) (1998), <http://dx.doi.org/10.1103/PhysRevD.58.025004>, 025004, arXiv:hep-ph/9804375.
- [8] L.D. Landau, E.M. Lifshitz, *The Classical Theory of Fields*, 1975.
- [9] G. Esposito-Farèse, C. Pitrou, J.-P. Uzan, Vector theories in cosmology, *Phys. Rev. D* 81 (6) (2010), <http://dx.doi.org/10.1103/PhysRevD.81.063519>, 063519, arXiv:0912.0481.
- [10] A. Golovnev, A. Klementev, On hyperbolicity violations in cosmological models with vector fields, *J. Cosmol. Astropart. Phys.* 2 (2014) 33, <http://dx.doi.org/10.1088/1475-7516/2014/02/033>, arXiv:1311.0601.
- [11] M. Born, L. Infeld, Foundations of the new field theory, *Proc. R. Soc. Lond. Ser. A, Math. Phys. Sci.* 144 (1934) 425–451, <http://dx.doi.org/10.1098/rspa.1934.0059>.
- [12] D.A. Rasheed, Non-linear electrodynamics: zeroth and first laws of black hole mechanics, *ArXiv High Energy Physics - Theory e-prints arXiv:hep-th/9702087*.

- [13] M. Demianski, Static electromagnetic geon, *Found. Phys.* 16 (1986) 187–190, <http://dx.doi.org/10.1007/BF01889380>.
- [14] N. Bretón, R. García-Salcedo, Nonlinear electrodynamics and black holes, *ArXiv High Energy Physics - Theory e-prints* arXiv:hep-th/0702008.
- [15] N. Bretón, Geodesic structure of the Born–Infeld black hole, *Class. Quantum Gravity* 19 (2002) 601–612, <http://dx.doi.org/10.1088/0264-9381/19/4/301>.
- [16] Y.S. Myung, Y.-W. Kim, Y.-J. Park, Thermodynamics and phase transitions in the Born–Infeld–anti-de Sitter black holes, *Phys. Rev. D* 78 (8) (2008), <http://dx.doi.org/10.1103/PhysRevD.78.084002>, 084002, arXiv:0805.0187.
- [17] G.J. Olmo, D. Rubiera-García, Palatini $f(R)$ black holes in nonlinear electrodynamics, *Phys. Rev. D* 84 (12) (2011), <http://dx.doi.org/10.1103/PhysRevD.84.124059>, 124059, arXiv:1110.0850.
- [18] W. Heisenberg, H. Euler, Folgerungen aus der Diracschen Theorie des Positrons, *Z. Phys.* 98 (1936) 714–732, <http://dx.doi.org/10.1007/BF01343663>.
- [19] J. Schwinger, On gauge invariance and vacuum polarization, *Phys. Rev.* 82 (1951) 664–679, <http://dx.doi.org/10.1103/PhysRev.82.664>.
- [20] L. Labun, J. Rafelski, QED energy–momentum trace as a force in astrophysics, *Phys. Lett. B* 687 (2010) 133–138, <http://dx.doi.org/10.1016/j.physletb.2010.02.083>, arXiv:0810.1323.
- [21] L. Labun, J. Rafelski, Dark energy simulacrum in nonlinear electrodynamics, *Phys. Rev. D* 81 (6) (2010), <http://dx.doi.org/10.1103/PhysRevD.81.065026>, 065026, arXiv:0811.4467.
- [22] J.M. Bardeen, B. Carter, S.W. Hawking, The four laws of black hole mechanics, *Commun. Math. Phys.* 31 (1973) 161–170, <http://dx.doi.org/10.1007/BF01645742>.
- [23] J. Díaz-Alonso, D. Rubiera-García, Thermodynamic analysis of black hole solutions in gravitating nonlinear electrodynamics, arXiv:1204.2506.
- [24] L. Smarr, Mass formula for Kerr black holes, *Phys. Rev. Lett.* 30 (1973) 71–73, <http://dx.doi.org/10.1103/PhysRevLett.30.71>.
- [25] L. Smarr, Mass formula for Kerr black holes, *Phys. Rev. Lett.* 30 (1973) 521, <http://dx.doi.org/10.1103/PhysRevLett.30.521>.
- [26] N. Bretón, Smarr's formula for black holes with non-linear electrodynamics, *Gen. Relativ. Gravit.* 37 (2005) 643–650, <http://dx.doi.org/10.1007/s10714-005-0051-x>, arXiv:gr-qc/0405116.
- [27] H.A. González, M. Hassaine, C. Martínez, Thermodynamics of charged black holes with a nonlinear electrodynamics source, *Phys. Rev. D* 80 (10) (2009), <http://dx.doi.org/10.1103/PhysRevD.80.104008>, 104008, arXiv:0909.1365.
- [28] L.D. Landau, E.M. Lifshitz, *Mechanics*, 1976.
- [29] C.W. Misner, K.S. Thorne, J.A. Wheeler, *Gravitation*, 1973.
- [30] N. Deruelle, R. Ruffini, Quantum and classical relativistic energy states in stationary geometries, *Phys. Lett. B* 52 (1974) 437–441, [http://dx.doi.org/10.1016/0370-2693\(74\)90119-1](http://dx.doi.org/10.1016/0370-2693(74)90119-1).
- [31] L.D. Landau, E.M. Lifshitz, *Electrodynamics of Continuous Media*, 1960.
- [32] D.R. Smith, W.J. Padilla, D.C. Vier, S.C. Nemat-Nasser, S. Schultz, Composite medium with simultaneously negative permeability and permittivity, *Phys. Rev. Lett.* 84 (2000) 4184–4187, <http://dx.doi.org/10.1103/PhysRevLett.84.4184>.
- [33] R.A. Shelby, D.R. Smith, S. Schultz, Experimental verification of a negative index of refraction, *Science* 292 (2001) 77–79, <http://dx.doi.org/10.1126/science.1058847>.
- [34] V.A. De Lorenci, N. Figueiredo, H.H. Fliche, M. Novello, Dyadosphere bending of light, *Astron. Astrophys.* 369 (2001) 690–693, <http://dx.doi.org/10.1051/0004-6361:20010089>, arXiv:astro-ph/0102296.
- [35] R. Ruffini, L. Vitagliano, Irreducible mass and energetics of an electromagnetic black hole, *Phys. Lett. B* 545 (2002) 233–237, [http://dx.doi.org/10.1016/S0370-2693\(02\)02633-3](http://dx.doi.org/10.1016/S0370-2693(02)02633-3), arXiv:astro-ph/0209072.
- [36] C. Cherubini, A. Geralico, H.J.A. Rueda, $e^- - e^+$ pair creation by vacuum polarization around electromagnetic black holes, *Phys. Rev. D* 79 (12) (2009), <http://dx.doi.org/10.1103/PhysRevD.79.124002>, 124002–+, arXiv:0905.3274.
- [37] D. Kothawala, S. Sarkar, T. Padmanabhan, Einstein's equations as a thermodynamic identity: the cases of stationary axisymmetric horizons and evolving spherically symmetric horizons, *Phys. Lett. B* 652 (2007) 338–342, <http://dx.doi.org/10.1016/j.physletb.2007.07.021>, arXiv:gr-qc/0701002.
- [38] R. Ruffini, Fundamental physics from black holes, neutron stars and gamma-ray bursts, *Internat. J. Modern Phys. D* 20 (2011) 1797–1872, <http://dx.doi.org/10.1142/S0218271811019876>, arXiv:1107.0862.
- [39] T. Damour, R. Ruffini, Quantum electrodynamic effects in Kerr–Newmann geometries, *Phys. Rev. Lett.* 35 (1975) 463–466, <http://dx.doi.org/10.1103/PhysRevLett.35.463>.

GRAVITATIONAL WAVES VERSUS X-RAY AND GAMMA-RAY EMISSION IN A SHORT GAMMA-RAY BURST

F. G. OLIVEIRA^{1,2}, JORGE A. RUEDA^{1,2}, AND R. RUFFINI^{1,2}

¹ Dipartimento di Fisica and ICRA, Sapienza Università di Roma, P.le Aldo Moro 5, I-00185 Rome, Italy;

fe.fisica@gmail.com, jorge.rueda@icra.it, ruffini@icra.it

² ICRANet, P.zza della Repubblica 10, I-65122 Pescara, Italy

Received 2013 December 5; accepted 2014 March 13; published 2014 May 14

ABSTRACT

Recent progress in the understanding of the physical nature of neutron star equilibrium configurations and the first observational evidence of a genuinely short gamma-ray burst (GRB), GRB 090227B, allows us to give an estimate of the gravitational waves versus the X-ray and gamma-ray emission in a short GRB.

Key words: binaries: close – equation of state – gamma-ray burst: individual (GRB 090227B) – gravitational waves – stars: neutron

1. INTRODUCTION

The first systematic analysis of the temporal distribution of T_{90} , the observed duration of prompt emission from gamma-ray bursts (GRBs), made for the sample of GRBs observed by the BATSE instrument on board the Compton Gamma-Ray Observer satellite (Meegan et al. 1992), revealed a bimodal shape. This showed the existence of two different kinds of sources: *long* and *short* GRBs were defined as being longer or shorter than $T_{90} = 2$ s.

Muccino et al. (2013) recently probed the existence of *genuine* short GRBs, theoretically predicted by the Fireshell model (Ruffini et al. 2001b, 2002) as bursts with the same inner engine as the long bursts but endowed with a severely low value of the baryon load, $B \equiv M_B c^2 / E_{e^+e^-}^{\text{tot}} \lesssim 10^{-5}$. Here M_B is the mass of the baryons engulfed by the expanding ultrarelativistic e^+e^- plasma whose total energy is denoted by $E_{e^+e^-}^{\text{tot}}$; see Section 3 for further details. The emission from these GRBs mainly consists of a first emission, the proper GRB (P-GRB), followed by a softer emission squeezed on the first one. The typical separation between the two components is expected to be shorter than 1–10 ms. No afterglow emission is expected from these sources.

Indeed, the time-resolved spectral analysis of the *Fermi*-GBM and *Konus-Wind* satellites data of GRB 090227B by Muccino et al. (2013) has led to an estimate of $B = (4.13 \pm 0.05) \times 10^{-5}$ for the baryon load for this burst. The parameters inferred for GRB 090227B thus lead to the identification of the progenitor of the genuine short GRB in a neutron star binary (see Section 3 and Muccino et al. 2013 for details): (1) the natal kicks velocities imparted on a neutron star binary at birth can be even larger than 200 km s^{-1} . Therefore, a binary system can run away to the halo of its host galaxy, clearly pointing to a very low average number density of the circumburst medium (CBM); (2) the very large total energy, which we can indeed infer in view of the absence of beaming, and the very short timescale of emission again point to a neutron star binary; (3) as we shall show in Section 2, the very small value of the baryon load is strikingly consistent with two neutron stars having small crusts, in line with the recent neutron star theory (Rotondo et al. 2011; Rueda et al. 2011; Belvedere et al. 2012).

The aim of this work is to make a detailed analysis of the neutron star binary progenitor of GRB 090227B. We compute the structure of the neutron star components following our recent model of neutron stars fulfilling global charge neutrality and including the strong, weak, electromagnetic, and

gravitational interactions in the framework of general relativity and relativistic nuclear mean field theory. We simulate the evolution of the binary and compute the radiation emitted in the form of gravitational waves which leads to the shrinking of the orbit and final merging. We compare and contrast the results of the dynamics as described by the classical test-mass limit approximation with the more accurate description based on the one-body formalism (Buonanno & Damour 1999, 2000; Damour et al. 2000; Damour 2001; Damour & Nagar 2010). We estimate the detectability of this kind of neutron star binaries by the Advanced LIGO interferometer. We also compute the total energy output in gravitational waves and compare it with the emission of the system in X-rays and gamma rays.

2. NEUTRON STAR STRUCTURE

We have recently proved how the consistent treatment of neutron star equilibrium configurations, taking into account strong, weak, electromagnetic, and gravitational interactions, provides a solution to the general relativistic Thomas–Fermi equations, coupled with the Einstein–Maxwell system of equations (Rotondo et al. 2011; Rueda et al. 2011; Belvedere et al. 2012). These new Einstein–Maxwell–Thomas–Fermi (EMTF) equations supersede the traditional Tolman–Oppenheimer–Volkoff (TOV) equations, which impose the condition of local charge neutrality throughout the configuration (Tolman 1939; Oppenheimer & Volkoff 1939). We have shown that this latter imposition of a TOV-like treatment explicitly violates the thermodynamic equilibrium of the star, which is ensured by the constancy of the generalized electro-chemical potentials (Klein potentials) of each system species along the whole configuration (Rotondo et al. 2011; Rueda et al. 2011).

The solution of the EMTF coupled differential equations self-consistently introduces the presence of the electromagnetic interactions in addition to the nuclear, weak, and gravitational interactions within the framework of general relativity. The weak interactions are accounted for by requesting the β -stability, and the strong interactions are modeled via the σ - ω - ρ nuclear model, where σ , ω , and ρ are the mediator massive vector mesons within the relativistic mean field theory, à la Boguta & Bodmer (1977). The nuclear model is fixed once the values of the coupling constants and the masses of the three mesons are fixed: in this work, as in the previous ones (Belvedere et al. 2012, 2014), we adopt the NL3 parameter set (Lalazissis et al. 1997). The supranuclear core is composed of a degenerate gas

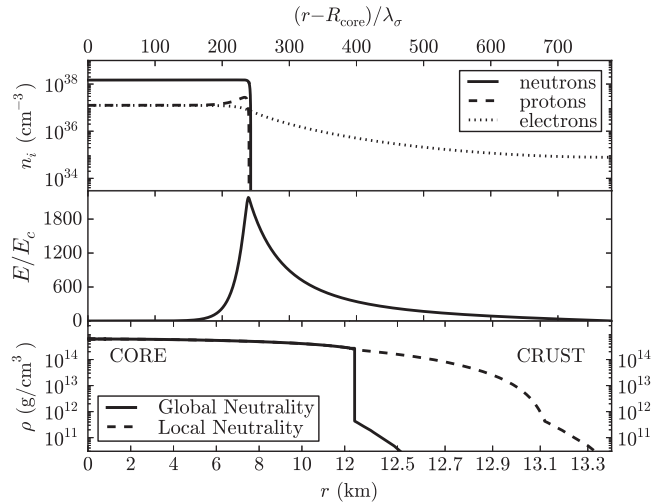


Figure 1. Upper panel: particle density profiles in the core-crust boundary interface in units of cm^{-3} . Middle panel: electric field in the core-crust transition layer in units of the critical field E_c . Lower panel: density profile inside a neutron star with central density $\rho(0) \sim 5\rho_{\text{nuc}}$. We show here the differences between the solution obtained from the TOV equations (locally neutral case) and the globally neutral solution presented in Belvedere et al. (2012). In this example, the density at the edge of the crust is $\rho_{\text{crust}} = \rho_{\text{drip}} = 4.3 \times 10^{11} \text{ g cm}^{-3}$ and $\lambda_\sigma = \hbar/(m_\sigma c) \sim 0.4 \text{ fm}$ denotes the σ -meson Compton wavelength.

of neutrons, protons, and electrons in β -equilibrium. The crust in its outer region $\rho \leq \rho_{\text{drip}} \approx 4.3 \times 10^{11} \text{ g cm}^{-3}$ is composed of ions and electrons, and in its inner region, at $\rho_{\text{drip}} < \rho < \rho_{\text{nuc}}$, where $\rho_{\text{nuc}} \approx 2.7 \times 10^{14} \text{ g cm}^{-3}$ is the nuclear saturation density, there is an additional component of free neutrons dripped out from nuclei.

The solution of the EMTF equations of equilibrium leads to a new structure of neutron stars that is very different from the traditional configurations obtained through the TOV equations (see Figure 1): the core is positively charged as a consequence of the balance between gravitational and Coulomb forces which results in the appearance of a Coulomb potential energy $eV \sim m_\pi c^2$ deep. The core-crust transition starts at $\rho = \rho_{\text{nuc}}$. The transition is marked by the existence of a thin, $\Delta r \sim$ few hundreds of femometers, electron layer fully screening the core charge. In this transition layer the electric field becomes overcritical, $E \sim m_\pi^2 c^3 / (e\hbar)$, and the particle densities decrease until the base of the crust, which is reached when global charge neutrality is achieved. Consequently, the core is matched to the crust at a density $\rho_{\text{crust}} \leq \rho_{\text{nuc}}$.

For each central density, there exists an entire family of core-crust interface boundaries and, correspondingly, a family of crusts with different masses M_{crust} and thicknesses ΔR_{crust} . The larger ρ_{crust} , the smaller the thickness of the core-crust interface, the peak of the electric field, and the larger the M_{crust} and ΔR_{crust} . Configurations with $\rho_{\text{crust}} > \rho_{\text{drip}}$ possess both inner and outer crusts while in the cases with $\rho_{\text{crust}} \leq \rho_{\text{drip}}$, the neutron stars have only outer crusts. In the limit $\rho_{\text{crust}} \rightarrow \rho_{\text{nuc}}$, both Δr and E of the transition layer vanish, and the solution approaches that given by local charge neutrality (see Figures 3 and 5 in Belvedere et al. 2012). All of the above features lead to a new mass–radius relation of neutron stars; see Belvedere et al. (2012) and Figure 2. The extension to the case of uniformly rotating neutron stars has been recently achieved in Belvedere et al. (2014).

It is also worth mentioning that in Belvedere et al. (2012) we showed the agreement of this new mass–radius relation with

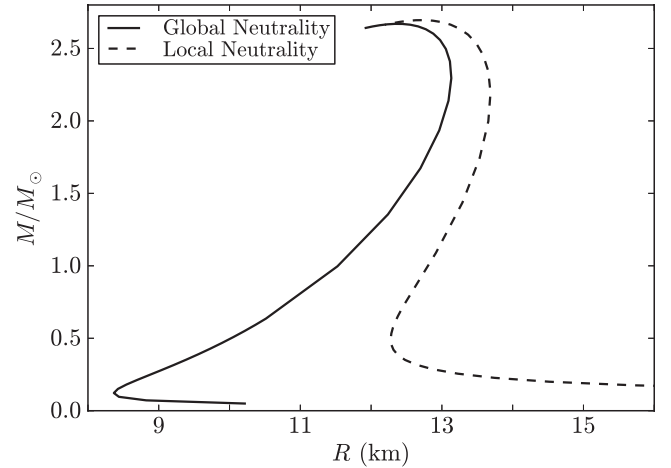


Figure 2. Mass–radius relation obtained with the traditional locally neutral TOV treatment case and the global charge neutrality configurations with $\rho_{\text{crust}} = \rho_{\text{drip}}$ (Belvedere et al. 2012). Configurations lying between the solid and dashed curves have $\rho_{\text{crust}} > \rho_{\text{drip}}$ and so they possess an inner crust.

Table 1
Critical Mass and Corresponding Radius of Globally Neutral Neutron Stars for Selected Nuclear Equations of State

	NL3	NL-SH	TM1	TM2
$M_{\text{crit}} (M_\odot)$	2.67	2.68	2.58	2.82
R (km)	12.33	12.54	12.31	13.28

the most stringent observational constraints on the mass–radius relation of neutron stars, which are provided by the largest mass, the largest radius, the highest rotational frequency, and the maximum surface gravity observed from pulsars (Trümper 2011). They are imposed by the mass of PSR J1614–2230 $M = 1.97 \pm 0.04 M_\odot$ (Demorest et al. 2010), the lower limit to the radius of RX J1856–3754 (Trümper et al. 2004), the 716 Hz PSR J1748–2246ad (Hessels et al. 2006), and the surface gravity of the neutron star in the low-mass X-ray binary X7 from which 90% confidence level contours of constant R_∞ can be extracted (Heinke et al. 2006).

It is known that uncertainties in the behavior of the nuclear matter at densities larger than the nuclear saturation density $n_{\text{nuc}} \approx 0.16 \text{ fm}^{-3}$, reached in the core of a neutron star, lead to a variety of nuclear equations of state which lead to different numerical estimates of the neutron star parameters, in particular the mass–radius relation. However, as we have mentioned above, the current observational constraints strongly favor stiff nuclear equations of state, such as those obtained from relativistic mean field models á la Boguta & Bodmer (1977) used here, which provide high values for the critical mass of the neutron star, larger than the mass of PSR J1614–2230. This has recently been reconfirmed by the measurements of the high mass of PSR J0348+0432, $M = 2.01 \pm 0.04 M_\odot$ (Antoniadis et al. 2013).

In Table 1 we show the critical mass and corresponding radius of globally neutral neutron stars obtained for selected parameterizations of the nuclear model used in Belvedere et al. (2012): NL3 (Lalazissis et al. 1997) NL-SH (Sharma et al. 1993), TM1 (Sugahara & Toki 1994), and TM2 (Hirata et al. 1995).

3. PARAMETERS OF GRB 090227B

In parallel, the theoretical progress in the Fireshell model of GRBs (see Ruffini et al. 2001c, 2001b, 2001a) led to

Table 2
Properties of GRB 090227B

$E_{\text{tot}}^{\text{GRB}}$ (erg)	B	Γ_{tr}	z	Δt (s)	$\langle n_{\text{CBM}} \rangle$ (cm^{-3})
2.83×10^{53}	4.13×10^{-5}	1.44×10^4	1.61	0.35	1.9×10^{-5}

Notes. $E_{\text{tot}}^{\text{GRB}}$ is the total energy emitted in the GRB, B is the baryon load, Γ_{tr} is the Lorentz factor at transparency, the cosmological redshift is denoted by z , the intrinsic duration of the GRB is Δt , and the average density of the CBM is $\langle n_{\text{CBM}} \rangle$. We refer to Muccino et al. (2013) for additional details.

an alternative explanation of the Norris–Bonnell sources as disguised short burst (Bernardini et al. 2007, 2008; Caito et al. 2009, 2010; de Barros et al. 2011): canonical long bursts exploding in halos of their host galaxies, with an average value of the CBM density $\langle n_{\text{CBM}} \rangle \approx 10^{-3}$ particles cm^{-3} .

We now turn to the analysis of GRB 090227B. We first recall that the canonical GRB within the Fireshell model has two components: an emission occurring at the transparency of the optically thick expanding e^+e^- baryon plasma (Ruffini et al. 2000), the P-GRB, followed by the extended afterglow, due to the interactions between the accelerated baryons and the CBM of average density $\langle n_{\text{CBM}} \rangle$. Such an extended afterglow is composed of the prompt emission as well as the late phase of the afterglow (Bianco & Ruffini 2005b, 2005a). The relative energy of these two components, for a given total energy of the plasma $E_{e^+e^-}^{\text{tot}} = E_{\text{tot}}^{\text{GRB}}$, where $E_{\text{tot}}^{\text{GRB}}$ is the observed GRB energy, is uniquely a function of the baryon load $B = M_B c^2 / E_{\text{tot}}^{\text{GRB}} = M_B c^2 / E_{e^+e^-}^{\text{tot}}$, where M_B is the mass of the baryons engulfed by the expanding ultrarelativistic e^+e^- plasma.

As we mentioned, an extremely low value of the baryon load, $B \lesssim 10^{-5}$, together with a low density of the CBM, lead to a genuinely short GRB emission, in which no afterglow emission is observed. This is indeed the case of GRB 090227B.

From the 16 ms time-binned light curves, a significant thermal emission in the first 96 ms, which has been identified with the P-GRB, has been found (Muccino et al. 2013). The subsequent emission is identified with the extended afterglow. The P-GRB of 090227B has the highest temperature ever observed, $k_B T = 517$ keV, where k_B is the Boltzmann constant. The results of the fit of the light curve and spectrum of GRB 090227B are summarized in Table 2. In particular, we show the total energy emitted $E_{\text{tot}}^{\text{GRB}}$, the baryon load B , the Lorentz factor at transparency Γ_{tr} , the cosmological redshift z , the intrinsic duration of the GRB emission Δt , and the average density of the CBM $\langle n_{\text{CBM}} \rangle$; we refer to Muccino et al. (2013) for further details.

4. INFERENCE OF NEUTRON STAR BINARY PARAMETERS

We now infer the binary component parameters. It is clear that the merging of two neutron stars will lead to a GRB if the total mass of the binary satisfies

$$M_1 + M_2 \gtrsim M_{\text{crit}} = 2.67 M_{\odot}, \quad (1)$$

where M_{crit} is the critical mass over which a neutron star undergoes gravitational collapse to a black hole. For the numerical estimates, we adopt the neutron star configurations obtained with the NL3 parameterization of the nuclear model (see Table 1).

Assuming for simplicity a binary with twin components $M_1 = M_2 = M$, we obtain masses $M = 1.335 M_{\odot}$ and correspondingly radii $R_1 = R_2 = 12.24$ km (see Figure 2

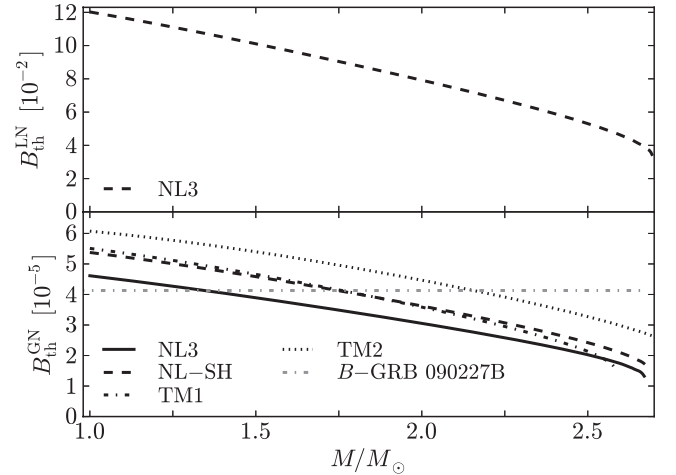


Figure 3. Theoretical baryon load expected to be left by a binary neutron star merger as given by Equation (2), for $\eta = 0.1$, as a function of the total mass M . Upper panel: locally neutral neutron stars, $B_{\text{th}}^{\text{LN}}$, for the NL3 parameterization of the nuclear model (black dashed curve) in units of 10^{-2} . Lower panel: globally neutral neutron stars, $B_{\text{th}}^{\text{GN}}$, for the NL3, NL-SH, TM1, and TM2 parameterizations of the nuclear model. We indicate the observed baryon load of GRB 090227B, $B = 4.13 \times 10^{-5}$, with the dashed-dotted gray horizontal line; see Table 2 and Muccino et al. (2013).

and Belvedere et al. 2012). The mass of the corresponding crust of each component is $M_{\text{crust}} \approx 3.6 \times 10^{-5} M_{\odot}$ and the thickness of the crust is $\Delta R_{\text{crust}} \sim 0.47$ km. For the other nuclear parameterizations of the nuclear model, the maximum stable mass and corresponding radius are given by Table 1, and consequently the parameters of the single neutron star components change accordingly if described by such models, including the estimate of the baryon load, as shown below.

The location of the binary in the very low interstellar density medium of galactic halos makes it possible to probe the neutron star theory and equation of state through knowledge of the baryon load B inferred by fitting the GRB light curve and spectrum. The GRB interacts with the baryonic matter ejected from the neutron star crusts during the binary coalescence. Thus, a theoretical expectation of the baryon load B left in a binary neutron star merger is

$$B_{\text{th}} = \eta \frac{M_{\text{crust}}^{\text{tot}} c^2}{E_{\text{tot}}^{\text{GRB}}}, \quad (2)$$

where η is the fraction of the total crustal mass, $M_{\text{crust}}^{\text{tot}} = M_{1,\text{crust}} + M_{2,\text{crust}} = 2M_{\text{crust}} = 7.2 \times 10^{-5} M_{\odot}$, which is ejected. We assume that the mass ejected during the merger comes from the crust of the two neutron star components of the system, as should be expected from a symmetric binary merger.

In Figure 3 we have plotted the theoretical baryon load given by Equation (2) for GRB 090227B, namely using $E_{\text{tot}}^{\text{GRB}} = 2.83 \times 10^{53}$ erg, as a function of the mass M of the neutron star for the nuclear equations of state of Table 1. For the locally neutral case, for the sake of comparison we use only the result for the NL3 parameterization.

The agreement of the observed baryon load of GRB 090227B (see Table 2 and Muccino et al. 2013) with the low mass of the crust obtained from the globally neutral neutron stars of Belvedere et al. (2012) is evident (see Figure 3). It can be compared and contrasted with those obtained enforcing the local charge neutrality condition. For the specific binary neutron star system adopted here, we obtain a theoretical prediction of the

baryon load from Equation (2) with $\eta = 1$, $B_{\text{th}} \approx 4.5 \times 10^{-4}$, or a mass of the baryons $M_B = M_{\text{crust}}^{\text{tot}} \approx 7.2 \times 10^{-5} M_{\odot}$, to be confronted with that obtained from the fitting procedure of GRB 090227B, $B \sim 4.13 \times 10^{-5}$, corresponding to $M_B = B \times E_{\text{tot}}^{\text{GRB}}/c^2 \sim 0.7 \times 10^{-5} M_{\odot}$. A perfect agreement requires $\eta \approx 0.1$ for the NL3 nuclear model, while the other nuclear parameterizations require a slightly lower value of η ; see Figure 3. The above theoretical predictions of the neutron star crust mass M_{crust} , and consequently, the value of E_{crust}^B and B , have been inferred for a crust with a density at its edge equal to the neutron drip density $\rho_{\text{drip}} \sim 4.3 \times 10^{11} \text{ g cm}^{-3}$. Neutron star crusts with densities $\rho < \rho_{\text{drip}}$ are predicted by the new neutron star theory (Belvedere et al. 2012); therefore, there is still room for smaller values of the baryonic matter ejected in a binary process, and, consequently, to still shorter genuinely short GRBs.

The mass-energy of the baryon ejecta obtained from the estimate (Equation (2)) provides values for locally neutral neutron stars 10^2 – 10^3 larger than those analyzed before (see Figure 3), due to the more massive crusts obtained from the TOV-like treatment (see Belvedere et al. 2012 for details). It implies that Equation (2) gives $M_B \sim 10^{-3}$ – $10^{-2} M_{\odot}$ in such a case, in line with previous results obtained from the numerical simulation of the dynamical evolution of neutron star binaries (see, e.g., Ruffert & Janka 2001; Goriely et al. 2011), where locally neutral neutron stars are employed.

Turning to a possible alternative scenario, the crust supported by strange quark stars has densities strictly lower than ρ_{drip} and therefore they have crust masses $\sim 10^{-5} M_{\odot}$ (see, e.g., Alcock et al. 1986; Glendenning & Weber 1992 for details), similar to the crust of the globally neutron stars (Belvedere et al. 2012). This leads to the natural question of whether strange stars could also be a viable explanation to the low value of the baryon load of short GRBs. In addition, the quark core-crust transition is also characterized by overcritical electric fields. However, the softness of the equation of state of strange quark matter leads to a mass–radius relation for these stars characterized by a low maximum stable mass and small radii, ruled out by the current observational constraints of pulsars which put a lower limit to the radius of a compact star with $M = 1.4 M_{\odot}$, $R \gtrsim 12 \text{ km}$ (Trümper 2011), and the most massive compact star observed, PSR J0348+0432 with $M = 2.01 \pm 0.04 M_{\odot}$ (Antoniadis et al. 2013).

5. GRAVITATIONAL WAVE EMISSION

The gravitational waves’ signals from neutron star binaries are the most likely to be detected by the Advanced LIGO³-VIRGO⁴ interferometers. It is expected that these will be operational in a few years with a improved sensitivity approximately a factor of 10 better than the first generation of detectors. The connection between short gamma-ray signals and gravitational waves’ signals as a coincidence of the same event would, in principle, allow us to understand more about the origin of short GRBs (see Kobayashi & Mészáros 2003 and references therein).

Here we use the adiabatic approximation to estimate the gravitational wave emission from the binary neutrons star. We used the above values of the neutron star binary progenitor estimated for the short GRB 090227B at a cosmological redshift $z = 1.61$ (Muccino et al. 2013). We adopt circular orbits for simplicity. First, we compute the dynamics following the classic

non-relativistic test-mass limit approximation and compare it with the more accurate description given by the one-body formalism, which accounts for the effects of general relativity.

5.1. Classical Dynamics

The orbital angular velocity of the binary with components (M_1, R_1) and (M_2, R_2) orbiting each other in a circular orbit of radius r is given by

$$\Omega = \sqrt{\frac{G(M_1 + M_2)}{r^3}}, \quad (3)$$

and its total binding energy is

$$E_b = -\frac{1}{2} \frac{GM_1 M_2}{r}. \quad (4)$$

The leading term driving the loss of binding energy via gravitational wave emission is given by

$$-\frac{dE_b}{dt} = \frac{32}{5} \frac{G^4 (M_1 + M_2)(M_1 M_2)^2}{c^5 r^5}, \quad (5)$$

which leads to a decrease of the separation r with time and, consequently, a shortening of the orbital period $P = 2\pi/\Omega$ dictated by (Landau & Lifshitz 1980)

$$\frac{1}{P} \frac{dP}{dt} = \frac{3}{2} \frac{1}{r} \frac{dr}{dt} = -\frac{3}{2} \frac{1}{E_b} \frac{dE_b}{dt}. \quad (6)$$

The loss of orbital binding energy by the emission of gravitational waves from the neutron star system in spiral phase for non-relativistic and point-like particles can be written as a function of the gravitational waves’ frequency f as

$$\frac{dE_b}{df} = -\frac{1}{3} (\pi G)^{2/3} \mathcal{M}^{5/3} f^{-1/3}, \quad (7)$$

where $\mathcal{M} = (M_1 M_2)^{3/5} / (M_1 + M_2)^{1/5}$ is the chirp mass.

5.2. Effective One-body Dynamics

The effective one-body (EOB) formalism (Buonanno & Damour 1999, 2000; Damour et al. 2000; Damour 2001; Damour & Nagar 2010) maps the conservative dynamics of a binary system of non-spinning objects onto the geodesic dynamics of one body of reduced mass $\mu = M_1 M_2 / M$, where $M = M_1 + M_2$ is the total binary mass. The effective metric is a modified Schwarzschild metric given by

$$ds^2 = -A(r)dt^2 + B(r)dr^2 + r^2(d\theta^2 + \sin^2\theta d\phi^2), \quad (8)$$

where the rescaled radial coordinate $r = c^2 r_{12} / (GM)$ has been introduced, where r_{12} is the distance between the two stars. The radial potential is given by

$$A(u; \nu) = 1 - 2u + 2\nu u^3 + a_4 \nu u^4 + a_5 \nu u^5, \quad (9)$$

where $u = 1/r = GM/(c^2 r_{12})$, $\nu = M_1 M_2 / (M_1 + M_2)^2$ is the symmetric mass ratio (see Figure 4), with the values of the three and four post-Newtonian (PN)-level coefficients given by $a_4 = 94/3 - (41/32)\pi^2$ and $a_5(\nu) = a_5^{c0} + \nu a_5^{c1}$ (see Bini & Damour 2013 for details). We will denote the Padé approximant of the order of (n, m) as P_n^m , which, when applied to $A(u; \nu)$,

³ <http://www.advancedligo.mit.edu>

⁴ <http://www.cascina.virgo.infn.it>

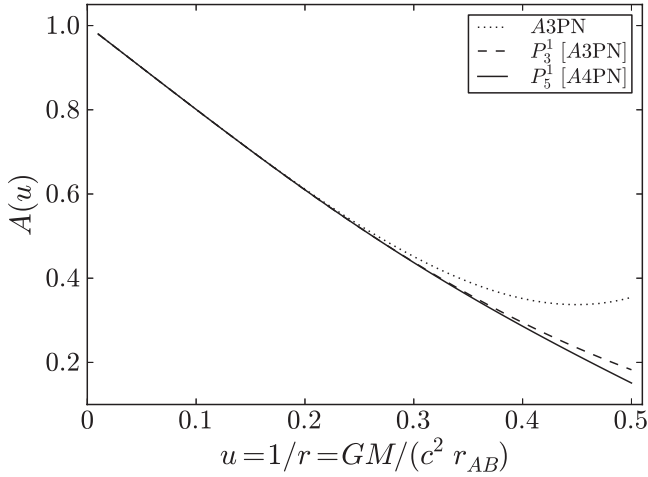


Figure 4. Comparison between the EOB radial potential as a function of the u parameter for the cases: $A(u; \nu) = 3\text{PN}$ (dotted), $P_3^1[A(u; \nu) = 3\text{PN}]$ (dashed), and $P_5^1[A(u; \nu) = 4\text{PN}]$ (solid), where $P_n^m[\cdot]$ is the Padé approximant.

ensures the convergence of the solution near the merger point (see Damour & Nagar 2009 and references therein).

The EOB Hamiltonian is

$$H = Mc^2 \sqrt{1 + 2\nu(\hat{H}_{\text{eff}} - 1)}, \quad (10)$$

and the effective Hamiltonian is described by

$$\hat{H}_{\text{eff}}^2 = A(u) + p_\phi^2 B(u), \quad (11)$$

where $B(u) = u^2 A(u)$ and the angular momentum for the circular orbit is given by

$$p_\phi^2 = -\frac{A'(u)}{[u^2 A(u)]}, \quad (12)$$

where the prime represents the derivative with respect to u .

We must write \hat{H}_{eff} as a function of the orbital angular velocity Ω , or orbital frequency f . To do so, we must write the u parameter as a function of Ω or f , which is obtained from the angular Hamilton equation of motion in the circular case

$$GM\Omega(u) = \frac{1}{u} \frac{\partial H}{\partial p_\phi} = \frac{MA(u)p_\phi(u)u^2}{H\hat{H}_{\text{eff}}}. \quad (13)$$

We follow the binary evolution up to the *contact* orbital frequency, Ω_c , which we compute at the location of the innermost stable circular orbit, R_{ISCO} , or when the two stars effectively *touch* each other, namely at $r_{AB,\text{min}} = R_1 + R_2$, if $R_{\text{ISCO}} < R$. Within the EOB formalism, the value of R_{ISCO} is given by the solution of the equation

$$A'(u_{\text{ISCO}})B''(u_{\text{ISCO}}) - A''(u_{\text{ISCO}})B'(u_{\text{ISCO}}) = 0, \quad (14)$$

which, for our binary neutron star, gives $u_{\text{ISCO}} = [0.25, 0.24, 0.2, 0.2]$ for $A(u) = 1-2u$ (test-mass limit dynamics, $R_{\text{ISCO}} = 6GM/c^2$), $A(u; \nu) = 3\text{PN}$, $P_3^1[A(u) = 3\text{PN}]$, and $P_5^1[A(u; \nu) = 4\text{PN}]$, respectively. Since $u_{\text{max}} = GM/(c^2 r_{AB,\text{min}}) = 0.16 < u_{\text{ISCO}}$, our contact point is given by u_{max} and not by u_{ISCO} . Therefore, in the present case, the contact orbital frequency is given by $\Omega_c = \Omega(u_{\text{max}})$. In Figure 5, we show the result of the numerical integration of the above equation for the present binary system.

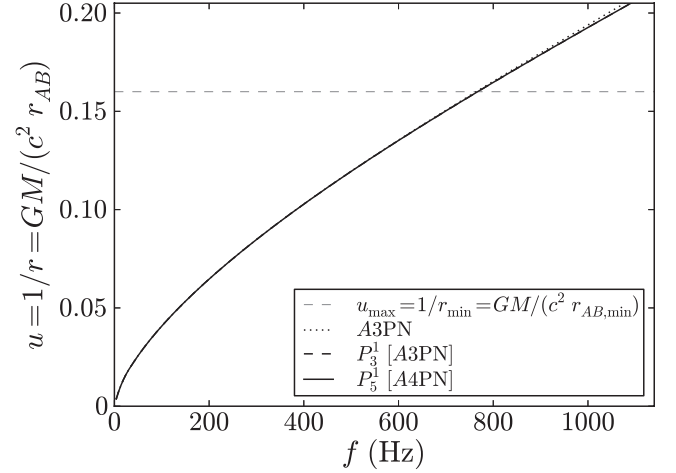


Figure 5. u parameter as a function of the source frequency obtained from Equation (13) in the case of a symmetric binary, $M_1 = M_2$, so $\nu = 1/4$. Here $r_{AB,\text{min}} = R_1 + R_2$ is the end point of the adiabatic approximation of the EOB formalism, which, in this case, is the point where the two neutron stars touch each other.

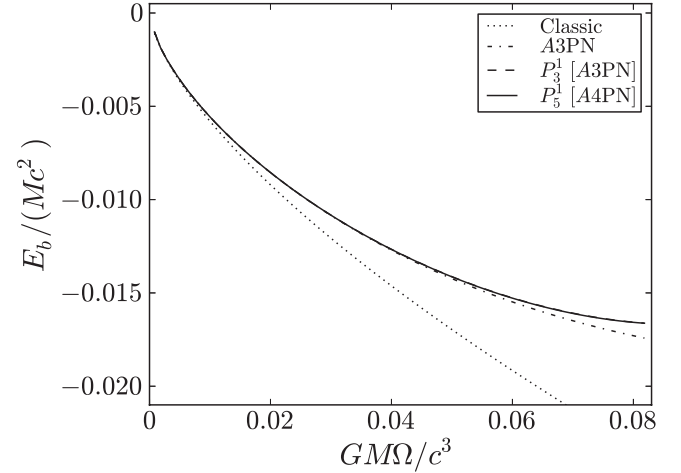


Figure 6. Comparison of the EOB binding energies using the radial potential $A(u; \nu) = 3\text{PN}$, $P_3^1[A(u; \nu) = 3\text{PN}]$, and $P_5^1[A(u; \nu) = 4\text{PN}]$ and the classic dynamics.

The binding energy as a function of the orbital frequency (see Figure 6) is

$$E_b(\Omega) = H - Mc^2 = Mc^2[\sqrt{1 + 2\nu(\hat{H}_{\text{eff}} - 1)} - 1], \quad (15)$$

and the gravitational energy spectrum is obtained through the derivative $dE_b/d\Omega$.

6. DETECTABILITY: SIGNAL-TO-NOISE RATIO

A positive detection of the gravitational waves' emission implies that the signal overcomes some minimum threshold value of the signal-to-noise ratio (S/N). The S/N appropriate for the matched-filtering search is given by (see Flanagan & Hughes 1998, for details)

$$S/N^2 = 4 \int_0^\infty \frac{|\tilde{h}(f)|^2}{S_h^2(f)} df, \quad (16)$$

where $\tilde{h}(f)$ is the Fourier transform of the gravitational waveform $h(t)$ and $S_h(f)$ is the strain noise spectral density (units

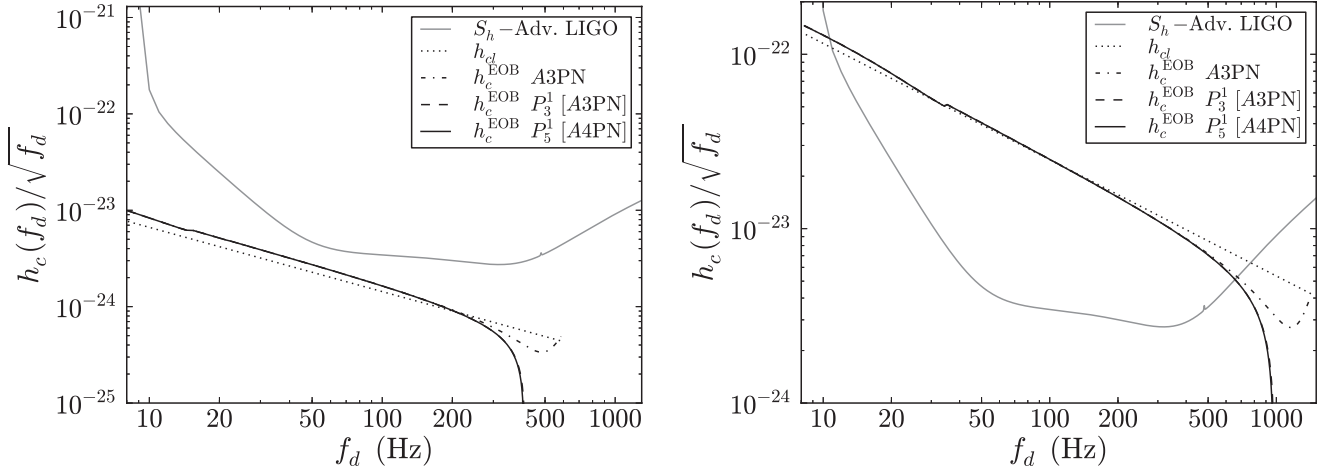


Figure 7. Left panel: comparison of the characteristic gravitational waves' amplitude per unit square root frequency, $h_c(f_d)/\sqrt{f_d}$ (see Equation (18)) with the noise density spectrum $S_h(f)$ of the Advanced LIGO interferometer. We use the binary neutron star parameters inferred for the short GRB 090227B, including the cosmological redshift $z = 1.61$. The comparison is made for both the dynamics given by the non-relativistic point-like particles approximation described in Section 5.1 (dotted black curve) and the dynamics obtained from the EOB formalism described in Section 5.2. In the case of the EOB approach, the radial potential $A(u; \nu)$ was calculated using the post-Newtonian (PN) approximation. The dotted-dashed black curve is $A(u; \nu) = 3\text{PN}$. Using the Padé approximant we calculated the $P_3^1[A(u; \nu) = 3\text{PN}]$ (dashed black curve) and the $P_5^1[A(u; \nu) = 4\text{PN}]$ (solid black curve). The noise spectral density of Advanced LIGO, $S_h(f)$, is represented by the solid gray curve. Right panel: same as left panel but for a redshift $z = 0.09$, which would give a gravitational wave detection with $\langle S/N \rangle = 5$ by Advanced LIGO.

$1/\sqrt{\text{Hz}}$) in the interferometer. Besides its dependence on the waveform, the above S/N in general depends on the orientation and position of the source with respect to the interferometer.

After making an rms average over all the possible source orientations, positions, and wave polarizations, the S/N given by Equation (16) becomes

$$\langle S/N^2 \rangle = \int_{f_{\min}}^{f_{\max}} df_d \frac{h_c^2(f_d)}{5 f_d^2 S_h^2(f_d)}, \quad (17)$$

where we have introduced the characteristic gravitational waves' amplitude, h_c , defined using the Fourier transform of the gravitational waveform $h(t)$, $h_c(f) = f |\tilde{h}(f)|$, and it is given by

$$h_c^2(f) = \frac{2(1+z)^2 G}{\pi^2 d_L^2} \frac{dE_b}{c^3 df} [(1+z)fd]. \quad (18)$$

where z is the cosmological redshift, $f_d = f/(1+z)$ the gravitational wave frequency at the detector, $f = \Omega/\pi$ the frequency in the source frame, Ω is the orbital frequency, the minimal bandwidth frequency of the detector is f_{\min} , and $f_{\max} = f_c/(1+z)$ is the maximal bandwidth frequency, where $f_c = \Omega_c/\pi$ is the binary contact frequency. In this work, we use a standard cosmological model with $H_0 = 75 \text{ km s}^{-1} \text{ Mpc}^{-1}$, $\Omega_M = 0.27$, and $\Omega_\Lambda = 0.73$, and a luminosity distance $d_L(z) = (c/H_0)(1+z) \int_0^z [\Omega_M(1+x)^3 + \Omega_\Lambda]^{-1/2} dx$. In this work, we adopt work $\langle S/N \rangle = 5$, as threshold value for a positive detection following previous works (see, e.g., Kobayashi & Mészáros 2003).

The rms averaged S/N given by Equation (17) depends only on the distance to the source, i.e., the cosmological redshift, and the energy spectrum, dE_b/df , of the gravitational waves; we refer the reader to Flanagan & Hughes (1998) for further details on the rms averaging.

In order to assess the detectability of the source in the spiraling-in phase, the integration in Equation (17) is carried out from the minimum bandwidth frequency of the interferometer all the way up to the contact frequency, namely the maximum frequency which is given by the merger point, namely when the two stars touch each other.

We now compare and contrast the characteristic amplitude per square root frequency, $h_c(f_d)/\sqrt{f_d}$, with the strain noise spectral density $S_h(f)$ of the Advanced LIGO interferometer, as a function of the frequency at the detector, f_d . In this work, we use the *Optimal NSNS* noise curve of the LIGO Document T0900288-v3, which is optimized for a $1.4 M_\odot$ neutron star, and gives a $\langle S/N \rangle = 8$ at a distance of 200 Mpc for a single interferometer.⁵ The comparison is made for both the dynamics given by the non-relativistic point-like particles approximation (see Section 5.1) and the dynamics obtained from the EOB formalism (see Section 5.2).

In the left panel of Figure 7, we use the theoretically estimated redshift of GRB 090227B, $z = 1.61$, which results in a contact frequency at the detector, $f_{\max} \approx 1534.19/(1+1.61) \text{ Hz} = 587.81 \text{ Hz}$. At such a redshift, $\langle S/N \rangle \approx 0.32$ for Advanced LIGO, a much lower value than the threshold for a positive detection.

At this point, it is natural to ask at which distance the gravitational waves' emission from the progenitor of GRB 090227B would have been detectable by the Advanced LIGO interferometer. We find that a $\langle S/N \rangle = 5$ would be produced if the GRB would be located at a redshift $z \approx 0.09$, namely at a distance $d_L \approx 381 \text{ Mpc}$. We show in the right panel of Figure 7 the results for this hypothetical redshift for detection. In this case, the contact frequency at the detector is, $f_{\max} \approx 1534.19/(1+0.09) \text{ Hz} = 1407.51 \text{ Hz}$. The above numerical values are obtained for the most accurate case, $P_5^1[A(u; \nu) = 4\text{PN}]$.

So far, we have discussed the issue of the conditions for a positive or negative detection by the Advanced LIGO interferometer of the spiraling phase of the progenitor of a genuine short GRB, as the binary neutron star progenitor of GRB 090227B. A different question are the conditions under which such a

⁵ <https://dcc.ligo.org/LIGO-T0900288/public>—the curve represent the incoherent sum of the principal noise sources best understood at this time, namely the quantum, seismic, and thermal noises. In addition, there will be technical noise sources. This is not a guaranteed performance, but a good guide to the overall curve and an early approximation to the anticipated sensitivity reachable by Advanced LIGO.

Table 3
Upper Limit for the Total GW Emission, $\Delta E_{\text{GW}}^{\text{max}}$ (erg)

Classic	EOB A3PN	EOB P_3^1 [A3PN]	EOB P_5^1 [A4PN]
9.6×10^{52}	9.68×10^{52}	7.41×10^{52}	7.42×10^{52}

detection could give us reliable information on the structure of the neutron star components. In such a case, a much higher value of the S/N is needed. For instance, Damour et al. (2012) recently estimated that a $\langle S/N \rangle \approx 16$ is necessary to obtain knowledge of the neutron star equation of state, extracted from the tidal polarizability parameters of the binary components. This would imply a still shorter distance to the source than that one derived above.

7. TOTAL ENERGY OUTPUT

The gravitational waves' emission dominates the energy loss during the spiraling phase while the X-rays and gamma rays dominate from the coalescence with the final emission of a short GRB if the total mass of the binary exceeds the critical mass for neutron star gravitational collapse. Thus, an upper limit for the gravitational wave emission can be obtained from the energy difference between the initial binary at the time $t_0 = 0$ with a separation r_0 and energy E_0 , and the binary at the time t_f and a separation $r_f = r_{AB,\text{min}} = R_1 + R_2$, with energy E_f , when the two components touch each other.

An absolute upper limit for the gravitational wave energy emission, $\Delta E_{\text{GW}}^{\text{max}}$, can therefore be determined by the assumption of an infinite initial separation $r_0 \rightarrow \infty$, namely

$$\Delta E_{\text{GW}}^{\text{max}} = |E_b(t_f) - E_b(t_0)|. \quad (19)$$

For the neutron star binary discussed in this work for GRB 090227B, we obtain the absolute upper bound shown in Table 3. The gravitational wave energy emission $\Delta E_{\text{GW}}^{\text{max}}$, in the case of the genuinely short GRB 090227B, is one order of magnitude smaller than the emitted electromagnetic energy $E_{\text{tot}}^{\text{GRB}} = 2.83 \times 10^{53}$ erg (see Table 2).

It is also worth to mention that this numerical value for $\Delta E_{\text{GW}}^{\text{max}}$ is an upper limit with respect to full numerical integrations of the gravitational wave radiation emitted in the neutron star binaries during the entire process of spiraling and merging (see, e.g., Ruffert & Janka 2001).

Additional contributions to the power of the gravitational wave due to higher multipole moments of the components, such as angular momentum J and quadrupole moment Q (deformation), are conceptually relevant corrections to the above formulas (see, e.g., Ryan 1995 and references therein, for details); however, they are quantitatively negligible for the present purpose. For instance, the first correction due to the spin angular momentum J of the neutron star components is given by $-11/4 j \Omega M$ in geometric units, where $j = cJ/(GM^2)$ is the dimensionless angular momentum parameter. This correction is only of the order of 10^{-2} for a binary orbit of very high angular frequency \sim kHz and for neutron stars with $M = 1.335 M_\odot$ and $j = 0.4$. We recall that the fastest observed pulsar, PSR J1748–2246ad, has a rotation frequency of 716 Hz (Hessels et al. 2006), which gives $j \sim 0.51 I_{45}/(M_0/M_\odot)^2 = 0.26 I_{45}$ with the latter value for a canonical neutron star of $M = 1.4 M_\odot$ where I_{45} is the moment of inertia in units of 10^{45} g cm². The first correction due to the quadrupole deformation multipole moment Q of the neutron star, given by

$-2Q\Omega^{4/3}M^{-5/3}$, is of the order of 10^{-3} for the same parameters with $Q \approx 4 \times 10^{43}$ g cm² \approx 3 km³, with the latter value in geometric units.

8. CONCLUSIONS

We show that the observations of the genuinely short GRB 090227B lead to crucial information about the binary neutron star progenitor. The data obtained from the electromagnetic spectrum allows us to probe crucial aspects of the correct theory of neutron stars and their equations of state. The baryon load parameter B obtained from the analysis of GRB 090227B leads to a most remarkable agreement of the baryonic matter expected to be ejected in a neutron star binary merger and validate the choice of the parameters of the binary components, $M_1 = M_2 = 1.34 M_\odot$ and $R_1 = R_2 = 12.24$ km. This represents a test of the actual neutron star parameters described by the recently developed self-consistent theory of neutron stars (Belvedere et al. 2012) which takes into account the strong, weak, electromagnetic, and gravitational interactions within general relativity and satisfy the condition of global charge neutrality.

We have discussed how the inference of the neutron star parameters, mass and radius, and the expected baryon load produced during the merger process depends on the nuclear equation of state as well as on the condition of global and local charge neutrality. We have also argued that the current observational constraints of pulsars on the mass–radius relation of compact stars rule out an alternative scenario given by strange quark stars, although they have core–crust transition and crust properties similar to those of the globally neutral neutron stars of Belvedere et al. (2012).

We computed the dynamics of the neutron star binary progenitor prior to the merger and emission of the GRB. We compare and contrast the classic description of the dynamics with the more general one given by the framework of the EOB formalism, which we use up to 4-PN order. We have shown that the classic binary dynamics overestimate the energy output in gravitational waves with respect to the more accurate dynamics of the EOB formalism. In addition, we showed the necessity of using the Padè approximant in order to keep the solution stable close to the merger point.

We estimate the detectability of GRB 090227B by the Advanced LIGO interferometer by computing the S/N up to the contact point of the binary components, for the theoretically inferred cosmological redshift, $z = 1.61$ (Muccino et al. 2013); see the left panel of Figure 7. We find that, at such a redshift, the gravitational waves' signal would produce a $\langle S/N \rangle \approx 0.32$, a value lower than necessary for a positive detection, $\langle S/N \rangle = 5$. We turn to estimate the redshift at which Advanced LIGO would detect this GRB with a $\langle S/N \rangle = 5$ (see Figure 7, right panel) we obtained $z \approx 0.09$ or a distance to the source $d_L \approx 381$ Mpc. Unfortunately, in the last 40 yr, no such a GRB has been observed.

From the dynamics, we estimated the total energy release in form of gravitational waves up to the point where the stars come in contact with each other (see Table 3); we compare and contrast it with the energy in X-rays and gamma rays released in the final emission of the GRB. We conclude that the emission of X-rays and gamma rays in a short GRB by a binary neutron star merger is at least one order of magnitude larger than the gravitational wave emission in the entire life of the binary including the last plunge.

We thank the anonymous referee for the comments and suggestions which helped to improve the presentation of our results. F. G. Oliveira acknowledges the support given by the International Relativistic Astrophysics Erasmus Mundus Joint Doctorate Program under the grant 2012–1710 from EACEA of the European Commission.

REFERENCES

- Alcock, C., Farhi, E., & Olinto, A. 1986, *ApJ*, **310**, 261
- Antoniadis, J., Freire, P. C. C., Wex, N., et al. 2013, *Sci*, **340**, 448
- Belvedere, R., Boshkayev, K., Rueda, J. A., & Ruffini, R. 2014, *NuPhA*, **921**, 33
- Belvedere, R., Pugliese, D., Rueda, J. A., Ruffini, R., & Xue, S.-S. 2012, *NuPhA*, **883**, 1
- Bernardini, M. G., Bianco, C. L., Caito, L., et al. 2007, *A&A*, **474**, L13
- Bernardini, M. G., Bianco, C. L., Caito, L., et al. 2008, in *AIP Conf. Ser.* 966, *Relativistic Astrophysics*, ed. C. L. Bianco & S. S. Xue (Melville, NY: AIP), 7
- Bianco, C. L., & Ruffini, R. 2005a, *ApJL*, **633**, L13
- Bianco, C. L., & Ruffini, R. 2005b, *ApJL*, **620**, L23
- Bini, D., & Damour, T. 2013, *PhRvD*, **87**, 121501
- Boguta, J., & Bodmer, A. R. 1977, *NuPhA*, **292**, 413
- Buonanno, A., & Damour, T. 1999, *PhRvD*, **59**, 084006
- Buonanno, A., & Damour, T. 2000, *PhRvD*, **62**, 064015
- Caito, L., Amati, L., Bernardini, M. G., et al. 2010, *A&A*, **521**, A80
- Caito, L., Bernardini, M. G., Bianco, C. L., et al. 2009, *A&A*, **498**, 501
- Damour, T. 2001, *PhRvD*, **64**, 124013
- Damour, T., Jaranowski, P., & Schäfer, G. 2000, *PhRvD*, **62**, 084011
- Damour, T., & Nagar, A. 2009, *PhRvD*, **79**, 081503
- Damour, T., & Nagar, A. 2010, *PhRvD*, **81**, 084016
- Damour, T., Nagar, A., & Villain, L. 2012, *PhRvD*, **85**, 123007
- de Barros, G., Amati, L., Bernardini, M. G., et al. 2011, *A&A*, **529**, A130
- Demorest, P. B., Pennucci, T., Ransom, S. M., Roberts, M. S. E., & Hessels, J. W. T. 2010, *Natur*, **467**, 1081
- Flanagan, É. E., & Hughes, S. A. 1998, *PhRvD*, **57**, 4535
- Glendenning, N. K., & Weber, F. 1992, *ApJ*, **400**, 647
- Goriely, S., Chamel, N., Janka, H.-T., & Pearson, J. M. 2011, *A&A*, **531**, A78
- Heinke, C. O., Rybicki, G. B., Narayan, R., & Grindlay, J. E. 2006, *ApJ*, **644**, 1090
- Hessels, J. W. T., Ransom, S. M., Stairs, I. H., et al. 2006, *Sci*, **311**, 1901
- Hirata, D., Toki, H., & Tanihata, I. 1995, *NuPhA*, **589**, 239
- Kobayashi, S., & Mészáros, P. 2003, *ApJ*, **589**, 861
- Lalazissis, G. A., König, J., & Ring, P. 1997, *PhRvC*, **55**, 540
- Landau, L. D., & Lifshitz, E. M. 1980, *Statistical Physics. Part I* (Oxford: Pergamon Press)
- Meegan, C. A., Fishman, G. J., Wilson, R. B., et al. 1992, *Natur*, **355**, 143
- Muccino, M., Ruffini, R., Bianco, C. L., Izzo, L., & Penacchioni, A. V. 2013, *ApJ*, **763**, 125
- Oppenheimer, J. R., & Volkoff, G. M. 1939, *PhRv*, **55**, 374
- Rotondo, M., Rueda, J. A., Ruffini, R., & Xue, S.-S. 2011, *PhLB*, **701**, 667
- Rueda, J. A., Ruffini, R., & Xue, S.-S. 2011, *NuPhA*, **872**, 286
- Ruffert, M., & Janka, H.-T. 2001, *A&A*, **380**, 544
- Ruffini, R., Bianco, C. L., Chardonnet, P., Fraschetti, F., & Xue, S.-S. 2001a, *ApJL*, **555**, L117
- Ruffini, R., Bianco, C. L., Chardonnet, P., Fraschetti, F., & Xue, S.-S. 2001b, *ApJL*, **555**, L113
- Ruffini, R., Bianco, C. L., Chardonnet, P., Fraschetti, F., & Xue, S.-S. 2001c, *ApJL*, **555**, L107
- Ruffini, R., Bianco, C. L., Chardonnet, P., Fraschetti, F., & Xue, S.-S. 2002, *ApJL*, **581**, L19
- Ruffini, R., Salmonson, J. D., Wilson, J. R., & Xue, S.-S. 2000, *A&A*, **359**, 855
- Ryan, F. D. 1995, *PhRvD*, **52**, 5707
- Sharma, M. M., Nagarajan, M. A., & Ring, P. 1993, *PhLB*, **312**, 377
- Sugahara, Y., & Toki, H. 1994, *NuPhA*, **579**, 557
- Tolman, R. C. 1939, *PhRv*, **55**, 364
- Trümper, J. E. 2011, *PrPNP*, **66**, 674
- Trümper, J. E., Burwitz, V., Haberl, F., & Zavlin, V. E. 2004, *NuPhS*, **132**, 560

L E

On binary-driven hypernovae and their nested late X-ray emission

R. Ruffini^{1,2,3,4}, M. Muccino^{1,2}, C. L. Bianco^{1,2}, M. Enderli^{1,3}, L. Izzo^{1,2}, M. Kovacevic^{1,3}, A. V. Penacchioni⁴,
G. B. Pisani^{1,3}, J. A. Rueda^{1,2,4}, and Y. Wang^{1,2}

¹ Dip. di Fisica and ICRA, Sapienza Università di Roma, piazzale Aldo Moro 5, 00185 Rome, Italy
e-mail: marco.muccino@icra.it

² ICRANet, piazza della Repubblica 10, 65122 Pescara, Italy

³ Université de Nice Sophia Antipolis, CEDEX 2, Grand Château Parc Valrose, BP 2135, 06103 Nice, France

⁴ ICRANet-Rio, Centro Brasileiro de Pesquisas Físicas, rua Dr. Xavier Sigaud 150, 22290-180 Rio de Janeiro, Brazil

Received 14 March 2014 / Accepted 28 April 2014

ABSTRACT

Context. The induced gravitational collapse (IGC) paradigm addresses the very energetic (10^{52} – 10^{54} erg) long gamma-ray bursts (GRBs) associated to supernovae (SNe). Unlike the traditional “collapsar” model, an evolved FeCO core with a companion neutron star (NS) in a tight binary system is considered as the progenitor. This special class of sources, here named “binary-driven hypernovae” (BdHNe), presents a composite sequence composed of four different episodes with precise spectral and luminosity features.

Aims. We first compare and contrast the steep decay, the plateau, and the power-law decay of the X-ray luminosities of three selected BdHNe (GRB 060729, GRB 061121, and GRB 130427A). Second, to explain the different sizes and Lorentz factors of the emitting regions of the four episodes, for definiteness, we use the most complete set of data of GRB 090618. Finally, we show the possible role of r-process, which originates in the binary system of the progenitor.

Methods. We compare and contrast the late X-ray luminosity of the above three BdHNe. We examine correlations between the time at the starting point of the constant late power-law decay t_a^* , the average prompt luminosity (L_{iso}), and the luminosity at the end of the plateau L_a . We analyze a thermal emission (~ 0.97 – 0.29 keV), observed during the X-ray steep decay phase of GRB 090618.

Results. The late X-ray luminosities of the three BdHNe, in the rest-frame energy band 0.3–10 keV, show a precisely constrained “nested” structure. In a space–time diagram, we illustrate the different sizes and Lorentz factors of the emitting regions of the three episodes. For GRB 090618, we infer an initial dimension of the thermal emitter of $\sim 7 \times 10^{12}$ cm, expanding at $\Gamma \approx 2$. We find tighter correlations than the Dainotti–Willingale ones.

Conclusions. We confirm a constant slope power-law behavior for the late X-ray luminosity in the source rest frame, which may lead to a new distance indicator for BdHNe. These results, as well as the emitter size and Lorentz factor, appear to be inconsistent with the traditional afterglow model based on synchrotron emission from an ultra-relativistic ($\Gamma \sim 10^2$ – 10^3) collimated jet outflow. We argue, instead, for the possible role of r-process, originating in the binary system, to power the mildly relativistic X-ray source.

Key words. supernovae: general – binaries: general – gamma-ray burst: general – black hole physics – stars: neutron – nuclear reactions, nucleosynthesis, abundances

1. Introduction

The induced gravitational collapse (IGC) paradigm has been widely illustrated (Ruffini et al. 2006, 2007, 2008; Rueda & Ruffini 2012; Izzo et al. 2012a). It assumes that long, energetic (10^{52} – 10^{54} erg) gamma-ray bursts (GRBs) associated to supernovae (SNe) originate in a close binary system composed of an evolved massive star (likely a FeCO core) in the latest phases of its thermonuclear evolution and a neutron star (NS) companion. From an observational point of view, the complete time sequence of the IGC paradigm binary system has been identified in GRB 090618 (Izzo et al. 2012b), GRB 101023 (Penacchioni et al. 2012), GRB 110907B (Penacchioni et al. 2013), and GRB 970828 (Ruffini et al. 2013). We name these especially energetic systems, here, fulfilling the IGC paradigm, “binary-driven hypernovae” (BdHNe), to differentiate them from the traditional less energetic hypernovae.

In this Letter we introduce the IGC paradigm space-time diagram for the four distinct emission episodes (see Fig. 1): *Episode 1* corresponds to the onset of the FeCO core SN explosion, creating a new-NS (ν -NS, see A). Part of the SN ejecta triggers an accretion process onto the NS companion (see Rueda & Ruffini 2012; Izzo et al. 2012a, and B in Fig. 1), and a prolonged

interaction between the ν -NS and the NS binary companion occurs (C). This leads to a spectrum with an expanding thermal component plus an extra power law (see Fig. 16 in Izzo et al. 2012b, and Fig. 4 in Ruffini et al. 2013).

Episode 2 occurs when the companion NS reaches its critical mass and collapses to a black hole (BH), emitting the GRB (D) with Lorentz factors $\Gamma \approx 10^2$ – 10^3 (for details, see e.g. Ruffini et al. 2010; Izzo et al. 2012b; Ruffini et al. 2013).

Episode 3, observed in the X-rays, shows very precise behavior consisting of a steep decay, starting at the end point of the prompt emission (see E), and then a plateau phase, followed by a late constant power-law decay (see, e.g., Izzo et al. 2012b; Penacchioni et al. 2012; Ruffini et al. 2013).

Episode 4, not shown in Fig. 1, corresponds to the optical SN emission due to the ^{56}Ni decay (see Arnett 1996) occurring after ~ 10 – 15 days in the cosmological rest frame. In all BdHNe, the SN appears to have the same luminosity as in the case of SN 1998bw (Amati et al. 2007). Although the presence of the SN is implicit in all the sources fulfilling the IGC paradigm, it is only detectable for GRBs at $z \lesssim 1$, in view of the limitations of the current optical telescopes.

We are going to see in this Letter that Episodes 1 and 2 can differ greatly in luminosity and timescale from source to source,

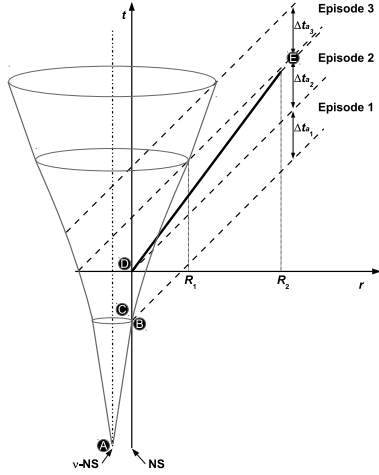


Fig. 1. IGC space–time diagram (not in scale) illustrates the relativistic motion of Episode 2 ($\Gamma \approx 500$, thick line) and the non-relativistic Episode 1 ($\Gamma \approx 1$) and Episode 3 ($\Gamma \approx 2$). Emissions from different radii, R_1 ($\sim 10^{13}$ cm) and R_2 ($\sim 10^{16}$ – 10^{17} cm), contribute to the transition point (E). Clearly, the X-ray luminosity originates in the SN remnant or in the newly-born BH, but not in the GRB.

while we confirm that in Episode 3, the late X-ray luminosities overlap: they follow a common power-law behavior with a constant slope in the source rest frame (Pisani et al. 2013). We point out here that the starting point of this power-law component is a function of the GRB isotropic energy E_{iso} .

The main goals of this Letter consist in a) comparing and contrasting the steep decay, the plateau, and the power-law decay of the X-ray luminosities as functions of E_{iso} by considering three selected GRBs (060729, 061121, and 130427A); b) pointing out the difference in the size and the Lorentz factors of the emitting regions of Episodes 1, 2, and 3 (for definiteness we use as prototype the source with the most complete dataset, GRB 090618); c) drawing attention to the possible role of the r-process, originating in the binary system of the progenitor, to power the mildly relativistic X-ray emission in the late phases of Episode 3.

2. The case of GRB 090618

We illustrate the difference in the emitting region sizes in the three episodes and their corresponding Lorentz factors:

Episode 1 has a thermal component expanding from $\sim 10^9$ cm to $\sim 10^{10}$ cm on a rest-frame timescale of ~ 30 s with an average velocity of $\sim 4 \times 10^8$ cm s $^{-1}$ (see Izzo et al. 2012b). The total energy is 4.1×10^{52} erg, well above the traditional kinetic energy expected in the early phases of a SN, and it originates in the accretion of the material of the SN ejecta on the companion NS in the binary system (Rueda & Ruffini 2012; Ruffini et al. 2013).

Episode 2 has been shown to be the ultra-relativistic prompt emission episode (e.g., the actual GRB) stemming from the collapse of the NS to a BH. Its isotropic energy is 2.5×10^{53} erg. The characteristic Lorentz factor at the transparency of the fireshell has been found to be $\Gamma = 490$ for GRB 090618. The characteristic spatial extension goes all the way up to $\sim 10^{16}$ – 10^{17} cm, reached at the end of Episode 2 (see Fig. 10 in Izzo et al. 2012b).

Episode 3 has an isotropic energy of $\approx 6 \times 10^{51}$ erg. A striking feature occurs during its steep decay phase: in the early observed 150 s, Page et al. (2011) have found a thermal component with a decreasing temperature from ~ 0.97 keV to ~ 0.29 keV (see also Starling et al. 2012). The surface radius

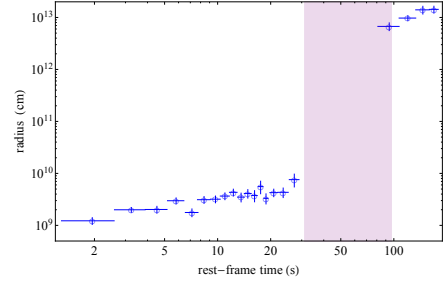


Fig. 2. Radii (open blue circles) of the emitting regions, measured in the cosmological rest frame. Episode 1 radius ranges from $\sim 10^9$ cm to $\sim 10^{10}$ and expands at $\Gamma \approx 1$ (Izzo et al. 2012b). The Episode 3 radius, in the early phases of the steep decay, starts from a value of $\sim 7 \times 10^{12}$ cm and expands at $\Gamma \approx 2$. The Episode 2 rest-frame duration is indicated by the shaded purple region. The expansion velocity at late times is expected to approach the asymptotic value of $0.1c$ observed in the optical spectra (Della Valle 2011), in the absence of any further acceleration process.

of the emitter can be inferred from the observed temperature T_0 and flux F_{BB} of the thermal component. We have, in fact (Izzo et al. 2012b),

$$r \approx \Gamma d_l (1+z)^{-2} \sqrt{F_{BB} / (\sigma T_0^4)}, \quad (1)$$

where d_l is the luminosity distance in the Λ CDM cosmological model and σ the Stefan-Boltzmann constant. As usual, $\Gamma = 1/\sqrt{1-\beta^2}$, where $\beta = v/c$ is the expansion velocity in units of the speed of light c .

In parallel, the relation between the detector arrival time t_a^d , the cosmological rest-frame arrival time t_a and the laboratory time t , is given by $t_a^d \equiv t_a(1+z) = t(1-\beta \cos \theta)(1+z)$, where θ is the displacement angle of the considered photon emission point from the line of sight (see, e.g., Bianco et al. 2001). We can then deduce the expansion velocity β , assumed to be constant, from the ratio between the variation of the emitter radius Δr and the emission duration in laboratory frame Δt , i.e. $\beta = \Delta r / (c \Delta t)$. Using the condition $\beta \leq \cos \theta \leq 1$ (Bianco et al. 2001), we obtain $0.75 \leq \beta \leq 0.89$ and, correspondingly, $1.50 \leq \Gamma \leq 2.19$ and radii $r \sim 10^{13}$ cm (see Fig. 2).

As is clear from Fig. 1, a sharp transition occurs between the end of Episode 2, where the characteristic dimensions reached by the GRB are $\sim 10^{16}$ – 10^{17} cm, and the emission at the beginning of X-ray luminosity, with an initial size of $\sim 7 \times 10^{12}$ cm. This leads to the conclusion that the X-ray emission of Episode 3 originates in the SN ejecta or in the accretion on the newly born BH and, anyway, not from the GRB.

3. The “nested” structure of Episode 3

We now turn to show the “nested” structure of the late X-ray luminosity. Pisani et al. (2013) have shown that the X-ray rest-frame 0.3–10 keV luminosity light curves present a constant decreasing power-law behavior, at $t_a \geq 10^4$ s, with typical slopes of $-1.7 \leq \alpha_X \leq -1.3$. This has been proven in a sample of six BdHNe: GRBs 060729, 061007, 080319B, 090618, 091127, and 111228, hereafter *golden sample* (GS, see, e.g., Izzo et al. 2013; Pisani et al. 2013). That the late X-ray emission could play a fundamental role as a distance indicator has been explored inferring the redshifts of GRBs 101023 and 110709B (Penacchioni et al. 2012, 2013). The IGC paradigm also allowed predicting ~ 10 – 15 days in the cosmological rest frame before its discovery, the occurrence of the SN associated to GRB 130427A, the most luminous source ever observed in γ rays with $E_{\text{iso}} \approx 10^{54}$ erg

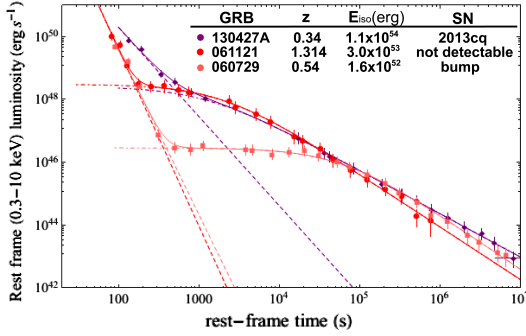


Fig. 3. Rest-frame 0.3–10 keV re-binned luminosity light curves of GRB 130427A (purple), GRB 061121 (red, shifted by 50 s in rest frame), and GRB 060729 (pink). The light curves are fitted by using a power-law for the steep decay phase (dashed lines) and the function in Eq. (2) for the plateau and the late decay phases (dot-dashed curves).

and $z = 0.34$ (Xu et al. 2013b; Flores et al. 2013). This was later confirmed by the observations (de Ugarte Postigo et al. 2013; Levan et al. 2013; Watson et al. 2013; Xu et al. 2013a).

We compare and contrast GRB 130427A X-ray data with GRB 060729, a member of the GS, and GRB 061121, which shows the general behavior of BdHNe. GRB 060729, at $z = 0.54$, has $E_{\text{iso}} = 1.6 \times 10^{52}$ erg (Grupe et al. 2007) and a SN bump in its optical afterglow (Cano et al. 2011). GRB 061121, at $z = 1.314$ (Bloom et al. 2006), has $E_{\text{iso}} = 3.0 \times 10^{53}$ erg, and its Episode 4 is clearly missing in view of the high cosmological redshift.

In Fig. 3 we have plotted the rebinned rest-frame 0.3–10 keV luminosity light curves of GRBs 130427A, 060729, and 061121. Their steep decay is modeled by a power-law function, i.e. $L_p(t_a/100)^{-\alpha_p}$, where L_p and α_p are the power-law parameters. The plateau and the late power-law decay are instead modeled by using the following phenomenological function

$$L(t_a) = L_X (1 + t_a/\tau)^{\alpha_X}, \quad (2)$$

where L_X , α_X , and τ , respectively, are the plateau luminosity, the late power-law decay index, and the characteristic timescale of the end of the plateau. From Eq. (2), we have defined the end of the plateau at the rest-frame time $t_a^* = \tau[(1/2)^{1/\alpha_X} - 1]$, when the luminosity of the plateau is half of the initial one, $L_a(t_a^*) = L_X/2$.

From this fitting procedure, we can conclude that the three BdHN systems considered here share the following properties:

- the power-law decay for the more energetic sources starts directly from the steep decay, well before the $t_a \approx 2 \times 10^4$ s, as indicated in Pisani et al. (2013); consequently, the plateau shrinks as a function of the increasing E_{iso} (see Fig. 3);
- the luminosities in the power-law decay are uniquely functions of the cosmological rest-frame arrival time t_a independently on the E_{iso} of each source (see Fig. 3);
- most remarkably, the overlapping of the X-ray light curves reveals a “nested” structure of BdHN Episodes 3.

In our sample of BdHNe, we verify the applicability of the Dainotti-Willingale relations $\langle L_{\text{iso}} \rangle - t_a^*$ and $L_a - t_a^*$ (Dainotti et al. 2008, 2011b; Willingale et al. 2007), where $\langle L_{\text{iso}} \rangle = E_{\text{iso}}/t_{a,90}$ is the averaged luminosity of the prompt and $t_{a,90}$ is the rest-frame t_{90} duration of the burst. The resulting correlations, $\log_{10} Y_i = m_i \log_{10} X_i + q_i$, are shown in Fig. 4. The parameters of each BdHN and the best fit parameters, m_i and q_i (where $i = 1, 2$), are summarized in Table 1. As is clear from the extra scatter values σ_i , our total BdHN sample provides tighter correlations. The extra scatter of the $L_a - t_a^*$, $\sigma = 0.26$, is less than the Dainotti et al. (2011a) ones, i.e., $\sigma = 0.76$ for the whole sample of 62 bursts and

$\sigma = 0.40$ for the best subsample of eight bursts (*U0095*). The Dainotti-Willingale correlations consider X-ray afterglows characterized by a steep decay, a plateau phase, and a late power-law decay (Nousek et al. 2006; Zhang et al. 2006), independently of their energetics. In our BdHN sample we limit the attention to a) the most energetic sources, 10^{52} – 10^{54} erg, b) the presence of four emission episodes (neglecting Episode 4 for $z > 1$), and c) sources with determined redshift and complete data at $t_a = 10^4$ – 10^6 s. All these conditions appear to be necessary to fulfill the nested structure in Fig. 3 and the tighter correlations between the astrophysical parameters $\langle L_{\text{iso}} \rangle$, L_a , and t_a^* in Fig. 4.

To explain the above nested power-law decay and constrained correlations, we consider the decay of heavy elements produced in the r-process as a viable energy source (Burbidge et al. 1957), originating in binary NS mergers (see, e.g., Li & Paczyński 1998; Janka et al. 1999; Rosswog et al. 2004; Oechslin et al. 2007; Goriely et al. 2011; Piran et al. 2014).

Li & Paczyński (1998) have shown that the emission from the surface of an optically thick expanding ejecta in an adiabatic regime provides a flat light curve (see also Arnett 1982). This can explain, in principle, the observed steep decay and plateau phase of Episode 3 (see Fig. 3). After the ejecta becomes transparent, the heating source term due to the nuclear decays of the heavy nuclei, generated via r-process, becomes directly observable and dominates. The avalanche of decays with different lifetimes then provides the total energy release per unit mass per time that follows a power-law distribution, whose decay index has been estimated to be $-1.4 \lesssim \alpha \lesssim -1.1$ (Metzger et al. 2010). These values are strikingly similar to the ones we have found in the late X-ray luminosity.

This power-law behavior is different from the exponential decay observed in the optical light curves of traditional SN, powered by the decay of a single element ($^{56}\text{Ni} \rightarrow ^{56}\text{Co} \rightarrow ^{56}\text{Fe}$), which is not produced in the avalanche of many decays as in the r-process.

4. Conclusions

To summarize, short GRBs have been shown to come from binary NS mergers (see, e.g., Goodman 1986; Paczynski 1986; Eichler et al. 1989; Meszaros & Rees 1997; Rosswog et al. 2003; Lee et al. 2004; and more recently Muccino et al. 2013). Our subclass of long, extremely energetic (10^{52} – 10^{54} erg) sources is also initially driven by a tight binary system, formed by a ν -NS and a companion NS, surrounded by the SN ejecta (see Fig. 1). Then we denoted these most energetic GRBs by “BdHNe”. This is clearly different from the gravitational collapse of a single massive progenitor star described by the collapsar model (Woosley 1993; MacFadyen & Woosley 1999; Woosley & Bloom 2006).

We compared and contrasted the late X-ray luminosities of three BdHNe with different E_{iso} , finding a nested structure. We showed tight correlations between $\langle L_{\text{iso}} \rangle$, L_a and t_a^* (see Fig. 4 and Table 1) in agreement with the Dainotti-Willingale ones.

The above scaling laws, the nesting, and the initial dimension of $\sim 7 \times 10^{12}$ cm and Lorentz factor of $\Gamma \approx 2$ obtained from the steep decay of the X-ray luminosity put stringent limits on alternative theoretical models. They do not appear to be explainable within the traditional fireball jetted model, originating in the synchrotron radiation emitted by a decelerating relativistic shell with $\Gamma \sim 10^2$ and colliding with the circumburst medium at distances $\sim 10^{16}$ cm (see, e.g., Sari et al. 1998; Piran 2005; Meszaros 2006; Gehrels et al. 2009, and reference therein). In this Letter we alternatively proposed that the late X-ray luminosity comes from the wide angle emission of the SN ejecta or

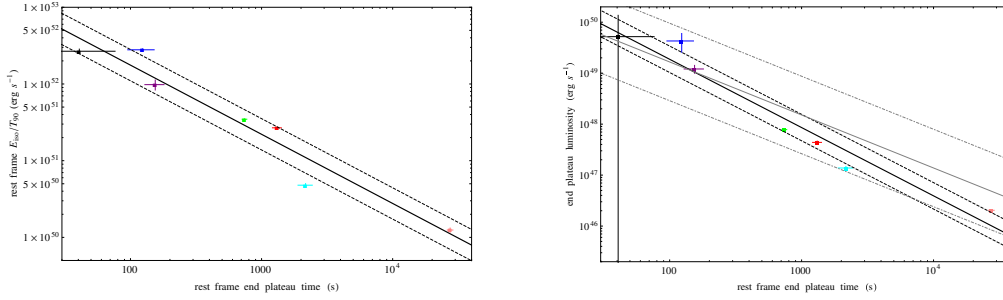


Fig. 4. The $\langle L_{\text{iso}} \rangle - t_a^*$ (left) and the $L_a - t_a^*$ (right) correlations (solid black lines) and the corresponding 1σ confidence levels (dashed black lines). The sources considered are GRB 060729 (pink), GRB 061007 (black), GRB 080319B (blue), GRB 090618 (green), GRB 091127 (red), GRB 111228A (cyan), and GRB 130427A (purple). The tighter BdHNe $L_a - t_a^*$ correlation is compared to the one in Dainotti et al. (2011a), corresponding to $m = -1.04$ and $q = 51.30$ (solid gray line) and $\sigma = 0.76$ (dot-dashed gray lines).

Table 1. List of the quantities of the sources considered and best fit parameters of the correlations in Fig. 4.

GRB	$\langle L_{\text{iso}} \rangle$ (10^{50} erg/s)	t_a^* (ks)	L_a (10^{47} erg/s)
060729	1.25 ± 0.08	27.4 ± 1.4	0.20 ± 0.01
061007	267 ± 18	0.041 ± 0.036	$521 \pm \text{unc}$
080319B	279 ± 7	0.12 ± 0.03	430 ± 170
090618	34.7 ± 0.3	0.74 ± 0.03	7.81 ± 0.17
091127	26.8 ± 0.3	1.31 ± 0.10	4.39 ± 0.26
111228A	4.79 ± 0.24	2.17 ± 0.27	1.38 ± 0.10
130427A	98 ± 15	0.16 ± 0.03	121 ± 21
Correlation	m_i	q_i	σ_i
$\langle L_{\text{iso}} \rangle - t_a^*$	$-(0.90 \pm 0.09)$	54.0 ± 0.3	0.20 ± 0.05
$L_a - t_a^*$	$-(1.34 \pm 0.14)$	52.0 ± 0.4	0.26 ± 0.08

in the accretion on the newly born BH. We call the attention on the role of the energy release in the SN ejecta from the decay of very heavy nuclei generated by r-process in binary NSs (Li & Paczyński 1998). This heavy nuclei avalanche decay (see, e.g., Metzger et al. 2010) may well explain the late X-ray luminosity of Episode 3. This emission follows the steep decay and plateau phase of the adiabatic optically thick expansion, prior to reaching transparency (see Fig. 3).

In the case of binary systems with longer periods and/or a lower accretion rate, which do not allow the NS companion to reach its critical mass and to form a BH, Episode 2 is missing. The presence of the companion NS will nevertheless strip the H and He envelopes of the core progenitor star. These sources have low energetic bursts ($E_{\text{iso}} < 10^{52}$ erg), such as GRB 060218 and GRB 980425, and their X-ray luminosity light curves do not overlap with the ones of our more energetic sample of BdHNe. These systems do not conform to the IGC paradigm and are traditional hypernovae¹.

Acknowledgements. This work made use of data supplied by the UK Swift Science Data Center at the University of Leicester. M.E., M.K., and G.B.P. are supported by the Erasmus Mundus Joint Doctorate Program by grant Nos. 2012-1710, 2013-1471, and 2011-1640, respectively, from the EACEA of the European Commission. We warmly thank the anonymous referee for very constructive suggestions that improved the presentation of this Letter.

References

Amati, L., Della Valle, M., Frontera, F., et al. 2007, A&A, 463, 913
 Arnett, D. 1996, Space Sci. Rev., 78, 559
 Arnett, W. D. 1982, ApJ, 253, 785
 Bianco, C. L., Ruffini, R., & Xue, S.-S. 2001, A&A, 368, 377
 Bloom, J. S., Perley, D. A., & Chen, H. W. 2006, GCN Circ., 5826
 Burbidge, E. M., Burbidge, G. R., Fowler, W. A., & Hoyle, F. 1957, Rev. Mod. Phys., 29, 547
 Cano, Z., Bersier, D., Guidorzi, C., et al. 2011, MNRAS, 413, 669
 Dainotti, M. G., Cardone, V. F., & Capozziello, S. 2008, MNRAS, 391, L79

¹ <http://nsm.utdallas.edu/texas2013/proceedings/3/1/Ruffini.pdf>

Dainotti, M. G., Fabrizio Cardone, V., Capozziello, S., Ostrowski, M., & Willingale, R. 2011a, ApJ, 730, 135
 Dainotti, M. G., Ostrowski, M., & Willingale, R. 2011b, MNRAS, 418, 2202
 de Ugarte Postigo, A., Xu, D., Leloudas, G., et al. 2013, GCN Circ., 14646, 1
 Della Valle, M. 2011, International Journal of Modern Physics D, 20, 1745
 Eichler, D., Livio, M., Piran, T., & Schramm, D. N. 1989, Nature, 340, 126
 Flores, H., Covino, S., Xu, D., et al. 2013, GRB Coordinates Network, Circular Service, 14491, 1
 Gehrels, N., Ramirez-Ruiz, E., & Fox, D. B. 2009, ARA&A, 47, 567
 Goodman, J. 1986, ApJ, 308, L47
 Goriely, S., Bauswein, A., & Janka, H.-T. 2011, ApJ, 738, L32
 Grupe, D., Gronwall, C., Wang, X.-Y., et al. 2007, ApJ, 662, 443
 Izzo, L., Rueda, J. A., & Ruffini, R. 2012a, A&A, 548, L5
 Izzo, L., Ruffini, R., Penacchioni, A. V., et al. 2012b, A&A, 543, A10
 Izzo, L., Pisani, G. B., Muccino, M., et al. 2013, EAS Pub. Ser., 61, 595
 Janka, H.-T., Eberl, T., Ruffert, M., & Fryer, C. L. 1999, ApJ, 527, L39
 Lee, W. H., Ramirez-Ruiz, E., & Page, D. 2004, ApJ, 608, L5
 Levan, A. J., Fruchter, A. S., Graham, J., et al. 2013, GRB Coordinates Network, Circular Service, 14686, 1
 Li, L.-X., & Paczyński, B. 1998, ApJ, 507, L59
 MacFadyen, A. I., & Woosley, S. E. 1999, ApJ, 524, 262
 Meszaros, P. 2006, Rep. Prog. Phys., 69, 2259
 Meszaros, P., & Rees, M. J. 1997, ApJ, 482, L29
 Metzger, B. D., Martínez-Pinedo, G., Darbha, S., et al. 2010, MNRAS, 406, 2650
 Muccino, M., Ruffini, R., Bianco, C. L., Izzo, L., & Penacchioni, A. V. 2013, ApJ, 763, 125
 Nousek, J. A., Kouveliotou, C., Grupe, D., et al. 2006, ApJ, 642, 389
 Oechslin, R., Janka, H.-T., & Marek, A. 2007, A&A, 467, 395
 Paczynski, B. 1986, ApJ, 308, L43
 Page, K. L., Starling, R. L. C., Fitzpatrick, G., et al. 2011, MNRAS, 416, 2078
 Penacchioni, A. V., Ruffini, R., Izzo, L., et al. 2012, A&A, 538, A58
 Penacchioni, A. V., Ruffini, R., Bianco, C. L., et al. 2013, A&A, 551, A133
 Piran, T. 2005, Rev. Mod. Phys., 76, 1143
 Piran, T., Korobkin, O., & Rosswog, S. 2014 [arXiv:1401.2166]
 Pisani, G. B., Izzo, L., Ruffini, R., et al. 2013, A&A, 552, L5
 Rosswog, S., Ramirez-Ruiz, E., & Davies, M. B. 2003, MNRAS, 345, 1077
 Rosswog, S., Speith, R., & Wynn, G. A. 2004, MNRAS, 351, 1121
 Rueda, J. A., & Ruffini, R. 2012, ApJ, 758, L7
 Ruffini, R., Bernardini, M. G., Bianco, C. L., et al. 2008, in The Eleventh Marcel Grossmann Meeting, eds. H. Kleinert, R. T. Jantzen, & R. Ruffini (Singapore: World Scientific), 368
 Ruffini, R., Bernardini, M. G., Bianco, C. L., et al. 2006, in The Tenth Marcel Grossmann Meeting., eds. M. Novello, S. Perez Bergliaffa, & R. Ruffini (Singapore: World Scientific), 369
 Ruffini, R., Bernardini, M. G., Bianco, C. L., et al. 2007, ESA SP, 622, 561
 Ruffini, R., Vereshchagin, G., & Xue, S.-S. 2010, Phys. Rep., 487, 1
 Ruffini, R., Izzo, L., Muccino, M., et al. 2013, A&A, submitted [arXiv:1311.7432]
 Sari, R., Piran, T., & Narayan, R. 1998, ApJ, 497, L17
 Starling, R. L. C., Page, K. L., Pe'Er, A., Beardmore, A. P., & Osborne, J. P. 2012, MNRAS, 427, 2950
 Watson, A. M., Butler, N., Kutuyev, A., et al. 2013, GCN Circ., 14666, 1
 Willingale, R., O'Brien, P. T., Osborne, J. P., et al. 2007, ApJ, 662, 1093
 Woosley, S. E. 1993, ApJ, 405, 273
 Woosley, S. E., & Bloom, J. S. 2006, ARA&A, 44, 507
 Xu, D., de Ugarte Postigo, A., Kruehler, T., et al. 2013a, GCN Circ., 14597, 1
 Xu, D., de Ugarte Postigo, A., Schulze, S., et al. 2013b, GCN Circ., 14478, 1
 Zhang, B., Fan, Y. Z., Dyks, J., et al. 2006, ApJ, 642, 354

Surface tension of the core-crust interface of neutron stars with global charge neutralityJorge A. Rueda,^{1,2} Remo Ruffini,^{1,2,3} Yuan-Bin Wu,^{1,2,3,*} and She-Sheng Xue^{1,2}¹*Dipartimento di Fisica and ICRA, Sapienza Università di Roma, Piazzale Aldo Moro 5, I-00185 Rome, Italy*²*ICRANet, Piazza della Repubblica 10, I-65122 Pescara, Italy*³*ICRANet, University of Nice-Sophia Antipolis, 28 Avenue de Valrose, 06103 Nice Cedex 2, France*

(Received 24 October 2013; published 17 March 2014)

It has been shown recently that taking into account strong, weak, electromagnetic, and gravitational interactions, and fulfilling the global charge neutrality of the system, a transition layer will happen between the core and crust of neutron stars, at the nuclear saturation density. We use relativistic mean field theory together with the Thomas-Fermi approximation to study the detailed structure of this transition layer and calculate its surface and Coulomb energy. We find that the surface tension is proportional to a power-law function of the baryon number density in the core bulk region. We also analyze the influence of the electron component and the gravitational field on the structure of the transition layer and the value of the surface tension, to compare and contrast with known phenomenological results in nuclear physics. Based on the above results we study the instability against Bohr-Wheeler surface deformations in the case of neutron stars obeying global charge neutrality. Assuming the core-crust transition at nuclear density $\rho_{\text{core}} \approx 2.7 \times 10^{14} \text{ g cm}^{-3}$, we find that the instability sets the upper limit to the crust density, $\rho_{\text{crust}}^{\text{crit}} \approx 1.2 \times 10^{14} \text{ g cm}^{-3}$. This result implies a nonzero lower limit to the maximum electric field of the core-crust transition surface and makes inaccessible a limit of quasilocal charge neutrality in the limit $\rho_{\text{crust}} = \rho_{\text{core}}$. The general framework presented here can be also applied to study the stability of sharp phase transitions in hybrid stars as well as in strange stars, both bare and with outer crust. The results of this work open the way to a more general analysis of the stability of these transition surfaces, accounting for other effects such as gravitational binding, centrifugal repulsion, magnetic field induced by rotating electric field, and therefore magnetic dipole-dipole interactions.

DOI: [10.1103/PhysRevC.89.035804](https://doi.org/10.1103/PhysRevC.89.035804)

PACS number(s): 26.60.-c, 97.60.Jd, 04.20.-q, 04.40.Dg

I. INTRODUCTION

The relativistic mean field theory (RMFT) of nuclear matter and the Thomas-Fermi model have attracted great attention during the last few decades. The simplest relativistic model of nuclear matter that accounts for the saturation properties of symmetric nuclear matter includes one scalar field which gives the attractive long-range part of the nuclear force and one vector field which gives the repulsive short-range; these two meson fields interact with nucleons through Yukawa couplings. This so-called σ - ω model has been considered by Duerr [1], Miller and Green [2], and later by Walecka [3]. The physical understanding of this model has been very well studied in the literature [4–11]. As recognized in Ref. [5], it is necessary to introduce additional isovector fields to obtain agreement with the empirical symmetry energy of nuclear matter at the saturation density. The model, containing Dirac nucleons together with a self-interacting scalar σ and a vector meson ω as well as an isovector meson ρ , has been widely used to this end.

With a very limited number of parameters, the RMFT has been shown to be able to give a quantitative description of a variety of nuclear properties [12–14]. Recently, taking into account the electromagnetic and weak interactions, the RMFT with the Thomas-Fermi approximation has gained remarkable successes in understanding the inhomogeneous structures and properties of low-density nuclear matter which is realized in

supernovae cores or in the crusts of neutron stars (see, e.g., Refs. [15–18]). The surface properties of nuclear matter such as surface tension and curvature energy play an important role in the description of these structures and also in other phenomena, for instance saddle-point configurations in nuclear fission, fragment distributions in heavy-ion collisions, and phase transitions between different phases of nuclear matter.

The nuclear surface properties at saturation density have been analyzed for a long time in the semi-infinite nuclear matter model using RMFT [3] or effective field theory [19–21] with the Thomas-Fermi approximation or Hartree-Fock approximation [5,22–30]. In the supranuclear regime realized in the interior of neutron stars, there is the possibility that phase transition occurs from hadronic to pion and kaon condensed phase as well as to quark matter phase (see, e.g., [31–33]). The surface tension of the transition layer between the hadronic and kaon condensed or quark matter phases has been calculated in the semi-infinite matter model, and the surface tension plays an important role in the structure of the phase transition region [34,35]. In the low-density (density smaller than the saturation density) case, as pointed out in [36], the shape of constituent nuclei is expected to change from spherical droplet to the so-called nuclear pasta structures such as cylindrical rod, slab, cylindrical tube, and spherical bubble. The surface tensions of nuclear pasta structures have been investigated and it has been pointed out that the pasta phase strongly depends on the value of the surface tension [15,16,18].

The importance of the extension of the Thomas-Fermi approximation to general relativistic systems such as neutron

*Corresponding author: wuyb@icranet.org

stars was emphasized in Ref. [37]. We showed there that the traditionally imposed condition of local charge neutrality is not consistent with the field equations and microphysical equilibrium for a system of neutrons, protons, and electrons in β equilibrium and obeying relativistic quantum statistics. Thus, only the condition of global but not local charge neutrality can be imposed. This leads to the appearance of gravitopolarization in the cores of neutron stars. The generalization of such a work to the case where the strong interactions between nucleons are accounted for was presented in [38]. Both the Thomas-Fermi approximation and RMFT were used. It was shown that the Einstein-Maxwell-Thomas-Fermi (EMTF) system of equations within RMFT supersede the traditional Tolman-Oppenheimer-Volkoff (TOV) [39,40] equations used for the construction of neutron star configurations.

Realistic neutron star configurations, including all the interactions between particles and the presence of a crust below nuclear density, were constructed in Ref. [41] by solving numerically the EMTF equations fulfilling the condition of global charge neutrality. As pointed out in [41], the self-consistent solution of these new equations of equilibrium leads to the existence of a transition layer between the core and the crust of the star. This is markedly different from the neutron star structure obtained from the solution of the TOV equations imposing local charge neutrality (see e.g., [42]), leading to a new mass-radius (M - R) relation of neutron stars. The core-crust transition layer in our configurations occurs near the nuclear saturation density ρ_{nuc} . The core (bulk region) inside this transition layer is a hadronic phase, and the crust outside this transition is composed of the nuclei lattice and the ocean of relativistic degenerate electrons and possibly neutrons at densities below nuclear saturation and larger than the estimated neutron drip value $\sim 4.3 \times 10^{11} \text{ g cm}^{-3}$. Inside the transition region a very strong electric field which is overwhelming the critical value $E_c = m_e^2 c^3 / (e\hbar)$ for vacuum break-down is developed, where m_e is the electron rest-mass. The e^+e^- pair creation from vacuum is, however, forbidden in the system due to the Pauli blocking of degenerate electrons.

In this article we study the surface properties of this transition layer formed near the nuclear saturation density. We calculate all the contributions to the surface tension as well as the electrostatic energy stored in this core-crust layer. We analyze the stability of these systems under the Bohr-Wheeler fission mechanism [43]. We analyze the role of the influence of the gravitational field on the structure of the transition layer and the surface tension. We also compare and contrast the surface energy of these neutron stars with the phenomenological results in nuclear physics.

The article is organized as follows. In Sec. II, we present the general formulation of the surface tension as well as the Coulomb energy for this core-crust transition layer. We formulate in Sec. II A the relativistic equations for a system of neutrons, protons, and electrons fulfilling the strong, electromagnetic, and gravitational interactions as well as β equilibrium. In Sec. II B, we use the semi-infinite matter model [44] to formulate the equations governing the surface tension for the transition layer of this system when the electron density is nearly equal to the proton density in the core bulk region. In Sec. III, we study the surface tension and the

Coulomb energy, neglecting the presence of the crust and the gravitational interaction. We calculate the surface structure and solve these equations to obtain the surface tension and the Coulomb energy at the nuclear saturation density in Sec. III A. Then we study in Sec. III B the dependence of the surface tension and the Coulomb energy on the baryon number density. In Sec. IV, we study the influence of fermion densities in the outside region (crust) on the surface tension and the Coulomb energy. In Sec. V, we study the structure and the surface tension as well as the Coulomb energy for the core-crust transition region in the presence of the gravitational field. We finally summarize and conclude in Sec. VI. We use units with $\hbar = c = 1$ throughout the article.

II. RELATIVISTIC EQUATIONS OF MOTION AND SURFACE TENSION

A. Relativistic equations of motion

As described in Ref. [41], the system we consider is composed of degenerate neutrons, protons, and electrons fulfilling global charge neutrality and β equilibrium. We include the strong, electromagnetic, weak, and gravitational interactions. To describe the nuclear interactions, we employ the RMFT with the Thomas-Fermi approximation. We adopt the phenomenological nuclear model of Boguta and Bodmer [5].

We introduce the nonrotating spherically symmetric spacetime metric

$$ds^2 = e^{\nu(r)} dt^2 - e^{\lambda(r)} dr^2 - r^2 d\theta^2 - r^2 \sin^2 \theta d\varphi^2, \quad (1)$$

where the $\nu(r)$ and $\lambda(r)$ are only functions of the radial coordinate r .

Within the Thomas-Fermi approximation and mean-field approximation, we can obtain the full system of general relativistic equations. A detailed description of this model can be found in Ref. [41]. We are here interested in the core-crust transition layer, which as we have shown happens in a tiny region [41] with a characteristic length scale $\sim \lambda_e = \hbar / (m_e c) \sim 100 \text{ fm}$. Correspondingly, the metric functions are essentially constant in this region. Thus in the core-crust transition layer the system of equations can be written as

$$\frac{d^2 V}{dr^2} + \frac{2}{r} \frac{dV}{dr} = -4\pi e e^{\nu_{\text{core}}/2} e^{\lambda_{\text{core}}} (n_p - n_e), \quad (2)$$

$$\frac{d^2 \sigma}{dr^2} + \frac{2}{r} \frac{d\sigma}{dr} = e^{\lambda_{\text{core}}} [\partial_\sigma U(\sigma) + g_s n_s], \quad (3)$$

$$\frac{d^2 \omega}{dr^2} + \frac{2}{r} \frac{d\omega}{dr} = -e^{\lambda_{\text{core}}} (g_\omega J_0^\omega - m_\omega^2 \omega), \quad (4)$$

$$\frac{d^2 \rho}{dr^2} + \frac{2}{r} \frac{d\rho}{dr} = -e^{\lambda_{\text{core}}} (g_\rho J_0^\rho - m_\rho^2 \rho), \quad (5)$$

$$E_e^F = e^{\nu_{\text{core}}/2} \mu_e - eV = \text{const}, \quad (6)$$

$$E_p^F = e^{\nu_{\text{core}}/2} \mu_p + g_\omega \omega + g_\rho \rho + eV = \text{const}, \quad (7)$$

$$E_n^F = e^{\nu_{\text{core}}/2} \mu_n + g_\omega \omega - g_\rho \rho = \text{const}, \quad (8)$$

where the notations $\omega_0 \equiv \omega$, $\rho_0 \equiv \rho$, and $A_0 \equiv V$ for the time components of the meson fields have been introduced. Here $\mu_i = \sqrt{(P_i^F)^2 + \tilde{m}_i^2}$ and $n_i = (P_i^F)^3 / (3\pi^2)$ are the free chem-

ical potential and number density of the i -fermion species with Fermi momentum P_i^F . The particle effective masses are $\tilde{m}_N = m_N + g_s \sigma$ and $\tilde{m}_e = m_e$, where m_i stands for the rest mass of each i -fermion species. $e^{\nu_{\text{core}}} \equiv e^{\nu(R_{\text{core}})}$ and $e^{\lambda_{\text{core}}} \equiv e^{\lambda(R_{\text{core}})}$ are the metric functions evaluated at the core radius R_{core} . g_s , g_ω , and g_ρ are the coupling constants of the σ , ω , and ρ fields, e is the fundamental electric charge, and m_ω and m_ρ are the masses of ω and ρ . The scalar self-interaction potential is

$$U(\sigma) = \frac{1}{2} m_\sigma^2 \sigma^2 + \frac{1}{3} g_2 \sigma^3 + \frac{1}{4} g_3 \sigma^4, \quad (9)$$

with the σ meson mass m_σ and the third- and fourth- order constants of the self-scalar interactions g_2 and g_3 .

The generalized Fermi energies of electrons, protons, and neutrons, E_e^F , E_p^F , and E_n^F (so-called the Klein potentials [38]), are linked by the β equilibrium [45] of protons, neutrons, and electrons,

$$E_n^F = E_p^F + E_e^F. \quad (10)$$

The scalar density n_s is given by the expectation value

$$n_s = \langle \bar{\psi}_N \psi_N \rangle = \frac{2}{(2\pi)^3} \sum_{i=n,p} \int_0^{P_i^F} d^3k \frac{\tilde{m}_N}{\epsilon_i(k)}, \quad (11)$$

where $\epsilon_i(k) = \sqrt{k^2 + \tilde{m}_i^2}$ is the single-particle energy, and ψ_N is the nucleon isospin doublet. In the static case, the nonvanishing components of the currents are

$$J_0^{ch} = e^{\nu_{\text{core}/2} (n_p - n_e), \quad (12)$$

$$J_0^\omega = e^{\nu_{\text{core}/2} (n_n + n_p), \quad (13)$$

$$J_0^\rho = e^{\nu_{\text{core}/2} (n_p - n_n), \quad (14)$$

here $n_b = n_p + n_n$ is the baryon number density.

The parameters of the nuclear model, namely the coupling constants g_s , g_ω , and g_ρ , the meson masses m_σ , m_ω , and m_ρ , and the self-scalar interaction constants g_2 and g_3 are fixed by fitting nuclear experimental data. We here use the parameters of the NL3 parametrization [46], shown in Table I.

Since the equation of state (EOS) obtained from the RMFT is very stiff (see, e.g., [42]), it is natural to evaluate its consequences on causality. In order to do this, we compute the material sound velocity, $v_s^2 = d\varepsilon/d\mathcal{P}$, as a function of the central density $\rho(0) = \varepsilon(0)/c^2$ of the configuration, where $\varepsilon = T_0^0$ and $\mathcal{P} = -T_1^1$ are total energy-density and pressure of the system, T_0^0 and T_1^1 being the 0-0 and 1-1 components of the energy-momentum tensor [41].

The result is shown in Fig. 1. We recall that the instability against gravitational collapse sets in at the turning point in the M - $\rho(0)$ diagram, namely at the first maximum in the sequence of equilibrium configurations with increasing central density, namely $dM/d\rho(0) = 0$. Such a point gives us the

TABLE I. The parameters of the nuclear model from NL3.

m_σ (MeV)	508.194	g_ω	12.8680
m_ω (MeV)	782.501	g_ρ	4.4740
m_ρ (MeV)	763.000	g_2 (fm $^{-1}$)	-10.4310
g_s	10.2170	g_3	-28.8850

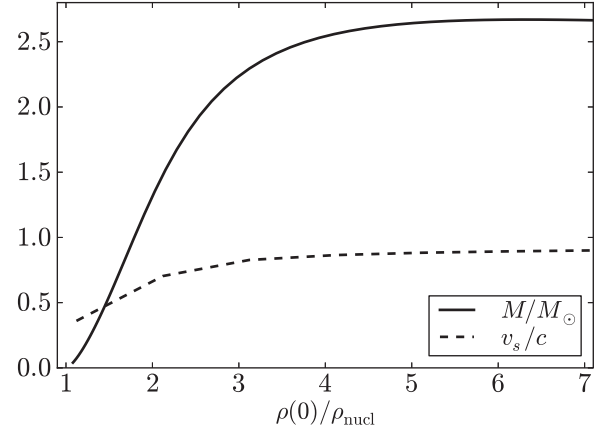


FIG. 1. The dependence of the total mass M of the star and the material sound velocity v_s on the central density $\rho(0)$ of the configuration.

maximum stable mass M_{max} , which for the present EOS is $M_{\text{max}} \approx 2.67 M_\odot$, where M_\odot is the solar mass. It can be seen from Fig. 1 that $v_s < c$, where c is the velocity of light, at any density in the entire range of $\rho(0)$ of the stable configurations, and therefore the used EOS does not violate causality.

It is important to mention that the above critical point for the gravitational collapse does not coincide with the point of backbending of the M - R relation (see, e.g., Figs. 6 and 14 in [41]). Therefore the backbending in the M - R diagram does not indicate any sort of instability.

B. Surface tension for semi-infinite matter

As shown in [41], in the bulk hadronic phase of neutron star cores, the charge separation is very small, so the electron density n_{eb} is nearly equal to the proton density n_{pb} . In addition, the core-crust transition layer has a characteristic length scale of the order of the electron Compton wavelength; this is very small compared to the radius of neutron stars. So it is a good approximation to use the semi-infinite matter model to construct the surface tension for the system we consider here. We construct the surface tension for the transition layer of this system following the method of Baym, Bethe, and Pethick (BBP) [44].

In the semi-infinite matter model, one assumes a plane surface with small thickness compared with the bulk region size separating two semi-infinite regions, represented here by the inside core bulk and the outside crust. The number density of the i -fermion species ($i = n, p, e$) $n_i(r)$ approaches the bulk density of the i -fermion species n_{ib} as the position $\bar{r} \equiv (r - R_{\text{core}}) \rightarrow -\infty$, and approaches the density in the outside region of the i -fermion species n_{io} as the $\bar{r} \rightarrow +\infty$. To construct the surface tension, one imagines a reference system with a sharp surface at $\bar{r} = a_i$ at which fermion densities and meson fields fall discontinuously from the core bulk region to the outside crust region. Following Ref. [44], the location of the reference surface for the i -fermion species is defined by the condition that the reference system has the same number of the i -fermion species as the original system. Following the definition of fermion number in the curved spacetime, Eq. (1)

(see, e.g., [47]), the i -fermion species number N_i is given by

$$N_i = 4\pi \int e^{\lambda/2} r^2 n_i(r) dr. \quad (15)$$

Since the metric functions are constant in the surface region we consider as described in Sec. II A, and the size of the surface region is very small compared to the radius of neutron stars, we can treat $e^{\lambda/2} r^2$ as a constant in the integral, the location of the reference surface for the i -fermion species is given by

$$\int_{-\infty}^{a_i} d\bar{r} [n_i(\bar{r}) - n_{ib}] + \int_{a_i}^{\infty} dr [n_i(\bar{r}) - n_{io}] = 0, \quad i = n, p, e. \quad (16)$$

Applying the definition of the reference surface in Eq. (16) to the neutron, proton, and electron distributions yields a slightly different reference surface.

Similar to the definition of the reference surface for the fermion, we define the location of the reference surfaces for meson fields by

$$\int_{-\infty}^{a_i} d\bar{r} [F_i(\bar{r}) - F_{ib}] + \int_{a_i}^{\infty} d\bar{r} [F_i(\bar{r}) - F_{io}] = 0, \quad i = \sigma, \omega, \rho, \quad (17)$$

where $F_i(\bar{r})$ is the time component of the i -meson field, F_{ib} is the time component of the i -meson field in the bulk region, and F_{io} is the time component of the i -meson field in the outside region.

The energy associated to the density $\varepsilon(r) = T_0^0$, where T_β^α is the energy-momentum tensor of the system, can be calculated in the spherically symmetric metric by (see, e.g., [47])

$$E_t = 4\pi \int e^{(v+\lambda)/2} r^2 \varepsilon(r) dr. \quad (18)$$

Thus, the total surface tension can be written as the sum of three contributions,

$$\sigma_t = \sigma_N + \sigma_e + \sigma_C, \quad (19)$$

where we have introduced the nuclear surface tension following the method of BBP [44],

$$\sigma_N = \sum_{i=n,p,\sigma,\omega,\rho} e^{(v_{\text{core}}+\lambda_{\text{core}})/2} \times \left\{ \int_{-\infty}^{a_i} [\epsilon_i(\bar{r}) - \epsilon_{ib}] d\bar{r} + \int_{a_i}^{\infty} [\epsilon_i(\bar{r}) - \epsilon_{io}] d\bar{r} \right\}, \quad (20)$$

the electron surface tension

$$\sigma_e = e^{(v_{\text{core}}+\lambda_{\text{core}})/2} \times \left\{ \int_{-\infty}^{a_e} [\epsilon_e(\bar{r}) - \epsilon_{eb}] d\bar{r} + \int_{a_e}^{\infty} [\epsilon_e(\bar{r}) - \epsilon_{eo}] d\bar{r} \right\}, \quad (21)$$

and the surface tension for the electric field as

$$\sigma_C = e^{(v_{\text{core}}+\lambda_{\text{core}})/2} \int_{-\infty}^{\infty} \epsilon_E(\bar{r}) d\bar{r}. \quad (22)$$

with $\epsilon_i(\bar{r})$ the energy density of the i species of fermion or meson fields, ϵ_{ib} is the energy density of the i species of fermion or meson fields in the bulk region, ϵ_{io} is the energy density of the i species of fermion or meson fields in the outside region, and $\epsilon_E(\bar{r}) = E^2/(8\pi)$ is the electrostatic energy density. In the curved spacetime equation (1), the electric field is given by (see, e.g., [41])

$$E = e^{-(\lambda_{\text{core}}+v_{\text{core}})/2} \frac{dV}{dr}. \quad (23)$$

It is important to clarify how the values of n_{io} and ϵ_{io} are obtained. As we showed in Ref. [41], the Einstein-Maxwell-Thomas-Fermi equations have to be solved under the constraint of global charge neutrality and not local charge neutrality, as in the traditional TOV-like treatment. In the latter locally neutral configurations, the continuity of total pressure leads to neutron stars with a crust starting from nuclear density, where the clusterization of nucleons starts to be preferred over the homogenous phase of the core, all the way up to low densities in the surface. The region between nuclear density and the neutron-drip density, $\rho_{\text{drip}} \approx 4.3 \times 10^{11} \text{ g cm}^{-3}$, is called the *inner crust*, and at lower densities, $\rho < \rho_{\text{drip}}$, the *outer crust*. In this case the continuity of the pressure does not ensure the continuity of the particle generalized chemical potentials. For electrons it implies an inconsistency since the mismatching of the electrochemical potential implies the existence of a Coulomb potential energy, not accounted for in such a treatment (see, e.g., Ref. [37]).

In the globally neutral case, there is a different core-crust boundary problem: the generalized fermion chemical potentials have to match, at the end of the core-crust transition boundary layer, their corresponding values at the base of the crust (outside region); i.e., they must satisfy a condition of continuity (see Ref. [41] for details). It implies that the values of n_{io} and ϵ_{io} depend on the density at the base of the crust under consideration.

We first consider below in Sec. III the surface tension of the system neglecting the presence of the crust. Then, the more realistic case of a neutron star with a crust is considered in Sec. IV. Configurations with only outer crust as well as configurations with both inner and outer crust are studied.

Turning to the Coulomb energy, it is important to remark that, owing to the small charge separation present in the system in the core bulk region, we can assume that the electric field only exists in the transition layer surface. Thus we can consider the electrostatic energy as a surface property of the system, hence contributing to the surface energy. This is a major difference between the present system and an ordinary nucleus where the electrostatic energy is a volume property.

The relation between the surface energy and Coulomb energy is very important for a nucleus. As shown by Bohr and Wheeler [43] when the condition

$$E_{\text{coul}} > 2E_{\text{sur}} \quad (24)$$

is satisfied, the nucleus becomes unstable against nuclear fission; here E_{coul} is the Coulomb energy of the nucleus and E_{sur} is the surface energy of the nucleus. It is important to recall that the idealized picture of the deformed nucleus of Bohr and Wheeler is represented by two positively charged

spheres joined by a nuclear attraction neck. It is thus the interplay of the Coulomb and nuclear surface energies that determines the lower energy state. Following this argument one could think that, since we are treating here a globally neutral system, such an instability mechanism is absent. However, the condition (24) can be also obtained by requesting that a uniformly charged spheroid, constructed from an axially symmetric deformation at constant volume of a uniformly charged sphere, be energetically favorable. From a careful look at the derivation of Eq. (24)—see, e.g., Ref. [48]—it can be seen that this result follows from the fact that Coulomb energy of the unperturbed system (the sphere) depends on the radius as $E_{\text{coul}} \propto R^{-1}$. Such an inverse radius dependence holds also in the case of a uniformly charged shell, and also in the case of the globally neutral massive nuclear density cores studied in Refs. [49,50], which fully reflect the properties of the system studied in this work. We then expect that the Bohr-Wheeler condition of instability against fission given by Eq. (24) applies also to our system. Clearly such a condition is obtained keeping the system at nuclear density and neglecting the extra binding effect of gravity.

In thermodynamics, the surface tension is related to the mechanical work needed to increase a surface area [51],

$$dW = \sigma dS, \quad (25)$$

here σ is the surface tension, dS is the variation of the surface area, and dW is the mechanical work needed to increase the surface area of the system. In this point of view, a system with a positive surface tension has an attractive nature, and a system with a negative surface tension has a repulsive nature.

Equations (19)–(22) show that the surface tension mainly depends on the fermion density and meson field profiles and the energy densities of fermions and meson fields. The energy density of the i -fermion species is given by

$$\epsilon_i(\bar{r}) = \frac{1}{8\pi^2} \left\{ P_i^F \sqrt{(P_i^F)^2 + \tilde{m}_i^2} [2(P_i^F)^2 + \tilde{m}_i^2] - \tilde{m}_i^4 \ln \frac{P_i^F + \sqrt{(P_i^F)^2 + \tilde{m}_i^2}}{\tilde{m}_i} \right\}, \quad (26)$$

and the energy densities of the meson fields are (see, e.g., [47])

$$\epsilon_\sigma(\bar{r}) = \frac{1}{2} e^{-\lambda_{\text{core}}} \left(\frac{d\sigma}{d\bar{r}} \right)^2 + U(\sigma), \quad (27)$$

$$\epsilon_\omega(\bar{r}) = \frac{1}{2} e^{-(\lambda_{\text{core}} + \nu_{\text{core}})} \left(\frac{d\omega}{d\bar{r}} \right)^2 + \frac{1}{2} e^{-\nu_{\text{core}}} m_\omega^2 \omega^2, \quad (28)$$

$$\epsilon_\rho(\bar{r}) = \frac{1}{2} e^{-(\lambda_{\text{core}} + \nu_{\text{core}})} \left(\frac{d\rho}{d\bar{r}} \right)^2 + \frac{1}{2} e^{-\nu_{\text{core}}} m_\rho^2 \rho^2, \quad (29)$$

$$\epsilon_E(\bar{r}) = e^{-(\lambda_{\text{core}} + \nu_{\text{core}})} \frac{1}{8\pi} \left(\frac{dV}{d\bar{r}} \right)^2. \quad (30)$$

We can solve Eqs. (2)–(8) together with the β equilibrium (10) to obtain the fermion density and meson field profiles. Following the similar method in Ref. [41], this system of equations can be numerically solved with appropriate conditions and approximations:

- (i) set a value for baryon number density of the bulk region $n_{bb} = n_{nb} + n_{pb}$;
- (ii) in the bulk core region the electron density n_{eb} is nearly equal to the proton density n_{pb} , i.e., $n_{pb} \simeq n_{eb}$;
- (iii) set values for $e^{\nu_{\text{core}}}$ and $e^{-\lambda_{\text{core}}}$;
- (iv) the values of n_{io} have to match their corresponding values at the edge of the crust.

III. SURFACE TENSION NEGLECTING THE PRESENCE OF A CRUST

A. Surface tension at nuclear saturation density

We first consider in this section the surface properties of this transition layer neglecting the presence of the crust and the gravitational interaction, i.e., $n_{io} = 0$ and $(e^{\nu_{\text{core}}}, e^{-\lambda_{\text{core}}}) \rightarrow 1$, as a special case to gain some physical insight into this transition layer. Also we assume here the baryon number density of the bulk region to be the nuclear saturation density, $n_{bb} = n_{nb} + n_{pb} = n_{\text{nucl}} = 0.16 \text{ fm}^{-3}$. The solution of Eqs. (2)–(8) in this case is shown in Fig. 2. Since the fermion densities tend to be zero in the outside region, the thickness of the surface region for electrons should be infinite. However, we just show the results up to a very small electron density here, due to the plot scale and the accuracy of the numerical calculation. As shown in Fig. 2, before a sharp decrease of the proton and neutron densities, there is a bump on the proton density profile due to Coulomb repulsion while the electron density profile decreases.

Using the definitions in Eqs. (19)–(22), we can calculate the surface tensions for this transition layer. The results are shown in Table II. In order to study the effect of the ρ meson, we also show in Table II the surface tensions in the case when the ρ meson is not present. The presence of ρ decreases the

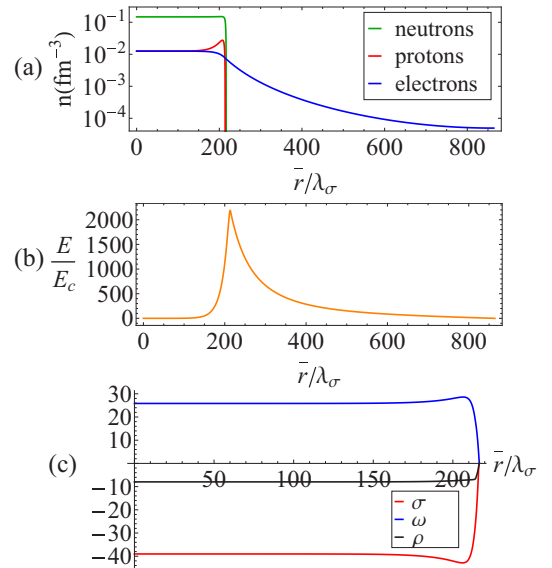


FIG. 2. (Color online) (a) Fermion density profiles in units of fm^{-3} . (b) Electric field in units of the critical field $E_c = m_e^2 c^3 / (e\hbar)$. (c) Meson fields σ , ω , and ρ in units of MeV. Here $n_{bb} = n_{\text{nucl}}$, $n_{io} = 0$, and $(e^{\nu_{\text{core}}}, e^{-\lambda_{\text{core}}}) \rightarrow 1$. $\lambda_\sigma = \hbar / (m_\sigma c) \sim 0.4 \text{ fm}$ is the Compton wavelength of the σ meson.

TABLE II. Total and specific surface tensions in MeV fm^{-2} of the transition layer with and without the presence of the ρ meson. We set here $n_{bb} = n_{\text{nucl}}$, $n_{io} = 0$, and $(e^{\nu_{\text{core}}}, e^{-\lambda_{\text{core}}}) \rightarrow 1$.

	σ_t	σ_N	σ_e	σ_C
$\sigma \omega$	6.28	7.07	-1.72	0.92
$\sigma \omega \rho$	3.10	7.30	-8.34	4.14

total surface tension σ_t but increases the Coulomb energy, and so σ_C . We can see that the difference of the surface tension for nucleons, σ_N , in the presence and absence of the ρ meson is relatively small with respect to the changes on the electron component and the electric field. We can explain this small difference from the fact that, although the ρ meson increases the proton to neutron density ratio, in neutron stars the β equilibrium in the presence of degenerate electrons leads to a high isospin asymmetry $1 - 2Z/A \approx 1$, hence the system is still dominated by the neutron component, as we show below.

It is interesting to compare the above results with the nuclear surface tension in the literature. The nuclear surface properties at saturation density have been widely discussed in relativistic and nonrelativistic models. The value of the nuclear surface tension in the literature is around $\sigma_L \sim 1 \text{ MeV fm}^{-2}$; see, e.g., Refs. [27,28]. The difference between our result in Table II and σ_L is mainly due to the fact that the presence of degenerate electrons changes the proton and neutron density profiles and also leads to a high isospin asymmetry of our system as a byproduct of the β -equilibrium condition. Especially, there is a bump on the density profiles in our system, which would not appear in the case of normal nuclear matter. Further discussion about this point is given below; see also Table III.

In order to understand where the surface tension comes from, we calculate the contribution of each fermion and meson field to the surface tension as

$$\sigma_n = \int_{-\infty}^{a_n} [\epsilon_n(z) - \epsilon_{nb}] dz + \int_{a_n}^{\infty} [\epsilon_n(z) - \epsilon_{no}] dz, \quad (31)$$

$$\sigma_p = \int_{-\infty}^{a_p} [\epsilon_p(z) - \epsilon_{pb}] dz + \int_{a_p}^{\infty} [\epsilon_p(z) - \epsilon_{po}] dz, \quad (32)$$

$$\sigma_e = \int_{-\infty}^{a_e} [\epsilon_e(z) - \epsilon_{eb}] dz + \int_{a_e}^{\infty} [\epsilon_e(z) - \epsilon_{eo}] dz, \quad (33)$$

$$\sigma_\sigma = \int_{-\infty}^{a_\sigma} [\epsilon_\sigma(z) - \epsilon_{\sigma b}] dz + \int_{a_\sigma}^{\infty} [\epsilon_\sigma(z) - \epsilon_{\sigma o}] dz, \quad (34)$$

$$\sigma_\omega = \int_{-\infty}^{a_\omega} [\epsilon_\omega(z) - \epsilon_{\omega b}] dz + \int_{a_\omega}^{\infty} [\epsilon_\omega(z) - \epsilon_{\omega o}] dz, \quad (35)$$

$$\sigma_\rho = \int_{-\infty}^{a_\rho} [\epsilon_\rho(z) - \epsilon_{\rho b}] dz + \int_{a_\rho}^{\infty} [\epsilon_\rho(z) - \epsilon_{\rho o}] dz. \quad (36)$$

The results are shown in Table III. For the sake of comparison we also show the results in the case of ordinary nuclear matter, namely for a system without the presence of electrons. As shown in Ref. [41], comparing to the profiles in the case without the presence of the ρ meson, the presence of the ρ meson leads to larger proton and electron densities, and a larger bump of proton density happens. This effect is felt indirectly by neutrons (although much less strongly), due to

TABLE III. Contribution of each fermion and meson field to the surface tension, in MeV fm^{-2} . First row: the transition layer without the presence of the ρ meson. Second row: the transition layer with the presence of the ρ meson. Third row: normal nuclear matter (without the presence of electrons). We set $n_{bb} = n_{\text{nucl}}$, $n_{io} = 0$, and $(e^{\nu_{\text{core}}}, e^{-\lambda_{\text{core}}}) \rightarrow 1$.

	σ_n	σ_p	σ_e	σ_σ	σ_ω	σ_ρ
$n p e \sigma \omega$	3.54	-0.36	-1.72	3.16	0.73	
$n p e \sigma \omega \rho$	-27.35	-5.19	-8.34	22.20	19.93	-2.28
$n p \sigma \omega \rho$	19.43	12.23		-16.08	-13.83	-0.04

the coupled nature of the system of equations (2)–(8). There is no such bump of the profiles in the case of normal nuclear matter. Comparing the results of the three cases in Table III, the effect of the bump of proton density on the surface tension is significant. The bump on the profiles decreases the value of the surface tension for fermions and increases the one for bosons. These results provide evidence of large effect of electromagnetic interaction and electrons on the proton and neutron density profiles, and therefore on the global value of the surface energy of the system. It can be seen from Table III that we obtain a surface tension of ordinary nuclear matter at saturation density (see the last line), $\sigma_N \approx 1.7 \text{ MeV fm}^{-2}$. In our calculation, n_n is slightly larger than n_p according to the β equilibrium. This result is in agreement with the nuclear surface tension with a small neutron excess, e.g., in Ref. [27].

B. Influence of baryon number density on the surface tension

In order to study the dependence of the surface tension on the baryon number density, we calculate the surface tensions for different n_{bb} following the similar procedure in Sec. III A. The results are shown in Fig. 3. Here the presence of the crust and the gravitational interaction is neglected, i.e., $n_{io} = 0$ and $(e^{\nu_{\text{core}}}, e^{-\lambda_{\text{core}}}) \rightarrow 1$. From the results, the total surface tension can be fitted by

$$\sigma_{t,\text{fit}} = 1.05 + 2.02 \left(\frac{n_{bb}}{n_{\text{nucl}}} \right)^{3.33} (\text{MeV fm}^{-2}), \quad (37)$$

the surface tension for electric field can be fitted by

$$\sigma_{C,\text{fit}} = -0.37 + 4.50 \left(\frac{n_{bb}}{n_{\text{nucl}}} \right)^2 (\text{MeV fm}^{-2}), \quad (38)$$

and the surface tension for nucleons can be fitted by

$$\sigma_{N,\text{fit}} = 0.95 + 6.33 \left(\frac{n_{bb}}{n_{\text{nucl}}} \right)^{2.91} (\text{MeV fm}^{-2}). \quad (39)$$

As shown by BBP in [44], the phenomenological surface tension for nucleons within the Thomas-Fermi approximation can be written as

$$\sigma_{\text{sur}}^{\text{BBP}} = B(W_o - W_i)^{\frac{1}{2}} (n_i - n_o)^{\frac{3}{2}}, \quad (40)$$

where B is a constant, W_o and W_i are the binding energies per nucleon in the outside and inside bulk regions, n_o and n_i are the nucleon number densities in the outside and inside bulk regions. In the case of this section, we set the fermion

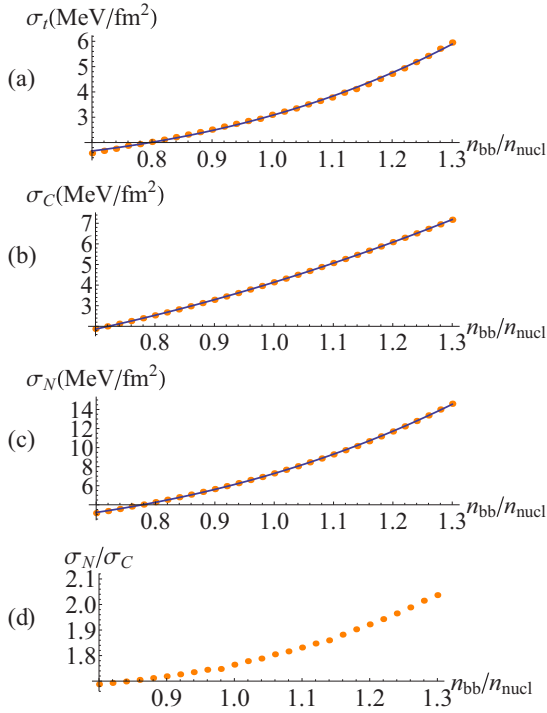


FIG. 3. (Color online) The dependence of the surface tension of the transition layer on the baryon number density in the bulk region. Here $n_{i_o} = 0$ and $(e^{v_{\text{core}}}, e^{-\lambda_{\text{core}}}) \rightarrow 1$. (a) The total surface tension σ_t , compared with the fit given in Eq. (37). (b) Surface tension for electric field σ_C , compared with the fit given in Eq. (38). (c) Surface tension for nucleons σ_N , compared with the fit given in Eq. (39). (d) Ratio of surface tension for nucleons and the surface tension for electric field σ_N/σ_C .

densities and meson fields to be zero in the outside region, i.e., $n_o = W_o = 0$. Since the fractional concentration of protons in the system we consider here is small, the binding energy per nucleon is [44]

$$W(k, x) = W(k, 0) + f(x) \approx 19.74k^2 - k^3 \frac{40.4 - 1.088k^3}{1 + 2.545k} + f(x), \quad (41)$$

where k is defined by $n = 2k^3/(3\pi^2)$, with n the nucleon number density, and x is the fractional concentration of protons. The function $f(x)$ is a small correction to $W(k, 0)$ since x is small in our system. From Eq. (41), one can estimate that the leading term in the binding energy W_i is the kinetic term, proportional to k^2 , i.e., $W_i \propto k^2 \propto n_{bb}^{2/3}$. Thus one can estimate that $\sigma_{\text{sur}}^{\text{BBP}} \propto n_{bb}^{11/6}$ in the BBP phenomenological result [44], where the effect of electromagnetic interaction on the profile of fermion density is neglected. This BBP phenomenological result is different from our result in Eq. (39). This is due to the fact that the electromagnetic interaction and the presence of electrons change the proton and neutron density profiles.

For σ_C , as shown in Eq. (38) the surface tension for the electric field is proportional to the square of the baryon number density. This result can be understood as follows.

The Thomas-Fermi equilibrium condition for electrons given by Eq. (6) tells us that the Coulomb potential in the bulk core is proportional to the bulk electron chemical potential, so $V_b \propto \mu_{eb}$, and since the electrons are ultrarelativistic at these densities we have $V_b \propto P_{eb}^F \propto n_{eb}^{1/3}$. The thickness of the layer is of order $\Delta r \sim n_{eb}^{-1/3}$ and so the electric field scales as $E \sim -\Delta V/\Delta r \sim V_b/\Delta r \propto n_{eb}^{2/3}$. Thus the contribution of the Coulomb energy to the surface tension satisfies $\sigma_C \propto E^2 \Delta r \propto n_{eb}$ and since in the bulk core we have $n_{eb} \simeq n_{pb}$ we obtain $\sigma_C \propto n_{eb} = y n_{bb}$, where $y = n_{pb}/n_{bb}$ is the proton fraction in the bulk region. In neutron stars the β equilibrium between neutrons, protons, and electrons leads to a highly nuclear isospin asymmetry ($y \ll 1$), and since the nucleons are approximately nonrelativistic and the electrons ultrarelativistic around nuclear saturation density, it can be estimated from Eq. (10) that the proton fraction is proportional to the baryon density, i.e., $y \propto n_{bb}$, and therefore we finally obtain our final result $\sigma_C \propto n_{bb}^2$.

In Fig. 3 we show also the nuclear-to-Coulomb surface tension ratio σ_N/σ_C . We find that this ratio is larger than unity for all baryon number densities we considered. This would in principle imply that the system is stable with respect to the Bohr-Wheeler condition (24) as we have previously discussed.

It is also worth mentioning that the result that $\sigma_N/\sigma_C > 1$ for every nucleon density in our system can be explained as the result of the penetration of the relativistic electrons into the nucleus (see Refs. [49,50] for details). This is allowed for configurations with sufficiently large sizes $r_0 A^{1/3} > \hbar/(m_e c)$ or mass numbers $A > \hbar^3/(r_0 m_e c)^3 \sim 10^7$, where $r_0 \approx 1.2$ fm. For systems with much larger mass numbers such as neutron stars, $A_{NS} \sim 10^{57}$, the penetration of electrons is such that they nearly neutralize the system and the electric field becomes appreciable only near the core surface [49,50].

However, the transition layer could be unbound if the gravitational binding energy of the shell to the core is smaller than its electrostatic energy. An approximate computation of the stability of the transition layer in the above sense can be found in Ref. [49], where it was shown within Newtonian gravity that the layer is gravitational bound provided the system has a number of baryons $A \gtrsim 0.004(Z/A)^{1/2}(m_{Pl}/m_N)^3 \sim 10^{55}(Z/A)^{1/2}$ or a mass $M = m_N A \gtrsim 0.01(Z/A)^{1/2} M_\odot$, where m_N and $m_{Pl} = (\hbar c/G)^{1/2}$ are the nucleon and Planck masses. It is clear that this stability requirement implies a lower limit for our globally neutral neutron stars. It would be interesting to perform a detailed calculation taking into account the effects of general relativity as well as of the magnetic field on the transition surface induced by rotation (see Ref. [52]) and the centrifugal potential acting on the shell. However, such calculation is out of the scope of this work and will be presented elsewhere.

IV. SURFACE TENSION IN THE PRESENCE OF THE CRUST

It was shown in Ref. [41] that the properties of the core-crust transition boundary layer depend on the nuclear parameters, especially on the nuclear surface tension, and on the density at the crust edge. The crust is composed of a nuclei lattice

in a background of degenerate electrons, whose density at the edge of the crust is denoted here as n_e^{crust} . There are in addition free neutrons in the crust when the density of the crust, ρ_{crust} , is higher than the neutron-drip value $\rho_{\text{drip}} \sim 4.3 \times 10^{11} \text{ g cm}^{-3}$ [44]. So when the density of the crust ρ_{crust} is smaller than the neutron-drip value, i.e. $\rho_{\text{crust}} < \rho_{\text{drip}}$, we set the proton and neutron densities to zero in the outside region while the electron density must match the value n_e^{crust} , i.e., $n_{eo} = n_e^{\text{crust}}$. In the cases when $\rho_{\text{crust}} > \rho_{\text{drip}}$ both neutrons and electrons have to match their corresponding crust values at the end of the core-crust transition layer, i.e., $n_{eo} = n_e^{\text{crust}}$ and $n_{no} = n_n^{\text{crust}}$, n_n^{crust} being the neutron density at the crust edge.

As shown by BBP [44] there is no proton-drip at any density of interest in these systems and therefore we keep zero as the outside proton density value. In order to set the matching density values for electrons and neutrons we use the relation of the free neutron and electron densities in Sec. 6 of the work by BBP [44]. At the neutron-drip point the electron Fermi momentum is around $P_{eo}^F \approx 26 \text{ MeV}$ or $P_{eo}^F/P_{eb}^F \approx 0.18$, where P_{eo}^F is the electron Fermi momentum in the outside region and P_{eb}^F is the electron Fermi momentum in the bulk region.

The results of the dependence of the surface tension on the outside electron densities and the density of the crust are shown in Fig. 4. Here we also neglect the presence of the gravitational interaction, i.e., $(e^{\nu_{\text{core}}}, e^{-\lambda_{\text{core}}}) \rightarrow 1$.

The results of Fig. 4 show that the Bohr-Wheeler condition (24) for the instability is reached at a crust density $\rho_{\text{crust}}^{\text{crit}} \sim$

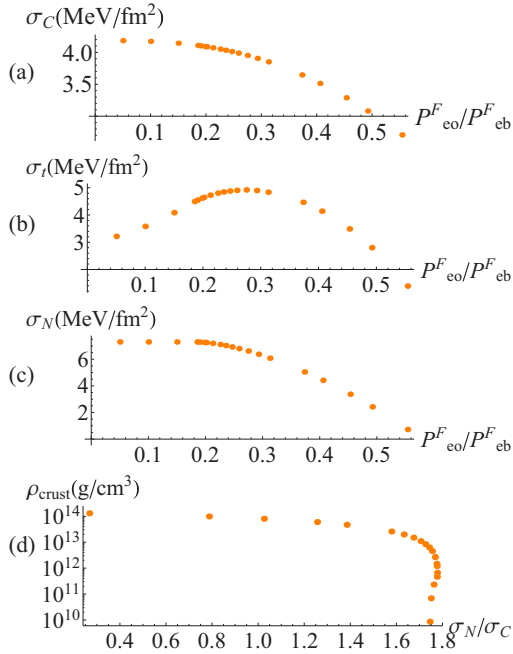


FIG. 4. (Color online) Dependence of the surface tension of the transition layer on the fermion densities in the outside region and the density of the crust. Here $n_{bb} = n_{\text{nuc}}$ and $(e^{\nu_{\text{core}}}, e^{-\lambda_{\text{core}}}) \rightarrow 1$. (a) Surface tension for the electric field, σ_C . (b) The total surface tension σ_t . (c) The surface tension for nucleons, σ_N . (d) Ratio of the surface tension for nucleons and the surface tension for the electric field, σ_N/σ_C , with respect to the density of the crust ρ_{crust} . The neutron drip point $\rho_{\text{drip}} \sim 4.3 \times 10^{11} \text{ g cm}^{-3}$ is around $P_{eo}^F/P_{eb}^F \approx 0.18$.

$1.2 \times 10^{14} \text{ g cm}^{-3}$, so the system becomes unstable against fission when $\rho_{\text{crust}} > \rho_{\text{crust}}^{\text{crit}}$, imposing a physical upper limit to the density at the edge of the crust. It becomes interesting to include the binding effect of gravity and any other attractive contribution that strengthens the stability of the system, which will be analyzed elsewhere. It is interesting that this upper limit on the crust density implies a lower limit to the maximum electric field in the core-crust transition region, limiting at the same time to approaching a state of quasi-local charge neutrality of the neutron star.

As shown in Fig. 4, the surface tension for the electric field decreases as increasing the electron number density in the outside region. The reason is that the increasing electron number density in the outside region [41] causes a decrease of the thickness of the interface and of the proton and electron density difference; i.e., the surface charge density decreases.

It is shown in Fig. 4 that the dependence of the surface tension for nucleons, σ_N , on the electron number density in the outside region is weak before the neutron drip point. The influence of electron density in the outside region on the surface structure of nucleons is small in this case. After the neutron drip point, the free neutrons in the outside region lower the surface tension significantly, as expected in the BBP phenomenological result [44]. In addition, as shown in Fig. 4, the total surface tension σ_t first increases and then decreases with increasing fermion densities in the outside region. This is due to the combination of the following two effects. (I) as shown in Table III, the contribution of electrons to the total surface tension is negative. For increasing electron density in the outside region, the effect of electrons on the surface tension becomes weaker. This increases the total surface tension. (II) After the neutron drip point, the surface tension for nucleons σ_N is lowered significantly by the free neutrons in the outside region.

V. EFFECTS OF THE GRAVITATIONAL INTERACTION ON THE SURFACE TENSION

We turn now to analyze the effects of the inclusion of the gravitational field on the surface tension of this transition layer. For the sake of simplicity, we make this analysis in the simplest case without a crust, considered in Sec. III.

As shown in Ref. [41], at the core radius (in this case the surface) of the neutron star, the metric functions are approximately the same as the Schwarzschild solution, so at the border of the star we have

$$e^{\nu_{\text{core}}} \approx e^{-\lambda_{\text{core}}} = 1 - \frac{2GM(R_{\text{core}})}{R_{\text{core}}}, \quad (42)$$

with $M(R_{\text{core}})$ the mass of the star. The results of the solution of Eqs. (2)–(8) are shown in Fig. 5 for the case $e^{\lambda_{\text{core}}} \approx e^{-\nu_{\text{core}}} = 1.5$.

Comparing to the results shown in Fig. 2, the fermion density and meson field profiles are similar to their counterparts in the case without the gravitational field. In Fig. 5 we see a larger proton density, a smaller neutron density, and a smaller size of the core-crust transition layer leading to a larger maximum of the electric field, comparing to Fig. 2.

Figure 6 shows the results of the dependence of the surface tension on the value of metric $e^{\lambda_{\text{core}}}$. As shown in Fig. 6, the total

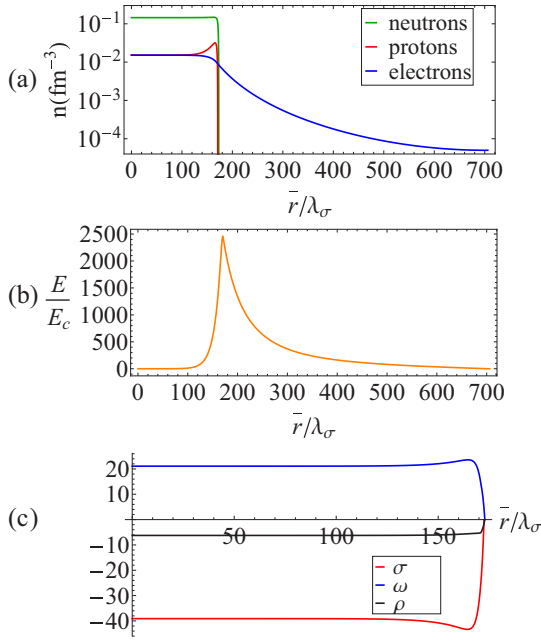


FIG. 5. (Color online) (a) Fermion density profiles in units of fm^{-3} . (b) Electric field in units of the critical field E_c . (c) Meson fields σ , ω , and ρ in units of MeV. Here we set $e^{\lambda_{\text{core}}} \approx e^{-\lambda_{\text{core}}} = 1.5$, $n_{bb} = n_{\text{nucl}}$, and $n_{i0} = 0$.

surface tension and the surface tension for nucleons increase as increasing the value of the metric $e^{\lambda_{\text{core}}}$. There are two effects which influence the characters of the total surface tension and

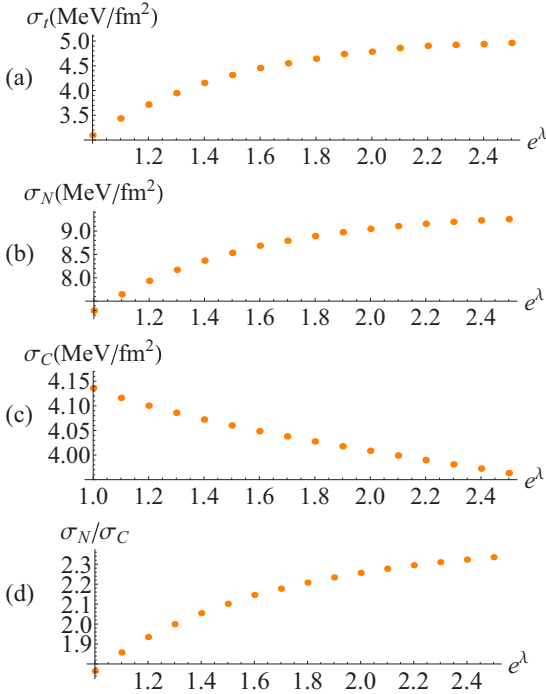


FIG. 6. (Color online) The dependence of the surface tension of the transition layer on the value of metric $e^{\lambda_{\text{core}}}$. (a) The total surface tension σ_t . (b) Surface tension for nucleons, σ_N . (c) Surface tension for electric field, σ_C . (d) Ratio of surface tension for nucleons and the surface tension for electric field, σ_N/σ_C . We set here $n_{bb} = n_{\text{nucl}}$ and $n_{i0} = 0$.

the surface tension for nucleons. First, as we have seen the presence of gravitational field changes the fermion density and meson field profiles. Second, the difference between the proton density and the neutron density becomes smaller when the value of the metric $e^{\lambda_{\text{core}}}$ increases, lowering the isospin asymmetry of the system. The combination of these two effects leads to the characters of the total surface tension and the surface tension for nucleons shown in Fig. 6. In addition, as shown in Fig. 6, the change of the value of the surface tension for the electric field when increasing the value of $e^{\lambda_{\text{core}}}$ is small. That is due to the balance of the following two effects: (I) the electric field in the surface region becomes larger (see Fig. 5); (II) the thickness of the surface becomes smaller, and then the Coulomb energy distributes in a smaller region. It can be also checked from Fig. 5 how in the limit $e^{\lambda_{\text{core}}} \rightarrow 1$ all quantities tend to the values found in Sec. III in the flat case.

VI. SUMMARY AND DISCUSSION

Taking into account strong, weak, electromagnetic, and gravitational interactions, and fulfilling the global charge neutrality of the system, a transition layer will happen between the core and crust of neutron stars [41]. This is different from the results from traditional TOV equations imposing local charge neutrality. This core-crust transition layer happens at the saturation density of nuclear matter. In this article, using RMFT together with the Thomas-Fermi approximation, we study the surface properties of this transition layer. In particular, we computed the surface tension and Coulomb energy of the transition shell and analyzed the role of each fermion component and meson fields in the determination of the properties of this core-crust transition layer.

Since the length scale of the core-crust transition layer ($\sim \lambda_e$) is much smaller than the radius of neutron stars and the electron density is nearly equal to the proton density in the bulk hadronic phase of neutron star cores, we applied the semi-infinite matter model as an approximation to construct the surface tension for this core-crust transition layer, following the method of BBP in Ref. [44]. We first presented the studies of this transition layer neglecting the presence of the gravitational interaction. We calculated the surface tension and the Coulomb energy for the transition layer of this system for different baryon number densities near the nuclear saturation density. The results show that the total surface tension as well as the surface tension for the electric field and the surface tension for nucleons are proportional to some power-law function of the baryon number density in the bulk region; see Eqs. (37)–(39). The difference between the surface energy of this neutron star matter and the phenomenological results [44] in nuclear physics has been analyzed. We also studied the surface structure for different fermion densities in the outside region, namely for different densities of the neutron star crust.

We also presented the analysis of the influence the gravitational field and on the structure of the transition layer and the surface tension. The results show that the fermion density and meson field profiles are similar to the case without the presence

of gravitational field, although some quantitative differences appear. We show that the total surface tension and the surface tension for nucleons increase with increasing value of the metric function $e^{\lambda_{\text{core}}}$.

We studied the instability against Bohr-Wheeler surface deformation for all the systems. We find that the instability sets in at a critical density of the crust $\rho_{\text{crust}}^{\text{crit}} \sim 1.2 \times 10^{14} \text{ g cm}^{-3}$. This implies a lower limit to the maximum electric field of the core-crust transition region and makes inaccessible a state of quasilocal charge neutrality for the neutron star, which will in principle be reached when the limit $\rho_{\text{crust}} = \rho_{\text{core}} \approx \rho_{\text{nucl}}$ is approached.

The results of this work open the way to more general studies relevant for the analysis of the stability of neutron stars and the core-crust transition surface. Some of the effects that need to be addressed for the stability of the shell include gravitational binding, centrifugal repulsion, magnetic field induced by rotating electric field, and hence magnetic dipole-dipole interactions. It would be interesting to perform a similar analysis for the case of strange stars both bare and in the presence of an outer crust.

It is also important to mention that surface effects and boundary layers are contained in the widely discussed nuclear pasta phases (see, e.g., Refs. [15–18], and references therein) expected in the low-density nuclear matter composing the inner crust of neutron stars. Those configurations also fulfill the condition of global charge neutrality. However, in there the condition of global charge neutrality is only imposed in the pasta phase while keeping the condition of local charge neutrality in the rest of the configuration, e.g., in the core of the neutron star. In contrast, in our model, the global charge neutrality is fulfilled in the whole configuration, which leads to the phenomenon of gravito-polarization in the core of the neutron star. Along this line, it would be interesting to study the differences of these two scenarios and to establish which is the configuration of minimum energy and therefore realized in nature. This is a very interesting question which deserves a detailed and deep analysis; however, it is out of the scope of the present work and we therefore leave it for a future publication.

To end, it is interesting to briefly discuss some of the observables which could shed light into the structure of the neutron star and therefore to probe the underlying theory.

On one hand, there might be some effects coming from the microscopic structure. One possibility could be some electromagnetic processes due to the strong electric field in the core-crust interface, such as an annihilation line of e^-e^+ to two photons. These e^-e^+ pairs can be produced by neutron star perturbations. However, this effect could be difficult to observe with the current instrumentation; we are planning to analyze in detail this interesting problem elsewhere.

On the other hand, as we have pointed out, from the macroscopic structure point of view the new structure of the neutron star leads to different radii due to the different size of the crust. This necessarily leads to the possibility of probing the theory of neutron stars and in particular the physics of the core-crust transition from reliable observations of their masses and radii. Such measurements can come for instance from observations of the thermal evolution of accreting and isolated neutron stars. In particular, observations of the cooling of the neutron star during its thermal relaxation phase ($t \lesssim 50 \text{ yr}$ after birth), where the core and the crust are thermally decoupled, carry crucial information on the core-crust transition density and therefore on the crust mass and size [53].

If we move on to the last stages of the life of a neutron star, it is clear that the electromagnetic structure of the neutron star is particularly relevant for the process of its gravitational collapse. A core endowed with electromagnetic structure leads to signatures and energetics markedly different from the ones of a core endowed uniquely of gravitational interactions *à la* Oppenheimer and Snyder [54]; see, e.g., Refs. [55–58]. As pointed out recently [59,60], in these cores there are electric processes that might lead to a vast e^-e^+ production in the process of collapse to a black hole.

ACKNOWLEDGMENT

Y.-B.W. is supported by the Erasmus Mundus Joint Doctorate Program by Grant No. 2011-1640 from the EACEA of the European Commission.

-
- [1] H. P. Duerr, *Phys. Rev.* **103**, 469 (1956).
 - [2] L. D. Miller and A. E. S. Green, *Phys. Rev. C* **5**, 241 (1972).
 - [3] J. D. Walecka, *Ann. Phys. (NY)* **83**, 491 (1974).
 - [4] J. Boguta and J. Rafelski, *Phys. Lett. B* **71**, 22 (1977).
 - [5] J. Boguta and A. R. Bodmer, *Nucl. Phys. A* **292**, 413 (1977).
 - [6] T. D. Lee and G. C. Wick, *Phys. Rev. D* **9**, 2291 (1974).
 - [7] T. D. Lee, *Rev. Mod. Phys.* **47**, 267 (1975).
 - [8] T. D. Lee and M. Margulies, *Phys. Rev. D* **11**, 1591 (1975).
 - [9] J. Boguta and H. Stocker, *Phys. Lett. B* **120**, 289 (1983).
 - [10] J. Boguta and S. A. Moszkowski, *Nucl. Phys. A* **403**, 445 (1983).
 - [11] J. Boguta, *Nucl. Phys. A* **501**, 637 (1989).
 - [12] B. D. Serot, *Rept. Prog. Phys.* **55**, 1855 (1992).
 - [13] P. Ring, *Prog. Part. Nucl. Phys.* **37**, 193 (1996).
 - [14] M. Bender, P.-H. Heenen, and P.-G. Reinhard, *Rev. Mod. Phys.* **75**, 121 (2003).
 - [15] T. Maruyama, T. Tatsumi, D. N. Voskresensky, T. Tanigawa, and S. Chiba, *Phys. Rev. C* **72**, 015802 (2005).
 - [16] S. S. Avancini, D. P. Menezes, M. D. Alloy, J. R. Marinelli, M. M. W. Moraes, and C. Providência, *Phys. Rev. C* **78**, 015802 (2008).
 - [17] M. Okamoto, T. Maruyama, K. Yabana, and T. Tatsumi, *Phys. Lett. B* **713**, 284 (2012).
 - [18] F. Grill, C. Providência, and S. S. Avancini, *Phys. Rev. C* **85**, 055808 (2012).
 - [19] R. J. Furnstahl, B. D. Serot, and H. B. Tang, *Nucl. Phys. A* **598**, 539 (1996).
 - [20] R. J. Furnstahl, B. D. Serot, and H. B. Tang, *Nucl. Phys. A* **615**, 441 (1997); **640**, 505 (1998).
 - [21] B. D. Serot and J. D. Walecka, *Int. J. Mod. Phys. E* **06**, 515 (1997).

- [22] M. Brack, C. Guet, and H.-B. Håkansson, *Phys. Rep.* **123**, 275 (1985).
- [23] M. M. Sharma, S. A. Moszkowski, and P. Ring, *Phys. Rev. C* **44**, 2493 (1991).
- [24] D. Von-Eiff, J. M. Pearson, W. Stocker, and M. K. Weigel, *Phys. Lett. B* **324**, 279 (1994).
- [25] D. Von-Eiff, W. Stocker, and M. K. Weigel, *Phys. Rev. C* **50**, 1436 (1994).
- [26] D. Von-Eiff, H. Freyer, W. Stocker, and M. K. Weigel, *Phys. Lett. B* **344**, 11 (1995).
- [27] M. Centelles, M. Del Estal, and X. Viñas, *Nucl. Phys. A* **635**, 193 (1998).
- [28] M. Del Estal, M. Centelles, and X. Viñas, *Nucl. Phys. A* **650**, 443 (1999).
- [29] S. K. Patra, M. Centelles, X. Viñas, and M. Del Estal, *Phys. Rev. C* **65**, 044304 (2002).
- [30] P. Danielewicz and J. Lee, *Nucl. Phys. A* **818**, 36 (2009).
- [31] N. K. Glendenning, *Phys. Rev. D* **46**, 1274 (1992).
- [32] N. K. Glendenning, *Phys. Rep.* **342**, 393 (2001).
- [33] N. K. Glendenning and J. Schaffner-Bielich, *Phys. Rev. C* **60**, 025803 (1999).
- [34] M. B. Christiansen, N. K. Glendenning, and J. Schaffner-Bielich, *Phys. Rev. C* **62**, 025804 (2000).
- [35] M. Alford, K. Rajagopal, S. Reddy, and F. Wilczek, *Phys. Rev. D* **64**, 074017 (2001).
- [36] D. G. Ravenhall, C. J. Pethick, and J. R. Wilson, *Phys. Rev. Lett.* **50**, 2066 (1983).
- [37] M. Rotonondo, J. A. Rueda, R. Ruffini, and S.-S. Xue, *Phys. Lett. B* **701**, 667 (2011).
- [38] J. A. Rueda, R. Ruffini, and S.-S. Xue, *Nucl. Phys. A* **872**, 286 (2011).
- [39] R. C. Tolman, *Phys. Rev.* **55**, 364 (1939).
- [40] J. R. Oppenheimer and G. Volkoff, *Phys. Rev.* **55**, 374 (1939).
- [41] R. Belvedere, D. Pugliese, J. A. Rueda, R. Ruffini, and S.-S. Xue, *Nucl. Phys. A* **883**, 1 (2012).
- [42] P. Haensel, A. Y. Potekhin, and D. G. Yakovlev, *Neutron Stars I: Equation of State and Structure* (Springer-Verlag, New York, 2007).
- [43] N. Bohr and J. A. Wheeler, *Phys. Rev.* **56**, 426 (1939).
- [44] G. Baym, H. A. Bethe, and C. J. Pethick, *Nucl. Phys. A* **175**, 225 (1971).
- [45] J. Boguta, *Phys. Lett. B* **106**, 255 (1981).
- [46] G. A. Lalazissis, J. König, and P. Ring, *Phys. Rev. C* **55**, 540 (1997).
- [47] T. D. Lee and Y. Pang, *Phys. Rev. D* **35**, 3678 (1987).
- [48] B. Cameron, *Eur. J. Phys.* **30**, 763 (2009).
- [49] M. Rotonondo, R. Ruffini, S.-S. Xue, and V. Popov, *Int. J. Mod. Phys. D* **20**, 1995 (2011).
- [50] M. Rotonondo, J. A. Rueda, R. Ruffini, and S.-S. Xue, *Phys. Rev. C* **83**, 045805 (2011).
- [51] P.-G. De Gennes, F. Brochard-Wyart, and D. Quéré, *Capillary and Wetting Phenomena: Drops, Bubbles, Pearls, Waves* (Springer, New York, 2003).
- [52] K. Boshkayev, M. Rotonondo, and R. Ruffini, *Int. J. Mod. Phys. Conf. Ser.* **12**, 58 (2012).
- [53] S. M. de Carvalho, R. Negreiros, J. A. Rueda, and R. Ruffini (unpublished).
- [54] J. R. Oppenheimer and H. Snyder, *Phys. Rev.* **56**, 455 (1939).
- [55] R. Ruffini, L. Vitagliano, and S.-S. Xue, *Phys. Lett. B* **573**, 33 (2003).
- [56] R. Ruffini, L. Vitagliano, and S.-S. Xue, *Phys. Lett. B* **559**, 12 (2003).
- [57] R. Ruffini and S.-S. Xue, *AIP Conf. Proc.* **1059**, 72 (2008).
- [58] R. Ruffini, G. V. Vereshchagin, and S.-S. Xue, *Phys. Rep.* **487**, 1 (2010).
- [59] W.-B. Han, R. Ruffini, and S.-S. Xue, *Phys. Rev. D* **86**, 084004 (2012).
- [60] R. Ruffini and S.-S. Xue, *Phys. Lett. A* **377**, 2450 (2013).

Relativistic Feynman-Metropolis-Teller treatment at finite temperaturesS. M. de Carvalho,^{*} M. Rotondo,[†] Jorge A. Rueda,[‡] and R. Ruffini[§]*Dipartimento di Fisica and ICRA, Sapienza Università di Roma, P.le Aldo Moro 5, I-00185 Rome, Italy
and ICRA Net, P.zza della Repubblica 10, I-65122 Pescara, Italy*

(Received 31 May 2013; revised manuscript received 14 October 2013; published 6 January 2014)

The Feynman-Metropolis-Teller treatment of compressed atoms has been recently generalized to relativistic regimes and applied to the description of static and rotating white dwarfs in general relativity. We present here the extension of this treatment to the case of finite temperatures and construct the corresponding equation of state (EOS) of the system; applicable in a wide regime of densities that includes both white dwarfs and neutron star outer crusts. We construct the mass-radius relation of white dwarfs at finite temperatures obeying this new EOS and apply it to the analysis of ultra-low-mass white dwarfs with $M \lesssim 0.2M_\odot$. In particular, we analyze the case of the white dwarf companion of PSR J1738 + 0333. The formulation is then extrapolated to compressed nuclear matter cores of stellar dimensions, systems with mass numbers $A \approx (m_{\text{Planck}}/m_n)^3$ or mass $M_{\text{core}} \approx M_\odot$, where m_{Planck} and m_n are the Planck and the nucleon mass. For $T \ll m_e c^2/k_B \approx 5.9 \times 10^9$ K, a family of equilibrium configurations can be obtained with analytic solutions of the ultrarelativistic Thomas-Fermi equation at finite temperatures. Such configurations fulfill global but not local charge neutrality and have strong electric fields on the core surface. We find that the maximum electric field at the core surface is enhanced at finite temperatures with respect to the degenerate case.

DOI: [10.1103/PhysRevC.89.015801](https://doi.org/10.1103/PhysRevC.89.015801)

PACS number(s): 05.30.Fk, 67.10.Db, 26.60.Kp

I. INTRODUCTION

We have recently generalized in Ref. [1] to relativistic regimes the classic work of Feynman, Metropolis, and Teller (FMT) [2], solving a compressed atom by use of the Thomas-Fermi equation in a Wigner-Seitz cell. The integration of this equation does not admit any regular solution for a pointlike nucleus and both the nuclear radius and the nuclear composition have necessarily to be taken into account [3,4]. This introduces a fundamental difference from the nonrelativistic Thomas-Fermi model where a pointlike nucleus is adopted. So this approach improves in the following aspects all previous treatments of the equation of state (EOS) of a compressed atom, including the classic works based on the uniform approximation by Chandrasekhar [5] and the EOS by Salpeter [6]: (1) in order to guarantee self-consistency with a relativistic treatment of the electrons, the pointlike assumption of the nucleus is abandoned, introducing a finite-sized nucleus; (2) the Coulomb interaction energy is fully calculated without any approximation by solving numerically the relativistic Thomas-Fermi equation for each given nuclear composition; (3) the inhomogeneity of the electron distribution inside each Wigner-Seitz cell; (4) the energy density of the system is calculated taking into account the contributions of the nuclei, of the Coulomb interactions, as well as of the relativistic electrons to the energy of the Wigner-Seitz cells; and (5) the β equilibrium among neutrons, protons, and electrons is also taken into account, leading to a self-consistent calculation of the threshold density for triggering the inverse β decay

of a given nucleus. The computation of the EOS is done by calculating the dependence of all these ingredients on the level of compression inside the star interior.

We have shown in Ref. [7] how all these effects together with general relativity are important in the determination of the macroscopic structure of white dwarfs as well as for the determination of their maximum stable mass against gravitational collapse. More recently, the relativistic FMT EOS has been used to determine general relativistic equilibrium configurations of rotating white dwarfs [8].

In Fig. 1 we show the mass-radius relation of $T = 0$ white dwarfs for the relativistic FMT, Salpeter, and Chandrasekhar EOS and compare them with the estimated masses and radii of white dwarfs from the Sloan Digital Sky Survey Data Release 4 (SDSS-E06 catalog) [9]. It can be clearly seen that for masses $\lesssim 0.7\text{--}0.8M_\odot$ deviations from the degenerate treatments are already evident. It is natural to expect that such deviations could be related to the neglected effects of finite temperatures on the structure of the white dwarf. Thus, besides being interesting on their own, the finite-temperature effects on the EOS and, consequently, on the mass-radius relation of the white dwarf are very important. In this work we extend our previous EOS [1], based on the degenerate relativistic FMT treatment, by introducing the effects of finite temperatures and use it to construct equilibrium configurations of white dwarfs at finite temperatures.

It is very interesting that there have been recently discovered ultra-low-mass white dwarfs with masses $\lesssim 0.2M_\odot$, which are companions of neutron stars in relativistic binaries; see, e.g., Refs. [10,11]. These low-mass white dwarfs represent the perfect arena to test the EOS of compressed matter since the central densities of these objects are expected to be $\lesssim 10^6$ g cm⁻³, where the degenerate approximation breaks down and therefore temperature effects cannot be neglected. Using the mass-radius relation at finite temperatures, we analyze in the

^{*}sheyse.martins@icra.it[†]michael.rotondo@icra.it[‡]jorge.rueda@icra.it[§]ruffini@icra.it

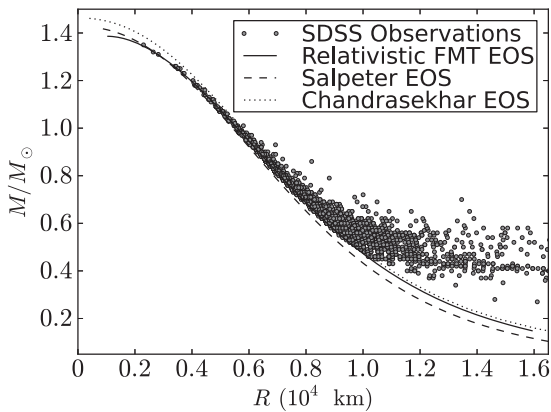


FIG. 1. Mass-radius relations of white dwarfs obtained with the relativistic FMT (solid black), Salpeter (dashed black), and Chandrasekhar (dotted black) EOS and their comparison with the estimated masses and radii of white dwarfs taken from the Sloan Digital Sky Survey Data Release 4 (SDSS-E06 catalog, gray circles) [9].

present work the structure of the white dwarf orbiting the pulsar PSR J1738 + 0333. We infer its mass, radius, surface gravity, and internal temperature and compare and contrast them with previous estimates.

The generalization of the relativistic FMT model presented in this work will be also useful to extend previous works in which the nonrelativistic Thomas-Fermi model has been used to describe the physics of the low-density layers of neutron stars, including their atmospheres (see, e.g., Ref. [12]). The proper treatment of the relativistic and Coulomb effects corrects the over- and underestimates of the total pressure at high and low densities, respectively, which occurs in nonrelativistic Thomas-Fermi models and in the approximate Coulomb corrections of Salpeter [6]; see Ref. [1] for further details.

In addition to the generalization of the EOS of compressed matter, we follow the steps in Ref. [1] and extrapolate the treatment to the case of compressed nuclear matter cores of stellar dimensions introduced in macroscopic cores composed of neutrons, protons, and electrons in β equilibrium and with mass numbers $A \sim (m_{\text{planck}}/m_n)^3 \sim 10^{57}$, hence, masses $M_{\text{core}} \sim M_{\odot}$, which are expected to be bound by self-gravity. These objects are idealized configurations that reflect the properties of macroscopic nuclear matter systems such as neutron stars.

The paper is organized as follows: first, in Sec. II, we describe the extension of the relativistic FMT treatment to finite temperatures. Then, in Sec. III, we summarize the results of the numerical integration of the equations and describe the general properties of the new EOS. In Sec. IV we construct the mass-radius relation of white dwarfs and show specifically the results for ${}^4\text{He}$ composition and in Sec. V we apply these results to the case of the ultra-low-mass white dwarf companion of PSR J1738 + 0333. In Sec. VI we extend the formulation of compressed matter to the case of the nuclear matter cores of stellar dimensions introduced in Ref. [1]. We finally discuss our results in Sec. VII.

II. THE RELATIVISTIC FMT TREATMENT AT FINITE TEMPERATURES

We now consider the equations of equilibrium of a relativistic gas of electrons at a temperature $T \neq 0$ surrounding a finite-sized and positively charged nucleus of mass and atomic numbers A and Z , respectively. The electron cloud is confined within a radius R_{WS} of a globally neutral Wigner-Seitz cell and the system is isothermal.

Following Ref. [1], we adopt a constant distribution of protons confined in a radius $R_c = \Delta \lambda_{\pi} Z^{1/3}$, where $\lambda_{\pi} = \hbar/(m_{\pi}c)$ is the pion Compton wavelength, with m_{π} the pion rest-mass. The parameter Δ is such that at nuclear density, $\Delta \approx (r_0/\lambda_{\pi})(A/Z)^{1/3}$, where $r_0 \approx 1.2$ fm; so in the case of ordinary nuclei $\Delta \approx 1$. Consequently, the proton number density can be written as

$$n_p(r) = \frac{3Z}{4\pi R_c^3} \theta(r - R_c) = \frac{3}{4\pi \lambda_{\pi}^3 \Delta^3} \theta(r - R_c), \quad (1)$$

where $\theta(r - R_c)$ is the Heaviside function centered at the core (nucleus) radius, $r = R_c$.

Clearly, the electron number density follows from Fermi-Dirac statistics and is given by

$$n_e = \frac{2}{(2\pi\hbar)^3} \int_0^{\infty} \frac{4\pi p^2 dp}{\exp\left[\frac{\tilde{E}(p) - \tilde{\mu}_e(p)}{k_B T}\right] + 1}, \quad (2)$$

where k_B is the Boltzmann constant, $\tilde{\mu}_e$ is the electron chemical potential without the rest-mass, and $\tilde{E}(p) = \sqrt{c^2 p^2 + m_e^2 c^4} - m_e c^2$, with p and m_e the electron momentum and rest-mass, respectively.

Introducing the degeneracy parameter $\eta = \tilde{\mu}_e/(k_B T)$, $t = \tilde{E}(p)/(k_B T)$, and $\beta = k_B T/(m_e c^2)$, we can write the electron number density as

$$n_e = \frac{8\pi\sqrt{2}}{(2\pi\hbar)^3} m^3 c^3 \beta^{3/2} [F_{1/2}(\eta, \beta) + \beta F_{3/2}(\eta, \beta)], \quad (3)$$

where

$$F_k(\eta, \beta) \equiv \int_0^{\infty} \frac{t^k \sqrt{1 + (\beta/2)t}}{1 + e^{t-\eta}} dt \quad (4)$$

is the relativistic Fermi-Dirac integral.

We consider temperatures that satisfy $T \ll m_e c^2/k_B \approx 6 \times 10^9$ K, so we will not take into account the presence of antiparticles. The Thomas-Fermi equilibrium condition for the relativistic electron gas is in this case given by

$$\tilde{\mu}_e(r) - eV(r) = k_B T \eta(r) - eV(r) = \text{const}, \quad (5)$$

where $V(r)$ is the Coulomb potential.

By introducing the dimensionless quantities $x = r/\lambda_{\pi}$, $x_c = R_c/\lambda_{\pi}$, and $\chi/r = \tilde{\mu}_e/(\hbar c)$ and replacing the above particle densities into the Poisson equation,

$$\nabla^2 V(r) = 4\pi e [n_p(r) - n_e(r)], \quad (6)$$

we obtain the generalization of the relativistic Thomas-Fermi equation to finite temperatures,

$$\frac{d^2\chi(x)}{dx^2} = -4\pi\alpha x \left\{ \frac{3}{4\pi\Delta^3}\theta(x_c - x) - \frac{\sqrt{2}}{\pi^2} \left(\frac{m_e}{m_\pi}\right)^3 \beta^{3/2} [F_{1/2}(\eta, \beta) + \beta F_{3/2}(\eta, \beta)] \right\}. \quad (7)$$

Equation (7) must be integrated subjected to the same boundary conditions as in the degenerate case, given by

$$\chi(0) = 0, \quad \left. \frac{d\chi}{dx} \right|_{x=0} > 0, \quad \left. \frac{d\chi}{dx} \right|_{x=x_{\text{WS}}} = \frac{\chi(x_{\text{WS}})}{x_{\text{WS}}}, \quad (8)$$

where the latter condition ensures the global charge neutrality at the Wigner-Seitz cell radius, R_{WS} , and $x_{\text{WS}} = R_{\text{WS}}/\lambda_\pi$ is the dimensionless cell radius.

We turn now to compute the energy of the Wigner-Seitz cell. For the present case of finite temperatures, the total energy of each cell can be split as

$$E_{\text{WS}} = E_N + E_k + E_C, \quad (9)$$

where

$$E_N = M_N(A, Z)c^2 + U_{\text{th}}, \quad U_{\text{th}} = \frac{3}{2}k_B T, \quad (10)$$

$$E_k = \int_0^{R_{\text{WS}}} 4\pi r^2 (\mathcal{E}_e - m_e n_e) dr, \quad (11)$$

$$E_C = \frac{1}{2} \int_0^{R_{\text{WS}}} 4\pi r^2 e [n_p(r) - n_e(r)] V(r) dr, \quad (12)$$

are the nucleus, kinetic, and Coulomb energy. For the nucleus mass $M_N(A, Z)$ we adopt experimental values, U_{th} is the thermal energy of nuclei which we here adopt as an ideal gas,¹ and the electron energy density \mathcal{E}_e is given by

$$\mathcal{E}_e = m_e c^2 n_e + \frac{\sqrt{2}}{\pi^2 \hbar^3} m_e^4 c^5 \beta^{5/2} [F_{3/2}(\eta, \beta) + \beta F_{5/2}(\eta, \beta)]. \quad (13)$$

The total density and pressure are then given by

$$\rho = \frac{E_{\text{WS}}}{c^2 V_{\text{WS}}}, \quad (14)$$

$$P = P_N + P_e, \quad (15)$$

where

$$P_N = \frac{2}{3} \frac{U_{\text{th}}}{V_{\text{WS}}} = \frac{k_B T}{V_{\text{WS}}}, \quad (16)$$

$$P_e = \frac{2^{3/2}}{3\pi^2 \hbar^3} m_e^4 c^5 \beta^{5/2} \left[F_{3/2}(\eta_{\text{WS}}, \beta) + \frac{\beta}{2} F_{5/2}(\eta_{\text{WS}}, \beta) \right], \quad (17)$$

with η_{WS} being the value of η at the boundary of the Wigner-Seitz cell with volume $V_{\text{WS}} = 4\pi R_{\text{WS}}^3/3$.

III. NUMERICAL INTEGRATION OF THE EQUATIONS AND THE EOS

For a given chemical composition (Z, A), temperature T (i.e., β), and dimensionless Wigner-Seitz cell radius x_{WS} , the relativistic Thomas-Fermi equation (7) is integrated subjected to the boundary conditions (8). We thus obtain both the Coulomb potential and the function η inside the given Wigner-Seitz cell. With the knowledge of η_{WS} , we proceed to evaluate first the energy of the cell by Eqs. (9)–(13) and, subsequently, the values of the density and pressure through Eqs. (14)–(17). For fixed chemical composition and temperature, we repeat the above steps for different cell radii to obtain different compression levels of the system; this leads to different densities and pressures, hence, the EOS. These steps can be then performed for different compositions and temperatures; the results are discussed below.

A. Properties of the EOS

As we showed in Ref. [1], as a result of the Coulomb interaction duly accounted for in the relativistic Thomas-Fermi treatment, the distribution of the electrons inside a Wigner-Seitz cell is not uniform. In order to show the effects of the temperature, in Fig. 2 we show, as an example, the electron number density inside a Wigner-Seitz cell of ⁵⁶Fe at a density of 30 g cm⁻³ and for temperatures $T = [0, 10^7, 10^{10}]$ K.

We can see in Fig. 2 how the effect of the temperature tends to homogenize the electron distribution inside the cell. In addition, we notice that the larger the temperature the larger the value of the electron density at the border of the Wigner-Seitz cell, thus increasing the electron pressure. This effect can be clearly seen in Fig. 3, where we show the value of the electron number density evaluated at

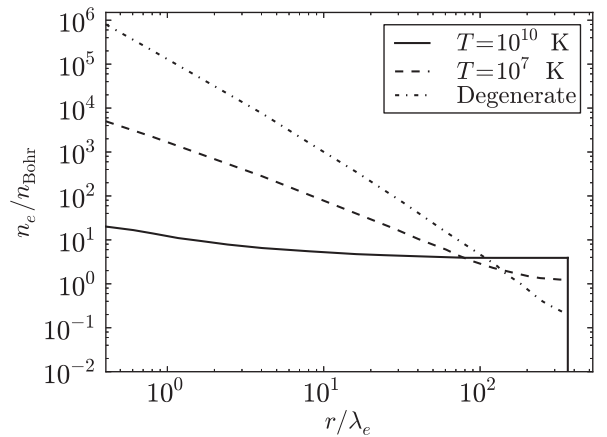


FIG. 2. Electron number density inside a Wigner-Seitz cell of ⁵⁶Fe at a density of 30 g cm⁻³ at selected temperatures. Here $n_{\text{Bohr}} = 3/(4\pi R_{\text{Bohr}}^3) \approx 1.6 \times 10^{24}$ cm⁻³, where $R_{\text{Bohr}} = \hbar/(e^2 m_e) \approx 5.3 \times 10^{-9}$ cm, is the Bohr radius. In this example we have used both low density and high temperatures up to 10¹⁰ K in order to show an extreme example of electron density flattening.

¹Quantum corrections to the ideal behavior of the ions considered here can be straightforwardly included following previous treatments such as in Refs. [13–15].

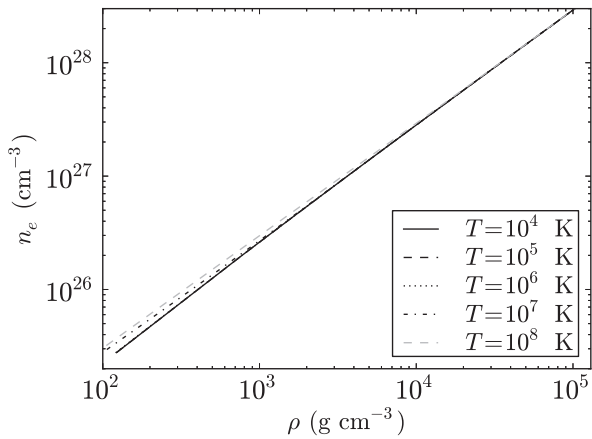


FIG. 3. Electron number density at the radius of a Wigner-Seitz cell of ^{12}C as a function of the density (14) for the selected temperatures $T = [10^4, 10^5, 10^6, 10^7, 10^8]$ K.

the cell radius, R_{WS} , as a function of the density for the temperatures $T = [10^4, 10^5, 10^6, 10^7, 10^8]$ K for a given chemical composition, ^{12}C .

The volume of the Wigner-Seitz cell, $V_{\text{WS}} = 4\pi R_{\text{WS}}^3/3$, determines the density of the system ρ given by Eq. (14); the smaller the volume the larger the density. In Fig. 4 we show the density of the system as a function of the Wigner-Seitz cell radius R_{WS} for a temperature $T = 10^7$ K and ^{12}C chemical composition. Small deviations of the R_{WS}^{-3} behavior are due to the inhomogeneity of the electron distribution inside the cell and to the contribution of the Coulomb and electron kinetic energy to the density.

In this line it is important to mention that often in the literature the density of the system is approximated as

$$\rho = \frac{A}{Z} M_u n_e, \quad (18)$$

which corresponds to the rest-mass density of nuclei in the system and where a uniform distribution of electrons is

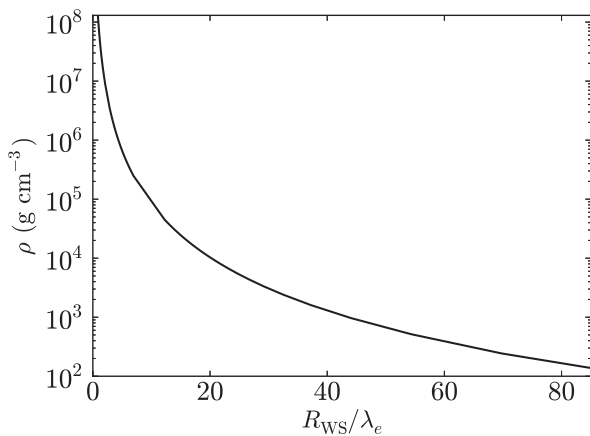


FIG. 4. Total density (in g cm^{-3}) of the system as a function of the radius of the Wigner-Seitz cell [in units of the electron Compton wavelength $\lambda_e = \hbar/(m_e c) \approx 3.9 \times 10^{-11}$ cm] in the case of ^{12}C at a temperature $T = 10^7$ K.

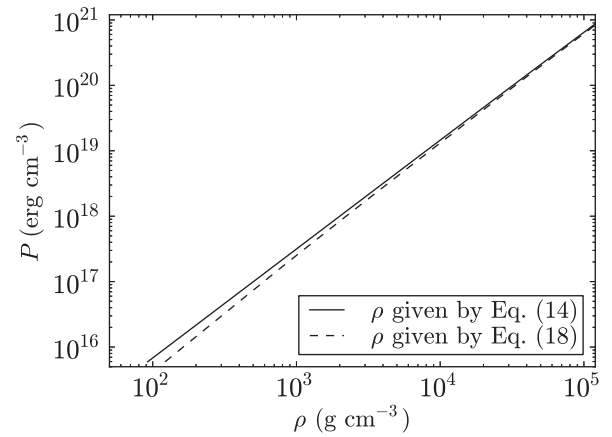


FIG. 5. Total pressure as a function of the matter density $\rho = AM_u n_e/Z$, given by Eq. (18), and $\rho = E_{\text{WS}}/(c^2 V_{\text{WS}})$, given by Eq. (14), which includes the thermal, kinetic, and Coulomb energy in the Wigner-Seitz cell. In this example the composition is ^{12}C and the temperature $T = 10^4$ K.

assumed. Here $M_u = 1.6604 \times 10^{-24}$ g is the unified atomic mass. We can see from Eq. (9) that this is equivalent to neglecting the thermal, kinetic, and Coulomb energy of the cells as well as the inhomogeneity of the electron density. However, as we showed in Refs. [1,7], the inclusion of the Coulomb and electron kinetic energies are important at low and high densities, respectively. In particular, the contribution of the kinetic energy of the electrons to the energy density is fundamental in the determination of the critical density for the gravitational collapse of ^{12}C white dwarfs [7]. We show in Fig. 5 the effect on the EOS of using as density of the system only the nuclei rest-mass, Eq. (18), instead of the full mass density given by Eq. (14), which accounts for the total energy of the Wigner-Seitz cell given by Eq. (9).

The effects of finite temperatures are clearly expected to be important at low densities, where the system loses its degeneracy. The point where the EOS should start to deviate from its degenerate behavior can be estimated by equating the degenerate and ideal gas pressures for the electron component. Assuming the electrons as nonrelativistic, we have $n_e k_B T = (3\pi^2)^{2/3} \hbar^2 n_e^{5/3} / m_e$, from which we obtain that temperature effects are important for densities

$$\rho \lesssim 1.5 \times 10^3 \left(\frac{T}{10^7 \text{ K}} \right)^{3/2} \text{ g cm}^{-3}, \quad (19)$$

where we have used $A/Z \approx 2$ and $\rho \approx AM_u n_e/Z$. In Fig. 6 we compare the relativistic degenerate FMT EOS [1,7] and its generalization at finite temperatures presented in this work for the cases $T = 10^7$ and 10^8 K and ^{12}C chemical composition. For these specific temperatures we see that deviations of the degenerate EOS start at a density $\rho \approx 2 \times 10^4 \text{ g cm}^{-3}$ and $\approx 10^6 \text{ g cm}^{-3}$, respectively. For the same temperatures, Eq. (19) estimates deviations from degeneracy at $\rho \approx 1.5 \times 10^3 \text{ g cm}^{-3}$ and $\approx 4.8 \times 10^4 \text{ g cm}^{-3}$, respectively. Thus, the lower the temperature the better the estimate given by Eq. (19); the reason for this is that for larger temperatures the system will

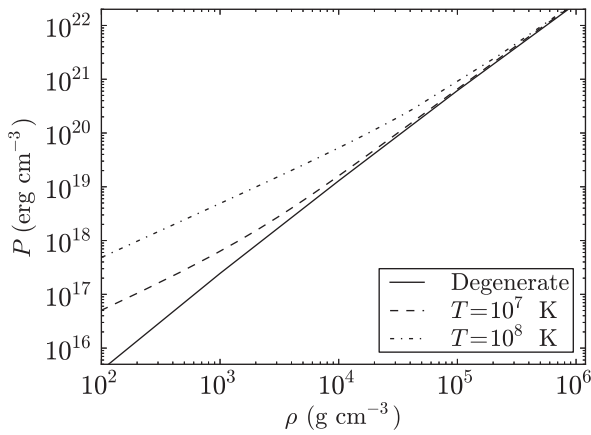


FIG. 6. Comparison of the EOS for ^{12}C at temperatures $T = [0, 10^7, 10^8]$ K.

lose the degeneracy at larger densities where the nonrelativistic approximation for the electrons breaks down.

In Fig. 7, we show the nuclei to electron pressure ratio in cells of ^{12}C as a function of the density and for selected temperatures. It can be seen that for all temperatures the ratio approaches the same constant value in the low-density regime. This is due to the fact that at sufficiently low densities the electron gas also becomes an ideal gas and, consequently, its pressure is approximately given by $P_e^{\text{id}} = Zk_B T/V_{\text{WS}}$. Therefore, the nuclei-to-pressure ratio approaches the limit $P_N/P_e^{\text{id}} = 1/Z$, where P_N is given by Eq. (16). In the example of Fig. 7 we have $Z = 6$ so $P_N/P_e^{\text{id}} \approx 0.17$. It is clear that the density at which each curve reaches such a constant value increases with the temperature, since at larger temperatures the electrons reach their ideal gas state at higher densities.

We summarize the finite-temperature generalization of the relativistic FMT EOS in Fig. 8, where we plot as an example the total pressure (15) as a function of the total density of the system (14) at temperatures $T = [10^4, 10^5, 10^6, 10^7, 10^8]$ K and for a chemical composition, ^{12}C . All the above features

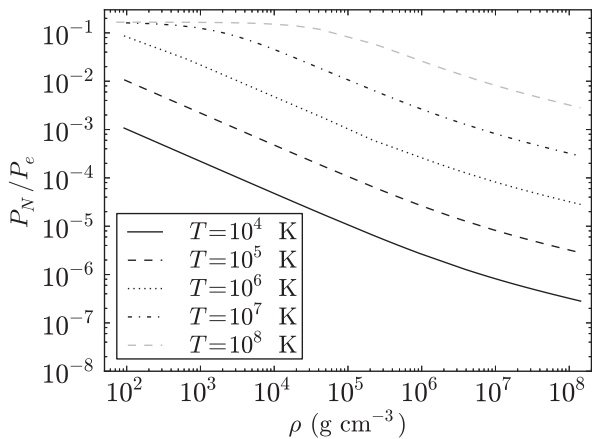


FIG. 7. Nuclei to electron pressure ratio as a function of the mass density in the case of ^{12}C white dwarf for selected temperatures in the range $T = 10^4$ – 10^8 K.

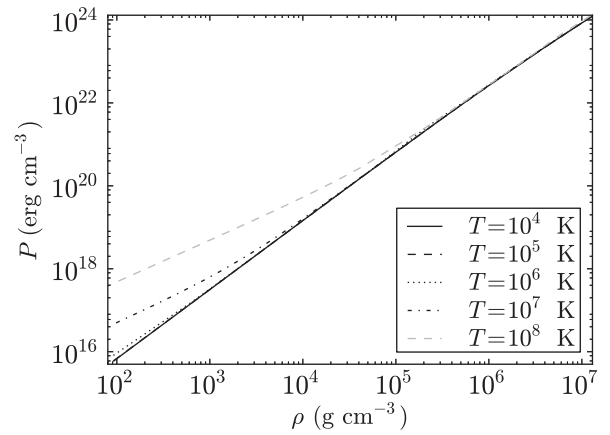


FIG. 8. Total pressure as a function of the mass density in the case of ^{12}C white dwarf for selected temperatures in the range $T = 10^4$ – 10^8 K.

of the EOS are general and therefore applied also to chemical compositions other than ^{12}C .

B. Inverse β decay and pycnonuclear reactions

We turn now to the finite-temperature effects on the inverse β -decay instability. It is known that white dwarfs may become unstable against the inverse β -decay process $(Z, A) \rightarrow (Z - 1, A)$ through the capture of energetic electrons. In order to trigger such a process the electron energy must be larger than the mass difference between the initial nucleus (Z, A) and the final nucleus $(Z - 1, A)$. This threshold energy is denoted as ϵ_Z^β . Usually, $\epsilon_Z^\beta - 1 < \epsilon_Z^\beta$ is satisfied and therefore the initial nucleus undergoes two successive decays, i.e. $(Z, A) \rightarrow (Z - 1, A) \rightarrow (Z - 2, A)$; see, e.g., Refs. [6,16].

The critical density ρ_{crit}^β is then obtained numerically by looking for the density at which the electron energy equals ϵ_Z^β . In Table II of Ref. [7] we showed that, in the degenerate case, the threshold energies to trigger the inverse β process for ^4He , ^{12}C , ^{16}O , and ^{56}Fe are reached at densities $\rho_{\text{crit}}^\beta = 1.37 \times 10^{11}$, 3.88×10^{10} , 1.89×10^{10} , and 1.14×10^9 g cm $^{-3}$, respectively.

For the present finite-temperature case, from our numerical integration we found that the critical densities for the occurrence of the inverse β -decay instability are not affected so they are the same as in the degenerate approximation. This is due to the fact that the effects of temperatures $T \lesssim 10^8$ K become relevant at densities $\rho \lesssim 10^6$ g cm $^{-3}$, as can be seen from Figs. 6 and 8.

We turn now to the pycnonuclear reactions. In a nuclei lattice the nuclear reactions proceed with the overcoming of the Coulomb barrier between neighbor nuclei. At zero temperatures, $T = 0$, the Coulomb barrier can be overcome due to the zero-point energy of the nuclei (see, e.g., Refs. [16,17]),

$$E_p = \hbar\omega_p, \quad \omega_p = \sqrt{\frac{4\pi e^2 Z^2 \rho}{A^2 M_u^2}}. \quad (20)$$

The number of pycnonuclear reactions per unit volume per unit time increases with the density of the system [17] and any

effect that reduces the Coulomb barrier will increase the cross section of the reaction. The inclusion of the temperature could then lead to thermo-enhanced pycnonuclear rates (see, e.g., Refs. [17,18]). The astrophysical importance of pycnonuclear reactions, e.g., in the theory of white dwarfs, relies on the fact that, for instance, the $^{12}\text{C} + ^{12}\text{C}$ pycnonuclear fusion, leading to ^{24}Mg , is possible in a time scale shorter than a Hubble time, $\tau_{\text{pyc}} < 10$ Gyr, for densities $\sim 10^{10}$ g cm $^{-3}$. Such a density turns to be larger than the critical density $\sim 3 \times 10^9$ g cm $^{-3}$ for the double inverse β decay of ^{24}Mg into ^{24}Ne by electron capture (see, e.g., Refs. [6,16]), which destabilize the white dwarf due to sudden decrease of its electron pressure. Under such conditions, $^{12}\text{C} + ^{12}\text{C}$ fusion will indirectly induce the gravitational collapse of the white dwarf rather than to a supernova explosion.

Following the updated reaction rates of Ref. [18], we recently computed in Ref. [8] the critical density for pycnonuclear instability in general relativistic uniformly rotating ^{12}C white dwarfs at zero temperatures. It comes out that the instability agent of white dwarfs can be either general relativistic effects or inverse β -decay or pycnonuclear reactions or rotation through mass shedding or secular instabilities (see Ref. [8] for details).

The electrons around the nuclei screen the positive charge of the nucleus, reducing the Coulomb barrier; hence, their proper inclusion could, in principle, increase the reaction rates. On the other hand, we showed in Figs. 2 and 3 two different effects due to the finite temperature: (1) it tends to flatten the electron distribution, thus changing the electron screening of the Coulomb potential with respect to the degenerate case, and (2) it increases the electron density, hence, the pressure at the border of the cell. These effects clearly could lead not only to qualitative but also to quantitative differences in the estimate of the rates of the pycnonuclear reactions (see, e.g., Ref. [19]).

However, the inclusion of these combined effects within the pycnonuclear reactions treatment, following a fully relativistic approach of the electron gas and the Coulomb interactions as the one presented here, is a most difficult and complex task that deserves a detailed and separated analysis and therefore will not be addressed here.

IV. MASS-RADIUS RELATION

General relativistic effects are important in the high-density branch of white dwarfs; for instance, they lead to the gravitational collapse of the star prior to the trigger of the inverse β -decay instability in ^{12}C white dwarfs [7]. We here construct the mass-radius relation of white dwarfs in their entire range of stability, so we use the equations of hydrostatic equilibrium within the framework of general relativity. Assuming the spherically symmetric metric

$$ds^2 = e^{\nu(r)} c^2 dt^2 - e^{\lambda(r)} dr^2 - r^2 d\theta^2 - r^2 \sin^2 \theta d\phi^2, \quad (21)$$

the equations of equilibrium can be written in the Tolman-Oppenheimer-Volkoff form,

$$\frac{dv(r)}{dr} = \frac{2G}{c^2} \frac{4\pi r^3 P(r)/c^2 + M(r)}{r^2 \left[1 - \frac{2GM(r)}{c^2 r}\right]}, \quad (22)$$

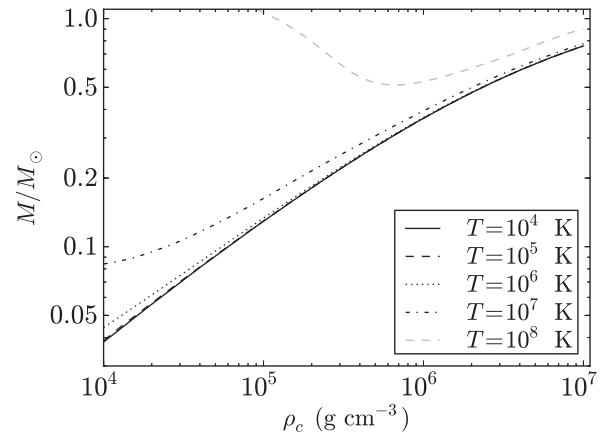


FIG. 9. Total mass versus central density for ^4He white dwarfs for selected temperatures from $T = 10^4$ K to $T = 10^8$ K.

$$\frac{dM(r)}{dr} = 4\pi r^2 \frac{\mathcal{E}(r)}{c^2}, \quad (23)$$

$$\frac{dP(r)}{dr} = -\frac{1}{2} \frac{dv(r)}{dr} [\mathcal{E}(r) + P(r)], \quad (24)$$

where we have introduced the mass enclosed at the distance r through $e^{-\lambda(r)} = 1 - 2GM(r)/(c^2 r)$, $\mathcal{E}(r) = c^2 \rho(r)$ is the energy density, and $P(r)$ is the total pressure, given by Eqs. (14) and (15).

These equations can be integrated for a wide range of central densities, temperatures, and selected chemical compositions, for instance ^4He , ^{12}C , ^{16}O , and ^{56}Fe . In Figs. 9 and 10, we show in particular the mass-central density and mass-radius relations of ^4He white dwarfs in the range of densities and radii where finite-temperature effects are more important.

The minima in these plots mark the transition from the ideal to the degenerate behavior of the electron gas: from left to right in the M - ρ_c relation and from right to left in the M - R relation. Thus these minima can be used to give an estimate of the minimum mass that a star should have to be able to burn stably a given chemical composition since the condition of a stable burning requires that the gas be nondegenerate.

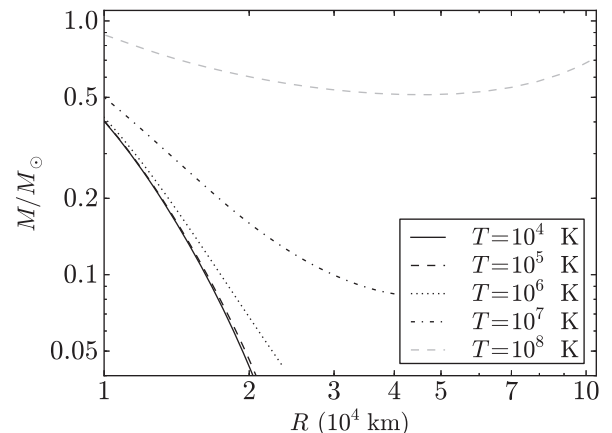


FIG. 10. Total mass versus radius for ^4He white dwarfs for selected temperatures from $T = 10^4$ K to $T = 10^8$ K.

Consequently, stable burning requires that the star lies on the branch of solutions on the left-hand side of the minimum of the M - ρ_c diagram or on the right-hand side of the minimum of the M - R diagram. For instance, helium burning is triggered at a temperature $T_{\text{He+He}} \approx 10^8$ K, so we can obtain from the solutions shown in Fig. 9 that the minimum mass for stable helium burning is $M_{\text{min}}^{\text{He+He}} \approx 0.51 M_{\odot}$. The corresponding radius and density of this configuration is 4.54×10^9 cm $\approx 0.065 R_{\odot}$ and 6.59×10^5 g cm $^{-3}$, respectively. A similar analysis can be done for the other compositions.

V. THE ULTRA-LOW-MASS WHITE DWARF COMPANION OF PSR J1738 + 0333

It is clear that the effects of the temperature are particularly important at low densities and, hence, for low-mass white dwarfs. We analyze here the specific case of the white dwarf companion of the millisecond pulsar PSR J1738 + 0333. We refer to Ref. [11] for details on the observations and technical aspects of the derivation of the binary parameters.

Antoniadis *et al.* [11] obtained, by use of the the Goodman High Throughput Spectrograph instrument of the Southern Astrophysical Research Telescope (SOAR) at Cerro Pachón, Chile, a photometric radius of the white dwarf, $R_{\text{WD}} = 0.042 \pm 0.004 R_{\odot}$. On the other hand, the analysis of the white dwarf atmosphere spectrum with the models of Ref. [20] led to an effective surface temperature, $T_{\text{eff}} = 9130 \pm 150$ K, and a logarithm of the surface gravity, $\log_{10}(g) = \log_{10}(GM_{\text{WD}}/R_{\text{WD}}^2) = 6.55 \pm 0.1$. Using the evolutionary mass-radius relation of Painei *et al.* [21], the mass of the white dwarf was estimated in Ref. [11] to be $M_{\text{WD}} = 0.181_{-0.005}^{+0.007} M_{\odot}$, with a corresponding radius of $R_{\text{WD}} = 0.037_{-0.003}^{+0.004} R_{\odot}$, in agreement with the photometric value.

A first attempt to obtain the mass of the white dwarf can be done directly from the observed data by combining the spectral and photometric analysis. Assuming the photometric radius as the star radius, the mass of the white dwarf would be $M_{\text{WD}} = g R_{\text{WD}}^2 / G \approx 0.23 M_{\odot}$, using the central values of R_{WD} and g , which is roughly consistent with the mass derived from the mass-radius relation of Ref. [21].

In order to compare our mass-radius relation at finite temperatures with the above results and infer the internal temperature of the white dwarf, we plotted in Figs. 11 and 12 our theoretical surface gravity-mass and radius relations for ${}^4\text{He}$ white dwarfs, together with the above observational constraints.

An inspection of Fig. 11 does not give us any information on the possible internal temperature of the white dwarf since, in principle, we do not have any *a priori* information on the mass. However, from Fig. 12 we clearly identify that the interior temperature of the white dwarf core should be $T \approx 2\text{--}3 \times 10^7$ K. In Fig. 13 we plot the mass-radius relation for ${}^4\text{He}$ white dwarfs with the observational constraints of the companion of PSR J1738 + 0333. We can now compare our results with an estimate obtained, for instance, using the relation found by Koester in Ref. [22] between the central and surface temperatures of the white dwarf, $T_{\text{eff}}^4/g = 2.05 \times 10^{-10} T_c^{2.56}$. Using the value $T_{\text{eff}} = 9130$ K and $\log_{10}(g) = 6.55$, this

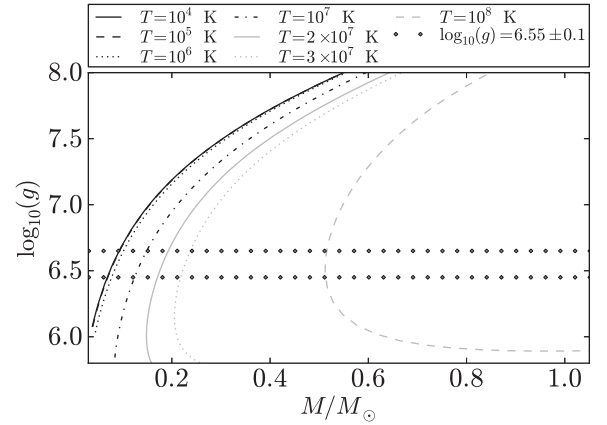


FIG. 11. Logarithm of the surface gravity, $\log_{10}(g) = \log_{10}(GM_{\text{WD}}/R_{\text{WD}}^2)$, as a function of the mass for ${}^4\text{He}$ white dwarfs for selected interior temperatures from $T = 10^4$ K to $T = 10^8$ K. The horizontal diamonds indicate the maximum and minimum best-fit values $\log_{10}(g) = 6.55 \pm 0.1$.

relation gives $T_c \approx 2.6 \times 10^7$ K, in full agreement with our inference. In this estimate we have neglected the contribution of the thickness of the envelope to the total surface radius of the white dwarf. However, this approximation does not introduce a large error since the envelope would be in this case at most $\sim 10^{-2} R_{\text{WD}}$ thick.

VI. APPLICATION TO NUCLEAR MATTER CORES OF STELLAR DIMENSIONS

In Ref. [1] we extended the relativistic FMT model to what we have called nuclear matter cores of stellar dimensions: macroscopic objects composed by neutrons, protons, and electrons in β equilibrium, with mass numbers $A \sim (m_{\text{Planck}}/m_n)^3 \sim 10^{57}$ and corresponding masses $M_{\text{core}} \sim M_{\odot}$.

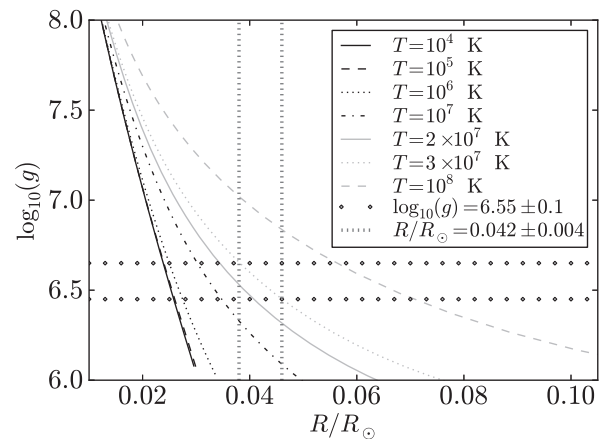


FIG. 12. Logarithm of the surface gravity, $\log_{10}(g) = \log_{10}(GM_{\text{WD}}/R_{\text{WD}}^2)$, as a function of the radius for ${}^4\text{He}$ white dwarfs for selected interior temperatures from $T = 10^4$ K to $T = 10^8$ K. The horizontal diamonds and the vertical tick dashed lines indicate the maximum and minimum best-fit values of the surface gravity, $\log_{10}(g) = 6.55 \pm 0.1$, and photometric radii $R_{\text{WD}} = 0.042 \pm 0.004 R_{\odot}$, respectively.

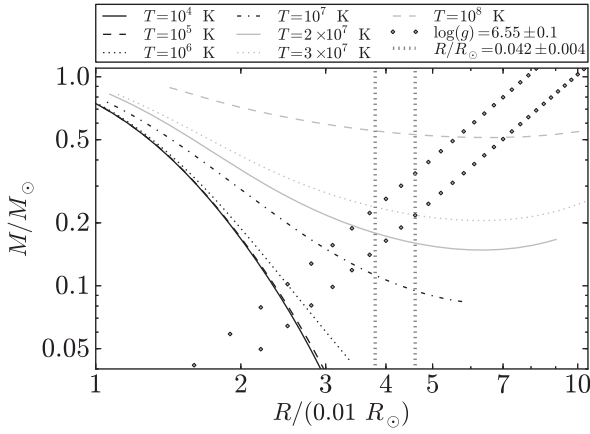


FIG. 13. Total mass versus radius for ${}^4\text{He}$ white dwarfs for selected interior temperatures from $T = 10^4$ K to $T = 10^8$ K. The diagonal diamonds and the vertical tick dashed lines indicate the maximum and minimum best-fit values of the surface gravity, $\log_{10}(g) = 6.55 \pm 0.1$ and photometric radii $R_{\text{WD}} = 0.042 \pm 0.004 R_{\odot}$, respectively.

These systems are expected to represent idealized cores of macroscopic systems of nuclear matter kept bound by self-gravity, such as the cores of neutron stars. We now follow our treatment in Ref. [1] and use the existence of scaling laws and proceed to the ultrarelativistic limit of the relativistic Thomas-Fermi equation at finite temperatures given by Eq. (7).

The β equilibrium of $N_n = A - Z$ neutrons, Z protons, and Z electrons gives, for massive cores, $N_n \gg Z$. Typically, in these systems we have $A/Z \approx 10^2$, so at nuclear density the neutron gas will have a Fermi energy E_n^F of the order of

$$E_n^F \simeq \frac{(P_n^F)^2}{2m_n} \simeq (3\pi^2)^{2/3} \frac{\hbar^2}{2m_n} \left(A \frac{\rho_{\text{nuc}}}{m_n} \right)^{2/3} \sim 60 \text{ MeV}, \quad (25)$$

where we have used a nuclear density value $\rho_{\text{nuc}} \approx 2.7 \times 10^{14} \text{ g cm}^{-3}$ and $1 - Z/A \approx 1$. Assuming a temperature such that $T \ll T_n^F = E_n^F/k_B \approx 7 \times 10^{11} \text{ K}$, the neutron chemical potential μ_n can be expanded as

$$\mu_n = E_n^F \left[1 - \frac{\pi^2}{12} \left(\frac{k_B T}{E_n^F} \right)^2 - \frac{\pi^4}{80} \left(\frac{k_B T}{E_n^F} \right)^4 + \dots \right]. \quad (26)$$

Correspondingly, the protons have Fermi energy $E_p^F \sim (Z/A)^{2/3} E_n^F \sim \text{MeV}$, so for temperatures $k_B T \ll E_p^F \approx 1 \text{ MeV}$, Eq. (26) applies also for protons,

$$\mu_p = E_p^F \left[1 - \frac{\pi^2}{12} \left(\frac{k_B T}{E_p^F} \right)^2 - \frac{\pi^4}{80} \left(\frac{k_B T}{E_p^F} \right)^4 + \dots \right]. \quad (27)$$

As a result, for temperatures $k_B T \lesssim 1 \text{ MeV}$, both neutrons and protons can be treated as degenerate particles, whereas in this limit electrons are semidegenerate and ultrarelativistic. In the case of ordinary nuclei, due their high isospin symmetry ($A/Z \approx 2$), both neutrons and protons can be treated as degenerate particles until $T \approx (Z/A)^{2/3} E_n^F/k_B \sim 38 \text{ MeV}$.

Since in the ultrarelativistic limit for electrons their kinetic energy ϵ is simply pc , the condition $\mu_e/(k_B T) \gg 1$ holds.

Consequently, the integral

$$I = \int_0^\infty \frac{f(\epsilon) d\epsilon}{\exp\left(\frac{\epsilon - \mu_e}{k_B T}\right) + 1}, \quad (28)$$

with $f(\epsilon) = \epsilon^2$ appearing in the electron density given by Eq. (2), can be expanded as

$$I = \int_0^{\mu_e} f(\epsilon) d\epsilon + 2(k_B T)^2 f'(\mu_e) \int_0^\infty \frac{z}{e^z + 1} dz + \frac{1}{3} (k_B T)^4 f'''(\mu_e) \int_0^\infty \frac{z^3}{e^z + 1} dz + \dots, \quad (29)$$

where

$$\int_0^\infty \frac{z^{x-1}}{e^z + 1} dz = (1 - 2^{1-x}) \Gamma(x) \sum_{n=1}^\infty \frac{1}{n^x}, \quad (30)$$

with Γ the Gamma function and μ_e the chemical potential of electrons and a prime denotes derivative with respect to ϵ . We thus obtain the result

$$I = \int_0^{\mu_e} f(\epsilon) d\epsilon + \frac{\pi^2}{6} (k_B T)^2 f'(\mu_e) + \frac{7\pi^4}{360} (k_B T)^4 f'''(\mu_e) + \dots, \quad (31)$$

and, retaining only the first term in T , we have

$$I \approx \frac{\mu_e^3}{3} + \frac{\pi^2}{6} (k_B T)^2 \mu_e. \quad (32)$$

As discussed in Ref. [1], for a nuclear massive core of stellar dimensions we can assume the plane-parallel approximation, which leads to the Poisson equation in the case of finite temperatures,

$$\frac{d^2 \hat{\phi}}{d\xi^2} = -\theta(\xi - \xi_c) + \hat{\phi}^3 + s \hat{\phi}, \quad (33)$$

where $\phi = 4^{1/3} (9\pi)^{-1/3} \chi \Delta / x$, $\hat{x} = kx$, where $k = (12/\pi)^{1/6} \sqrt{\alpha} \Delta^{-1}$, $\xi = \hat{x} - \hat{x}_c$, and $s = (2\pi^4)^{1/3} \Delta^2 (k_B T)^2 / (3^{4/3} m_\pi^2 c^2)$. Notice that the above equation is the ultrarelativistic version of Eq. (7) for semidegenerate electrons and how, in the limit $T \rightarrow 0$ ($s \rightarrow 0$), it leads to the ultrarelativistic Thomas-Fermi equation for fully degenerate massive cores obtained in Ref. [1].

The Coulomb potential is given by

$$eV(\xi) = \left(\frac{9\pi}{4} \right)^{1/3} \frac{1}{\Delta} m_\pi c^2 \hat{\phi}(\xi) - C, \quad (34)$$

with $C = (9\pi/4)^{1/3} \Delta^{-1} m_\pi c^2 \hat{\phi}(\xi_{\text{WS}})$, the electric field is

$$E(\xi) = - \left(\frac{3^5 \pi}{4} \right)^{1/6} \frac{\sqrt{\alpha} m_\pi c^3}{\Delta^2} \frac{d\hat{\phi}}{d\xi}, \quad (35)$$

and the electron number density is

$$n_e(\xi) = \frac{(m_\pi c^2)^3}{3\pi^2 \hbar^3 c^3} \left[\left(\frac{9\pi}{4} \right) \frac{1}{\Delta^3} \hat{\phi}^3(\xi) + \frac{\pi^2}{2} \left(\frac{9\pi}{4} \right)^{1/3} \frac{1}{\Delta} \left(\frac{k_B T}{m_\pi c^2} \right)^2 \hat{\phi}(\xi) \right]. \quad (36)$$

The global charge neutrality of the system imposes the boundary condition that the electric field vanishes at $\xi = \xi_{\text{WS}}$. This implies $d\hat{\phi}/d\xi|_{\xi=\xi_{\text{WS}}} = 0$. The function $\hat{\phi}$ and its first derivative $d\hat{\phi}/d\xi$ must be continuous at the surface $\xi = 0$ of the nuclear density core. This boundary-value problem can be solved analytically and indeed Eq. (33) has the first integral,

$$2\left(\frac{d\hat{\phi}}{d\xi}\right)^2 = \begin{cases} \hat{\phi}^4(\xi) + 2s\hat{\phi}^2 - 4\hat{\phi}(\xi) + 3 - 2s, & \xi \leq 0, \\ \hat{\phi}^4(\xi) + 2s\hat{\phi}^2 - \hat{\phi}^4(\xi_{\text{WS}}) - 2s\hat{\phi}^2(\xi_{\text{WS}}), & \xi > 0, \end{cases} \quad (37)$$

with boundary conditions at $\xi = 0$,

$$\hat{\phi}(0) = \frac{\hat{\phi}^4(\xi_{\text{WS}}) + 3}{4} + \frac{s}{2}[\hat{\phi}^2(\xi_{\text{WS}}) - 1], \quad (38)$$

$$\left.\frac{d\hat{\phi}}{d\xi}\right|_{\xi=0} = -\left\{\frac{\hat{\phi}^4(0) - \hat{\phi}^4(\xi_{\text{WS}})}{2} + s[\hat{\phi}^2(0) - \hat{\phi}^2(\xi_{\text{WS}})]\right\}^{1/2}. \quad (39)$$

The solution of Eq. (37) in the interior region $\xi \leq 0$ is then

$$\hat{\phi}(\xi) = 1 - (s+3)\left[1 + \left(\frac{s+1}{2}\right)^{1/2} \sinh(\beta - \sqrt{s+3}\xi)\right]^{-1}, \quad (40)$$

with

$$\sinh \beta = \sqrt{\frac{2}{s+1}} \left\{ \frac{11 + \hat{\phi}^4(\xi_{\text{WS}}) + 2s[\hat{\phi}^2(\xi_{\text{WS}}) + 1]}{1 - \hat{\phi}^4(\xi_{\text{WS}}) - 2s[\hat{\phi}^2(\xi_{\text{WS}}) - 1]} \right\}^{1/2}. \quad (41)$$

In the exterior region $\xi > 0$ the solution of Eq. (37) is

$$\hat{\phi}(\xi) = \frac{\sqrt{-s + \sqrt{s^2 + G}}}{\cos\left(\text{am}\left[(s^2 + G)^{1/4}(\xi - \xi_{\text{WS}}), \frac{1}{2} + \frac{s}{2\hat{\phi}^2(\xi_{\text{WS}})}\right]\right)}, \quad (42)$$

where $G = \hat{\phi}^4(\xi_{\text{WS}}) + 2s\hat{\phi}^2(\xi_{\text{WS}})$. It can be seen again how in the limit $T \rightarrow 0$ ($s \rightarrow 0$), the solution at finite temperatures given by Eqs. (40)–(42) becomes its degenerate counterpart obtained in Ref. [1].

From Eqs. (39) it follows that the peak of the electric field at the surface of the core is larger than the corresponding value obtained for $T = 0$. In fact, we have, for any temperature $T > 0$ and level of compression $\xi_{\text{WS}} \neq 0$,

$$\left|\left(\frac{d\hat{\phi}}{d\xi}\right)\right|_{\xi=0|T>0} > \left|\left(\frac{d\hat{\phi}}{d\xi}\right)\right|_{\xi=0|T=0}. \quad (43)$$

As in the degenerate case, in the limit $\xi_{\text{WS}} \rightarrow 0$, the global charge neutrality $N_e = Z$ and the local charge neutrality $n_e = n_p$ are recovered and at the surface of the massive core no electro-dynamical structure is present.

The above analytic equations can be used only in the ultra-relativistic regime of the electron gas; it can then be checked from the above formulation that at such high compressions we have $\hat{\phi}(\xi)|_{T>0} \approx \hat{\phi}(\xi)|_{T=0}$. More specifically, corrections due

to thermal effects on the density of ultrarelativistic electrons are smaller than 1% for $T \lesssim 0.1 \text{ MeV}/k_B \approx 10^9 \text{ K}$.

VII. CONCLUSIONS

The Feynman-Metropolis-Teller treatment [1] of compressed matter has been here generalized to the case of finite temperatures. We have thus obtained the EOS formed by nuclei and electrons by solving the finite-temperature relativistic Thomas-Fermi equation (7) within globally neutral Wigner-Seitz cells. We emphasize in this work the electron component and the Coulomb interaction between ions and electrons fully computed within a relativistic Thomas-Fermi approach with finite-sized nuclei, and therefore applicable to any relativistic regime of the electrons and densities. This work generalizes other treatments based on either a uniform distribution of electrons or the classic Thomas-Fermi treatment; see, e.g., Ref. [12]. The quantum corrections to the classic ideal ion fluid considered in this work can be straightforwardly introduced in their corresponding ranges of relevance, as done in previous treatments; see, e.g., Refs. [13–15,23].

We have shown the general features of the new EOS and compared and contrasted the effects due to the nonzero temperature with respect to the degenerate case. We have checked that the onset of the inverse β -decay instability is not modified for temperatures $T \lesssim 10^8 \text{ K}$ and therefore the zero-temperature critical densities computed in Ref. [7] can be safely used. The enhancement and flattening of the electron density inside the cell for larger temperatures could have relevant effect in the pycnonuclear reaction rates in the interior of white dwarfs and/or in the low density layers of accreting neutron stars.

Deviations from the degenerate EOS have been shown to occur in the regions of interest of low-mass white dwarfs and in the outermost layers of neutron star crusts. Ultra-low-mass white dwarfs, $M_{\text{WD}} \sim 0.2M_{\odot}$ [10,11], have been found in binary systems with neutron star companions. These objects have central densities $\lesssim 10^6 \text{ g cm}^{-3}$, where the degenerate approximation breaks down and so thermal effects cannot be neglected. We have analyzed here the specific case of PSR J1738+0333, whose mass and radius was estimated in Ref. [11] using the evolutionary mass-radius relation of Painei *et al.* [21]. They obtained $M_{\text{WD}} = 0.181_{-0.005}^{+0.007} M_{\odot}$, $R_{\text{WD}} = 0.037_{-0.003}^{+0.004} R_{\odot}$, in agreement with the spectrometric and photometric data. We inferred for this object an internal temperature $T \approx 2\text{--}3 \times 10^7 \text{ K}$, and a mass $M_{\text{WD}} \approx 0.2M_{\odot}$, assuming, for instance, the photometric radius, $R = 0.042R_{\odot}$, as the star radius. We checked also our result using the relation by Koester [22] between the internal and surface white dwarf temperatures, $T_{\text{eff}}^4/g = 2.05 \times 10^{-10} T_c^{2.56}$. Using the surface temperature and the logarithm of the surface gravity obtained from the spectral analysis, $T_{\text{eff}} = 9130 \text{ K}$ and $\log_{10}(g) = 6.55$, this relation gives $T_c \approx 2.6 \times 10^7 \text{ K}$, in full agreement with our results.

Following our previous work [1], we finally extrapolated the treatment to macroscopic systems with mass numbers $A \approx (m_{\text{Planck}}/m_n)^3 \sim 10^{57}$, corresponding to masses $M_{\text{core}} \approx M_{\odot}$. We showed that the presence of the temperature enhances the maximum electric field in the core surface of these objects.

ACKNOWLEDGMENTS

S.M.d.C. acknowledges the support given by the International Relativistic Astrophysics Erasmus Mundus Joint

Doctorate Program under Grant No. 2010–1816 from the EACEA of the European Commission. We are grateful to the referee for the comments and suggestions which helped us to improve the presentation of our results.

-
- [1] M. Rotonondo, J. A. Rueda, R. Ruffini, and S.-S. Xue, *Phys. Rev. C* **83**, 045805 (2011).
- [2] R. P. Feynman, N. Metropolis, and E. Teller, *Phys. Rev.* **75**, 1561 (1949).
- [3] J. Ferreira, R. Ruffini, and L. Stella, *Phys. Lett. B* **91**, 314 (1980).
- [4] R. Ruffini and L. Stella, *Phys. Lett. B* **102**, 442 (1981).
- [5] S. Chandrasekhar, *Astrophys. J.* **74**, 81 (1931).
- [6] E. E. Salpeter, *Astrophys. J.* **134**, 669 (1961).
- [7] M. Rotonondo, J. A. Rueda, R. Ruffini, and S.-S. Xue, *Phys. Rev. D* **84**, 084007 (2011).
- [8] K. Boshkayev, J. A. Rueda, R. Ruffini, and I. Siutsou, *Astrophys. J.* **762**, 117 (2013).
- [9] P.-E. Tremblay, P. Bergeron, and A. Gianninas, *Astrophys. J.* **730**, 128 (2011).
- [10] J. Antoniadis, P. C. C. Freire, N. Wex, T. M. Tauris, R. S. Lynch, M. H. van Kerkwijk, M. Kramer, C. Bassa, V. S. Dhillon, T. Driebe *et al.*, *Science* **340**, 448 (2013).
- [11] J. Antoniadis, M. H. van Kerkwijk, D. Koester, P. C. C. Freire, N. Wex, T. M. Tauris, M. Kramer, and C. G. Bassa, *Mon. Not. Roy. Astr. Soc.* **423**, 3316 (2012).
- [12] A. Thorolfsson, O. E. Roegvaldsson, J. Yngvason, and E. H. Gudmundsson, *Astrophys. J.* **502**, 847 (1998).
- [13] W. Stolzmann and T. Bloeker, *A&A* **314**, 1024 (1996).
- [14] G. Chabrier and A. Y. Potekhin, *Phys. Rev. E* **58**, 4941 (1998).
- [15] A. Y. Potekhin and G. Chabrier, *Phys. Rev. E* **62**, 8554 (2000).
- [16] S. L. Shapiro and S. A. Teukolsky, *J. Br. Astronom. Assoc.* **93**, 276 (1983).
- [17] E. E. Salpeter and H. M. van Horn, *Astrophys. J.* **155**, 183 (1969).
- [18] L. R. Gasques, A. V. Afanasjev, E. F. Aguilera, M. Beard, L. C. Chamon, P. Ring, M. Wiescher, and D. G. Yakovlev, *Phys. Rev. C* **72**, 025806 (2005).
- [19] A. Y. Potekhin and G. Chabrier, *A&A* **538**, A115 (2012).
- [20] D. Koester, [arXiv:0812.0482](https://arxiv.org/abs/0812.0482).
- [21] J. A. Panei, L. G. Althaus, and O. G. Benvenuto, *A&A* **353**, 970 (2000).
- [22] D. Koester, *A&A* **52**, 415 (1976).
- [23] A. Y. Potekhin and G. Chabrier, *A&A* **550**, A43 (2013).



Uniformly rotating neutron stars in the global and local charge neutrality cases

Riccardo Belvedere^{a,b,*}, Kuantay Boshkayev^d, Jorge A. Rueda^{a,b},
Remo Ruffini^{a,b,c}

^a *Dipartimento di Fisica and ICRA, Sapienza Università di Roma, P.le Aldo Moro 5, I-00185 Rome, Italy*

^b *ICRANet, P.zza della Repubblica 10, I-65122 Pescara, Italy*

^c *ICRANet, University of Nice-Sophia Antipolis, 28 Av. de Valrose, 06103 Nice Cedex 2, France*

^d *Physical–Technical Faculty, Al-Farabi Kazakh National University, Al-Farabi ave. 71, 050040 Almaty, Kazakhstan*

Received 21 June 2013; received in revised form 11 October 2013; accepted 8 November 2013

Available online 14 November 2013

Abstract

In our previous treatment of neutron stars, we have developed the model fulfilling global and not local charge neutrality. In order to implement such a model, we have shown the essential role by the Thomas–Fermi equations, duly generalized to the case of electromagnetic field equations in a general relativistic framework, forming a coupled system of equations that we have denominated Einstein–Maxwell–Thomas–Fermi (EMTF) equations. From the microphysical point of view, the weak interactions are accounted for by requesting the β stability of the system, and the strong interactions by using the σ – ω – ρ nuclear model, where σ , ω and ρ are the mediator massive vector mesons. Here we examine the equilibrium configurations of slowly rotating neutron stars by using the Hartle formalism in the case of the EMTF equations indicated above. We integrate these equations of equilibrium for different central densities ρ_c and circular angular velocities Ω and compute the mass M , polar R_p and equatorial R_{eq} radii, angular momentum J , eccentricity ϵ , moment of inertia I , as well as quadrupole moment Q of the configurations. Both the Keplerian mass-shedding limit and the axisymmetric secular instability are used to construct the new mass–radius relation. We compute the maximum and minimum masses and rotation frequencies of neutron stars. We compare and contrast all the results for the global and local charge neutrality cases.

© 2013 Elsevier B.V. All rights reserved.

Keywords: Nuclear physics; Astrophysics; Neutron stars; Quantum hydrodynamics; Field theory

* Corresponding author.

E-mail addresses: riccardo.belvedere@icra.it (R. Belvedere), kuantay@icra.it (K. Boshkayev), jorge.rueda@icra.it (J.A. Rueda), ruffini@icra.it (R. Ruffini).

1. Introduction

We have recently shown [22,23,2] that the equations of Tolman–Oppenheimer–Volkoff (TOV) [30,21] traditionally used to describe the neutron star equilibrium configurations, are superseded once the strong, weak, electromagnetic and gravitational interactions are taken into account. Instead, the Einstein–Maxwell system of equations coupled with the general relativistic Thomas–Fermi equations of equilibrium have to be used; what we called the Einstein–Maxwell–Thomas–Fermi (EMTF) system of equations. While in the TOV approach the condition of local charge neutrality, $n_e(r) = n_p(r)$ is imposed (see e.g. Haensel et al. [12] and references therein), the EMTF approach requests the less stringent condition of global charge neutrality, namely

$$\int \rho_{\text{ch}} d^3r = \int e[n_p(r) - n_e(r)] d^3r = 0, \quad (1)$$

where ρ_{ch} is the charge density, e is the fundamental electric charge, n_i is the particle density of the i -species, and the integral is carried out on the entire volume of the system.

The Lagrangian density taking into account all the interactions include the free-fields terms \mathcal{L}_g , \mathcal{L}_γ , \mathcal{L}_σ , \mathcal{L}_ω , \mathcal{L}_ρ (respectively for the gravitational, the electromagnetic, and the three mesonic fields), the three fermion species (electrons, protons and neutrons) term \mathcal{L}_f and the interacting part in the minimal coupling assumption, \mathcal{L}_{int} [23,2]:

$$\mathcal{L} = \mathcal{L}_g + \mathcal{L}_f + \mathcal{L}_\sigma + \mathcal{L}_\omega + \mathcal{L}_\rho + \mathcal{L}_\gamma + \mathcal{L}_{\text{int}}, \quad (2)$$

where¹

$$\begin{aligned} \mathcal{L}_g &= -\frac{R}{16\pi}, & \mathcal{L}_f &= \sum_{i=e,N} \bar{\psi}_i (i\gamma^\mu D_\mu - m_i) \psi_i, \\ \mathcal{L}_\sigma &= \frac{\nabla_\mu \sigma \nabla^\mu \sigma}{2} - U(\sigma), & \mathcal{L}_\omega &= -\frac{\Omega_{\mu\nu} \Omega^{\mu\nu}}{4} + \frac{m_\omega^2 \omega_\mu \omega^\mu}{2}, \\ \mathcal{L}_\rho &= -\frac{\mathcal{R}_{\mu\nu} \mathcal{R}^{\mu\nu}}{4} + \frac{m_\rho^2 \rho_\mu \rho^\mu}{2}, & \mathcal{L}_\gamma &= -\frac{F_{\mu\nu} F^{\mu\nu}}{16\pi}, \\ \mathcal{L}_{\text{int}} &= -g_\sigma \sigma \bar{\psi}_N \psi_N - g_\omega \omega_\mu J_\omega^\mu - g_\rho \rho_\mu J_\rho^\mu + e A_\mu J_{\gamma,e}^\mu - e A_\mu J_{\gamma,N}^\mu, \end{aligned}$$

where the description of the strong interactions between the nucleons is made through the σ – ω – ρ nuclear model in the version of Boguta and Bodmer [6]. Thus $\Omega_{\mu\nu} \equiv \partial_\mu \omega_\nu - \partial_\nu \omega_\mu$, $\mathcal{R}_{\mu\nu} \equiv \partial_\mu \rho_\nu - \partial_\nu \rho_\mu$, $F_{\mu\nu} \equiv \partial_\mu A_\nu - \partial_\nu A_\mu$ are the field strength tensors for the ω^μ , ρ and A^μ fields respectively, ∇_μ stands for covariant derivative and R is the Ricci scalar. We adopt the Lorenz gauge for the fields A_μ , ω_μ , and ρ_μ . The self-interaction scalar field potential is $U(\sigma)$, ψ_N is the nucleon isospin doublet, ψ_e is the electronic singlet, m_i states for the mass of each particle-specie and $D_\mu = \partial_\mu + \Gamma_\mu$, being Γ_μ the Dirac spin connections. The conserved currents are $J_\omega^\mu = \bar{\psi}_N \gamma^\mu \psi_N$, $J_\rho^\mu = \bar{\psi}_N \tau_3 \gamma^\mu \psi_N$, $J_{\gamma,e}^\mu = \bar{\psi}_e \gamma^\mu \psi_e$, and $J_{\gamma,N}^\mu = \bar{\psi}_N (1/2)(1 + \tau_3) \gamma^\mu \psi_N$, being τ_3 the particle isospin.

The nuclear model is fixed once the values of the coupling constants and the masses of the three mesons are fixed: for instance in the NL3 parameter set Lalazissis et al. [20] used in [2] and in this work we have $m_\sigma = 508.194$ MeV, $m_\omega = 782.501$ MeV, $m_\rho = 763.000$ MeV,

¹ We use spacetime metric signature (+,–,–,–) and geometric units $G = c = 1$ unless otherwise specified.

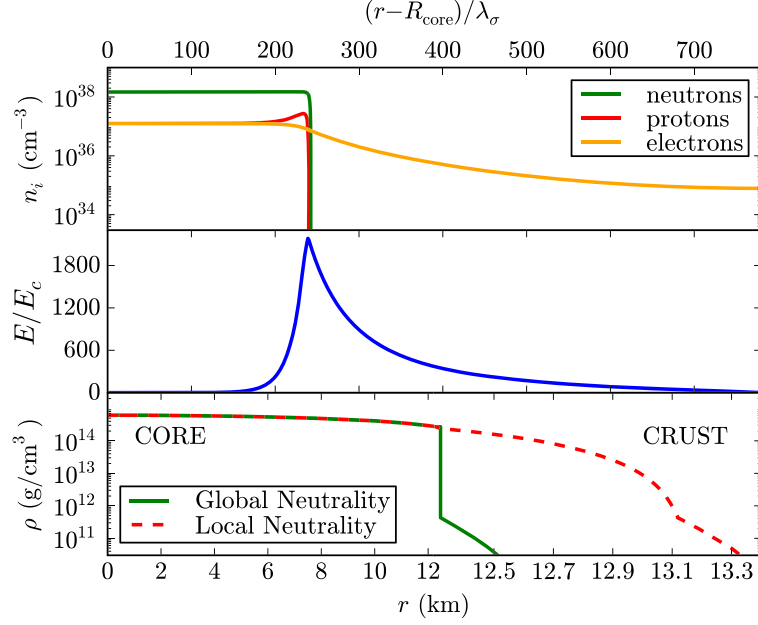


Fig. 1. In the top and center panels we show the neutron, proton, electron densities and the electric field in units of the critical electric field E_c in the core–crust transition layer, whereas in the bottom panel we show a specific example of a density profile inside a neutron star. In this plot we have used for the globally neutral case a density at the edge of the crust equal to the neutron drip density, $\rho_{\text{drip}} \sim 4.3 \times 10^{11} \text{ g cm}^{-3}$.

$g_\sigma = 10.2170$, $g_\omega = 12.8680$, $g_\rho = 4.4740$, plus two constants that give the strength of the self-scalar interactions, $g_2 = -10.4310 \text{ fm}^{-1}$ and $g_3 = -28.8850$.

From the equations of motion of the above Lagrangian we obtain the EMTF equations (see Rueda et al. [23]; Belvedere et al. [2] for details). The solution of the EMTF coupled differential equations leads to a new structure of the star, as shown in Fig. 1: a positively charged core at supranuclear densities, $\rho > \rho_{\text{nuc}} \sim 2.7 \times 10^{14} \text{ g cm}^{-3}$, surrounded by an electron distribution of thickness $\gtrsim \hbar/(m_e c)$ and, at lower densities $\rho < \rho_{\text{nuc}}$, a neutral ordinary crust.

The thermodynamic equilibrium is ensured by the constancy of the particle Klein potentials Klein [19] generalized to the presence of electrostatic and strong fields [22,23,2]

$$\frac{1}{u^t} [\mu_i + (q_i A_\alpha + g_\omega \omega_\alpha + g_\rho \tau_{3,i} \rho_\alpha) u^\alpha] = \text{constant}, \quad (3)$$

where the subscript i stands for each kind of particle, μ_i is the particle chemical potential, and q_i is the particle electric charge. In the static case only the time components of the vector fields, A_0 , ω_0 , ρ_0 are present. In the above equation $u^t = (g_{tt})^{-1/2}$ is the time component of the fluid four-velocity which satisfies $u_\alpha u^\alpha = 1$; g_{tt} is the t – t component of the spherically symmetric metric

$$ds^2 = e^\nu dt^2 - e^\lambda dr^2 - dr^2 - r^2(d\theta^2 + \sin^2\theta d\phi^2). \quad (4)$$

The equilibrium conditions (3) lead to a discontinuity in the density at the core–crust transition and, correspondingly, an overcritical electric field $\sim (m_\pi/m_e)^2 E_c$, where $E_c = m_e^2 c^3/(e\hbar) \sim 1.3 \times 10^{16} \text{ V cm}^{-1}$, appears in the core–crust boundary interface. The constancy of the Klein potentials is necessary to fulfill the requirement of thermodynamical equilibrium, together with the constancy of the gravitationally red-shifted temperature (Tolman condition) [29,19], if finite temperatures are considered (see e.g. Rueda et al. [23]). In particular, the continuity of the electron Klein potential leads to a decreasing of the electron chemical potential μ_e and density at the

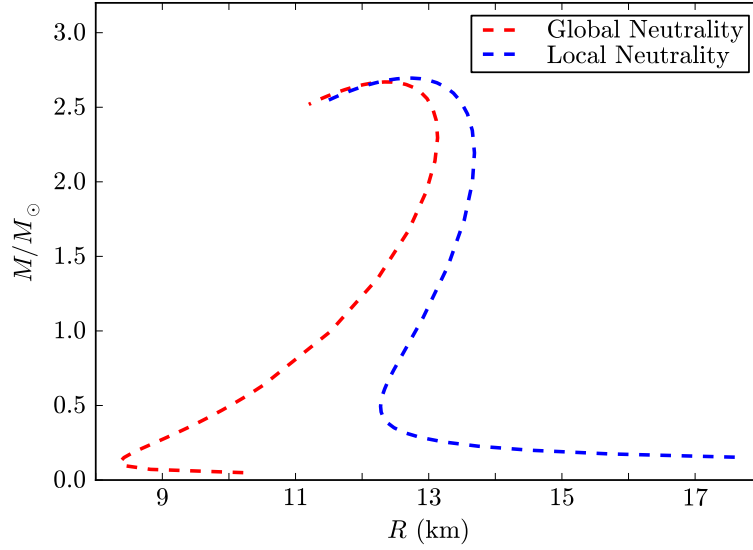


Fig. 2. Neutron star mass–radius relation in the static (non-rotating) case for both global and local charge neutrality configurations (see Belvedere et al. [2] for details). In this plot we have used for the globally neutral case a density at the edge of the crust equal to the neutron drip density, $\rho_{\text{drip}} \sim 4.3 \times 10^{11} \text{ g cm}^{-3}$.

core–crust boundary interface. They reach values $\mu_e^{\text{crust}} < \mu_e^{\text{core}}$ and $\rho_{\text{crust}} < \rho_{\text{core}}$ at the base of the crust, where global charge neutrality is achieved.

As we showed in [2], the solution of this new set of equilibrium equations leads to a more compact neutron star with a less massive and thinner crust. Consequently, it leads to a new mass–radius relation which markedly differs from the one given by the solution of the TOV equations in the case of local charge neutrality; see Fig. 2.

We extend in this work the previous results to the case when the neutron star is rotating as a rigid body. To this end we use the Hartle approach [13] which solves the Einstein equations accurately up to second order approximation in the angular velocity of the star, Ω (see next Section 2 for details).

In this rotating case, the condition of the constancy of the particle Klein potential has the same form as Eq. (3), but the fluid inside the star now moves with a four-velocity of a rigid rotating body, $u^\alpha = (u^t, 0, 0, u^\phi)$, with (see Hartle and Sharp [15] and Appendix A, for details)

$$u^t = (g_{tt} + 2\Omega g_{t\phi} + \Omega^2 g_{\phi\phi})^{-1/2}, \quad u^\phi = \Omega u^t, \quad (5)$$

where ϕ is the azimuthal angular coordinate with respect to which the metric is symmetric, namely the metric is independent of ϕ (axial symmetry). The metric functions $g_{\alpha\beta}$ are now given by Eq. (6) below. It is then clear that in a frame comoving with the rotating star, $u^t = (g_{tt})^{-1/2}$, and the Klein equilibrium condition becomes the same as Eq. (3), as expected.

We applied the Hartle formalism to the seed static solution obtained from the integration of the EMTF equations [2]. For the construction of the new mass–radius relation we take into account the Keplerian mass-shedding limit and the secular axisymmetric instability (see Section 3). We compute in Section 4 the mass M , polar R_p and equatorial R_{eq} radii, and angular momentum J , as a function of the central density and the rotation angular velocity Ω of stable neutron stars both in the globally and locally neutral cases. Based on the criteria of equilibrium we calculate the maximum stable neutron star mass and from the gravitational binding energy of the configurations establish the minimum mass under which the neutron star becomes gravitationally unbound. We construct in Section 5 the new neutron star mass–radius relation. In Section 6 we

calculate the moment of inertia as a function of the central density and total mass of the neutron star. The eccentricity ϵ , the rotational to gravitational energy ratio T/W , and quadrupole moment Q are shown in Section 7. The observational constraints on the mass–radius relation are discussed in Section 8. We finally summarize the results in Section 9.

2. Hartle slow rotation approximation

In his pioneering work, Hartle [13] computed the equilibrium equations of slowly rotating stars in the context of General Relativity. The solutions of the Einstein equations are obtained through a perturbative method, expanding the metric functions up to the second order in the angular velocity Ω . Under this assumption the structure of compact objects can be approximately described by the total mass M , angular momentum J and quadrupole moment Q . The slow rotation regime implies that the perturbations owing to the rotation are relatively small with respect to the known non-rotating geometry. The interior solution is derived by solving numerically a system of ordinary differential equations for the perturbation functions. The exterior solution for the vacuum surrounding the star, can be written analytically in terms of M , J , and Q (see Hartle [13]; Hartle and Thorne [16] for details). The numerical values for all the physical quantities are derived by matching the interior and the exterior solution on the border of the star.

The spacetime metric for the rotating configuration up to the second order of Ω is given by [13]

$$ds^2 = e^\nu(1 + 2h) dt^2 - e^\lambda \left[1 + \frac{2m}{r - 2M_0} \right] dr^2 - r^2(1 + 2k) [d\theta^2 + \sin^2 \theta (d\phi - \omega dt)^2], \quad (6)$$

where $\nu = \nu(r)$, $\lambda = \lambda(r)$, and $M_0 = M^{J=0}(r)$ are the metric functions and mass profiles of the corresponding seed non-rotating star with the same central density as the rotating one; see Eq. (4). The functions $h = h(r, \theta)$, $m = m(r, \theta)$, $k = k(r, \theta)$ and the fluid angular velocity in the local inertial frame, $\omega = \omega(r)$, have to be calculated from the Einstein equations. Expanding up to the second order the metric in spherical harmonics we have

$$h(r, \theta) = h_0(r) + h_2(r)P_2(\cos \theta), \quad (7)$$

$$m(r, \theta) = m_0(r) + m_2(r)P_2(\cos \theta), \quad (8)$$

$$k(r, \theta) = k_0(r) + k_2(r)P_2(\cos \theta), \quad (9)$$

where $P_2(\cos \theta)$ is the Legendre polynomial of second order. Because the metric does not change under transformations of the type $r \rightarrow f(r)$, we can assume $k_0(r) = 0$.

The functions $h = h(r, \theta)$, $m = m(r, \theta)$, $k = k(r, \theta)$ have analytic form in the exterior (vacuum) spacetime and they can be found in Appendix A. The mass, angular momentum, and quadrupole moment are computed from the matching condition between the interior and exterior metrics.

First the angular momentum is computed. It is introduced the angular velocity of the fluid relative to the local inertial frame, $\bar{\omega}(r) = \Omega - \omega(r)$. It can be shown from the Einstein equations at first order in Ω that $\bar{\omega}$ satisfies the differential equation

$$\frac{1}{r^4} \frac{d}{dr} \left(r^4 j \frac{d\bar{\omega}}{dr} \right) + \frac{4}{r} \frac{dj}{dr} \bar{\omega} = 0, \quad (10)$$

where $j(r) = e^{-(\nu+\lambda)/2}$ with ν and λ the metric functions of the seed non-rotating solution (4).

From the matching equations, the angular momentum of the star results to be given by

$$J = \frac{1}{6} R^4 \left(\frac{d\bar{\omega}}{dr} \right)_{r=R}, \quad (11)$$

so the angular velocity Ω is related to the angular momentum as

$$\Omega = \bar{\omega}(R) + \frac{2J}{R^3}. \quad (12)$$

The total mass of the rotating star, M , is given by

$$M = M_0 + \delta M, \quad \delta M = m_0(R) + J^2/R^3, \quad (13)$$

where δM is the contribution to the mass owing to rotation. The second order functions m_0 and p_0^* (related to the pressure perturbation) are computed from the solution of the differential equation

$$\frac{dm_0}{dr} = 4\pi r^2 \frac{d\mathcal{E}}{dP} (\mathcal{E} + P) p_0^* + \frac{1}{12} j^2 r^4 \left(\frac{d\bar{\omega}}{dr} \right)^2 - \frac{1}{3} \frac{dj^2}{dr} r^3 \bar{\omega}^2, \quad (14)$$

$$\begin{aligned} \frac{dp_0^*}{dr} = & -\frac{m_0(1 + 8\pi r^2 P)}{(r - 2M_0)^2} - \frac{4\pi r^2 (\mathcal{E} + P)}{(r - 2M_0)} p_0^* \\ & + \frac{1}{12} \frac{j^2 r^4}{(r - 2M_0)} \left(\frac{d\bar{\omega}}{dr} \right)^2 + \frac{1}{3} \frac{d}{dr} \left(\frac{r^3 j^2 \bar{\omega}^2}{r - 2M_0} \right), \end{aligned} \quad (15)$$

where \mathcal{E} and P are the total energy density and pressure.

Turning to the quadrupole moment of the neutron star, it is given by

$$Q = \frac{J^2}{M_0} + \frac{8}{5} \mathcal{K} M_0^3, \quad (16)$$

where \mathcal{K} is a constant of integration. This constant is fixed from the matching of the second order function h_2 obtained in the interior from

$$\frac{dk_2}{dr} = -\frac{dh_2}{dr} - h_2 \frac{dv}{dr} + \left(\frac{1}{r} + \frac{1}{2} \frac{dv}{dr} \right) \left[-\frac{1}{3} r^3 \bar{\omega}^2 \frac{dj^2}{dr} + \frac{1}{6} r^4 j^2 \left(\frac{d\bar{\omega}}{dr} \right)^2 \right], \quad (17)$$

$$\begin{aligned} \frac{dh_2}{dr} = & h_2 \left\{ -\frac{dv}{dr} + \frac{r}{r - 2M_0} \left(\frac{dv}{dr} \right)^{-1} \left[8\pi (\mathcal{E} + P) - \frac{4M_0}{r^3} \right] \right\} - \frac{4(k_2 + h_2)}{r(r - 2M_0)} \left(\frac{dv}{dr} \right)^{-1} \\ & + \frac{1}{6} \left[\frac{r}{2} \frac{dv}{dr} - \frac{1}{r - 2M_0} \left(\frac{dv}{dr} \right)^{-1} \right] r^3 j^2 \left(\frac{d\bar{\omega}}{dr} \right)^2 \\ & - \frac{1}{3} \left[\frac{r}{2} \frac{dv}{dr} + \frac{1}{r - 2M_0} \left(\frac{dv}{dr} \right)^{-1} \right] r^2 \bar{\omega}^2 \frac{dj^2}{dr}, \end{aligned} \quad (18)$$

with its exterior counterpart (see Hartle [13] and Appendix A).

It is worth to underline that the influence of the induced magnetic field owing to the rotation of the charged core of the neutron star in the globally neutral case is negligible [8]. In fact, for a rotating neutron star of period $P = 10$ ms and radius $R \sim 10$ km, the radial component of the magnetic field B_r in the core interior reaches its maximum at the poles with a value $B_r \sim 2.9 \times 10^{-16} B_c$, where $B_c = m_e^2 c^3 / (e \hbar) \approx 4.4 \times 10^{13}$ G is the critical magnetic field for vacuum polarization. The angular component of the magnetic field B_θ , instead, has its maximum

value at the equator and, as for the radial component, it is very low in the interior of the neutron star core, i.e. $|B_\theta| \sim 2.9 \times 10^{-16} B_c$. In the case of a sharp core–crust transition as the one studied by Belvedere et al. [2] and shown in Fig. 1, this component will grow in the transition layer to values of the order of $|B_\theta| \sim 10^2 B_c$ (see Boshkayev et al. [8] for further details). However, since we are here interested in the macroscopic properties of the neutron star, we can ignore at first approximation the presence of electromagnetic fields in the macroscopic regions where they are indeed very small, and safely apply the original Hartle formulation without any generalization.

3. Stability of uniformly rotating neutron stars

3.1. Secular axisymmetric instability

In a sequence of increasing central density in the M – ρ_c curve, $\rho_c \equiv \rho(0)$, the maximum mass of a non-rotating neutron star is defined as the first maximum of such a curve, namely the point where $\partial M / \partial \rho_c = 0$. This derivative defines the secular instability point, and, if the perturbation obeys the same equation of state (EOS) as the equilibrium configuration, it coincides also with the dynamical instability point (see e.g. Shapiro and Teukolsky [24]). In the rotating case, the situation becomes more complicated and in order to find the axisymmetric dynamical instability points, the perturbed solutions with zero frequency modes (the so-called neutral frequency line) have to be calculated. Friedman et al. [10] however, following the works of Sorkin [25,26], described a turning-point method to obtain the points at which secular instability is reached by uniformly rotating stars. In a constant angular momentum sequence, the turning point is located in the maximum of the mass–central density relation, namely the onset of secular axisymmetric instability is given by

$$\left[\frac{\partial M(\rho_c, J)}{\partial \rho_c} \right]_{J=\text{constant}} = 0, \quad (19)$$

and once the secular instability sets in, the star evolves quasi-stationarily until it reaches a point of dynamical instability where gravitational collapse sets in [27].

The above equation defines an upper limit for the mass at a given J for a uniformly rotating star, however this criterion is a sufficient but not necessary condition for the instability. This means that all the configurations with the given angular momentum J on the right side of the turning point defined by Eq. (19) are secularly unstable, but it does not imply that the configurations on the left side of it are stable. An example of dynamically unstable configurations on the left side of the turning-point limiting boundary in neutron stars was recently shown in [28], for a specific EOS.

3.2. Keplerian mass-shedding instability

The maximum velocity for a particle to remain in equilibrium on the equator of a star, kept bound by the balance between gravitational and centrifugal force, is the Keplerian velocity of a free particle computed at the same location. As shown, for instance in [27], a star rotating at Keplerian rate becomes unstable due to the loss of mass from its surface. The mass shedding limiting angular velocity of a rotating star is the Keplerian angular velocity evaluated at the equator, $r = R_{\text{eq}}$, i.e. $\Omega_K^{J \neq 0} = \Omega_K(r = R_{\text{eq}})$. Friedman [11] introduced a method to obtain the maximum possible angular velocity of the star before reaching the mass-shedding limit; however Torok et al. [31] and Bini et al. [5], showed a simpler way to compute the Keplerian angular

velocity of a rotating star. They showed that the mass-shedding angular velocity, $\Omega_K^{J \neq 0}$, can be computed as the orbital angular velocity of a test particle in the external field of the star and co-rotating with it on its equatorial plane at the distance $r = R_{\text{eq}}$. For the Hartle external solution, this is given by

$$\Omega_K^{J \neq 0}(r) = \sqrt{\frac{M}{r^3}} [1 - jF_1(r) + j^2F_2(r) + qF_3(r)], \quad (20)$$

where $j = J/M^2$ and $q = Q/M^3$ are the dimensionless angular momentum and quadrupole moment. Further details and the analytical expression of the functions F_i can be found in [Appendix A](#).

3.3. Gravitational binding energy

Besides the above stability requirements, one should check if the neutron star is gravitationally bound. In the non-rotating case, the binding energy of the star can be computed as

$$W_{J=0} = M_0 - M_{\text{rest}}^0, \quad M_{\text{rest}}^0 = m_b A_{J=0}, \quad (21)$$

where M_{rest}^0 is the rest-mass of the star, m_b is the rest-mass per baryon, and $A_{J=0}$ is the total number of baryons inside the star. So the non-rotating star is considered bound if $W_{J=0} < 0$.

In the slow rotation approximation the total binding energy is given by [\[16\]](#)

$$W_{J \neq 0} = W_{J=0} + \delta W, \quad \delta W = \frac{J^2}{R^3} - \int_0^R 4\pi r^2 B(r) dr, \quad (22)$$

where

$$\begin{aligned} B(r) = & (\mathcal{E} + P) p_0^* \left\{ \frac{d\mathcal{E}}{dP} \left[\left(1 - \frac{2M}{r}\right)^{-1/2} - 1 \right] - \frac{du}{dP} \left(1 - \frac{2M}{r}\right)^{-1/2} \right\} \\ & + (\mathcal{E} - u) \left(1 - \frac{2M}{r}\right)^{-3/2} \left[\frac{m_0}{r} + \frac{1}{3} j^2 r^2 \bar{\omega}^2 \right] \\ & - \frac{1}{4\pi r^2} \left[\frac{1}{12} j^2 r^4 \left(\frac{d\bar{\omega}}{dr} \right)^2 - \frac{1}{3} \frac{dj^2}{dr} r^3 \bar{\omega}^2 \right], \end{aligned} \quad (23)$$

where $u = \mathcal{E} - m_b n_b$ is the internal energy of the star, with n_b the baryon number density.

We will therefore request that the binding energy be negative, namely $W_{J \neq 0} < 0$. As we will show below in [Section 4.2.2](#), this condition leads to a minimum mass for the neutron star under which the star becomes gravitationally unbound.

4. Structure of uniformly rotating neutron stars

We show now the results of the integration of the Hartle equations for the globally and locally charge neutrality neutron stars; see e.g. [Fig. 1](#). Following [Belvedere et al. \[2\]](#), we adopt, as an example, globally neutral neutron stars with a density at the edge of the crust equal to the neutron drip density, $\rho_{\text{crust}} = \rho_{\text{drip}} \approx 4.3 \times 10^{11} \text{ g cm}^{-3}$.

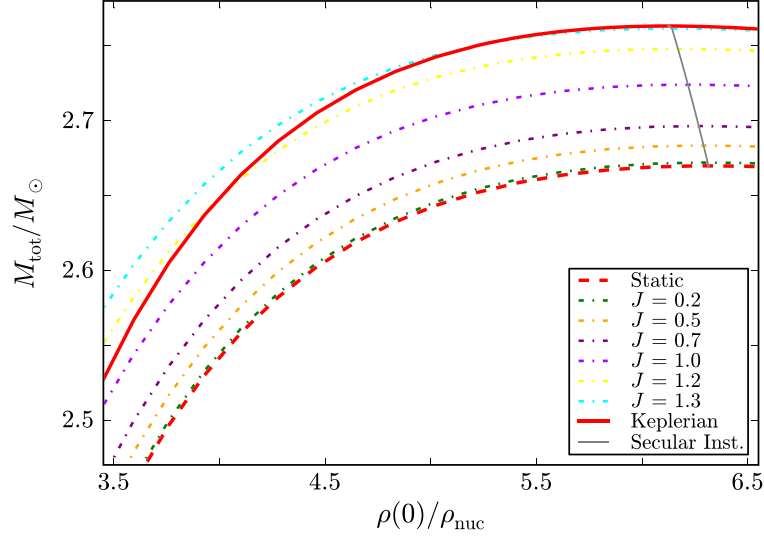


Fig. 3. Total mass versus central density of globally neutral neutron stars. The solid line represents the configuration with Keplerian angular velocity, the dashed line represents the static configuration, the dotted-dashed lines represent the J -constant sequences (in units of 10^{11} cm^2). The gray line joins all the turning points of the J -constant sequences, so it defines the secular instability boundary.

4.1. Secular instability boundary

In Fig. 3 we show the mass-central density curve for globally neutral neutron stars in the region close to the axisymmetric stability boundaries. Specifically we show some J -constant sequences to show that indeed along each of these curves there exist a maximum mass point (turning point). The line joining all the turning points defines the secular instability limit. In Fig. 3 the axisymmetric stable zone is on the left side of the instability line.

Clearly we can transform the mass-central density relation in a mass–radius relation. In Fig. 4 we show the mass versus the equatorial radius of the neutron star that correspond to the range of densities of Fig. 3. In this plot the stable zone is on the right side of the instability line.

We can construct a fitting curve joining the turning points of the J -constant sequences line which determines the secular axisymmetric instability boundary. Defining $M_{\text{max},0}$ as the maximum stable mass of the non-rotating neutron star constructed with the same EOS, we find that for globally neutral configurations the instability line is well fitted by the function

$$\frac{M_{\text{sec}}^{\text{GCN}}}{M_{\odot}} = 21.22 - 6.68 \frac{M_{\text{max},0}^{\text{GCN}}}{M_{\odot}} - \left(77.42 - 28 \frac{M_{\text{max},0}^{\text{GCN}}}{M_{\odot}} \right) \left(\frac{R_{\text{eq}}}{10 \text{ km}} \right)^{-6.08}, \quad (24)$$

where $12.38 \text{ km} \lesssim R_{\text{eq}} \lesssim 12.66 \text{ km}$, and $M_{\text{max},0}^{\text{GCN}} \approx 2.67 M_{\odot}$.

The turning points of locally neutral configurations in the mass-central density plane are shown in Fig. 5. The corresponding mass–equatorial radius plane is plotted in Fig. 6.

For locally neutral neutron stars, the secular instability line is fitted by

$$\frac{M_{\text{sec}}^{\text{LCN}}}{M_{\odot}} = 20.51 - 6.35 \frac{M_{\text{max},0}^{\text{LCN}}}{M_{\odot}} - \left(80.98 - 29.02 \frac{M_{\text{max},0}^{\text{LCN}}}{M_{\odot}} \right) \left(\frac{R_{\text{eq}}}{10 \text{ km}} \right)^{-5.71}, \quad (25)$$

where $12.71 \text{ km} \lesssim R_{\text{eq}} \lesssim 13.06 \text{ km}$, and $M_{\text{max},0}^{\text{LCN}} \approx 2.70 M_{\odot}$.

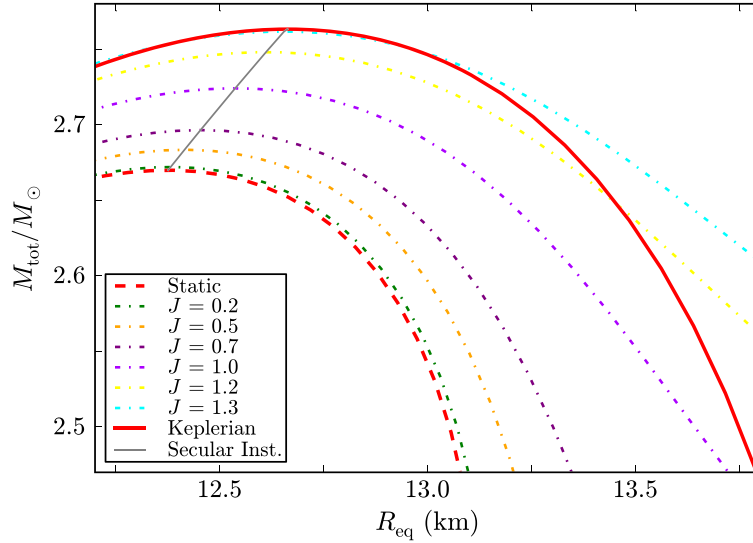


Fig. 4. Total mass versus equatorial radius of globally neutral neutron stars. The solid line represents the configuration with Keplerian angular velocity, the dashed line represents the static configuration, the dotted-dashed lines represent the J -constant sequences (in units of 10^{11} cm^2). The gray curve joins all the turning points of the J -constant sequences, so it defines the secular instability boundary.

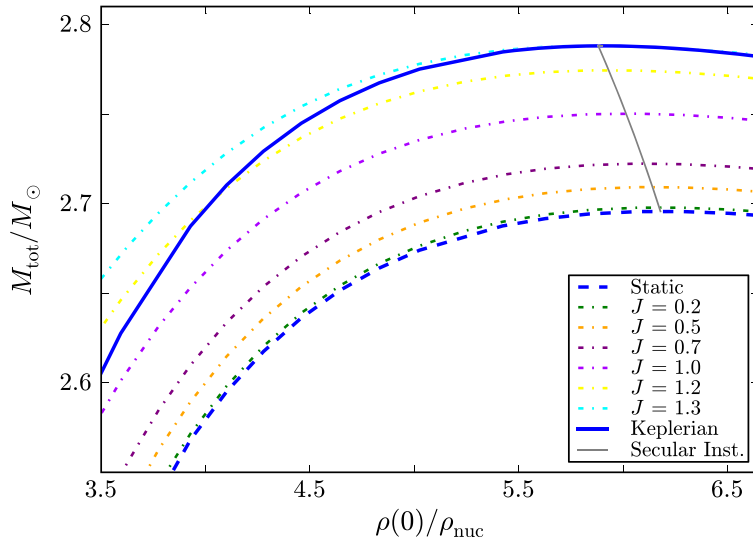


Fig. 5. Total mass versus central density of locally neutral neutron stars. The solid line represents the configuration with Keplerian angular velocity, the dashed line represents the static configuration, the dotted-dashed lines represent the J -constant sequences (in units of 10^{11} cm^2). The gray line joins all the turning points of the J -constant sequences, so it defines the secular instability boundary.

4.2. Keplerian mass-shedding sequence

We turn now to analyze in detail the behavior of the different properties of the neutron star along the Keplerian mass-shedding sequence. For the sake of reference we have indicated in the following plots stars with the selected masses $M \approx [1, 1.4, 2.04, 2.5]M_{\odot}$. The cyan star indicates the fastest observed pulsar, PSR J1748–2446ad Hessels et al. [18], with a rotation frequency of $f \approx 716 \text{ Hz}$. The gray filled circles indicate the last stable configuration of the Keplerian sequence, namely the point where the Keplerian and the secular stability boundaries cross each other.

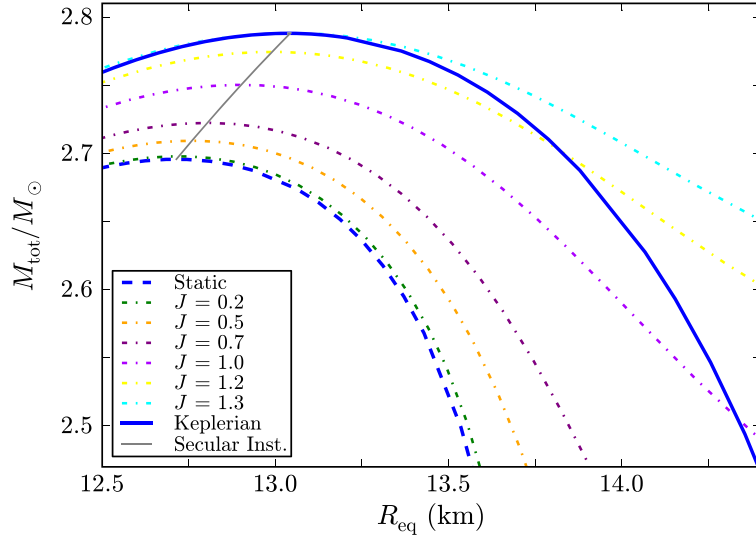


Fig. 6. Total mass versus equatorial radius of locally neutral neutron stars. The solid line represents the configuration with Keplerian angular velocity, the dashed line represents the static configuration, the dotted-dashed lines represent the J -constant sequences (in units of 10^{11} cm^2). The gray curve joins all the turning points of the J -constant sequences, so it defines the secular instability boundary.

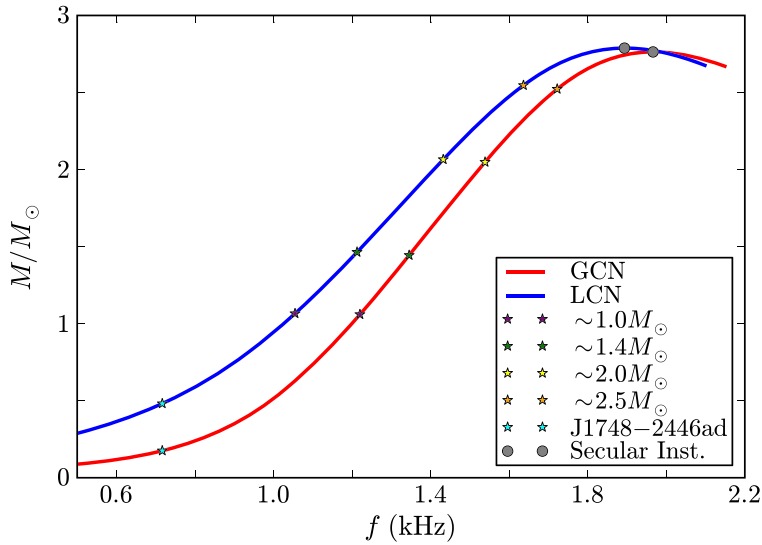


Fig. 7. Total mass versus rotational Keplerian frequency both for the global (red in the web version) and local (blue in the web version) charge neutrality cases.

4.2.1. Maximum mass and rotation frequency

The total mass of the rotating star is computed from Eq. (13). In Fig. 7 is shown the total mass of the neutron star as a function of the rotation frequency for the Keplerian sequence. It is clear that for a given mass, the rotational frequency is higher for a globally neutral neutron star with respect to the locally neutral one.

The configuration of maximum mass, $M_{\text{max}}^{J \neq 0}$, occurs along the Keplerian sequence, and it is found before the secular instability line crosses the Keplerian curve. Thus, the maximum mass configuration is secularly stable. This implies that the configuration with maximum rotation frequency, f_{max} , is located beyond the maximum mass point, specifically at the crossing point between the secular instability and the Keplerian mass-shedding sequence. The results are summarized in Table 1.

Table 1

$M_{\max}^{J=0}$ and $R_{\max}^{J=0}$: maximum mass and corresponding radius of non-rotating stars as computed in [2]; $M_{\max}^{J \neq 0}$ and $R_{\max}^{J \neq 0}$: maximum mass and corresponding radius of rotating stars; δM_{\max} and $\delta R_{\text{eq}}^{\max}$: increase in mass and radius of the maximum mass configuration with respect to its non-rotating counterpart; f_{\max} and P_{\min} : maximum rotation frequency and associated minimum period.

	Global neutrality	Local neutrality
$M_{\max}^{J=0}$ (M_{\odot})	2.67	2.70
$R_{\max}^{J=0}$ (km)	12.38	12.71
$M_{\max}^{J \neq 0}$ (M_{\odot})	2.76	2.79
$R_{\max}^{J \neq 0}$ (km)	12.66	13.06
δM_{\max}	3.37%	3.33%
$\delta R_{\text{eq}}^{\max}$	2.26%	2.75%
f_{\max} (kHz)	1.97	1.89
P_{\min} (ms)	0.51	0.53

It is important to discuss briefly the validity of the present perturbative solution for the computation of the properties of maximally rotating neutron stars. The expansion of the radial coordinate of a rotating configuration $r(R, \theta)$ in powers of angular velocity is written as [13]

$$r = R + \xi(R, \theta) + O(\Omega^4), \quad (26)$$

where ξ is the difference in the radial coordinate, r , between a point located at the polar angle θ on the surface of constant density $\rho(R)$ in the rotating configuration, and the point located at the same polar angle on the same constant density surface in the non-rotating configuration. In the slow rotation regime, the fractional displacement of the surfaces of constant density due to the rotation have to be small, namely $\xi(R, \theta)/R \ll 1$, where $\xi(R, \theta) = \xi_0(R) + \xi_2(R)P_2(\cos \theta)$ and $\xi_0(R)$ and $\xi_2(R)$ are function of R , proportional to Ω^2 . From Table 1, we can see that the configuration with the maximum possible rotation frequency has a maximum fractional displacement $\delta R_{\text{eq}}^{\max} = \xi(R, \pi/2)/R$ as low as $\approx 2\%$ and $\approx 3\%$, for the globally and locally neutral neutron stars respectively.

In this line, it is worth to quote the results of Benhar et al. [3], who showed that the inclusion of a third-order expansion Ω^3 in the Hartle's method improves the value of the maximum rotation frequency by less than 1% for different EOS. The reason for this is that as mentioned above, along the Keplerian sequence the deviations from sphericity decrease with density and frequency (see Figs. 16 and 17), which ensures the accuracy of the perturbative solution.

Turning to the increase of the maximum mass, Weber and Glendenning [34] showed that the mass of maximally rotating neutron stars, computed with the Hartle's second order approximation, is accurate within an error as low as $\lesssim 4\%$.

4.2.2. Minimum mass and rotation frequency

We compute now the gravitational binding energy of the neutron star from Eq. (22) as a function of the central density and angular velocity. We make this for central densities higher than the nuclear density, thus we impose the neutron star to have a supranuclear hadronic core. In Fig. 8 we plot the binding energy W of the neutron star as a function of the neutron star mass along the Keplerian sequence. For the sake of comparison we show also the binding energy of the non-rotating configurations.

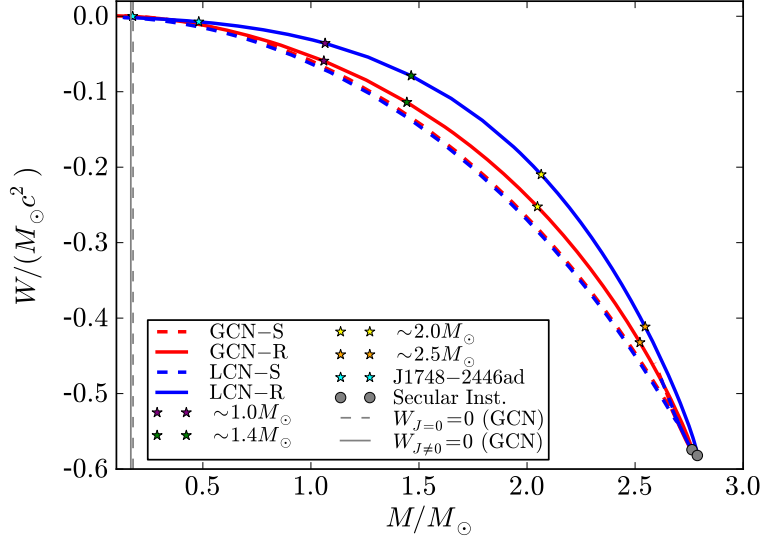


Fig. 8. Neutron star binding energy versus total mass along the Keplerian sequence both for the global (red in the web version) and local (blue in the web version) charge neutrality.

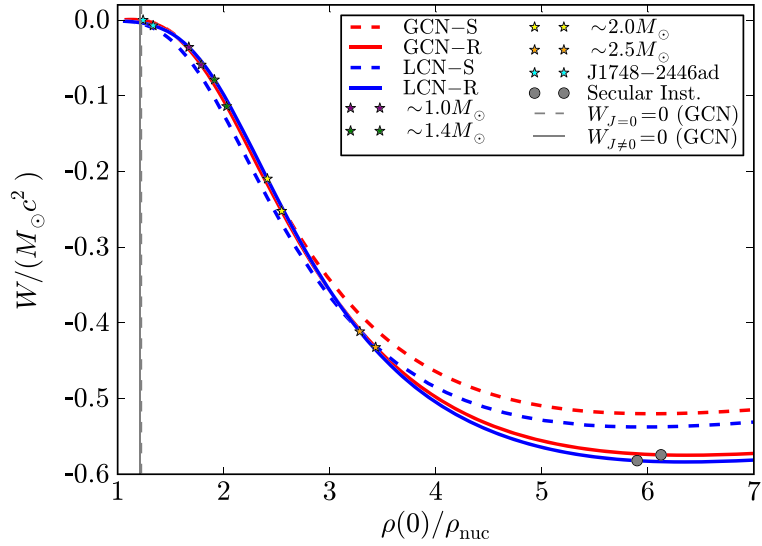


Fig. 9. Neutron star binding energy versus central density along the Keplerian sequence both for the global (red in the web version) and local (blue in the web version) charge neutrality.

We found that the globally neutral neutron stars studied here are bound up to some minimum mass at which the gravitational binding energy vanishes. For the static and Keplerian configurations we find that $W_{J=0} = 0$, and $W_{J\neq 0} = 0$ respectively at

$$M_{\min}^{J=0} \approx 0.177M_{\odot}, \quad M_{\min}^K \approx 0.167M_{\odot}, \quad (27)$$

where with the superscript K we indicate that this value corresponds to the minimum mass on the Keplerian sequence. Clearly this minimum mass value decreases with decreasing frequency until it reaches the above value $M_{\min}^{J=0}$ of the non-rotating case.

We did not find any unbound configuration in the local charge neutrality case for the present EOS (see Fig. 8). The corresponding plot of W as a function of the central density is shown in Fig. 9.

The configuration with the minimum mass, $M_{\min}^K \approx 0.167M_{\odot}$, has a rotation frequency

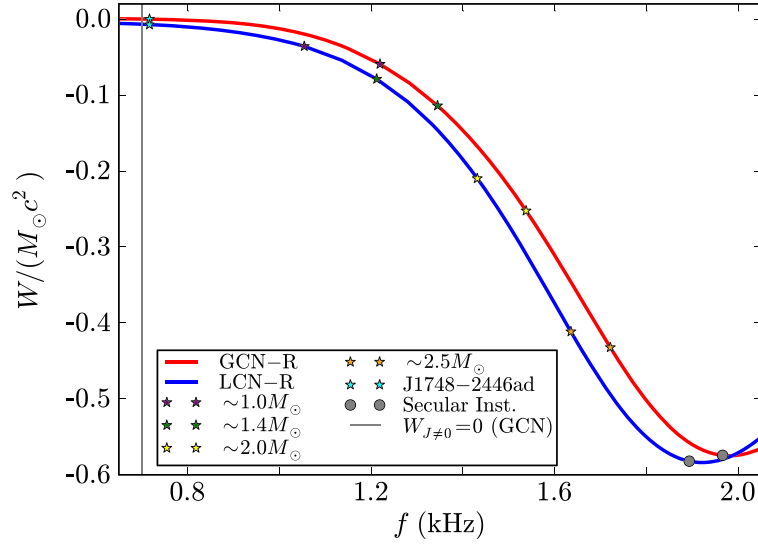


Fig. 10. Neutron star binding energy versus frequency for the Keplerian sequence both for the global (red in the web version) and local (blue in the web version) charge neutrality neutron stars.

$$f_{\min}^K = f(M_{\min}^K) \approx 700.59 \text{ Hz}, \quad (28)$$

that is the minimum rotation rate that globally neutral configurations can have along the Keplerian sequence in order to be gravitationally bound. Interestingly, the above value is slightly lower than the frequency of the fastest observed pulsar, PSR J1748–2446ad, which has a frequency of 716 Hz (Hessels et al. [18]). Further discussions on this issue are given below in Section 8.

In Fig. 10 we show in detail the dependence of W on the rotation frequency.

5. Neutron star mass–radius relation

We summarize now the above results in form of a new mass–radius relation of uniformly rotating neutron stars, including the Keplerian and secular instability boundary limits. In Fig. 11 we show a summary plot of the equilibrium configurations of rotating neutron stars. In particular we show the total mass versus the equatorial radius: the dashed lines represent the static (non-rotating, $J = 0$) sequences, while the solid lines represent the corresponding Keplerian mass-shedding sequences. The secular instability boundaries are plotted in pink-red and light blue color for the global and local charge neutrality cases, respectively.

It can be seen that due to the deformation for a given mass the radius of the rotating case is larger than the static one, and similarly the mass of the rotating star is larger than the corresponding static one. It can be also seen that the configurations obeying global charge neutrality are more compact with respect to the ones satisfying local charge neutrality.

6. Moment of inertia

The neutron star moment of inertia I can be computed from the relation

$$I = \frac{J}{\Omega}, \quad (29)$$

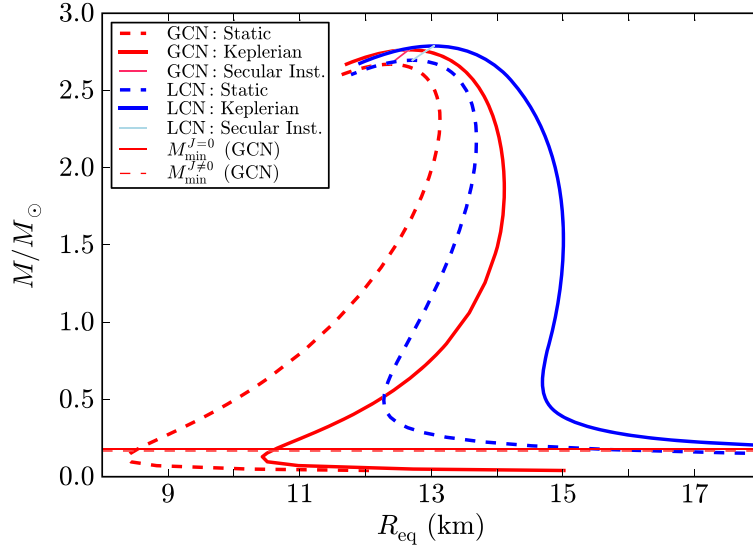


Fig. 11. Total mass versus total equatorial radius for the global (red) and local (blue) charge neutrality cases. The dashed curves represent the static configurations, while the solid lines are the uniformly rotating neutron stars. The pink-red and light-blue color lines define the secular instability boundary for the globally and locally neutral cases, namely the lines given by Eqs. (24) and (25), respectively. (For interpretation of the references to color in this figure, the reader is referred to the web version of this article.)

where J is the angular momentum and Ω are related via Eq. (12). Since J is a first-order quantity and so proportional to Ω , the moment of inertia given by Eq. (29) does not depend on the angular velocity and does not take into account deviations from the spherical symmetry. This implies that Eq. (11) gives the moment of inertia of the non-rotating unperturbed seed object. In order to find the perturbation to I , say δI , the perturbative treatment has to be extended to the next order Ω^3 , in such a way that $I = I_0 + \delta I = (J_0 + \delta J)/\Omega$, becomes of order Ω^2 , with δJ of order Ω^3 (see e.g. Hartle [14]; Benhar et al. [3]). In this work we keep the solution up to second order and therefore we proceed to analyze the behavior of the moment of inertia for the non-rotating configurations. In any case, as we will show in Section 8 even the fastest observed pulsars rotate at frequencies much lower than the Keplerian rate, and under such conditions we expect that the moment of inertia can be approximated with high accuracy by the one of the corresponding static configurations.

In Figs. 12 and 13 we show the behavior of the total momentum of inertia, i.e. $I = I_{\text{core}} + I_{\text{crust}}$, with respect to the total mass and central density for both globally and locally neutral non-rotating neutron stars.

We can see from Figs. 12 and 13 that the total moment of inertia is quite similar for both global and local charge neutrality cases. This is due to the fact that the globally neutral configurations differ from the locally ones mostly in the structure of the crust, which however contributes much less than the neutron star core to the total moment of inertia (see below in Section 6.1).

6.1. Core and crust moment of inertia

In order to study the single contribution of the core and the crust to the moment of inertia of the neutron star, we shall use the integral expression for the moment of inertia. Multiplying Eq. (10)

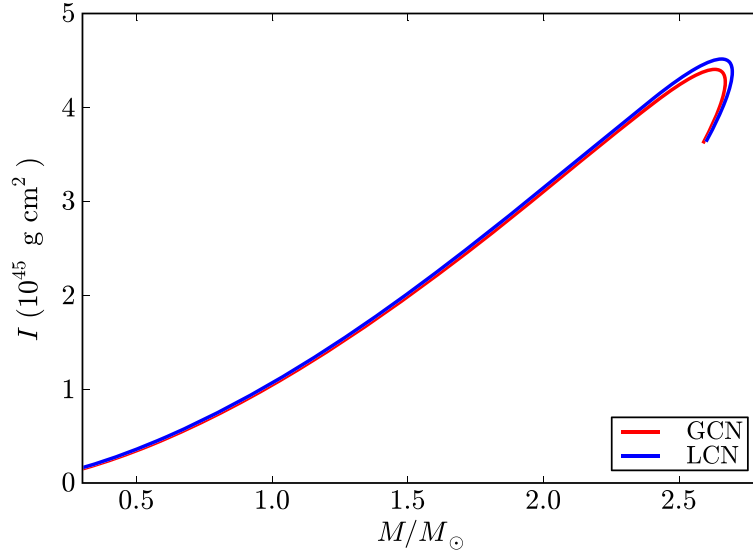


Fig. 12. Total moment of inertia versus total mass both for globally (red in the web version) and locally (blue in the web version) neutral non-rotating neutron stars.

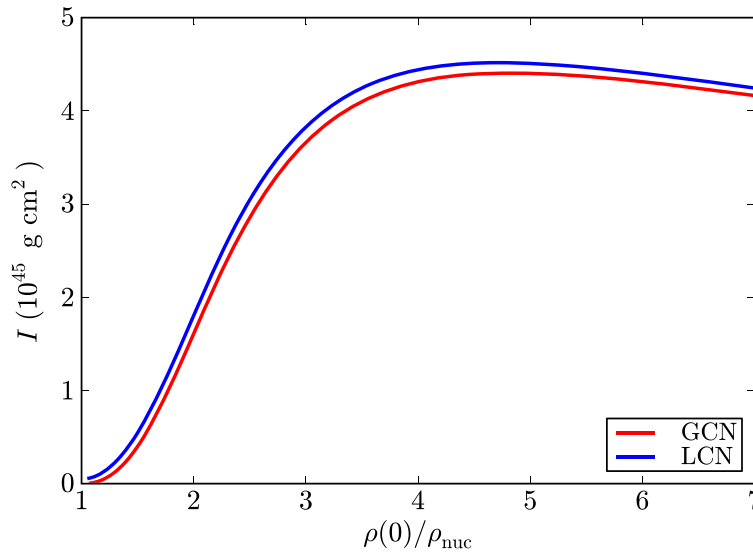


Fig. 13. Total moment of inertia versus central density for globally (red in the web version) and locally (blue in the web version) neutral non-rotating neutron stars.

by r^3 and making the integral of it we obtain²

$$I(r) = -\frac{2}{3} \int_0^r r^3 \frac{dj}{dr} \frac{\bar{\omega}(r)}{\Omega} dr = \frac{8\pi}{3} \int_0^r r^4 (\mathcal{E} + P) e^{(\lambda-\nu)/2} \frac{\bar{\omega}(r)}{\Omega} dr, \quad (30)$$

where the integration is carried out in the region of interest. Thus, the contribution of the core, I_{core} , is obtained integrating from the origin up to the radius of the core, and the contribution of the crust, I_{crust} , integrating from the base of the crust to the total radius of the neutron star.

² It is clear that this expression approaches, in the weak field limit, the classic Newtonian expression $I_{\text{Newtonian}} = (8\pi/3) \int r^4 \rho dr$ where ρ is the mass density [13].

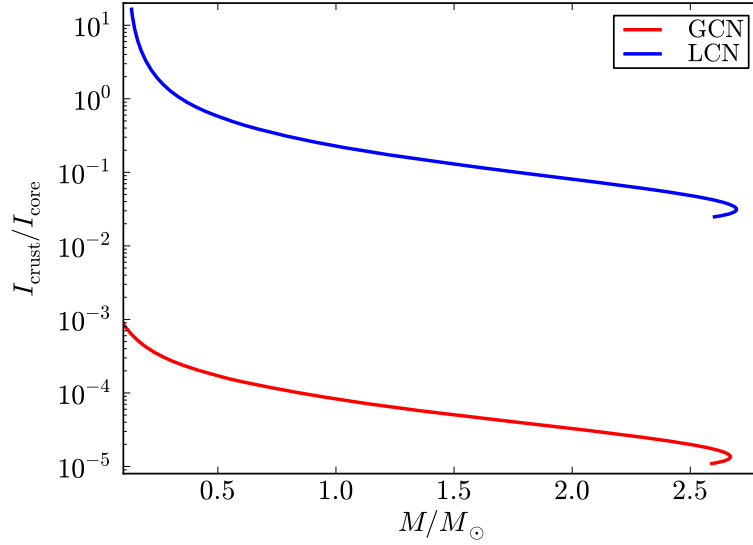


Fig. 14. Crust to core moment of inertia ratio versus the total mass of both globally and locally neutral non-rotating neutron stars.

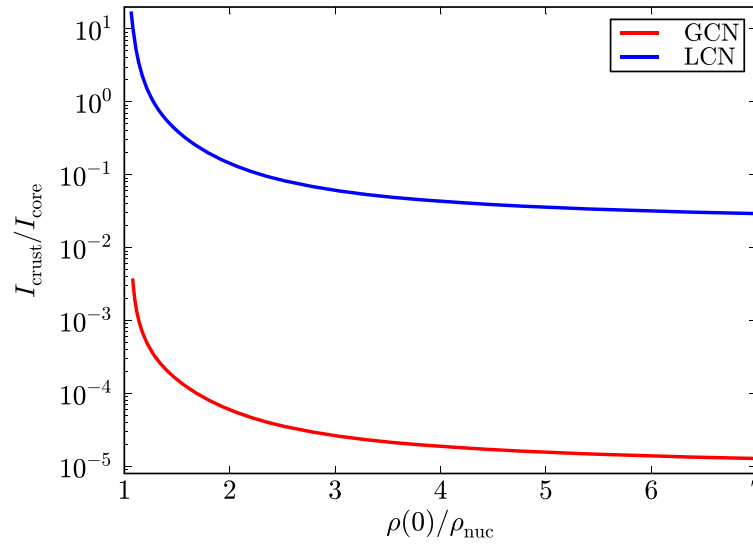


Fig. 15. Crust to core moment of inertia ratio versus the central density both globally and locally neutral non-rotating neutron stars.

We show in Figs. 14 and 15 the ratio between the moment of inertia of the crust and the one of the core as a function of the total mass and central density, respectively, for both the globally and locally neutral configurations.

7. Deformation of the neutron star

In this section we explore the deformation properties of the neutron star. The behavior of the eccentricity, the rotational to gravitational energy ratio, as well as the quadrupole moment, are investigated as a function of the mass, density, and rotation frequency of the neutron star.

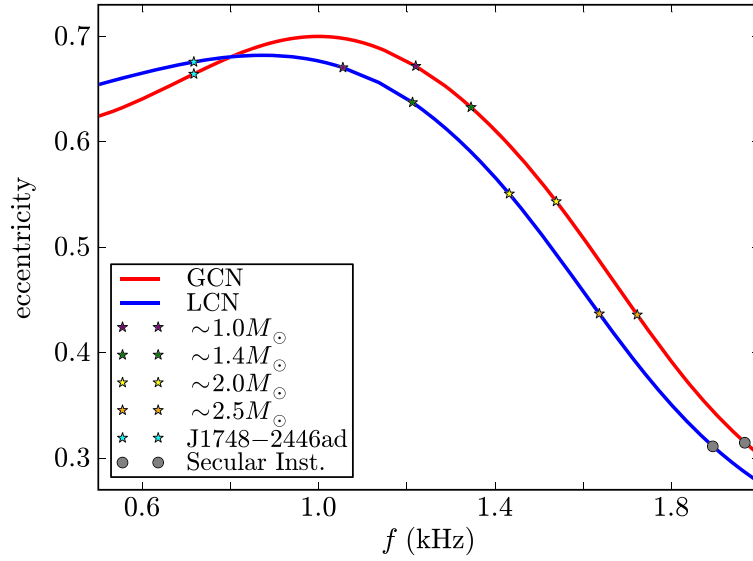


Fig. 16. Eccentricity (31) versus frequency for the Keplerian sequence both for the global (red in the web version) and local (blue in the web version) charge neutrality cases.

7.1. Eccentricity

A measurement of the level of deformation of the neutron star can be estimated with the eccentricity

$$\epsilon = \sqrt{1 - \left(\frac{R_p}{R_{\text{eq}}}\right)^2}, \quad (31)$$

where R_p and R_{eq} are the polar and equatorial radii of the configuration. Thus, $\epsilon = 0$ defines the spherical limit and $0 < \epsilon < 1$ corresponds to oblate configurations.

In Fig. 16, we show the behavior of the total eccentricity (31), as a function of the neutron star frequency.

We can see that in general the globally neutral neutron star has an eccentricity larger than the one of the locally neutral configuration for almost the entire range of frequencies and the corresponding central densities, except for the low frequencies $f \lesssim 0.8$ kHz and central densities $\rho(0) \lesssim 1.3\rho_{\text{nuc}}$; see also Fig. 17. Starting from low values of the frequency f and central density $\rho(0)$, the neutron stars increase their oblateness, and after reaching the maximum value of the eccentricity, the compactness increases and the configurations tend to a more spherical shape.

7.2. Rotational to gravitational energy ratio

Other property of the star related to the centrifugal deformation of the star is the ratio between the gravitational energy and the rotational energy of the star. The former is given by Eq. (22), whereas the latter is

$$T = \frac{1}{2}I\Omega^2. \quad (32)$$

We show in Fig. 18 the ratio $T/|W|$ as a function of the mass of the neutron stars along the Keplerian sequence. In Fig. 19 instead we plot the dependence of the ratio on the central density and in Fig. 20 on the Keplerian frequency.

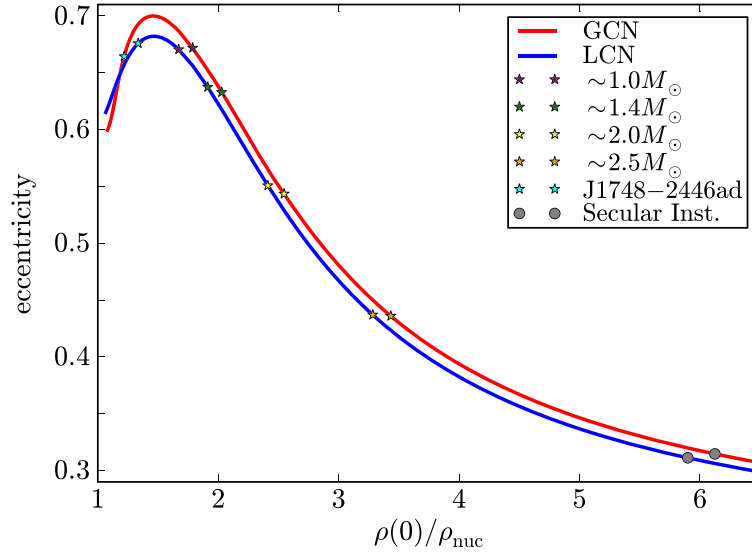


Fig. 17. Eccentricity (31) versus central density for the Keplerian sequence both for the global (red in the web version) and local (blue in the web version) charge neutrality cases.

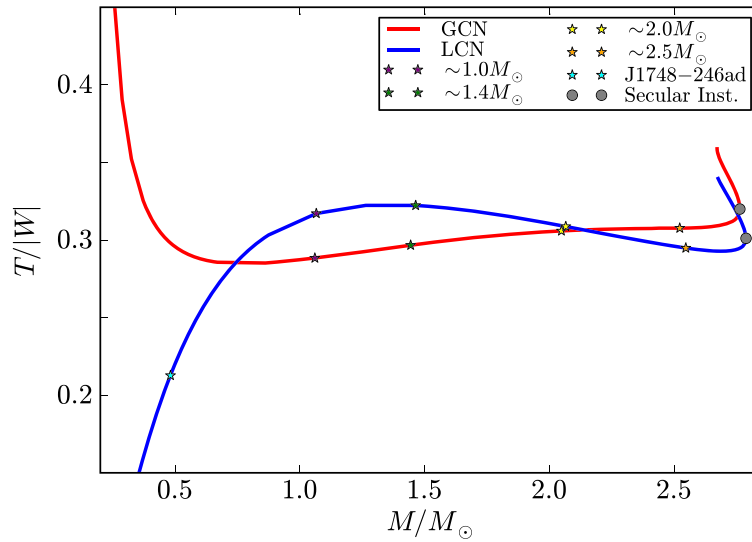


Fig. 18. Rotational to gravitational binding energy ratio versus total mass along the Keplerian sequence both for the global (red in the web version) and local (blue in the web version) charge neutrality.

7.3. Quadrupole moment

In Figs. 21 and 22 we show the quadrupole moment, Q given by Eq. (16), as a function of the total mass and central density for both globally and locally neutral neutron stars along the Keplerian sequence. The dependence of Q on the rotation frequency is shown in Fig. 23. We have normalized the quadrupole moment Q to the quantity MR^2 of the non-rotating configuration with the same central density.

8. Observational constraints

In Fig. 24 we show the above mass–radius relations together with the most recent and stringent constraints indicated by Trümper [32]:

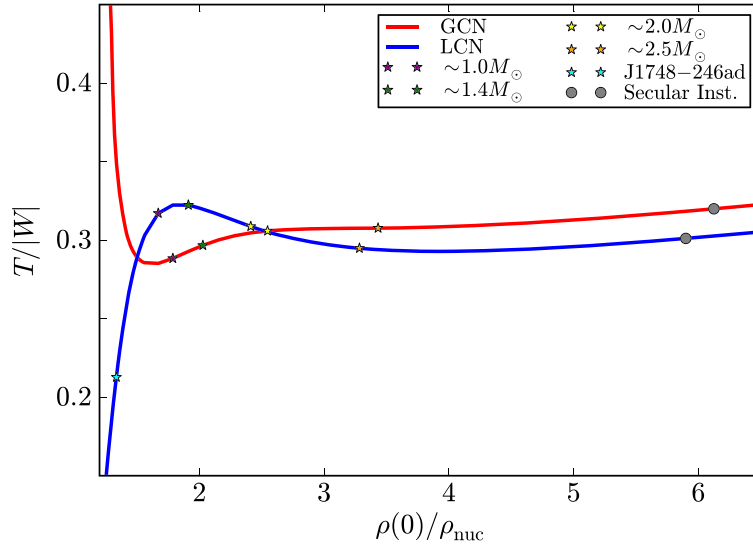


Fig. 19. Rotational to gravitational binding energy ratio versus central density along the Keplerian sequence both for the global (red in the web version) and local (blue in the web version) charge neutrality.

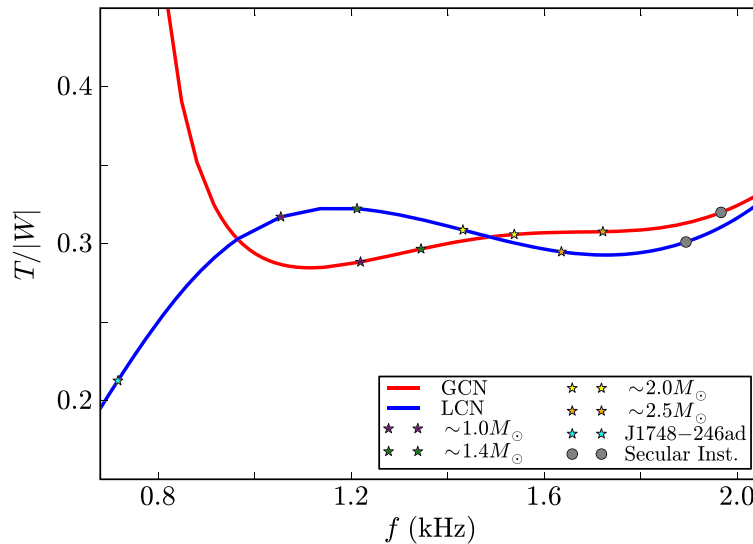


Fig. 20. Rotational to gravitational binding energy ratio versus frequency along the Keplerian sequence both for the global (red in the web version) and local (blue in the web version) charge neutrality cases.

- (1) *The largest mass.* Until 2013 it was given by the mass of the 3.15 millisecond pulsar PSR J1614–2230 $M = 1.97 \pm 0.04M_{\odot}$ Demorest et al. [9], however the recent reported mass $2.01 \pm 0.04M_{\odot}$ for the neutron star in the relativistic binary PSR J0348+0432 [1] puts an even more stringent request to the nuclear EOS. Thus, the maximum mass of the neutron star has to be larger than the mass of PSR J0348+0432, this constraint is represented by the orange-color stars in Fig. 24.
- (2) *The largest radius.* It is given by the lower limit to the radius of RX J1856–3754. The lower limit to the radius as seen by an observer at infinity is $R_{\infty} = R[1 - 2GM/(c^2R)]^{-1/2} > 16.8$ km, as given by the fit of the optical and X-ray spectra of the source [33]; so in the mass–radius relation this constraint reads $2GM/c^2 > R - R^3/(R_{\infty}^{\min})^2$, with $R_{\infty}^{\min} = 16.8$ km. We represent this constraint with the dotted-dashed curve in Fig. 24.

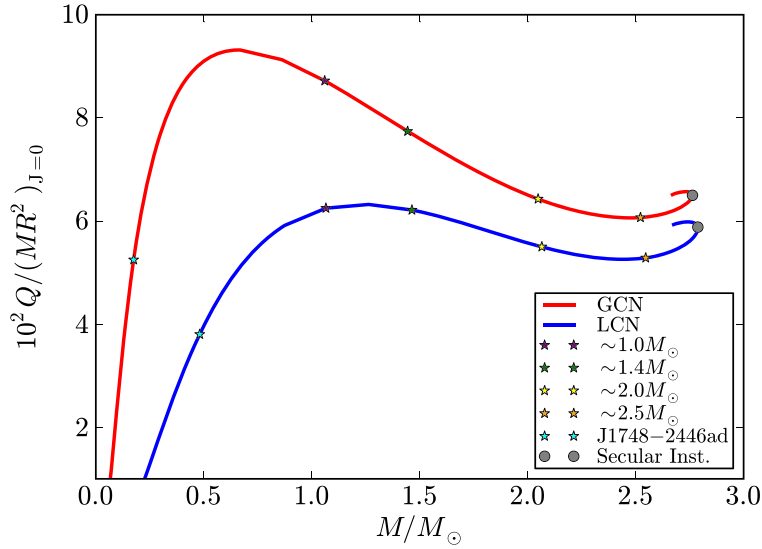


Fig. 21. Total quadrupole moment versus total mass along the Keplerian sequence both for the global (red in the web version) and local (blue in the web version) charge neutrality cases. The quadrupole moment Q is here in units of the quantity MR^2 of the non-rotating configuration with the same central density.

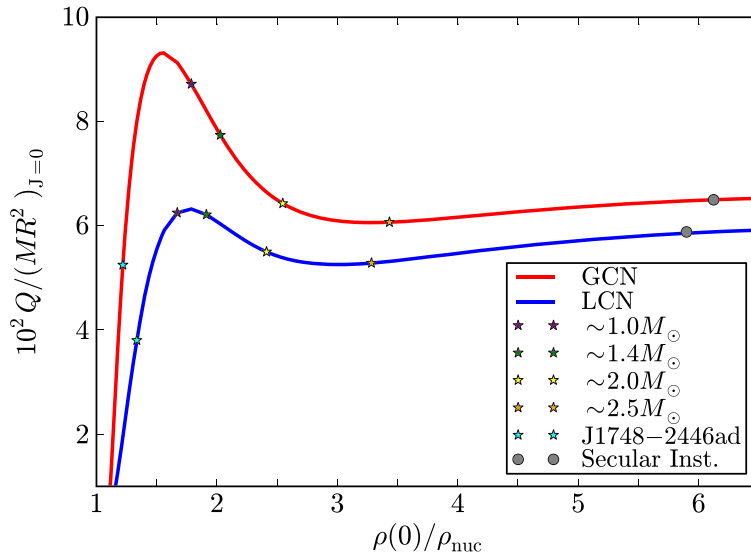


Fig. 22. Total quadrupole moment versus central density along the Keplerian sequence both for the global (red in the web version) and local (blue in the web version) charge neutrality cases. The quadrupole moment Q is here in units of the quantity MR^2 of the non-rotating configuration with the same central density.

- (3) *The maximum surface gravity.* Using a neutron star of $M = 1.4M_\odot$ to fit the Chandra data of the low-mass X-ray binary X7, it turns out that the radius of the star satisfies at 90% confidence level, $R = 14.5^{+1.8}_{-1.6}$ km, which gives $R_\infty = [15.64, 18.86]$ km, respectively, Heinke et al. [17]. Using the same formula as before, $2GM/c^2 > R - R^3/(R_\infty^{\min})^2$, we obtain the dotted curves shown in Fig. 24.
- (4) *The highest rotation frequency.* The fastest observed pulsar is PSR J1748–2446ad with a frequency of 716 Hz (Hessels et al. [18]). We show the constant rotation frequency sequence $f = 716$ Hz for both globally (dashed pink) and locally (dashed light blue) neutral neutron stars.

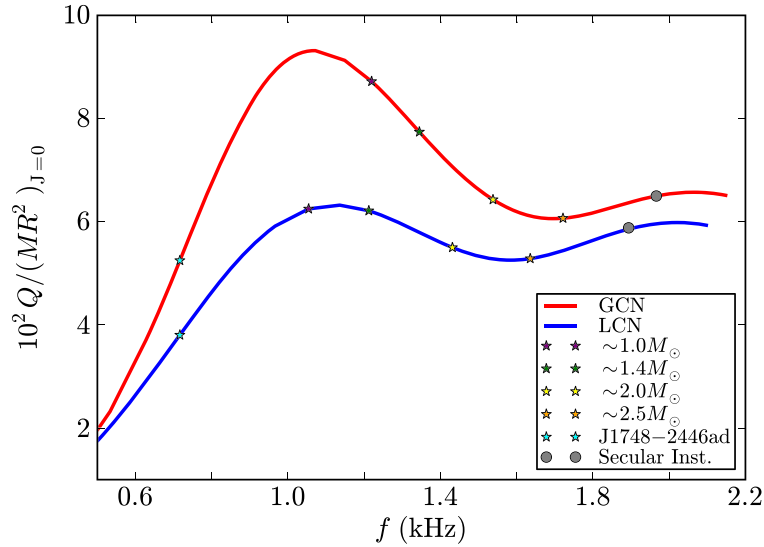


Fig. 23. Total quadrupole moment versus frequency along the Keplerian sequence both for the global (red in the web version) and local (blue in the web version) charge neutrality cases. The quadrupole moment Q is here in units of the quantity MR^2 of the non-rotating configuration with the same central density.

We indicated with cyan-color stars the point where these curves cross the corresponding Keplerian sequences in the two cases (see Fig. 24).

Every f -constant sequence crosses the stability region of the objects in two points: these crossing points define the minimum and maximum possible mass that an object rotating with such a frequency may have in order to be stable. In the case of PSR J1748–2446ad, the cut of the $f = 716$ Hz constant sequence with the Keplerian curve establishes the minimum mass of this pulsar. We find that its minimum mass is $\approx 0.175M_{\odot}$ and corresponding equatorial radius 10.61 km for the globally neutral neutron star. For the locally neutral configuration we found $\approx 0.48M_{\odot}$ and 14.8 km, respectively for the minimum mass and corresponding equatorial radius. This implies that the mass of PSR J1748–2446ad is poorly constrained to be larger than the above values.

It is interesting that the above minimum mass, given by its constant rotation frequency sequence, is slightly larger than the minimum mass for bound configurations on the Keplerian sequence, $M_{\min}^K \approx 0.167M_{\odot}$; see Eq. (27). In fact, as we shown in Eq. (28) the minimum rotation frequency along the Keplerian sequence for bound configurations in the globally neutral case is, $f_{\min}^K \approx 700.59$ Hz, which is slightly lower than the frequency of PSR J1748–2446ad. It would imply that PSR J1748–2446ad is very likely rotating at a rate much lower than the Keplerian one.

Similarly to what presented in Belvedere et al. [2] for the static neutron stars and introduced by Trümper [32], the above observational constraints show a preference on stiff EOS that provide highest maximum masses for neutron stars. Taking into account the above constraints, the radius of a canonical neutron star of mass $M = 1.4M_{\odot}$ is strongly constrained to $R \geq 12$ km, disfavoring at the same time strange quark matter stars. It is evident from Fig. 24 that mass–radius relations for both the static and the rotating case presented here, are consistent with all the observational constraints. In Table 2 we show the radii predicted by our mass–radius relation both for the static and the rotating case for a canonical neutron star as well as for the most massive neutron stars discovered, namely, the millisecond pulsar PSR J1614–2230 Demorest et al. [9], $M = (1.97 \pm 0.04)M_{\odot}$, and the most recent PSR J0348+0432, $M = (2.01 \pm 0.04)M_{\odot}$ [1].

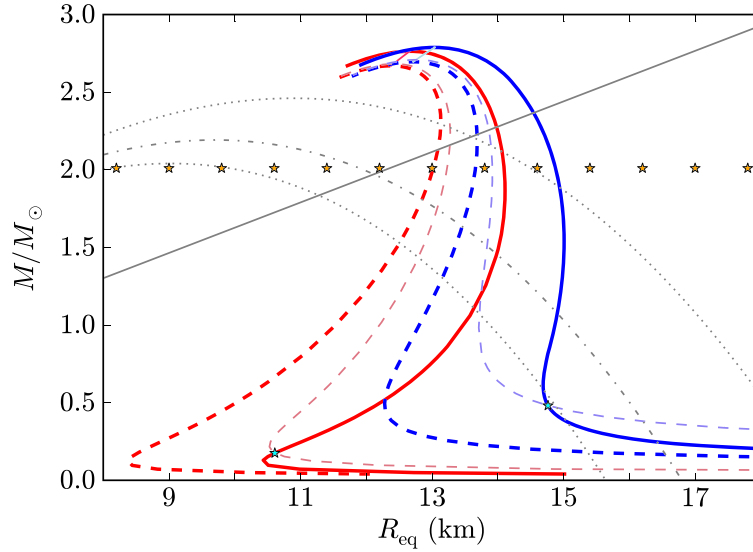


Fig. 24. Observational constraints on the mass–radius relation given by Trümper [32] and the theoretical mass–radius relation presented in this work in Fig. 11. The red lines represent the configuration with global charge neutrality, while the blue lines represent the configuration with local charge neutrality. The pink-red line and the light-blue line represent the secular axisymmetric stability boundaries for the globally neutral and the locally neutral case, respectively. The red and blue solid lines represent the Keplerian sequences and the red and blue dashed lines represent the static cases presented in [2]. (For interpretation of the references to color in this figure, the reader is referred to the web version of this article.)

Table 2

Radii for a canonical neutron star of $M = 1.4M_{\odot}$ and for PSR J1614–2230 Demorest et al. [9], $M = (1.97 \pm 0.04)M_{\odot}$, and PSR J0348+0432 [1], $M = (2.01 \pm 0.04)M_{\odot}$. These configurations are computed under the constraint of global charge neutrality and for a density at the edge of the crust equal to the neutron drip density. The nuclear parameterizations NL3 has been used.

$M(M_{\odot})$	$R^{J=0}$ (km)	$R_{\text{eq}}^{J \neq 0}$ (km)
1.40	12.313	13.943
1.97	12.991	14.104
2.01	13.020	14.097

9. Concluding remarks

We have constructed equilibrium configurations of uniformly rotating neutron stars in both the global charge neutrality and local charge neutrality cases, generalizing our previous work [2]. To do this we have applied the Hartle method to the seed static solution obtained from the integration of the Einstein–Maxwell–Thomas–Fermi equations [2]. We calculated the mass, polar and equatorial radii, angular momentum, moment of inertia, quadrupole moment, and eccentricity, as functions of the central density and the rotation angular velocity of the neutron star.

The Keplerian mass-shedding limit and the secular axisymmetric instability have been analyzed for the construction of the region of stability of rotating neutron stars. We have given fitting curves of the secular instability boundary in Eqs. (24) and (25) for global and local charge neutrality, respectively. With this analysis we have established in Section 4.2.1 the maximum mass and maximum rotation frequency of the neutron star. We computed in Section 4.2.2 the gravitational binding energy of the configurations as a function of the central density and rotation rate.

Table 3

Maximum mass, maximum frequency, minimum period, minimum mass of globally and locally neutral neutron stars.

	Global neutrality	Local neutrality
$M_{\max}^{J=0} (M_{\odot})$	2.67	2.70
$M_{\max}^{J \neq 0} (M_{\odot})$	2.76	2.79
f_{\max} (kHz)	1.97	1.89
P_{\min} (ms)	0.51	0.53
$M_{\min}^{J=0} (M_{\odot})$	0.18	–
$M_{\min}^K (M_{\odot})$	0.17	–
f_{\min}^K (kHz)	0.70	–

We did this for central densities higher than the nuclear one, so imposing that the neutron star has a supranuclear hadronic core. We found that, in the globally neutral case, there is a minimum mass under which the neutron star becomes gravitationally unbound. Along the Keplerian sequence, to this minimum mass object we associate a minimum frequency under which an object rotating at the Keplerian rate becomes unbound; see Eq. (28). We found that locally neutral neutron stars with supranuclear cores remained always bound for the present EOS. In Table 3 we summarize all these results.

We finally analyzed in Section 8 the current observational constraints on the mass–radius relation of neutron stars. We constructed the constant frequency sequence of PSR J1748–2446ad to obtain the minimum possible mass of this source, which is given by the crossing point of the $f = 716$ Hz constant sequence with the Keplerian one. It gives $\approx 0.17M_{\odot}$ and $\approx 0.48M_{\odot}$ for the global and charge neutrality cases, respectively. The very low mass inferred for PSR J1748–2446ad assuming that it rotates at the Keplerian rate implies that its frequency is unlikely to be actually the Keplerian. Otherwise, it would imply that PSR J1748–32446ad could be the less massive neutron star ever observed.

It would be interesting to analyze the generality of the neutron star features shown in this work since the most recent measurement of the mass PSR J0348+0432, $M = (2.01 \pm 0.04)M_{\odot}$ [1], favors stiff nuclear EOS as the one used here.

Appendix A. The Hartle solution and equatorial circular orbits

A.1. The Hartle–Thorne vacuum solution

It is possible to write the Hartle–Thorne metric given by Eq. (6) in an analytic closed-form in the exterior vacuum case as function of the total mass M , angular momentum J , and quadrupole moment Q of the rotating star. The angular velocity of local inertial frames $\omega(r)$, proportional to Ω , and the functions h_0 , h_2 , m_0 , m_2 , k_2 , proportional to Ω^2 , are derived from the Einstein equations (see Hartle [13]; Hartle and Thorne [16] for details). Following this prescriptions the Eq. (6) become:

$$ds^2 = \left(1 - \frac{2M}{r}\right) \left[1 + 2k_1 P_2(\cos \theta) + 2 \left(1 - \frac{2M}{r}\right)^{-1} \frac{J^2}{r^4} (2 \cos^2 \theta - 1)\right] dt^2 \\ + \frac{4J}{r} \sin^2 \theta dt d\phi - \left(1 - \frac{2M}{r}\right)^{-1} \left[1 - 2 \left(k_1 - \frac{6J^2}{r^4}\right) P_2(\cos \theta)\right]$$

$$\begin{aligned}
 & - 2 \left(1 - \frac{2M}{r} \right)^{-1} \frac{J^2}{r^4} \Big] dr^2 \\
 & - r^2 [1 - 2k_2 P_2(\cos \theta)] (d\theta^2 + \sin^2 \theta d\phi^2),
 \end{aligned} \tag{A.1}$$

where

$$\begin{aligned}
 k_1 &= \frac{J^2}{Mr^3} \left(1 + \frac{M}{r} \right) + \frac{5}{8} \frac{Q - J^2/M}{M^3} Q_2^2(x), \\
 k_2 &= k_1 + \frac{J^2}{r^4} + \frac{5}{4} \frac{Q - J^2/M}{M^2 r \sqrt{1 - 2M/r}} Q_2^1(x),
 \end{aligned}$$

and

$$\begin{aligned}
 Q_2^1(x) &= (x^2 - 1)^{1/2} \left[\frac{3x}{2} \ln \left(\frac{x+1}{x-1} \right) - \frac{3x^2 - 2}{x^2 - 1} \right], \\
 Q_2^2(x) &= (x^2 - 1) \left[\frac{3}{2} \ln \left(\frac{x+1}{x-1} \right) - \frac{3x^3 - 5x}{(x^2 - 1)^2} \right],
 \end{aligned}$$

are the associated Legendre functions of the second kind, being $P_2(\cos \theta) = (1/2)(3 \cos^2 \theta - 1)$ the Legendre polynomial, and where it has been effectuated the re-scaling $x = r/M - 1$. The constants M , J and Q are the total mass, angular momentum and mass quadrupole moment of the rotating object, respectively. This form of the metric corrects some misprints of the original paper by Hartle and Thorne [16] (see also Berti et al. [4]; Boshkayev et al. [7]). To obtain the exact numerical values of M , J and Q , the exterior and interior metrics have to be matched at the surface of the star. It is worthy underline that in the terms involving J^2 and Q , the total mass M can be substituted by $M^{J=0}$ since δM is already a second order term in the angular velocity.

A.2. Angular velocity of equatorial circular orbits

It is possible to obtain the analytical expression for the angular velocity Ω given by Eq. (20) with respect to an observer at infinity, taking into account the parameterization of the four-velocity u of a test particle on a circular orbit in equatorial plane of axisymmetric stationary spacetime, regarding as parameter the angular velocity Ω itself:

$$u = \Gamma [\partial_t + \Omega \partial_\phi], \tag{A.2}$$

where Γ is a normalization factor such that $u^\alpha u_\alpha = 1$. Normalizing and applying the geodesics conditions we get the following expressions for Γ and $\Omega = u^\phi / u^t$

$$\Gamma = \pm (g_{tt} + 2\Omega g_{t\phi} + \Omega^2 g_{\phi\phi})^{-1/2}, \tag{A.3}$$

$$g_{tt,r} + 2\Omega g_{t\phi,r} + \Omega^2 g_{\phi\phi,r} = 0. \tag{A.4}$$

Thus, the solution of Eqs. (A.3–A.4) can be written as

$$\Omega_{\text{orb}}^\pm(r) = \frac{u^\phi}{u^t} = \frac{-g_{t\phi,r} \pm \sqrt{(g_{t\phi,r})^2 - g_{tt,r} g_{\phi\phi,r}}}{g_{\phi\phi,r}}, \tag{A.5}$$

where $+/-$ stands for co-rotating/counter-rotating orbits, u^ϕ and u^t are the angular and time components of the four-velocity respectively, and a colon stands for partial derivative with respect to the corresponding coordinate. To determine the mass shedding angular velocity (the

Keplerian angular velocity) of the neutron stars, we need to consider only the co-rotating orbit, so from here and thereafter we take into account only the plus sign in Eq. (A.3) and we write $\Omega_{\text{orb}}^+(r) = \Omega_{\text{orb}}(r)$.

For the Hartle external solution given by Eq. (A.1) we obtain Eq. (20) with

$$\begin{aligned}
 F_1 &= \left(\frac{M}{r}\right)^{3/2}, \\
 F_2 &= \frac{48M^7 - 80M^6r + 4M^5r^2 - 18M^4r^3}{16M^2r^4(r-2M)} + \frac{40M^3r^4 + 10M^2r^5 + 15Mr^6 - 15r^7}{16M^2r^4(r-2M)} + F, \\
 F_3 &= \frac{6M^4 - 8M^3r - 2M^2r^2 - 3Mr^3 + 3r^4}{16M^2r(r-2M)/5} - F, \\
 F &= \frac{15(r^3 - 2M^3)}{32M^3} \ln \frac{r}{r-2M}.
 \end{aligned}$$

The maximum angular velocity possible for a rotating star at the mass-shedding limit is the Keplerian angular velocity evaluated at the equator ($r = R_{\text{eq}}$), i.e.

$$\Omega_K^{J \neq 0} = \Omega_{\text{orb}}(r = R_{\text{eq}}). \quad (\text{A.6})$$

In the static case, i.e. when $j = 0$ hence $q = 0$ and $\delta M = 0$ we have the well-known Schwarzschild solution and the orbital angular velocity for a test particle $\Omega_K^{J=0}$ on the surface ($r = R$) of the neutron star is given by

$$\Omega_K^{J=0} = \sqrt{\frac{M^{J=0}}{R_{M^{J=0}}^3}}. \quad (\text{A.7})$$

References

- [1] J. Antoniadis, P.C.C. Freire, N. Wex, T.M. Tauris, R.S. Lynch, M.H. van Kerkwijk, M. Kramer, C. Bassa, V.S. Dhillon, T. Driebe, J.W.T. Hessels, V.M. Kaspi, V.I. Kondratiev, N. Langer, T.R. Marsh, M.A. McLaughlin, T.T. Pennucci, S.M. Ransom, I.H. Stairs, J. van Leeuwen, J.P.W. Verbiest, D.G. Whelan, A massive pulsar in a compact relativistic binary, *Science* 340 (Apr. 2013) 448.
- [2] R. Belvedere, D. Pugliese, J.A. Rueda, R. Ruffini, S.-S. Xue, Neutron star equilibrium configurations within a fully relativistic theory with strong, weak, electromagnetic, and gravitational interactions, *Nucl. Phys. A* 883 (2012) 1–24.
- [3] O. Benhar, V. Ferrari, L. Gualtieri, S. Marassi, Perturbative approach to the structure of rapidly rotating neutron stars, *Phys. Rev. D* 72 (4) (2005) 044028.
- [4] E. Berti, F. White, A. Maniopoulou, M. Bruni, Rotating neutron stars: an invariant comparison of approximate and numerical space-time models, *Mon. Not. R. Astron. Soc.* 358 (2005) 923–938.
- [5] D. Bini, K. Boshkayev, R. Ruffini, I. Siutsou, Equatorial circular geodesics in the Hartle–Thorne spacetime, *Nuovo Cimento C* 36 (2013) 31.
- [6] J. Boguta, A.R. Bodmer, Relativistic calculation of nuclear matter and the nuclear surface, *Nucl. Phys. A* 292 (1977) 413–428.
- [7] K. Boshkayev, H. Quevedo, R. Ruffini, Gravitational field of compact objects in general relativity, *Phys. Rev. D* 86 (6) (2012) 064043.
- [8] K. Boshkayev, M. Rotondo, R. Ruffini, On magnetic fields in rotating nuclear matter cores of stellar dimensions, *Int. J. Mod. Phys. Conf. Ser.* 12 (2012) 58–67.
- [9] P.B. Demorest, T. Pennucci, S.M. Ransom, M.S.E. Roberts, J.W.T. Hessels, A two-solar-mass neutron star measured using Shapiro delay, *Nature* 467 (2010) 1081–1083.
- [10] J.L. Friedman, J.R. Ipser, R.D. Sorkin, Turning-point method for axisymmetric stability of rotating relativistic stars, *Astrophys. J.* 325 (1988) 722–724.
- [11] J.L. Friedman, L. Parker, J.R. Ipser, Rapidly rotating neutron star models, *Astrophys. J.* 304 (1986) 115–139.

- [12] P. Haensel, A.Y. Potekhin, D.G. Yakovlev (Eds.), *Neutron Stars 1: Equation of State and Structure*, Astrophysics and Space Science Library, vol. 326, 2007.
- [13] J.B. Hartle, Slowly rotating relativistic stars. I. Equations of structure, *Astrophys. J.* 150 (1967) 1005.
- [14] J.B. Hartle, Slowly rotating relativistic stars. IX: Moments of inertia of rotationally distorted stars, *Astrophys. Space Sci.* 24 (1973) 385–405.
- [15] J.B. Hartle, D.H. Sharp, Variational principle for the equilibrium of a relativistic, rotating star, *Astrophys. J.* 147 (1967) 317.
- [16] J.B. Hartle, K.S. Thorne, Slowly rotating relativistic stars. II. Models for neutron stars and supermassive stars, *Astrophys. J.* 153 (1968) 807.
- [17] C.O. Heinke, G.B. Rybicki, R. Narayan, J.E. Grindlay, A hydrogen atmosphere spectral model applied to the neutron star X7 in the globular cluster 47 Tucanae, *Astrophys. J.* 644 (2006) 1090–1103.
- [18] J.W.T. Hessels, S.M. Ransom, I.H. Stairs, P.C.C. Freire, V.M. Kaspi, F. Camilo, A radio pulsar spinning at 716 Hz, *Science* 311 (2006) 1901–1904.
- [19] O. Klein, On the thermodynamical equilibrium of fluids in gravitational fields, *Rev. Mod. Phys.* 21 (1949) 531–533.
- [20] G.A. Lalazissis, J. König, P. Ring, New parametrization for the Lagrangian density of relativistic mean field theory, *Phys. Rev. C* 55 (1997) 540–543.
- [21] J.R. Oppenheimer, G.M. Volkoff, On massive neutron cores, *Phys. Rev.* 55 (1939) 374–381.
- [22] M. Rotondo, J.A. Rueda, R. Ruffini, S.-S. Xue, The self-consistent general relativistic solution for a system of degenerate neutrons, protons and electrons in β -equilibrium, *Phys. Lett. B* 701 (2011) 667–671.
- [23] J.A. Rueda, R. Ruffini, S.-S. Xue, The Klein first integrals in an equilibrium system with electromagnetic, weak, strong and gravitational interactions, *Nucl. Phys. A* 872 (2011) 286–295.
- [24] S.L. Shapiro, S.A. Teukolsky, *Black holes, white dwarfs, and neutron stars: The physics of compact objects*, 1983.
- [25] R. Sorkin, A criterion for the onset of instability at a turning point, *Astrophys. J.* 249 (1981) 254.
- [26] R.D. Sorkin, A stability criterion for many parameter equilibrium families, *Astrophys. J.* 257 (1982) 847.
- [27] N. Stergioulas, Rotating stars in relativity, *Living Rev. Relativ.* 6 (2003) 3.
- [28] K. Takami, L. Rezzolla, S. Yoshida, A quasi-radial stability criterion for rotating relativistic stars, *Mon. Not. R. Astron. Soc.* 416 (2011) L1–L5.
- [29] R.C. Tolman, On the weight of heat and thermal equilibrium in general relativity, *Phys. Rev.* 35 (1930) 904–924.
- [30] R.C. Tolman, Static solutions of Einstein’s field equations for spheres of fluid, *Phys. Rev.* 55 (1939) 364–373.
- [31] G. Torok, P. Bakala, Z. Stuchlik, P. Cech, Modeling the twin peak QPO distribution in the atoll source 4U 1636-53, *Acta Astron.* 58 (2008) 1–14.
- [32] J.E. Trümper, Observations of neutron stars and the equation of state of matter at high densities, *Prog. Part. Nucl. Phys.* 66 (2011) 674–680.
- [33] J.E. Trümper, V. Burwitz, F. Haberl, V.E. Zavlin, The puzzles of RX J1856.5-3754: neutron star or quark star?, *Nucl. Phys. B, Proc. Suppl.* 132 (2004) 560–565.
- [34] F. Weber, N.K. Glendenning, Application of the improved Hartle method for the construction of general relativistic rotating neutron star models, *Astrophys. J.* 390 (1992) 541–549.

What Can We Extract from Quasiperiodic Oscillations?[‡]

K. Boshkayev^{1,2,3*}, D. Bini^{2,3**}, J. Rueda^{2,3***},
A. Geralico^{2,3****}, M. Muccino^{2,3*****}, and I. Siutsou^{2,3*****}

¹*Physical and Technical Faculty of al-Farabi Kazakh National University,
al-Farabi ave. 71, 050040 Almaty, Kazakhstan*

²*Dipartimento di Fisica, Università di Roma “Sapienza,” Piazzale Aldo Moro 5, I-00185 Roma, Italy*

³*ICRANet, Piazzale della Repubblica 10, I-65122 Pescara, Italy*

Received April 16, 2014; in final form, June 19, 2014

Abstract—In the light of the relativistic precession model, we present a detailed analysis extending the ones performed in the Schwarzschild and Kerr spacetimes. We consider the kilohertz quasiperiodic oscillations in the Hartle-Thorne spacetime which describes a rotating and deformed object. We derive analytic formulas for epicyclic frequencies in the Hartle-Thorne spacetime, and by means of these frequencies we interpret the kilohertz quasiperiodic oscillations of low-mass X-ray binaries of the atoll and Z sources, on the basis of the relativistic precession model. Particularly we perform an analysis for the Z source GX 5-1. We show that the quasiperiodic oscillations data can provide information on the parameters, namely, the mass, angular momentum and quadrupole moment of compact objects in low-mass X-ray binaries.

DOI: 10.1134/S0202289314040033

1. INTRODUCTION

It is believed that quasi-periodic oscillations (QPOs) data of the X-ray flux from low-mass X-ray binaries (LMXBs) may be used to test general relativity (GR) in the strong field regime [1–4]. QPOs appear in variabilities of several LMXBs including those which contain a neutron star (NS). A certain kind of these oscillations, the so-called kilohertz (kHz) (or high-frequency) QPOs, come often in pairs with frequencies $f_L = f_{\text{per}} = f_\phi - f_r$, where f_ϕ is the azimuthal (Keplerian) frequency, f_r is the radial epicyclic frequency of Keplerian motion, and $f_U = f_\phi = f_K$ is typically in the range ~ 50 – 1300 Hz. This is of the same order as the range of frequencies characteristic of orbital motion close to a compact object. Accordingly, most of the kHz QPO models involve orbital motion in the inner regions of an accretion disk (see [5, 6]).

To explain the QPOs, various types of models have been proposed. These are: (i) beat-frequency models,

where one assumes that there is some beating of an orbital frequency by the spin frequency of the central object, (ii) relativistic precession models where the QPOs are associated with the orbital motion and the periastron or nodal precession of a particular orbit, (iii) relativistic resonance models, where a kind of resonance between the orbital and epicyclic frequencies is assumed wherever they have simple integer ratios, and finally (iv) preferred radii models, where some mechanism chooses a particular radius. These models generally assume geodesic or almost geodesic orbits of the fluid elements in the accretion disc to be the source of the observed frequencies (see, e.g., [5]), while there are also models in which the frequencies are produced from oscillatory modes of the entire disc (see, e.g., [5]). In one way or another, all of these models use the properties of orbits around the compact object onto which the accretion takes place. In our discussion we will refer to the models that assume that the QPOs are caused by frequencies associated with the orbital motion of the material in the accretion disc, such as the relativistic precession models (RPM) (see [2, 8]).

The RPM has been proposed in a series of papers [1, 2, 4]. It explains the kHz QPOs as a direct manifestation of modes of relativistic epicyclic motion of blobs arising at various radii r in the inner parts of the accretion disk. The model identifies the lower and upper kHz QPOs with the periastron precession f_{per} and Keplerian f_K frequency.

*E-mail: kuantay@mail.ru, kuantay@icra.it

**E-mail: binid@icra.it

***E-mail: jorge.rueda@icra.it

****E-mail: geralico@icra.it

*****E-mail: marco.muccino@icra.it

*****E-mail: siutsou@icranet.org

[‡]Based on a plenary talk given at the 11th International Conference on Gravitation, Astrophysics and Cosmology of Asia-Pacific Countries (ICGAC-11), October 1–5, 2013, Almaty, Kazakhstan.

In the past years, the RPM has been considered among the candidates for explaining the twin-peak QPOs in several LMXBs, and related constraints on the sources have been discussed (see, e.g., [6, 9–13]. While some of the early works discuss these constraints in terms of both NS mass and spin and include also the NS oblateness [3, 14], most of the published implications for individual sources focus on the NS mass and neglect its rotation, not to mention its oblateness.

In this paper, we perform an analysis of a mass estimate carried out by Stella [2] and Boutloukos et al. [15]. In particular, we consider rotating spacetimes that comprehend the effects of frame-dragging and quadrupole moment of the source and fit directly the correlation between the twin QPO frequencies. We show that good fits can be reached for the case of three parameters, the mass, angular momentum and quadrupole moment, rather than for the preferred combination of mass and angular momentum [16]. The importance of the quadrupole moment has been emphasized in several works [8, 17–21]. Since the angular momentum of the source is in a nontrivial way related to its quadrupole moment, they should be considered together.

2. THE HARTLE-THORNE METRIC

The Hartle-Thorne (HT) metric, describing the exterior field of a slowly rotating slightly deformed object, is given by

$$\begin{aligned}
 ds^2 = & - \left(1 - \frac{2M}{r}\right) \left[1 + 2k_1 P_2(\cos \theta)\right. \\
 & + 2 \left(1 - \frac{2M}{r}\right)^{-1} \frac{J^2}{r^4} (2 \cos^2 \theta - 1) \left. dt^2\right. \\
 & + \left(1 - \frac{2M}{r}\right)^{-1} \left[1 - 2k_2 P_2(\cos \theta)\right. \\
 & \quad \left. - 2 \left(1 - \frac{2M}{r}\right)^{-1} \frac{J^2}{r^4}\right] dr^2 \\
 & + r^2 [1 - 2k_3 P_2(\cos \theta)] (d\theta^2 + \sin^2 \theta d\phi^2) \\
 & \quad - 4 \frac{J}{r} \sin^2 \theta dt d\phi
 \end{aligned} \tag{1}$$

where

$$\begin{aligned}
 k_1 = & \frac{J^2}{Mr^3} \left(1 + \frac{M}{r}\right) - \frac{5Q - J^2/M}{8M^3} Q_2^2 \left(\frac{r}{M} - 1\right), \\
 k_2 = & k_1 - \frac{6J^2}{r^4}, \\
 k_3 = & k_1 + \frac{J^2}{r^4} - \frac{5Q - J^2/M}{4M^2 r}
 \end{aligned}$$

$$\times \left(1 - \frac{2M}{r}\right)^{-1/2} Q_2^1 \left(\frac{r}{M} - 1\right),$$

$$P_2(x) = \frac{1}{2}(3x^2 - 1),$$

$$Q_2^1(x) = (x^2 - 1)^{1/2} \left[\frac{3x}{2} \ln \frac{x+1}{x-1} - \frac{3x^2 - 2}{x^2 - 1} \right],$$

$$Q_2^2(x) = (x^2 - 1) \left[\frac{3}{2} \ln \frac{x+1}{x-1} - \frac{3x^3 - 5x}{(x^2 - 1)^2} \right].$$

Here $P_2(x)$ is Legendre's polynomial of the first kind, Q_l^m are the associated Legendre polynomials of the second kind, and the constants M , J and Q are the total mass, angular momentum and quadrupole parameter of a rotating star, respectively. The Hartle-Thorne metric is an approximate solution of vacuum Einstein field equations that describes the exterior of any slowly and rigidly rotating, stationary and axially symmetric body. The metric is given with an accuracy up to the second order terms in the body's angular momentum, and the first order in its quadrupole moment. The approximate Kerr metric [22] in the Boyer-Lindquist coordinates (t, R, Θ, ϕ) up to second order terms in the rotation parameter a can be obtained from (1) by setting

$$J = -Ma, \quad Q = J^2/M, \tag{2}$$

and making a coordinate transformation given by

$$\begin{aligned}
 r = & R + \frac{a^2}{2R} \left[\left(1 + \frac{2M}{R}\right) \left(1 - \frac{M}{R}\right)\right. \\
 & \quad \left. - \cos^2 \Theta \left(1 - \frac{2M}{R}\right) \left(1 + \frac{3M}{R}\right) \right], \\
 \theta = & \Theta + \frac{a^2}{2R^2} \left(1 + \frac{2M}{R}\right) \sin \Theta \cos \Theta.
 \end{aligned} \tag{3}$$

3. THE EPICYCLIC FREQUENCIES

The properties of congruences of nearly circular geodesic orbits in stationary and axially symmetric spacetime such as the HT spacetime are studied because of their fundamental role in the theory of accretion disks around compact objects with strong gravity. The radial epicyclic frequency and vertical epicyclic frequency are the most important characteristics of these orbits. Analytic formulas for the frequencies in the Schwarzschild, Kerr and Hartle-Thorne metrics have been published many times by several authors (see, e.g., [23–27] and are well known. Here we give a more explicit derivation of the frequencies for the HT metric in the equatorial plane.

The Keplerian angular velocity (angular frequency) ω_K for the Hartle-Thorne solution is given by

$$\omega_K^2(u) = \omega_{K0}^2(u) [1 \mp j F_1(u)]$$

$$+j^2 F_2(u) + qF_3(u)], \quad (4)$$

where (+/-) stands for co-rotating/counter-rotating geodesics, $j = J/M^2$ and $q = Q/M^3$ are the dimensionless angular momentum and quadrupole parameter, and $u = M/r$. Other quantities are defined as follows:

$$\begin{aligned} \omega_{K0}^2(u) &= u^3/M^2, & F_1(u) &= 2u^{3/2}, \\ F_2(u) &= (48u^7 - 80u^6 + 12u^5 + 26u^4 - 40u^3 \\ &\quad - 10u^2 - 15u + 15)[8u^2(1 - 2u)]^{-1} - F(u), \\ F_3(u) &= -\frac{5(6u^4 - 8u^3 - 2u^2 - 3u + 3)}{8u^2(1 - 2u)} + F(u), \\ F(u) &= \frac{15(1 - 2u^3)}{16u^3} \ln\left(\frac{1}{1 - 2u}\right). \end{aligned}$$

Let us consider oscillations around circular orbits in the plane $\theta = \pi/2$. Since $U_t = -E$ and $U_\phi = L$ are integrals of motion, a perturbation of the 4-velocity is

$$\delta U_\alpha = (-\delta E, \delta U_r(t), \delta U_\theta(t), \delta L). \quad (5)$$

To calculate the epicyclic frequencies of these oscillations, we can use the 4-velocity in the circular orbit

$$g^{\alpha\beta} U_\alpha U_\beta = \epsilon, \quad (6)$$

where $\epsilon = 0, -1$, and calculate it in the perturbed trajectory:

$$\begin{aligned} &g^{\alpha\beta}(r + \delta r, \theta + \delta\theta)(U_\alpha + \delta U_\alpha) \\ &\quad \times (U_\beta + \delta U_\beta) = \epsilon, \quad (7) \\ &\left(\delta r \frac{\partial g^{\alpha\beta}}{\partial r} + \delta\theta \frac{\partial g^{\alpha\beta}}{\partial \theta} + \frac{\delta r^2}{2} \frac{\partial^2 g^{\alpha\beta}}{\partial r^2} + \frac{\delta\theta^2}{2} \frac{\partial^2 g^{\alpha\beta}}{\partial \theta^2} \right. \\ &\quad \left. + \delta r \delta\theta \frac{\partial^2 g^{\alpha\beta}}{\partial r \partial \theta} + \dots \right) U_\alpha U_\beta \\ &+ 2g^{\alpha\beta}(r, \theta) \delta U_\alpha U_\beta + g^{\alpha\beta}(r, \theta) \delta U_\alpha \delta U_\beta = 0. \quad (8) \end{aligned}$$

Since $\theta = \pi/2$ is the symmetry plane, all derivatives in $\partial\theta$ are equal to 0 (but not in $\partial\theta^2$). The equation of circular orbits can be written as

$$g_{,r}^{\alpha\beta} U_\alpha U_\beta = 0, \quad (9)$$

where $g_{,r}^{\alpha\beta}$ is the derivative of the metric tensor with respect to r . As a result, the first nonvanishing terms give us

$$\begin{aligned} &\left(\frac{\delta r^2}{2} \frac{\partial^2 g^{\alpha\beta}}{\partial r^2} + \frac{\delta\theta^2}{2} \frac{\partial^2 g^{\alpha\beta}}{\partial \theta^2} \right) U_\alpha U_\beta \\ &+ (U^t)^2 [g_{rr} \dot{\delta r}^2 + g_{\theta\theta} \dot{\delta\theta}^2] = C, \quad (10) \end{aligned}$$

where the dot denotes a derivative with respect to t and

$$C = 2g^{t\phi}(E\delta L + L\delta E + \delta E\delta L)$$

$$-g^{tt}(\delta E^2 + 2E\delta E) - g^{\phi\phi}(\delta L^2 + 2L\delta L), \quad (11)$$

is a constant. Explicitly, using the fact that $U_\alpha = (-E, 0, 0, L)$ is a constant, we have after division by E^2

$$\begin{aligned} &\left(\frac{\delta r^2}{2} \frac{\partial^2}{\partial r^2} + \frac{\delta\theta^2}{2} \frac{\partial^2}{\partial \theta^2} \right) (g^{tt} - 2g^{t\phi}l + g^{\phi\phi}l^2) \\ &+ (g^{t\phi}l - g^{tt})^2 [g_{rr} \dot{\delta r}^2 + g_{\theta\theta} \dot{\delta\theta}^2] = C/E^2, \quad (12) \end{aligned}$$

where $l = -U_\phi/U_t$ is the specific orbital angular momentum of a test particle per unit energy. Taking a derivative of (12) with respect to t , one has the equation of uncoupled harmonic oscillations with angular frequencies given by

$$\omega_x^2 = \frac{\partial_{xx}(g^{tt} - 2g^{t\phi}l + g^{\phi\phi}l^2)}{2g_{xx}(g^{t\phi}l - g^{tt})^2}, \quad x = r \text{ or } \theta. \quad (13)$$

Defining an effective potential by $U_{\text{eff}}(r, \theta, l) = g^{tt} - 2l g^{t\phi} + l^2 g^{\phi\phi}$, which can be used to find a general formula for epicyclic frequencies on the equatorial plane, the previous expression becomes

$$\omega_x^2 = \frac{(g_{tt} + \omega_K g_{t\phi})^2}{2g_{xx}} \left(\frac{\partial^2 U_{\text{eff}}}{\partial x^2} \right)_l, \quad x \in (r, \theta), \quad (14)$$

where $\omega_K = U^\phi/U^t$ is the orbital angular velocity of a test particle.

The radial frequencies are given by

$$\begin{aligned} \omega_r^2(u) &= \omega_{r0}^2(u) [1 \pm jX_1(u) + j^2X_2(u) \\ &\quad + qX_3(u)], \quad (15) \end{aligned}$$

where

$$\begin{aligned} \omega_{r0}^2(u) &= u^3(1 - 6u)/M^2, \\ X_1(u) &= \frac{6u^{3/2}(1 + 2u)}{(1 - 6u)}, \quad (16) \end{aligned}$$

$$\begin{aligned} X_2(u) &= X(u) - (384u^8 - 720u^7 - 112u^6 \\ &\quad + 404u^5 + 162u^4 + 130u^3 - 635u^2 + 375u - 60) \\ &\quad \times [8u^2(1 - 2u)(1 - 6u)]^{-1}, \quad (17) \end{aligned}$$

$$\begin{aligned} X_3(u) &= \frac{5(48u^5 + 30u^4 + 26u^3 - 127u^2 + 75u - 12)}{8u^2(1 - 2u)(1 - 6u)} \\ &\quad - X(u), \quad (18) \end{aligned}$$

$$X(u) = \frac{15(1 - 2u)(2u^2 + 13u - 4)}{16u^3(1 - 6u)} \ln\left(\frac{1}{1 - 2u}\right). \quad (19)$$

The vertical frequencies are given by

$$\begin{aligned} \omega_\theta^2(u) &= \omega_{\theta0}^2(u) [1 \mp jY_1(u) \\ &\quad + j^2Y_2(u) + qY_3(u)], \quad (20) \end{aligned}$$

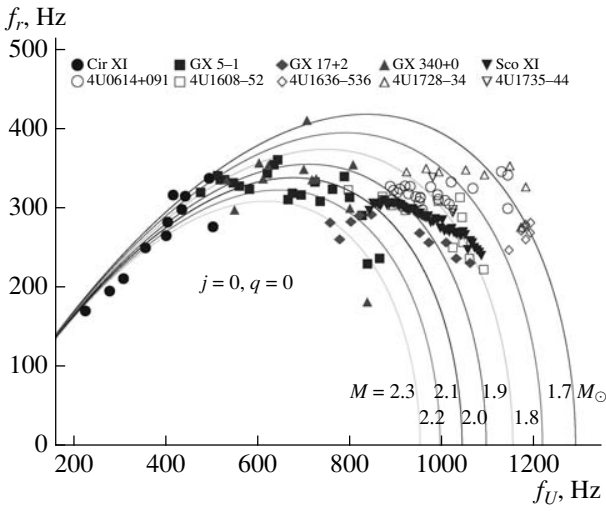


Fig. 1. The radial frequency f_r versus the upper frequency f_U for the Schwarzschild spacetime ($j = 0$, $q = 0$). From top to bottom $M = [1.7, 1.8, 1.9, 2.0, 2.1, 2.2, 2.3, 2.4]M_\odot$.

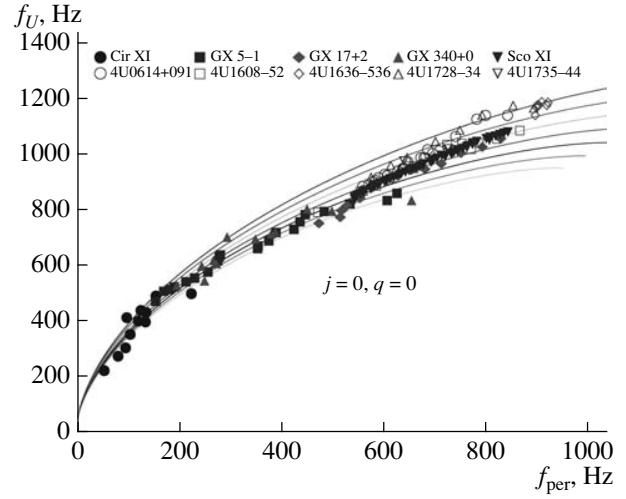


Fig. 2. The upper frequency f_U versus the periastron frequency $f_{\text{per}} = f_\phi - f_r$ for the Schwarzschild spacetime ($j = 0$, $q = 0$). From top to bottom, the mass $M = [1.7, 1.8, 1.9, 2.0, 2.1, 2.2, 2.3, 2.4]M_\odot$.

where

$$\omega_{\theta 0}^2(r) = u^3/M^2, \quad Y_1(u) = 6u^{3/2}, \quad (21)$$

$$Y_2(u) = \left(48u^7 - 224u^6 + 28u^5 + 66u^4 + 170u^3 - 295u^2 + 165u - 30 \right) \times [8u^2(1-2u)]^{-1} + Y(u), \quad (22)$$

$$Y_3(u) = -\frac{5(6u^4 + 34u^3 - 59u^2 + 33u - 6)}{8u^2(1-2u)} - Y(u), \quad (23)$$

$$Y(u) = \frac{15(2-u)(1-2u)^2}{16u^3} \ln\left(\frac{1}{1-2u}\right). \quad (24)$$

4. DETERMINATION OF THE MASS, ANGULAR MOMENTUM AND QUADRUPOLE MOMENT

Spacetimes around rotating NSs can be with a high precision approximated by the three-parameter Hartle–Thorne solution of the Einstein field equations ([28]; see [29]). The solution contains the mass M , angular momentum J and quadrupole moment Q (supposed to reflect the rotationally induced oblateness of the star). It is known that in most situations modeled with the present NS equations of state (EoS), the NS external geometry is very different from the Kerr geometry (representing the limit of the HT geometry for $\tilde{q} \equiv QM/J^2 \rightarrow 1$). However, the situation changes if the NS mass approaches its maximum

for a given EoS. For high masses, the quadrupole moment does not induce large differences from the Kerr geometry since \tilde{q} takes values close to unity. Nevertheless, this does not mean that one can easily neglect the quadrupole moment. For this reason, in this work we extend the analysis of [2] involving the Hartle–Thorne solution.

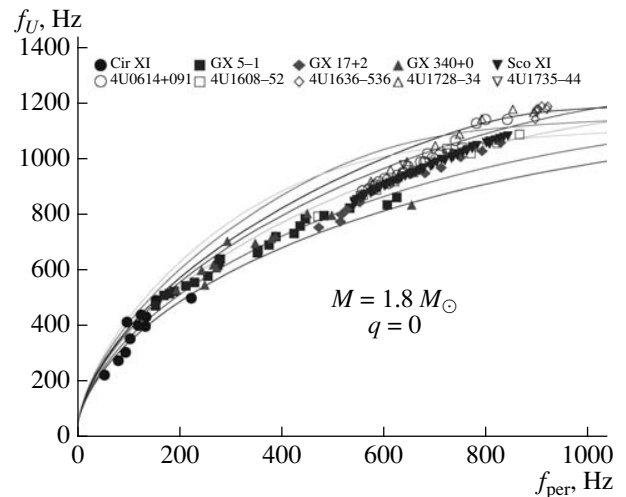


Fig. 3. The upper frequency f_U versus the periastron frequency f_{per} for fixed $M = 1.8M_\odot$ and $q = 0$. From bottom to top (or from right to left) $j = [-0.5, -0.3, -0.1, 0, 0.1, 0.3, 0.5]$.

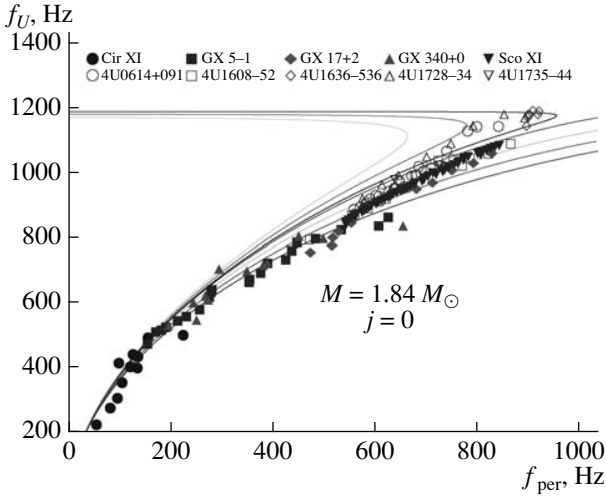


Fig. 4. The upper frequency f_U versus the periastron frequency f_{per} for fixed $M = 1.84M_{\odot}$ and $j = 0$. From bottom to top (or from right to left) $q = [-1.2, -0.7, -0.3, 0, 0.1, 0.3, 0.5]$.

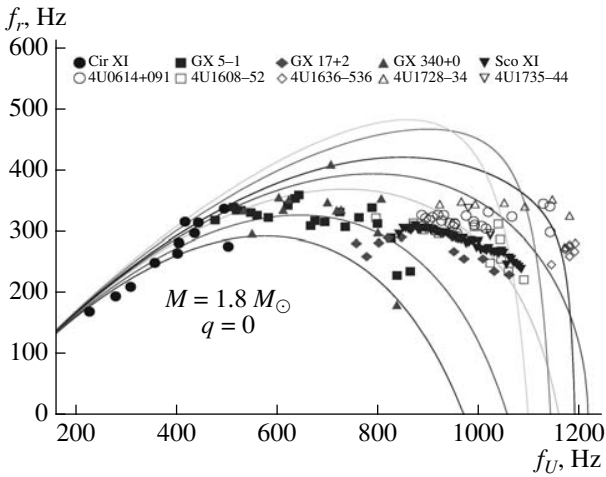


Fig. 5. The radial frequency f_r versus the upper frequency f_U for fixed $M = 1.8M_{\odot}$ and $q = 0$. From bottom to top $j = [-0.5, -0.3, -0.1, 0, 0.1, 0.3, 0.5]$.

Usually in the literature the QPOs data are given by the following frequencies:

$$\begin{aligned} f_{\phi}(u) &= \omega_K(u)/(2\pi), \\ f_r(u) &= \omega_r(u)/(2\pi), \\ f_{\theta}(u) &= \omega_{\theta}(u)/(2\pi). \end{aligned} \quad (25)$$

In Fig. 1, the radial frequency f_r is plotted versus the upper (Keplerian) frequency f_U in the Schwarzschild spacetime ($j = 0$, $q = 0$). The smaller mass, the higher radial frequency f_r . Note for ($j = 0$, $q = 0$), the Keplerian frequency f_K coincides with the vertical frequency f_{θ} . The Keplerian frequency

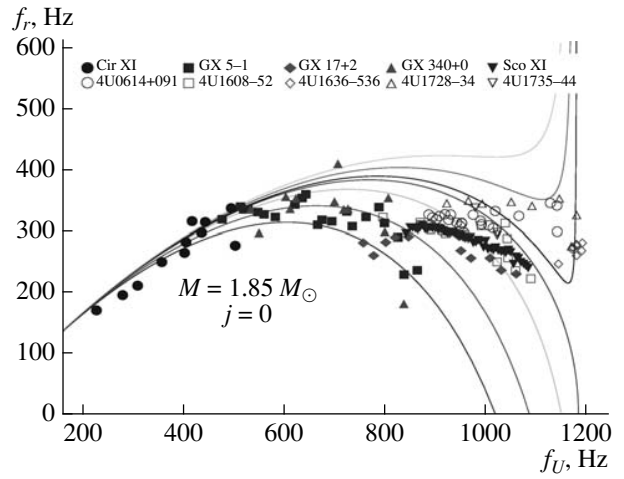


Fig. 6. The radial frequency f_r versus the upper frequency f_U for fixed $M = 1.85M_{\odot}$ and $j = 0$. From bottom to top $q = [-2, -1, -0.3, 0, 0.1, 0.3, 0.5]$.

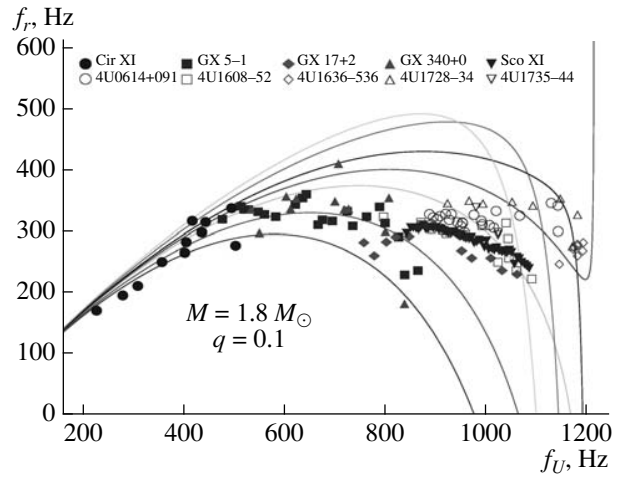


Fig. 7. The radial frequency f_r versus the upper frequency f_U for fixed $M = 1.8M_{\odot}$ and $q = 0.1$. From bottom to top $j = [-0.5, -0.3, -0.1, 0, 0.1, 0.3, 0.5]$.

f_{ϕ} versus the periastron frequency $f_{\text{per}} = f_{\phi} - f_r$ is shown in Fig. 2. The observational data points in Figs. 1 and 2 belong to Atoll (4U0614+091, 4U1608-52, 4U1636-536, 4U1728-34, 4U1735-44) and Z (GX 5-1, GX 17+2, GX 340+0, Sco X-1, Cir X-1) sources. For the sake of clarity, the error bars have been omitted. The QPOs data have been taken from [30–33] and references therein. For fixed mass and zero quadrupole parameter, different curves are shown in Figs. 3 and 5, varying the value of j . Figs. 4 and 6 show the frequencies around non-rotating deformed objects with fixed mass and different quadrupole moments. Indeed, the rotation and deformation of a central object (in our case a neutron

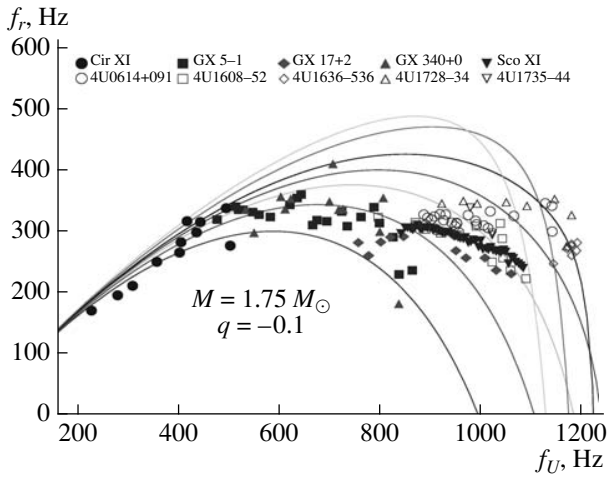


Fig. 8. The radial frequency f_r versus the upper frequency f_U for fixed $M = 1.75M_\odot$ and $q = -0.1$. From bottom to top $j = [-0.5, -0.25, -0.1, 0, 0.1, 0.3, 0.5]$.

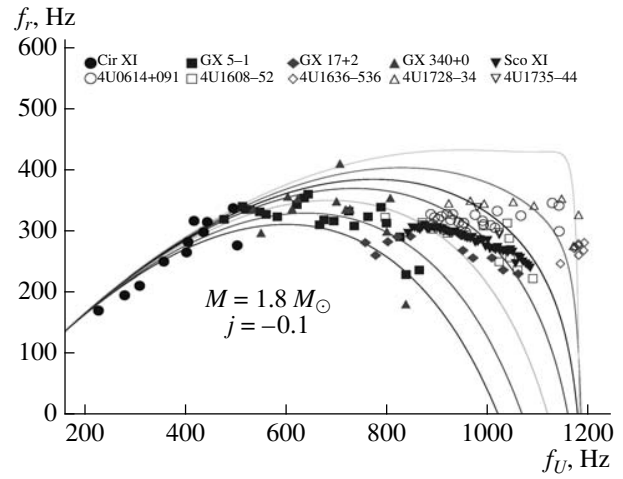


Fig. 10. The radial frequency f_r versus the upper frequency f_U for fixed $M = 1.8M_\odot$ and $j = -0.1$. From bottom to top $q = [-2, -1.2, -0.5, 0, 0.3, 0.6, 0.9]$.

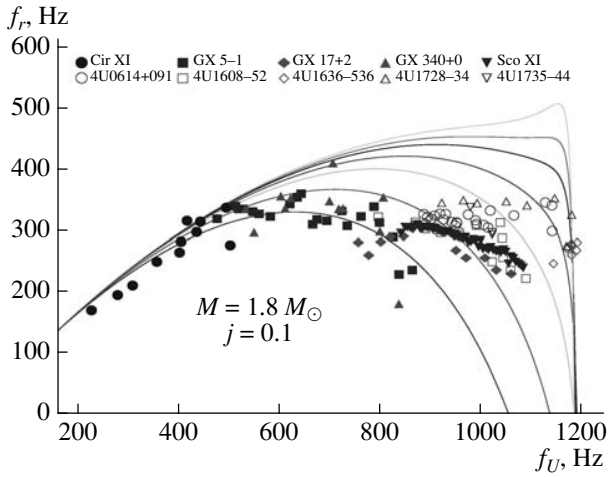


Fig. 9. The radial frequency f_r versus the upper frequency f_U for fixed $M = 1.8M_\odot$ and $j = 0.1$. From bottom to top $q = [-2.2, -1, -0.3, 0, 0.2, 0.3, 0.4]$.

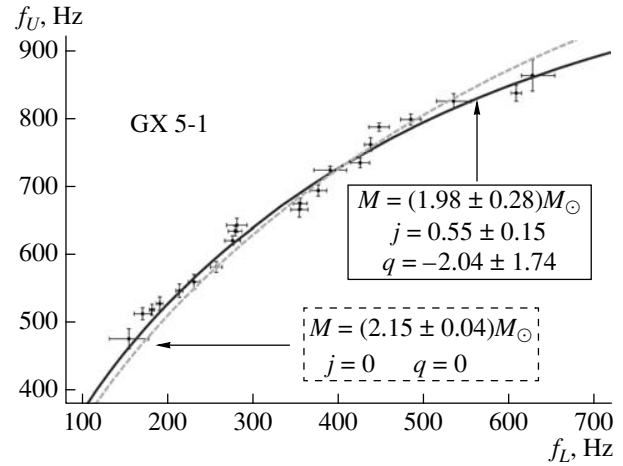


Fig. 11. The upper frequency f_U versus the lower frequency f_L for the Z source GX 5-1. The dashed green line corresponds to the static case, and the solid red line corresponds to the rotating case.

star) play a pivotal role in describing quasiperiodic oscillations. Figs. 7–10 show the radial frequencies versus the upper frequencies depending on M , j and q of the central source.

In this work, we have used the minimum set of parameters such as the total mass M , the dimensionless angular momentum j and the quadrupole parameter q of the source. Unfortunately, from observations it is hard to obtain precise values of LMXB masses. Different references show contradictory numbers. For example, Sco X-1 is the well-known X-ray binary system classified as a low-mass X-ray binary; the neutron star is roughly 1.4 solar masses, while the donor star is only 0.42 solar masses [34]. However,

Refs. [2, 35, 36] present various values for the neutron star mass.

Fig. 11 shows the best fits for the upper frequency versus the lower frequency for the Z source GX 5-1. Here we see that the fit with all three parameters is better than the fit with only one parameter, the mass M . A statistical test gives $\chi^2 = 0.998$ for the three-parameter fit and $\chi^2 = 0.993$ for the one-parameter fit.

5. CONCLUSION

In this paper we have derived formulas for epicyclic frequencies of test particles in the Hartle-Thorne

spacetime. With the help of these frequencies and according to the relativistic precession model, we have interpreted the quasi-periodic oscillations of the low-mass X-ray binaries. We have constructed the dependence of the higher frequencies with respect to the lower frequencies varying the main parameters of the central compact object such as the mass, angular momentum and quadrupole moment. Eventually for Z source GX 5-1 we have performed the fitting analysis and found the best fit to estimate the mass, angular momentum and quadrupole moment. We have shown that the three-parameter fit is better than the one- and two-parameter ones. For better analyses one needs to consider more sources with refined data. It would be interesting to perform further calculations assigning the neutron star equation of state and construct mass-radius, mass-angular momentum, angular velocity-quadrupole moment etc. relations in order to compare and contrast the theory with observations. The first step in this direction was recently undertaken by Belvedere et al. [37], where the authors construct equilibrium configurations of uniformly rotating neutron stars taking into account all fundamental interactions in a self-consistent relativistic fashion. Construction of an angular momentum-quadrupole moment relation from a theoretical point of view and its comparison with the best fit of observational data will be the issue of future investigations.

ACKNOWLEDGMENTS

The authors thank ICRANet for support. One of them (K.B.) thanks Mariano Méndez for fruitful discussions.

REFERENCES

1. L. Stella and M. Vietri, in: Abstracts of the 19th Texas Symposium on Relativistic Astrophysics and Cosmology, ed. J. Paul, T. Montmerle, and E. Aubourg (CEA Saclay, 1998).
2. L. Stella and M. Vietri, *Phys. Rev. Lett.* **82**, 17 (1999).
3. L. Stella, M. Vietri, and S. M. Morsink, *Ap. J.* **524**, L63 (1999).
4. L. Stella and M. Vietri, in: Proc. Ninth Marcel Grossmann Meeting, University of Rome "La Sapienza," 2-8 July 2000, ed. V. G. Gurzadyan, R. T. Jantzen, and R. Ruffini (World Scientific, 2002), Part A, 426.
5. M. van der Klis, in: *Compact Stellar X-Ray Sources*, ed. W. H. G. Lewin and M. van der Klis (Cambridge University Press, 2006), p. 39; astro-ph/0410551.
6. F. K. Lamb and S. Boutloukos, in: *Astrophysics and Space Science Library* **352**, Short-Period Binary Stars: Observations, Analyses, and Results, ed. E. F. Milone, D. A. Leahy, and D. Hobill (Dordrecht, Springer, 2007).
7. L. Rezzolla, S. Yoshida, and O. Zanotti, *Mon. Not. R. Astron. Soc.* **344**, 978 (2003).
8. G. Pappas, *Mon. Not. R. Astron. Soc.* **422**, 2581 (2012).
9. V. Karas, *Ap. J.* **526**, 953 (1999).
10. C. M. Zhang, H. X. Yin, Y. H. Zhao, F. Zhang, and L. M. Song, *Mon. Not. R. Astron. Soc.* **366**, 1373 (2006).
11. T. Belloni, M. Méndez, J. Homan, *Mon. Not. R. Astron. Soc.* **376**, 1133 (2007).
12. C. M. Yan, Y. Zhang, H. X. Yin, Y. H. Yan, and Y. H. Zhao, *Astron. Nachr.* **330**, 398 (2009).
13. D. Barret and M. Boutelier, *Mon. Not. R. Astron. Soc.* **384**, 1519 (2008).
14. S. M. Morsink and L. Stella, *Ap. J.* **513**, 827 (1999).
15. S. Boutloukos, M. van der Klis, D. Altamirano, M. Klein-Wolt, R. Wijnands, P. G. Jonker, and R. P. Fender, *Ap. J.* **653**, 1435; also **664**, 596 (2006).
16. G. Török, P. Bakala, E. Šrámková, Z. Stuchlík, and M. Urbanec, *Ap. J.* **714**, 748 (2010).
17. H. Quevedo and L. Parkes, *Gen. Rel. Grav.* **21**, 1047 (1989).
18. D. Bini, A. Geralico, O. Luongo and H. Quevedo, *Class. Quantum Grav.* **26**, 225006 (2009).
19. D. Bini, K. Boshkayev, and A. Geralico, *Class. Quantum Grav.* **29**, 145003 (2012).
20. L. A. Pachón, J. A. Rueda, and C. A. Valenzuela-Toledo, *Ap. J.* **756**, 82 (2012).
21. D. Bini, K. Boshkayev, R. Ruffini, and I. Siutsou, *Nuovo Cim.* **36C**, 1 (2013).
22. R. P. Kerr, *Phys. Rev. Lett.* **11**, 237 (1963).
23. M. A. Abramowicz and W. Kluzniak, *Astroph. Space Sci.* **300**, 127 (2005).
24. R. W. Wald, *General Relativity* (University of Chicago Press, Chicago, 1984).
25. A. T. Okazaki, S. Kato, and J. Fukue, *Publ. Astron. Soc. Japan* **39**, 457 (1987).
26. C. A. Perez, A. S. Silbergleit, R. V. Wagoner, and D. E. Lahr, *Ap. J.* **476**, 589 (1997).
27. M. A. Abramowicz et al., gr-qc/0312070.
28. J. B. Hartle and K. S. Thorne, *Ap. J.* **153**, 807 (1968).
29. E. Berti, F. White, A. Maniopoulou, and M. Bruni, *Mon. Not. R. Astron. Soc.* **358**, 923 (2005).
30. M. Méndez, M. van der Klis, R. Wijnands, E. C. Ford, J. van Paradijs, and B. A. Vaughan, *Ap. J.* **505**, L23 (1998).
31. M. Méndez and M. van der Klis, *Ap. J.* **517**, L51 (1999).
32. M. Méndez and M. van der Klis, *Mon. Not. R. Astron. Soc.* **318**, 938 (2000).
33. M. Méndez and T. Belloni, *Mon. Not. R. Astron. Soc.* **381**, 790 (2007).
34. D. Steeghs and J. Casares, *Ap. J.* **568**, 273 (2002).
35. C. Zhang, *Int. J. Mod. Phys. D.* **10**, 625 (2001).
36. B. Mukhopadhyay, *Ap. J.* **694**, 387 (2009).
37. R. Belvedere, K. Boshkayev, J. A. Rueda, and R. Ruffini, *Nucl. Phys. A* **921**, 33 (2014).